NOVEL DESIGNS FOR UNDULATOR BASED POSITRON SOURCES

M. Jenkins

Cockcroft Institute, Warrington, Cheshire, UK

Lancaster University, Lancaster, UK

June 29, 2015

Abstract

Proposed high energy electron-positron linear colliders require a high flux of positrons. To achieve this a number of new positron source designs have been proposed. One of these is an undulator-based positron source, which is the baseline positron source design for the International Linear Collider. The undulator-based positron source for the International Linear Collider uses a helical undulator to produce a intense photon beam that generates positrons through the pair-production mechanism. As a helical undulator is used the photon beam is polarised and this results in polarised positrons being produced.

This thesis investigates the undulator-based positron source design and aims to optimise it for positron production at the International Linear Collider. To do this the undulator is studied in detail as there is a large scope to design a bespoke undulator for positron production. As the particle physics community is interested in having a high positron polarisation the undulator-based positron source needs to be optimised for yield and polarisation. In order to optimise the design of the helical undulator we derive an analytical equation for the radiation produced by a helical undulator. This is done to provide some understanding of how the different undulator parameters affect the photon spectrum produced by a helical undulator. In addition to the analytical equation, new software is used to calculate the photon spectra produced by non-ideal undulators in order to evaluate how a realistic undulator-based positron source would function. Using suggestions proposed in this thesis we could expect to see an increase in positron yield of of 10.9 % and an increase in positron polarisation from 21.93 % to 41.93 %.

Declaration

I declare that this thesis is my own work and has not been submitted in substantially the same form for the award of a higher degree elsewhere. Where any published work has been used it has been appropriately reference.

Contents

List of Figures

List of Tables

Chapter 1

Introduction

For over 2,500 years there have been theories proposing that matter is made up of particles. In the 5^{th} and 6^{th} centuries BC ancient Indian and Greek philosophers proposed the doctrine of atomism. Atomism postulated that matter had two fundamental components; atoms, from the Greek word *atomos* which means indivisible, and the empty void. There was thought to be an infinite variety of atoms which were indestructible and immutable particles. Atoms travelled through the void either scattering off each other or coalescing to form the structures of the macroscopic world[2].

The philosophical idea of matter consisting of particles continued up to the the 17th century when it was expanded by Pierre Gassendi who proposed the particle theory of light[3]. Isaac Newton expanded upon the particle nature of light to explain reflection, refraction and diffraction[4]. The particle nature of matter remained based on philosophical reasoning rather than empirical evidence until the 19th century when John Dalton through his chemical experiments determined that each element was composed of a unique particle[5]. Believing these particles were fundamental he named them atoms.

By the end of the 19^{th} century it was known that atoms were not fundamental particles but were in fact made up of smaller particles. Through the 20^{th} century physicists have been accelerating these subatomic particles to higher and higher energies searching for the fundamental particles of matter. The first particle accelerators used electrostatic fields to accelerate particles however they were limited in their energy reach due to electrical breakdown. To overcome this limit particle accelerators which use radio frequency (RF) electromagnetic fields to accelerate particles were developed in the 1920's. The development of RF particle accelerators led to the discovery of new particles; in the 1960's the number and variety of new particles being discovered prompted the development of a self-consistent theory known as the *Standard Model*[6] which became firmly established with the discovery of quarks in the 1970's.

The Standard Model provided a theoretical framework which could explain the majority of questions in particle physics. However there remain questions which can not be answered by the Standard Model. In order to investigate predictions of and problems with the Standard Model and other theories in particle physics new experiments need to be conducted.

The experimental method used to test the Standard Model that is relevant to this thesis is use of high-energy particle colliders. These consist of two intense beams of particles being accelerated up to high energies and then being collided together inside a detector. There are three main categories of particle collider: lepton-lepton, hadron-hadron and lepton-hadron (see section 1.1). Some of the questions that could be answered by future lepton-lepton and lepton-hadron colliders are discussed in section 1.2.

This thesis is concerned with lepton-lepton colliders, specifically future linear machines colliding electrons and positrons. Two possible future linear machines are the International Linear Collider and the Compact Linear Collider: these are discussed in more detail in section 1.5. Both of these machines require a very high flux of electrons and positrons in order to provide enough particle interactions to ensure high precision measurements. Although a high electron flux, $10^{14}\,\mathrm{s}^{-1}$, is challenging it is possible to achieve by refining the current technology. The positron flux is much harder to achieve as there is no direct production mechanism. This thesis investigates the undulator-based positron source, one of the proposed high intensity positron source designs (see section 1.6), and attempts to use simulations with realistic undulator field patterns to attempt to optimise the design.

1.1 Particle Accelerators

To address the open questions of particle physics the development of new particle accelerators will be required. Most of these questions require that we look at high energies; the anticipated scale is of the order of tera-electron volts (TeV). However all the questions require that we search with particle accelerators with a high luminosity ($\mathcal{L}$), which is the rate of particle interactions per unit area per unit time. The instantaneous luminosity of a particle accelerator which has two bunches of particles, with populations of n_1 and n_2, colliding head on with a frequency f is given by

$$\mathcal{L} = f\frac{n_1 n_2}{4\pi\sigma_x\sigma_y} \tag{1.1}$$

where both bunches are assumed to be Gaussian and of identical size, where σ_x is the horizontal extent and σ_y is the vertical extent of the bunches[7].

Currently the only TeV-scale collider that is operating is the LHC, a circular proton-proton collider, at CERN. The LHC has successfully collided protons with a centre of mass energy greater

than 7 TeV and is currently being upgraded to run at its original design energy of 14 TeV[8]. The LHC is designed to make discoveries and has already discovered the Higgs boson; however, in order to make high-precision measurements of the properties of new particles a lepton-lepton collider is required.

1.1.1 Lepton-Lepton Colliders

Hadron colliders are limited in the precision with which they can measure some of the properties of particles. This limit arises from the nature of the particles that they collide, as hadrons are composite particles made up of quarks and gluons, which are known collectively as partons. As such the collisions that happen in hadron colliders are not actually between two hadrons but are parton collisions. It is impossible to identify exactly which quark or gluon interacted and as such it is not possible to exactly determine the initial energy of the collision. In comparison lepton-lepton colliders do not suffer from this problem as leptons are fundamental particles. Therefore the properties of the particles involved in the collisions are known to a much higher accuracy.

The fundamental nature of leptons allows physicists to perform energy scan experiments as the total energy of the leptons is used in the collision. This means it is possible to tune lepton-lepton colliders to have the exact energy required to produce a specific particle and therefore produce a large number of a particular particle to study its properties. There is interest in using one of the two proposed lepton-lepton colliders as a *Higgs-factory* in order to make very precise measurements of the Higgs coupling cross-sections to determine if it is a Standard Model Higgs[9].

Two proposed electron-positron colliders are the International Linear Collider (ILC) and the Compact Linear Collider (CLIC). The ILC is designed to run with a centre of mass energy range of 0.25 to 1.0 TeV. CLIC is designed to be built in stages, the first stage will provide collisions with a centre of mass energy of 0.5 TeV whilst the final stage would collide particles at 3 TeV. A detailed list of parameters for the ILC can be found in [10] and for CLIC in [11].

1.2 Questions in Particle Physics to be Answered by Future Linear Colliders

The Standard Model is a theory describing electromagnetic, strong and weak forces and their interactions with subatomic particles. The Standard Model has been developed throughout the late 20^{th} century and accurately describes the current experimental results. There are a number of open questions in particle physics that are not answered by the Standard Model. A thorough discussion of these questions is outside the scope of this thesis, but an overview of the main open

questions is given in [12, 13]. However as any future particle accelerator will be motivated by a physics case; a few of the more relevant questions are highlighted here.

1.2.1 The Higgs Boson

Current theory and experiments propose a new type of field, the Higgs field, that gives other matter its mass. The Higgs boson is the particle associated with this field. In 2012 the ATLAS and CMS collaborations at the Large Hadron Collider (LHC) announced the discovery of a new particle in the 125 GeV mass range. This particle is thought to be a Higgs boson, however to determine whether it is a Standard Model Higgs or a more exotic Higgs boson its properties and couplings must be measured accurately.

A key property of the Standard Model Higgs is that the coupling strength of the Higgs to each fermion and boson is proportional to the mass of the fermion or boson. These couplings can be measured at the LHC however due to the noisy environment at the interaction point of hadron machines the accuracy of this measurement is limited. In comparison the interaction region of a linear electron-positron machine is very *clean*. This means that these couplings can be measured more accurately.

In addition to the Standard Model Higgs couplings there are a number of new physics models that have Higgs coupling strengths that differ from the Standard Model by a quantity called the *Decoupling Limit*[14]. In much of the parameter space the Decoupling Limit is as small as 10 %. This means that for a large number of new physics models the Higgs coupling needs to be measured to better than 10 % to determine if the discovered particle is actually the Standard Model Higgs. This level of accuracy is only available at lepton-lepton machines. The International Linear Collider is expected to measure all couplings of the Higgs Boson to known fermions and bosons with an accuracy of better than 3 % [15].

1.2.2 Supersymmetry

Although the Standard Model has proved very accurate at predicting experimental results there are limits to the theory. Some of the most important limits of the Standard Model are:

- The gravitational force is not described at all.
- The gauge coupling constants for the three fundamental forces described in the Standard Model do not meet when extrapolated to the grand unification scale.
- Radiative corrections to the Higgs boson mass squared are quadratically divergent.
- There is no cold dark matter candidate, a stable massive electrically neutral particle that only interacts weakly, in the standard model.

Supersymmetry (SUSY) is an extension to the Standard Model which predicts a partner to every particle in the Standard Model[16]. SUSY provides one solution to the problems of the Standard Model described above. SUSY appears in superstring theories which provide a quantum description of gravity. SUSY particles are a key component of string theory. The discovery of SUSY particles could provide experimental proof of string theories. This means that the discovery of SUSY will advance work into unifying the four fundamental forces into a theory of everything.

SUSY prevents the mass of the Higgs boson from acquiring large radiative corrections as the contributions from Standard Model particles are cancelled by their supersymmetric partners. The SUSY particles change the evolution of the gauge coupling constants so that they now unify. As the particles predicted by SUSY have not yet been observed this means that if they exist they must be massive, weakly interacting or both. Under SUSY all particles gain a new property which is called R-parity[17]. R-parity describes the supersymmetric nature of the particles with Standard Model particles have a positive R-parity and their SUSY partners a negative R-parity. In R-parity symmetry-preserving models the lightest supersymmetric particle (LSP) is absolutely stable and in many scenarios has the correct properties to be a cold dark matter candidate.

Although the LHC is expected to detect the existence of SUSY particles a linear collider will have a key role to play in SUSY searches. This is because the properties of the SUSY particles will need to be measured with very high accuracy to distinguish between different SUSY models. The ILC will be able to make detailed measurements of the lightest tau *slepton*. This is important since it is expected to be the lightest *sfermion* and the next-to-lightest super particles (NLSP) over a large range of SUSY parameters in many important versions of the Minimal Super Symmetric Model[18]. Therefore the ILC can use results from the decays of the lightest tau *slepton* to identify which models of SUSY are no longer valid[19, 20].

1.2.3 Leptoquarks

A new type of boson that has couplings to an electro-quark pair is predicted to existing some models. These particles appear as squarks (supersymmetric partners of quarks) in certain models of supersymmetry which have R-parity violation. They also appear in various grand unification theories and extensions to colour theory. These new bosons have both leptonic and baryonic quantum numbers and are therefore referred to as *leptoquarks*. *Leptogluons* may also exist which could be produced by a fusion between electrons or positrons and a gluon in *ep* collisions.

Leptoquarks are expected to have a contribution to lepton flavour violation (LFV). LFV is where lepton number is not conserved at a vertex of a Feynman diagram. The two main channels used to search for LFV are $l \to \gamma l'$ and $Z \to ll'$[21]. A future linear collider has the

capability of producing a very high flux of Z bosons [22] and as a result is very suitable for LFV searches. Through measuring the branching ratio of LFV decays, particularly $Z \to ll'$, to very high accuracy the ILC or CLIC is expected to be able to infer the presence of leptoquarks if they exist.

1.3 Linear and Circular Colliders

Traditionally most high-energy physics colliders have been circular machines which accelerate two-beams of particles in opposing directions in a ring. The particles are bent into a circular orbit by magnetic fields. The particles can then travel in their orbit indefinitely if they are not perturbed from it. This means it is very easy to accelerate particles in circular machines as only one accelerating section is required as the particles will pass through the accelerating cavities gaining energy on every transit of the collider. Naively this would mean that it is very easy to build compact, high-energy circular machines. However, there is are practical limits on the maximum energy a particle can have in a given circular collider. These limits arise from te maximum achievable magnetic field strength and the emission of synchrotron radiation by a particle when travelling on a curved trajectory. In order to create a circular orbit dipole magnets (also called bending magnets) are used. The derivation of synchrotron radiation from a bending magnet is important to this thesis and is given in section 2.2.

1.3.1 The Synchrotron Radiation Problem

When a charged particle is accelerated it radiates. A detailed derivation on the radiation emitted by a charged particle travelling along an arbitrary path is included in Chapter 2. To discuss the synchrotron radiation problem in high energy accelerators we only need to consider the power radiated by a relativistic particle. The power radiated by a non relativistic point charge is given by the Larmor formula:

$$\mathbf{P}' = \frac{2q^2}{3c^3}|\mathbf{a}'|^2 \tag{1.2}$$

where q is the charge of the particle, c is the speed of light and $|\mathbf{a}'|^2$is given by

$$|\mathbf{a}'|^2 = a'_0 a'^0 + a'_k a'^k = \vec{a}.\vec{a} \tag{1.3}$$

In the instantaneous rest frame $a'_0 = 0$ therefore equation (1.2) in the covariant form is:

$$\mathbf{P} = \frac{2q^2}{3c^3}\vec{a}.\vec{a} \tag{1.4}$$

The Larmor formula has been modified so that it calculates the total power, P, radiated by

a relativistic charged particle [23]. In the laboratory reference frame the radiated power is:

$$P = \frac{2}{3} r_c mc\gamma^6 \left(\dot{\boldsymbol{\beta}}^2 - (\beta \times \dot{\boldsymbol{\beta}})^2 \right) \tag{1.5}$$

where $\beta = v/c$, $\dot{\boldsymbol{\beta}}$ is the derivative of $\boldsymbol{\beta}$ with respect to time and r_c is the classical radius of the charged particle which is:

$$r_c = \frac{q^2}{4\pi\epsilon_0 mc^2} \tag{1.6}$$

The product $\left(\dot{\boldsymbol{\beta}}^2 - (\beta \times \dot{\boldsymbol{\beta}})^2 \right)$ describes the motion of the particle. As we are interested in the difference between radiation from linear and circular accelerators we will decompose the particle's acceleration into two components parallel and perpendicular to $\boldsymbol{\beta}$:

$$\dot{\boldsymbol{\beta}} = \dot{\boldsymbol{\beta}}_{\parallel} + \dot{\boldsymbol{\beta}}_{\perp} \tag{1.7}$$

Substituting equation (1.7) into (1.5) allows us to calculate the power emitted by acceleration parallel to $\boldsymbol{\beta}$, $P_{\parallel}$, and acceleration perpendicular to $\boldsymbol{\beta}$, $P_{\perp}$.

$$P_{\parallel} = \frac{2}{3} r_c mc\gamma^6 \dot{\boldsymbol{\beta}}_{\parallel}^2 \tag{1.8}$$

$$P_{\perp} = \frac{2}{3} r_c mc\gamma^4 \dot{\boldsymbol{\beta}}_{\perp}^2 \tag{1.9}$$

These two equations are very similar except for the energy dependence. What equations (1.8) and (1.9) show is that for relativistic particles, where $\gamma >> 1$ the radiated power is less if the acceleration is parallel to the direction of motion compared to the case where the acceleration is orthogonal to the direction of motion.

Relating this back to circular and linear particle accelerators, typically the majority of acceleration experienced by a particle is parallel to the particle's direction of travel in a linear machine compared to circular machines which accelerate particles orthogonally. We can now expand the parallel and perpendicular components of $\dot{\boldsymbol{\beta}}$. Taking the parallel case first the acceleration is related to the accelerating force by:

$$m\dot{\boldsymbol{v}}_{\parallel} = \frac{1}{\gamma^3} \frac{\mathrm{d}\boldsymbol{p}_{\parallel}}{\mathrm{d}t} \tag{1.10}$$

As $\dot{\boldsymbol{\beta}}_{\parallel} = \dot{\boldsymbol{v}}_{\parallel}/c$ equation (1.8) becomes

$$P_{\parallel} = \frac{2}{3} \frac{r_c}{mc} \left(\frac{\mathrm{d}\boldsymbol{p}_{\parallel}}{\mathrm{d}t} \right)^2 \tag{1.11}$$

Therefore the power radiated parallel to the direction of motion is independent of the energy

of the particle. This means that the synchrotron radiation power from a linear machine only depends on the accelerating force applied to the particles. As a result synchrotron radiation does not limit the energy reach of a linear particle accelerator.

Now considering the case where the acceleration is perpendicular to the direction of motion we again need to calculate the accelerating force. In this case the accelerating force is due to the Lorentz force when there is no electric field:

$$\frac{\mathrm{d}\boldsymbol{p}_\perp}{\mathrm{d}t} = \gamma m \dot{\boldsymbol{v}}_\perp = q(\boldsymbol{v} \times \boldsymbol{B}) \tag{1.12}$$

where $\boldsymbol{B}$ is the magnetic field strength.

In a circular machine dipole magnets are used to steer the beam around the machine. Therefore we can replace the magnetic field in the Lorentz Force equation with the magnetic field of a dipole required to bend a particle with charge, q, into a circular path with a bending radius, ρ. Equation (1.12) now becomes

$$\frac{\mathrm{d}\boldsymbol{p}_\perp}{\mathrm{d}t} = \gamma m \dot{\boldsymbol{v}}_\perp = q\left(c\beta \times \frac{\beta\gamma mc}{q\rho}\right) \tag{1.13}$$

Substituting this into equation (1.9) means that the power radiated by a charged particle travelling in a circular orbit with a bending radius, ρ, is given by

$$P_\perp = \frac{2}{3}\frac{r_c}{\rho^2} mc^3 \beta^4 \gamma^4 \tag{1.14}$$

Unlike the parallel case the radiated power due to acceleration orthogonal to the direction of motion depends on the energy of the particle. Using the relationship $E = \gamma mc^2$ we can rewrite equation (1.14) as

$$P_\perp = \frac{2}{3}\frac{r_c}{\rho^2} \beta^4 \frac{E^4}{m^3 c^5} \tag{1.15}$$

This means that for relativistic particles where $\beta \approx 1$ the radiated power due to a transverse accelerating force scales as the particle energy to the fourth power and is inversely proportional to the mass of the particle cubed and the square of the bending radius.

To illustrate how synchrotron radiation affects circular particle accelerators we will consider the Large Electron-Positron (LEP) collider [24] and the LHC, both built at CERN. LEP was the highest centre of mass energy electron positron collider constructed. LEP was constructed in a tunnel with a circumference of 27 km. After LEP was decommissioned the LHC was constructed inside the LEP tunnel. Although the two machines have the same circumference their bending radii are slightly different. Even though the bending radii are not the same they are close enough

to allow a comparison of the power radiated by particles experiencing a transverse accelerating force in LEP and the LHC.

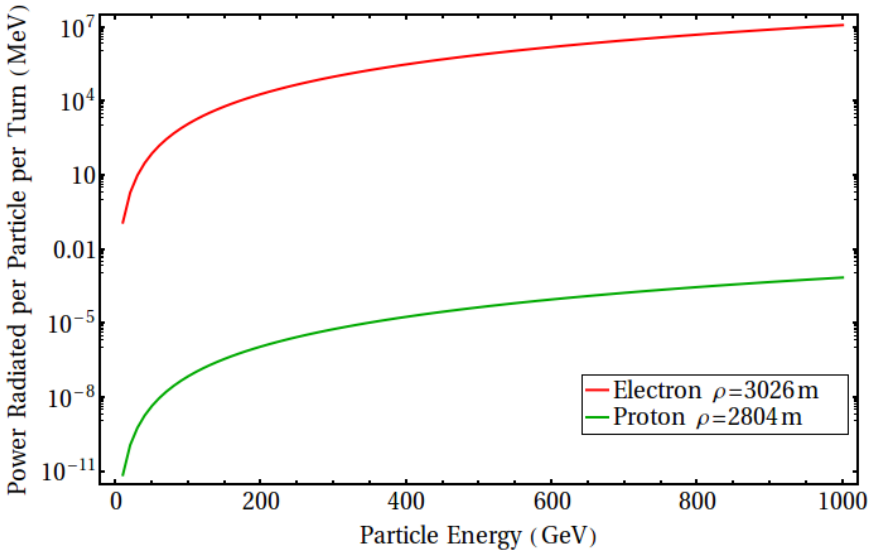

Figure 1.1: Plot of the synchrotron power radiated per turn as a function of beam energy for electrons and protons in the LEP tunnel calculated using equation (1.15). The red curve corresponds the the energy lost by an electron witha bending radius $\rho = 3026\,\text{m}$ and the green the energy lost by a proton $\rho = 2804\,\text{m}$.

Figure 1.1 shows the synchrotron power radiated per turn as a function of beam energy for electrons and protons in the LEP tunnel. From this plot we can see that the lower mass electrons radiate a lot more power than the heavier protons. The ILC is aiming for an initial centre of mass energy of 500 GeV; if a new electron positron collider which attempted to match the ILC centre of mass energy was built inside the LEP tunnel each electron at the collision energy would radiate 48.65 GeV per turn. This highlights why circular TeV scale lepton machines have to be linear as the power loss due to synchrotron radiation is extremely high and the only way to reduce it is to increase the bending radius which would mean that the accelerator would become impractically large.

1.4 Polarised Positrons

The polarisation of a particle beam is related to the intrinsic spin of the particles comprising the beam. The spin of a particle is a quantum mechanical property that describes the intrinsic angular momentum of that particle. Spin has no classical analogue unlike orbital angular momentum which is the quantum mechanical equivalent of classical angular momentum. The existence of spin was discovered in experiments such as the Stern-Gerlach experiment in which particles are observed to have angular momentum which cannot be explained by orbital angular momentum alone[25]. The polarisation of a particle beam along a specific direction is defined as [26]:

$$P = \frac{N^+ - N^-}{N^+ + N^-} \tag{1.16}$$

where N^+ and N^- are the number of particles with their spin parallel and anti parallel to the chosen quantisation axis respectively. An e^+e^- collider that has both beams longitudinally polarised allows the interaction cross-sections to be decomposed into σ_{RR}, σ_{LL}, σ_{RL} and σ_{LR} which are defined in Figure 1.2. The overall interaction cross-section for a polarised e^+e^- collider is given by:

$$\begin{aligned} \sigma_{P_{e^-}P_{e^+}} &= \frac{1}{4}[(1+P_{e^-})(1+P_{e^+})\sigma_{RR} + (1-P_{e^-})(1-P_{e^+})\sigma_{LL} \\ &\quad +(1+P_{e^-})(1-P_{e^+})\sigma_{RL} + (1-P_{e^-})(1+P_{e^+})\sigma_{LR}] \end{aligned} \tag{1.17}$$

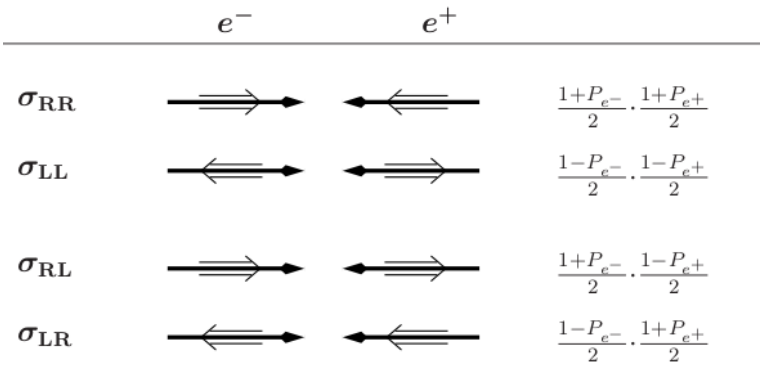

Figure 1.2: Definition of the interaction cross-sections for various longitudinal spin configurations in an e^+e^- collider. The bold arrow shows the direction of motion of the particle and the other arrow shows the spin direction. The fractional contribution of each cross-section to the overall interaction cross-section is a product of the first and final columns, P_{e^-} and P_{e^+} are calculated using Equation (1.16). This is reproduced from [12].

The two types of interaction in a e^+e^- collider are annihilation events and exchange events. In an annihilation process the helicities of the two-beams are directly coupled to each other. This means that for Standard Model processes where recombination is to a vector particle only particles with opposite helicities, LR and RL, can interact. If annihilation occurred when the particles had the same helicities, LL or RR, a scalar particle would be produced and this would be a sign of new physics as the only fundamental scalar particle in the Standard Model is the Higgs boson. Exchange processes can produce a particle that is either a vector, scalar or a fermion. The helicities of the two incoming particles are independent which means that all helicity configurations are possible.

For Standard Model annihilation processes only σ_{RL} and σ_{LR} contribute this means that the overall cross-section of interaction is:

$$\begin{aligned}\sigma_{P_{e^-}P_{e^+}} &= \frac{1+P_{e^-}}{2}\frac{1-P_{e^+}}{2}\sigma_{RL} + \frac{1-P_{e^-}}{2}\frac{1+P_{e^+}}{2}\sigma_{LR} \\ &= (1-P_{e^+}P_{e^-})\sigma_0[1-P_{\text{eff}}A_{LR}]\end{aligned} \tag{1.18}$$

where σ_0 is the unpolarised cross-section, P_{eff} is the effective polarisation and A_{LR} is the left right asymmetry. The effective luminosity $\mathcal{L}_{\text{eff}}$ such that the ratio $(\mathcal{L}/\mathcal{L}_{\text{eff}})$ is the fraction of interacting particles, where $\mathcal{L}$ is the luminosity as defined in Equation (1.1). The cross-section for the interaction defined in Equation (1.18) becomes:

$$\sigma_{P_{e^-}P_{e^+}} = 2\sigma_0\frac{\mathcal{L}_{\text{eff}}}{\mathcal{L}}(1-P_{\text{eff}}A_{LR}) \tag{1.19}$$

with

$$\sigma_0 = \frac{\sigma_{RL}+\sigma_{LR}}{4} \tag{1.20}$$

$$A_{LR} = \frac{\sigma_{LR}-\sigma_{RL}}{\sigma_{LR}+\sigma_{RL}} \tag{1.21}$$

$$P_{\text{eff}} = \frac{P_{e^-}-P_{e^+}}{1-P_{e^-}P_{e^+}} \tag{1.22}$$

$$\mathcal{L}_{\text{eff}} = \frac{1}{2}(1-P_{e^+}P_{e^-})\mathcal{L} \tag{1.23}$$

This means that by producing two polarised beams with different polarisations at an e^+e^- collider it is possible to increase the sensitivity of the machine to any left-right asymmetry. This can allow for more precise measurements of differences in interaction strengths and also help detect any events that are not part of the symmetric background.

The suppression of background events is extremely important for the detection of new physics. For example at an e^+e^- collider the two dominant production cross-sections for the Higgs boson are via WW fusion and Higgs-strahlung[27]. With polarised beams it is possible to measure the two couplings separately by suppressing WW production by colliding right-handed electrons with left-handed positrons[28]. This is because the W-boson only couples to left handed particles and right handed antiparticles.

1.5 Proposed High Energy Linear Colliders

The only high-energy linear e^+e^- collider ever built was the Stanford Linear Collider (SLC) which was completed in 1989[29]. The SLC was approximately 4 km long and achieved a centre of mass energy of nearly 100 GeV. By comparison the ILC is designed to achieve 5 to 10 times

the centre of mass energy of the SLC and is going to be 31 km long whilst CLIC is aiming to reach 30 times the SLC centre of mass energy and will be over 41 km long.

1.5.1 International Linear Collider

The International Linear Collider (ILC) is a proposed e^+e^- collider that is currently going through a technical design review (TDR) stage. The ILC has been designed as a superconducting linear collider that will have a centre of mass energy range of 0.5 to 1.0 TeV and a peak luminosity of $2 \times 10^{34} \mathrm{cm}^{-2} s^{-1}$. The current ILC layout is shown in Figure 1.3 which highlights the locations of the major subsystems including:

- The polarised electron source, based on a photo cathode DC gun
- The undulator-based positron source, located at the end of the electron main linac
- The electron and positron damping rings. These are designed to accept particles with an energy of 5 GeV
- Electron and Positron Main Linacs. Each linac consists of approximately 15 km of accelerating structures.
- Beam Delivery System
- Interaction Point (IP). As there is only one interaction point and two detectors a system is being developed to move the detectors in and out of the IP region.
- Detectors. The two detector collaborations at the ILC are the International Large Detector (ILD) [30] and the Silicon Detector (SiD)[31].

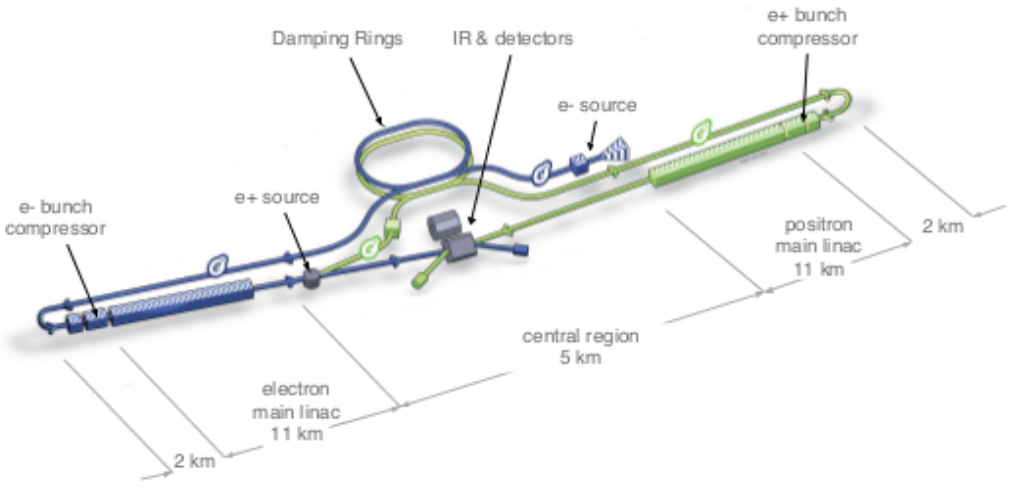

Figure 1.3: Schematic Layout of the International Linear Collider[32].

The ILC is designed to be constructed and upgraded in stages. The first stage is for a collider with a centre-of-mass energy of 500 GeV. To achieve this energy the superconducting radio frequency (SCRF) cavities have a nominal accelerating gradient requirement of 31.5 MV/m.

The ILC uses an electron source and injector system, based on a photo cathode DC electron gun, to create and accelerate electron bunches up to an energy of 5 GeV. These bunches then travel along the electron source to ring (ESTR) transfer line and are injected into the electron damping ring. The electron bunches are in the damping ring for 1 ms while their phase space volume is damped to achieve the parameters required to meet the luminosity goals. The electron bunches are extracted from the damping ring and travel along the ring to main linac (RTML) transfer line and are injected into the electron main linac.

In the main linac the electron beam is accelerated up to 250 GeV. Once the beam energy is at 250 GeV the electrons travel through a dogleg into the helical undulator of the positron source. The undulator section is several hundred metres long. At the end of the undulator section the electron beam passes through another dogleg back into the main linac. Whilst in the undulator the electrons lose approximately 2 % of their energy and so must be accelerated back up to 250 GeV before entering the beam delivery system (BDS). The BDS is used to transport the beam to the interaction point (IP). As the beam travels through the BDS it is collimated and focussed. The final section before the IP is called the *final focus* and this is used to ensure the beam is focussed to a very small spot size. Due to there only being one IP at the ILC and two detectors the final focus is split between the BDS and the detectors.

Positron Generation at the International Linear Collider

The energy loss experienced by the electrons travelling through the helical undulator is due to the generation of synchrotron radiation (SR). Due to the energy of the electrons this SR is in the gamma ray regime. The gamma rays are collimated and are then incident on a thin conversion target made of a high Z metal. Electron-positron pairs are created in the target through the pair-production mechanism. The electrons and positrons are captured and accelerated to 125 MeV. The electrons and positrons are then separated using a dipole magnet. The electrons are sent through a short transfer line to a dump. The positrons are then accelerated to 5 GeV before travelling along the positron source to ring (PSTR) transfer line to be injected into the positron damping ring. After damping the positrons are extracted and travel along the positron RTML. The positrons are injected into the positron main linac. They are accelerated up to 250 GeV and travel through the positron BDS to the IP where they collide with the electron beam. This positron source design is the main focus of this thesis. A more general overview of proposed positron sources for future linear colliders is given in section 1.6.

As the positron bunches are created from electron bunches travelling through the helical undulator this couples the electron and positron arms of the ILC. This coupling places constraints on the geometry and parameters of the machine to ensure that the arrival of a positron bunch exactly coincides with the arrival of an electron bunch at the IP. The possibility of uncoupling the electron and positron arms using a different positron source design is explored in chapter 7.

The International Linear Collider Parameters

The main ILC parameters are presented in Table 1.1. They are taken from the parameter table in the ILC Technical Design Report. The requirements of the particle physics community led to the decision to have a range of operational parameters rather than a single operating point. The different operating configurations span an energy range of 300 GeV. Since the changes in parameters that may be required during operation are not very predictable, an operating plane is defined, rather than an operating point. Designing the machine to work with a wide range of parameters introduces more challenges into the machine design. However this should make it easier for the machine to reach the design luminosity during operation.

Table 1.1: Main ILC TDR Beam Parameters[32].

Parameter	Symbol	Units	200	230	250	350	500
Bunch Charge	N	10^{10}	2.0	2.0	2.0	2.0	2.0
Number of Bunches	n_b		1312	1312	1312	1312	1312
RMS Bunch Length	z	μm	0.3	0.3	0.3	0.3	0.3
RMS Horizontal Beam Size at IP	x^*	nm	904	789	729	684	474
RMS Vertical Beam Size at IP	y^*	nm	7.8	7.7	7.7	5.9	5.9
Repetition Rate	f_{rep}	Hz	5	5	5	5	5
Electron Linac Rate	f_{linac}	Hz	10	10	10	5	5

1.5.2 Compact Linear Collider

The Compact LInear Collider (CLIC) is another proposed e^+e^- collider. The design for CLIC is currently evolving. The centre-of-mass energy at CLIC is intended to reach 3 TeV with a luminosity of the order $10^{34}\text{cm}^{-2}s^{-1}$. To achieve this CLIC is using a different accelerating technology to the ILC. The novel two-beam acceleration system that CLIC is using to reach the design energy along with the other major subsystems are shown in figure 1.4. These systems include:

- The polarised electron source - based on a photocathode DC gun.
- The unpolarised positron source - this is a hybrid target system.
- The electron and positron pre-damping rings - reduce the emittance of the particle beams created by the sources to a level that allows them to be injected into the damping ring.

- The electron and positron damping and pre-damping rings - reduce the emittance of the particle beams even further to the level required to achieve the design luminosity.
- The drive beam accelerator - accelerates a very high current electron beam to 2.38 GeV with a gradient of 2.4MV/m.
- Delay loops and combiner rings - change the timing structure of the high current drive beam to match that required by the main linacs.
- Power Extraction and Transfer Structures (PETS) - decelerate the drive beam to accelerate the physics beam.
- Electron and Positron Main Linacs - each linac consists of approximately 15 km of accelerating structures.
- Beam Delivery System - transports the particle beams from the end of the main linac to the Interaction Point.
- Interaction Point - because there is only one interaction point and two detectors a system is being developed to move the detectors.

The SCRF accelerating cavities that are planned for use at the ILC are limited in the acceleration gradient they can achieve. This is due to strong magnetic fields being generated in the SCRF cavities which can quench them. To reach higher centre-of-mass energies the length of the linacs can be increased but this increases the cost of the machine and becomes impractical. Instead CLIC uses a two-beam acceleration mechanism. This consists of a main linac constructed from normally-conducting RF cavities that are powered by a high current drive beam instead of klystrons.

The drive beam accelerator is 1 km long and accelerates the electron beam to 2.38 GeV. The drive beam accelerator is run at a repetition rate of 1.0 GHz. The drive beam produced at the end of the accelerator is made up of uniformly spaced bunches which do not match the structure of the main physics beam. To match the main physics beam a series of delay loops and combiner rings is used to restructure the beam. Figure 1.5 is a schematic of the delay loop and the beam structure before and after the delay loop. The drive beam travels through a RF deflector where the *even bunches* are kicked into a delay loop and the *odd bunches* travel straight through. This reduces the bunch spacing and creates a pulse structure in the beam.

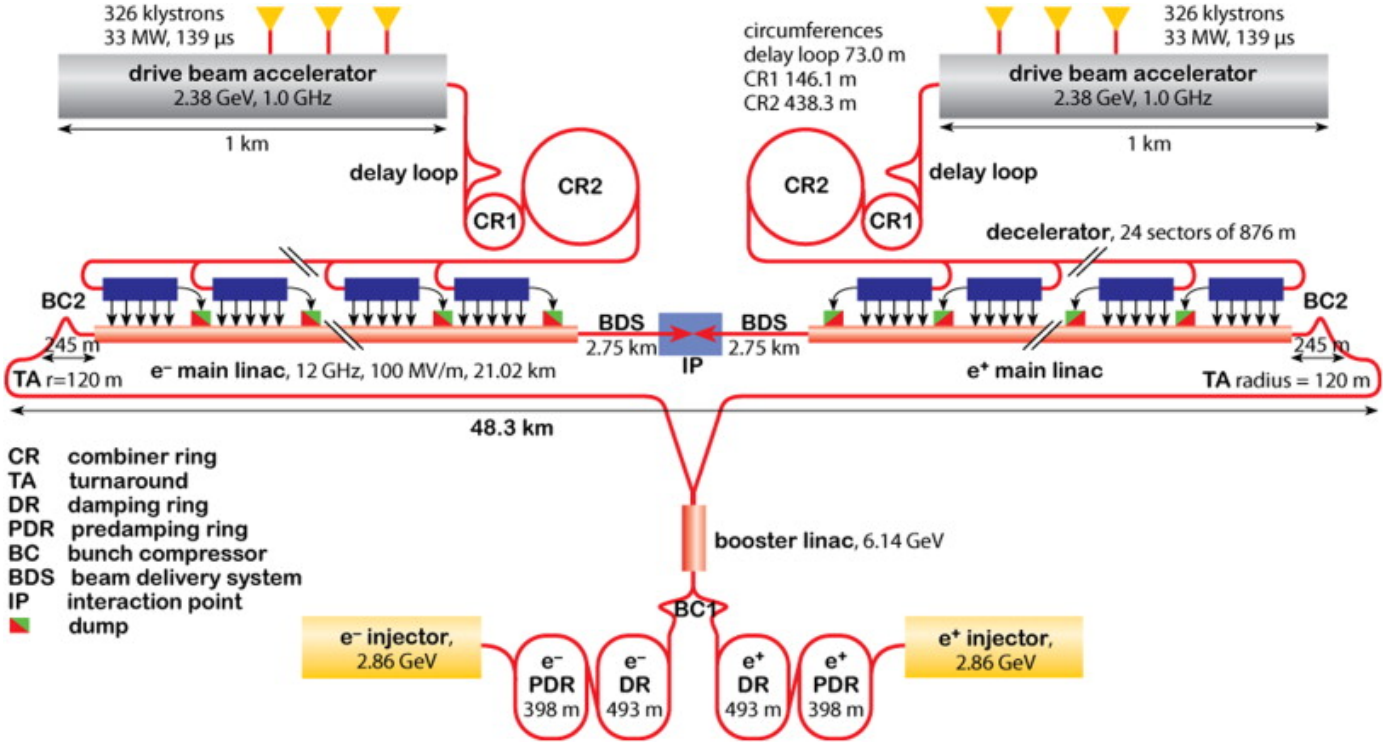

Figure 1.4: Schematic Layout of the Compact Linear Collider[33].

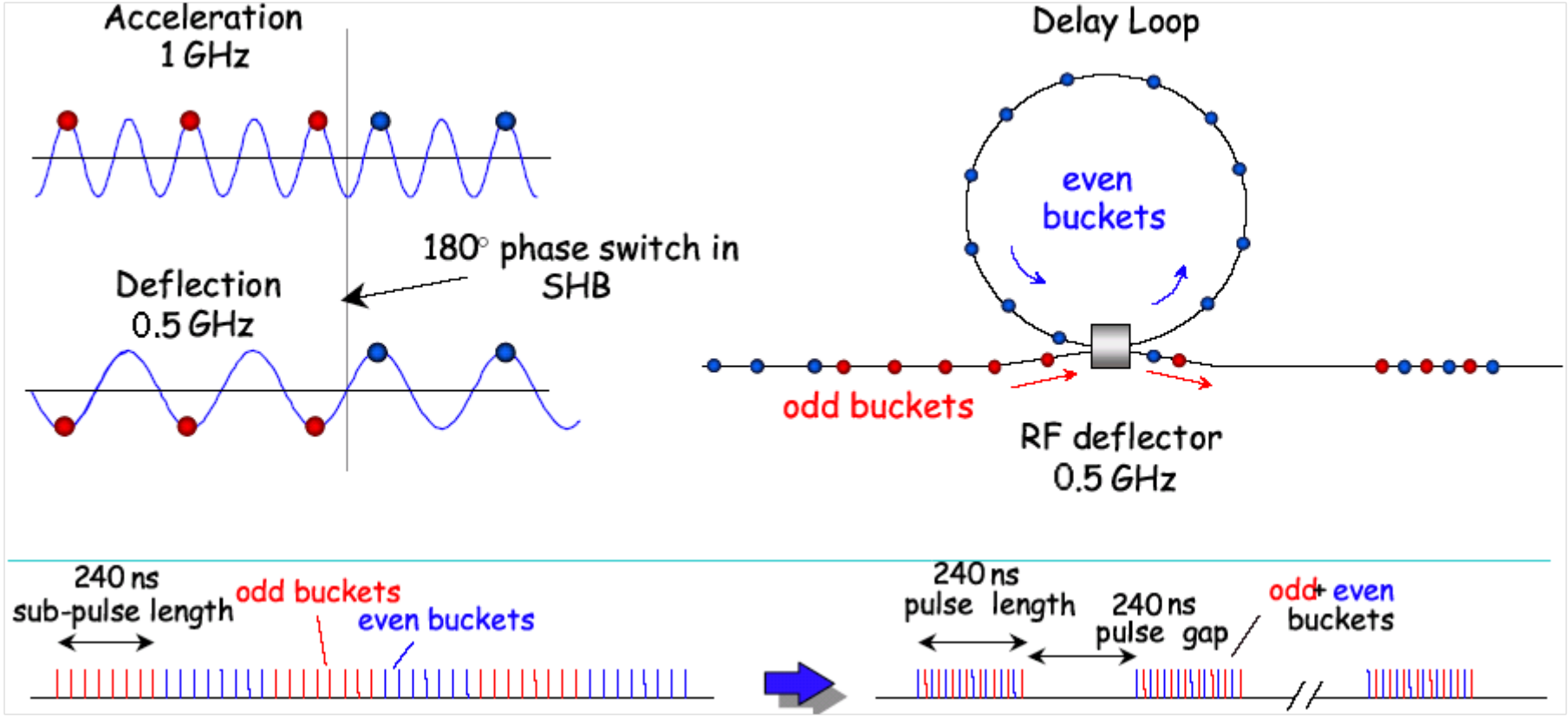

Figure 1.5: Schematic layout of the delay loop forming part of the drive beam accelerator at CLIC. An RF deflector is used to divert bunches into the delay loop until it is filled. The RF deflector is then turned off and an equal number of bunches travel through the RF deflector. As the bunches travel through the deflector they are interleaved with the bunches from the loop.

Once the beam has been through the delay loop it then travels through a number of combiner rings. The combiner rings perform a similar function to the delay loop however rather than reducing the bunch spacing by a factor of two they can reduce it by an integer factor of up to five. CLIC uses two combiner rings, the first with a combination factor of three and the second with a combination factor for four, to match the structure of the drive beam to the physics beam.

Once the drive beam has the correct timing structure it enters the decelerator section. This consists of 24 sections of Power Extraction and Transfer Structures (PETS). The PETS extract energy from the drive beam, decelerating it, and use transfer lines to power the RF cavities in the main linac with the extracted energy. This allows for a very high accelerating gradient, target gradient of 100 MV/m, in the main linac. There is a limitation of this method of acceleration which is that CLIC can only run at a limited number of pre-set centre-of-mass energies. This is due to the design of the PETS as they designed to be used in stages which means rather than having full control of the centre of mass energy the centre of mass energy has to be increased or decreased in steps.

Unlike at the ILC, the positron and electron arms of CLIC are uncoupled as CLIC uses a different positron source design. The baseline positron source design at CLIC is a hybrid-target positron source[33]. The positron and electron beams are created in two injection sections. These sections include a small normally-conducting linac that is used to accelerate the beams up to 2.86 GeV so that they can be injected into the pre-damping rings. The pre-damping rings are used to reduce the emittance of the electron and positron beams so that they have the correct phase space distribution to allow them to be injected into the damping rings. The damping rings reduce the phase space distribution even more so that the positron and electron beams have a small enough emittance to travel through the main linacs and reach the IP withe the correct beam parameters to generate the required luminosity. The electrons and positrons leave the damping rings and enter the first bunch compressor which reduces the RMS bunch length before injecting the beams into the booster linac which accelerates them up to 6.14 GeV. The beams then travel along two transfer lines to the turnarounds which are arcs with a radius of 120 m, made up of dipole and quadrupole magnets. The beams then go through the second bunch compressors to reduce the RMS bunch length even more before they are injected into the main linac. The CLIC main linacs are 21 km long with a frequency of 12 GHz, an accelerating gradient of 100 MV/m and a repetition rate of 50 Hz. Once the beams are accelerated up to the desired centre-of-mass energy, nominally 3 TeV, they exit the main linacs and travel through a 2.75 km BDS to the IP. Just as at the ILC, CLIC only has one IP but will have two detectors and so they will operate on a similar push-pull system as at the ILC.

Compact Linear Collider Parameters

CLIC has been design to be constructed in a number of stages. As the design of CLIC is still evolving the final number of construction stages and beam parameters for them have still to be finalised. Currently CLIC is planned to be constructed in two stages and the parameters for each of these stages are shown in Table 1.2. The parameters are taken from the CLIC CDR[11].

Table 1.2: Main CLIC CDR Beam Parameters.

Parameter	Symbol	Units	500 GeV	3 TeV
Bunch Charge	N	10^{10}	0.68	0.372
Number of Bunches per pulse	n_b		354	312
Repetition Rate	f_{rep}	Hz	50	50
Accelerating gradient	G	MV/m	80	100
Peak Luminosity	L_{total}	$10^{34}\mathrm{cm}^{-2}s^{-1}$	2.3	5.9

1.6 High Intensity Positron Sources

There are several designs proposed for high intensity positron sources for future linear colliders. A summary of the *conventional* positron source, undulator-based positron source, hybrid-target positron source and LASER-Compton positron source designs. This thesis concentrates on the undulator-based positron source design.

1.6.1 *Conventional* Positron Source

The SLC used a *conventional* positron source, a schematic of this type of source is shown in Figure 1.6. A *conventional* source consists of an electron beam with an energy of approximately 5 GeV impinging on a target made of a high Z material. The electrons interact with the atoms of the conversion target to produce positrons via the Bethe-Heitler pair production mechanism[34]. Figure 1.7 shows the Feynman diagram for this mechanism. The SLC used a 6 GeV electron beam impinging on a tungsten target four radiation lengths thick. The choice of beam energy and target thickness is due to the cross-section of interactions of the incoming electrons with the nucleons within the tungsten.

The positron yield achieved at the SLC was $6 \times 10^{12}\mathrm{e}^{+}/s$. However the positron yield requirements of the ILC and CLIC are much higher. Table 1.3 shows the positron yield requirements of these future colliders and how they compare to the SLC. The machine with the closest yield requirement to the SLC is CLIC, which needs 18 times the SLC yield. To achieve this increase in yield a new generation of high intensity positron sources are needed.

The next generation of high intensity positron sources use gamma rays incident on a target to produce positrons. This reduces the load on the targets and increases the efficiency of positron

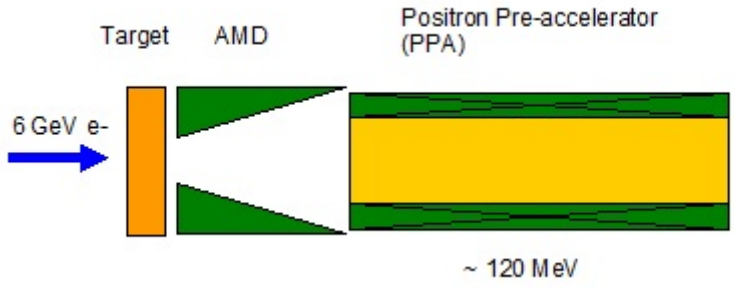

Figure 1.6: Schematic of a *Conventional* Positron Source. A 6 GeV electron beam generated from a dedicated electron gun and linac collides with a production target to pair-produce electrons and positrons which care captured and focused by an Adiabatic Matching Device (AMD) before being accelerated in a linac to 120 MeV.

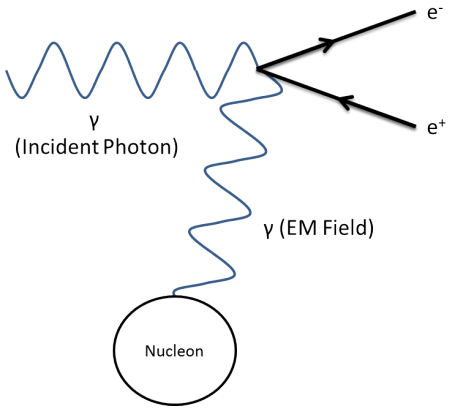

Figure 1.7: Diagram for the Bethe-Heitler pair-production mechanism.

production. There are three main types of sources in this new generation, they are the undulator-based positron source, hybrid target positron source and LASER-Compton positron source. Also there is work ongoing to develop the conventional positron source to achieve higher yields than that achieved at the SLC[35]. The different types of high intensity positron sources are being developed for different colliders and as such they all have different requirements of the source. Table 1.4 details which source design is the baseline source for each collider as well as any upgrade paths or alternatives source designs being investigated.

Table 1.3: Positron yield requirements of ILC and CLIC compared to the achieved positron yield at the SLC.

	SLC	ILC (500 GeV)	CLIC (3 TeV)
e^+per bunch at IP	4.0×10^{10}	2.0×10^{10}	0.372×10^{10}
e^+per bunch before DR	5.0×10^{10}	3.0×10^{10}	0.76×10^{10}
Bunches per pulse	1	1312	312
Repetition Rate (Hz)	120	5	50
Bunches per second	120	6560	15600
e^+/s	0.06×10^{14}	2.0×10^{14}	1.1×10^{14}

Table 1.4: High intensity positron sources for future colliders. B stands for baseline source, U stands for the upgrade source and A stands for alternative source.

	ILC	CLIC
Undulator-based	B	A
Hybrid Target	-	B
LASER Compton	A	U

1.6.2 Hybrid Target Positron Source

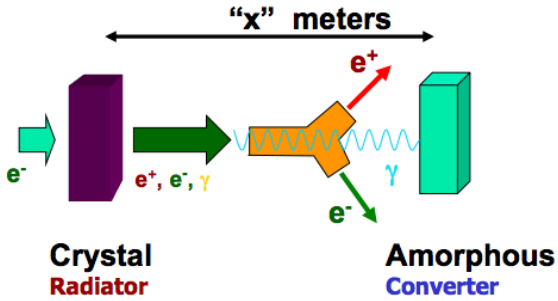

Figure 1.8: Schematic of a Hybrid Target Positron Source. An electron beam with an energy of less than 10 GeV is incident on a thin crystal target. The electrons radiate high energy photons as they traverse the crystal target. The electrons and any positrons that are produced from interactions within the crystal target are separated from the photon beam. The photons then impinge on a thick amorphous target usually made from a tungsten alloy. The photons interact inside the amorphous target producing positrons via the pair-production mechanism.

The Hybrid Target Positron Source is being developed at KEK, a schematic of this source is shown in Figure 1.8. The design of this source is an evolution of the *conventional* positron source design. The hybrid target source uses an electron beam with an energy of a few to 10 GeV and a thick target of high Z material as found in a *conventional* source. However, in a hybrid target source an additional target is placed in front of the thick target. This additional target is a thin crystalline target aligned so that a specific axis of the crystal is parallel to the electron trajectory. The electron beam impinges on the crystal target and as the electrons travel through the crystal the nuclei deflect the electrons. Due to the alignment of the nuclei and the electron beam the crystal target acts as a wiggler causing the electrons to emit synchrotron radiation. A dipole magnet is placed between the two targets to extract the electron beam as well as any electrons and positrons created by pair-production in the crystal target. The photons emitted within the crystalline target travel straight through the dipole magnet and impinge on the thick target. The photons then generate positrons in the target via the pair-production mechanism. To increase the survivability of the thick target it is designed to have an amorphous structure. This should reduce the effect of thermal shocks due to the photon beam within the target.

The Hybrid Target Positron Source is the baseline positron source at CLIC. Currently the design for CLIC has two hybrid target stations in parallel to allow for the load on the targets

to be reduced without affecting positron yield. To ensure survivability and to demonstrate the efficiency of the hybrid target source design experiments are being performed using the KEKB linac. The KEKB linac provides an 8 GeV electron beam to the crystalline target. The typical bunch charge used in the experiment was 1.5 nC and the repetition rate was varied between 1 and 25 Hz. The bunch charge is comparable to the bunch charge at CLIC. However, at KEKB there is only one bunch per pulse compared to over 300 bunches per pulse at CLIC. These ongoing experiments will allow for benchmarking of simulations as well as finalising the parameters of the source particularly the dimensions of the amorphous target.

1.6.3 LASER-Compton Positron Source

The proposal for a polarised positron source using Compton scattering of an electron beam and a laser to create gamma rays which are used to produce positrons was presented at Snowmass 2005 [36]. The LASER-Compton source was initially designed as an alternative source for the ILC. However, as the CLIC design developed the LASER-Compton scheme became the preferred upgrade path to provide polarised positrons at CLIC. The LASER-Compton source design is based on two physics processes, backward Compton scattering and pair-production, as shown in the schematic in Figure 1.9.

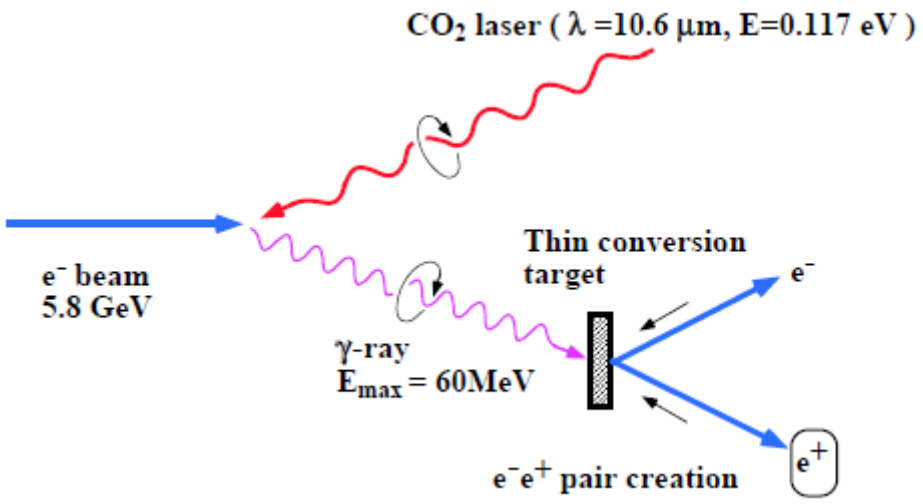

Figure 1.9: Schematic of the physics processes present in a LASER-Compton Positron Source[37].

The kinematics of Compton scattering are determined by the energy of the electron beam, the energy of the laser photons, the angle of interaction between the laser and electron beam and the backscattering angle which is the angle between the electron beam and the photons produced by Compton scattering. For a given electron beam and laser the peak energy of the backscattered photons occurs when the laser photons and electrons collide head on and the backscattering angle

is π. This is not a trivial setup to achieve and most experiments use complex mirror cavities to control the interaction between the laser photons and the electron beam. Experiments have been conducted to determine the expected photon energy spectrum that would be produced from a LASER-Compton source.

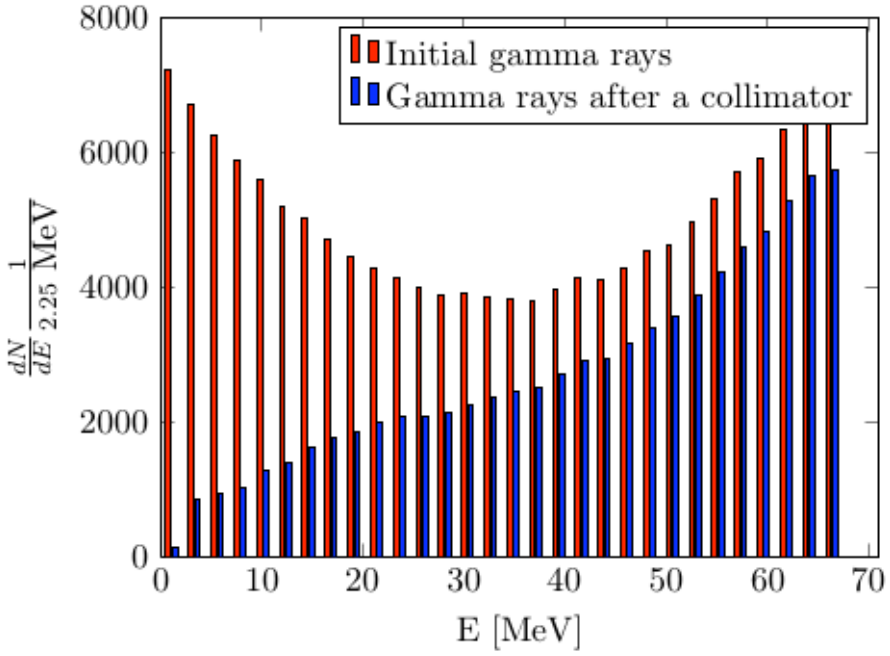

Figure 1.10: Plot showing the photon spectrum produced from a Compton source designed for the CLIC positron source[38]. The red spectrum is for the initial photon spectrum and the blue spectrum is the collimated photon spectrum.

The scattered photon spectrum is shown in Figure 1.10. The photon spectrum shows two peaks; one when the energy of the scattered photon is zero and the other at the maximum energy. Unlike the cross-section the polarisation of the scattered photons depends on the polarisation of the electron and laser separately.

The requirements on the laser light for this source design are much stricter than those on the electron beam. To produce the required number of gamma-rays for positron production a certain number of laser photons have to scatter off each electron. The ILC and CLIC need a gamma-ray flux of $10^{16}s^{-1}$. To achieve this a high laser power focused to a very small laser waist where the electrons will collide with the laser photons is required.

Due to the high bunch charge required at the ILC the design is to use a large number of electron laser interaction points. Each interaction point has a mirror cavity powered by a laser and the electron beam travels through each cavity in turn. The positrons produced from the gamma-rays generated at each interaction point are coalesced into one bunch in a damping ring. At CLIC the principle is to only have one interaction point that uses a very advanced non-planar four-mirror Fabry-Perot cavity to achieve the required laser power to produce the gamma-ray

flux. This is an area that is still undergoing a large amount of development and an experiment is being carried out at the Accelerator Test Facility at KEK in Japan [39].

Just as with the undulator-based source and the hybrid-target source the photons created from the Compton back scattering are incident on a thin conversion target. Positron and electron pairs are created within the conversion target through the pair-production mechanism. These pairs are then captured, accelerated and then separated with the electrons being dumped and the positrons being transported to the damping ring.

1.6.4 Undulator-based Positron Source

The undulator-based positron source was first developed for the proposed TESLA collider[40]. The principle behind an undulator-based positron source is to use a high-energy electron beam travelling through a long, 100 m, undulator to produce gamma rays. The gamma rays are then collimated and impinge on a thin conversion target made of high Z material. Positrons and electrons are produced in the conversion target from the incoming photons via the pair-production mechanism. The positrons and electrons are captured and then accelerated up to 125 MeV before the electrons and positrons are separated with the electrons being dumped and the positrons being transported towards the damping ring. Figure 1.11 shows the schematic of and undulator based positron source. An undulator-based positron source is the baseline positron source for the ILC. Chapter 3 covers all major components of an undulator based positron source in detail.

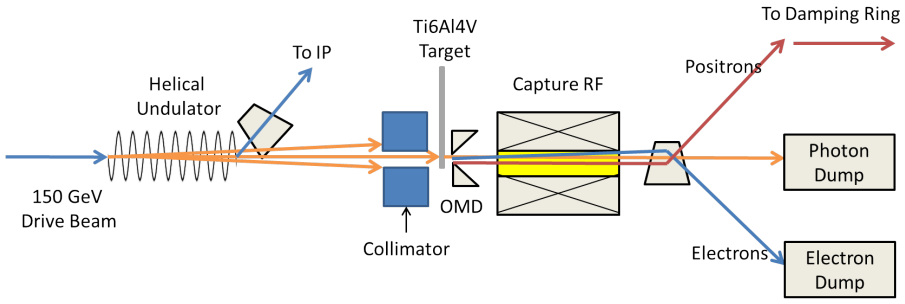

Figure 1.11: Schematic of an Undulator-based Positron Source showing the main components including the helical undulator, photon collimator, conversion target, Optical Matching Device (OMD), capture RF and dumps for the photons and electrons. For more details about these components see Chapter 3.

1.7 Thesis Outline

In Chapter 2 of the thesis the theory of synchrotron radiation generation by a charged particle will be described. This will then be used to discuss the radiation produced by electrons travelling

through dipole magnets.

Chapter 3 uses the mathematical framework of chapter 2 to derive the radiation produced by an electron travelling through an insertion device. Particular attention is paid to the details of the synchrotron radiation spectrum produced from an undulator.

In Chapter 4 the design of an undulator-based positron source will be outlined. The main components of the source will be explained with discussion of the relevant theoretical principals. The baseline ILC undulator-based positron source parameters from the ILC Technical Design Report[41] will be described. Included in Chapter 4 is work conducted by the author of the thesis on Nb_3Sn undulators as part of the ILC TDR research and development.

Chapter 5 will concentrate on the how the magnetic field in an undulator module effects the synchrotron radiation produced by an electron travelling through the module. This has been the main area of study for this thesis. Particular attention will be given to the spectrum produced from a *realistic* ILC undulator module. Novel undulator configurations will also be explored with the aim of achieving an optimal photon spectrum for positron production.

The different undulator spectra generated in Chapter 5 will be simulated through the ILC baseline positron source in Chapter 6. The source parameters will be optimised for various running options at the ILC including for a 500 GeV electron beam travelling through the undulator. The optimisation of different parameters will be done for yield, polarisation and both yield and polarisation.

Novel undulator-based positron source designs will be looked at in Chapter 7. These designs include a multi-target undulator-based positron source and using an undulator-based positron source as a positron amplifier. The possibility of using an FEL as a positron source is also explored.

Finally, Chapter 8 summarises the conclusions reached and suggests areas that would benefit from future work. This thesis presents theory and simulations of undulator-based positron sources for the ILC. However, there remains a large amount of work, especially experimental R&D, to realise the designs for the positrons sources and the colliders themselves.

Chapter 2

Synchrotron Radiation

The principle component of an undulator-based positron source is an undulator magnet. An undulator is a type of insertion device (ID). IDs are periodic magnetic structures that stimulate brilliant, forward-directed synchrotron radiation emission. The radiation is emitted by forcing beams of charged particles to perform *wiggles* or *undulations* as they travel through the ID.

This chapter will describe the theory of synchrotron radiation emission. This theory will then be applied to calculate the radiation from a dipole magnet. This will allow for the derivation of the radiation produced by an insertion device in chapter 3.

2.1 Synchrotron Radiation emitted by charged particles in accelerator-like orbits

In order to calculate the synchrotron radiation that is emitted by an ID first we need to be able to describe the radiation produced by a relativistic charged particle travelling along an arbitrary path. Synchrotron radiation is produced when a relativistic charged particle is accelerated. To calculate the radiation produced we need to define an observation position relative to an origin (Figure 2.1). If a photon emitted by a charged particle is observed then by the time the photon arrives at the observer the charged particle will have moved. Therefore we will need to use the *retarded time* in our calculations.

For a photon observed at time t and emitted at time t', the relationship between t and t' is given by

$$t = t' + \frac{R(t')}{c} \tag{2.1}$$

where $R(t')$ is the length of the path along which the photon travelled to the observer. As the

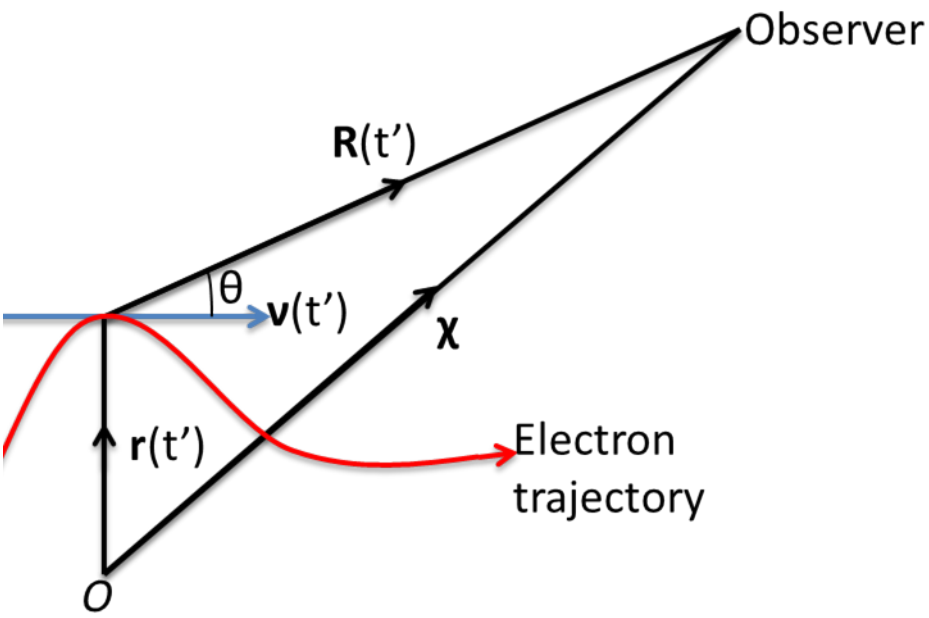

Figure 2.1: Position of an observer relative to the origin and the trajectory of a charged particle.

photon is the gauge boson of the electromagnetic force we can use the equations of electromagnetism to calculate the photon flux seen by an observer due to synchrotron radiation.

Maxwell's equations expressed in terms of the electric, **E**, and magnetic flux density, **B**, fields are

$$\nabla \cdot \mathbf{B} = 0 \tag{2.2}$$

$$\nabla \times \mathbf{E} + \frac{\partial \mathbf{B}}{\partial t} = 0 \tag{2.3}$$

$$\nabla \cdot \mathbf{E} = \frac{\rho}{\epsilon_0} \tag{2.4}$$

$$\nabla \times \mathbf{B} - \frac{1}{c^2}\frac{\partial \mathbf{E}}{\partial t} = \mu_0 \mathbf{J} \tag{2.5}$$

where ρ is the charge density, $\mathbf{J}$ is the current density, ϵ_0 is the permittivity of free space and μ_0 is the permeability of free space. Equations (2.2) and (2.3) have no source terms in them. This implies that the vector fields, **E** and **B**, can be expressed in terms of scalar and vector potentials, ϕ and $\mathbf{A}$[42].

We can express the electric field **E** as a function of the scalar and vector potentials as shown below

$$\mathbf{E} = -\nabla\phi - \frac{\partial \mathbf{A}}{\partial t} \tag{2.6}$$

and the magnetic field $\mathbf{B}$ in terms of the vector potential

$$\mathbf{B} = \nabla \times \mathbf{A} \tag{2.7}$$

Applying the Lorenz gauge condition [42]

$$\nabla \cdot \mathbf{A} + \frac{1}{c^2}\frac{\partial \phi}{\partial t} = 0 \tag{2.8}$$

to equations (2.4) and (2.5) will give two wave equations expressed in terms of the scalar and vector potentials, ϕ and $\mathbf{A}$, and the charge and current densities, ρ and $\mathbf{J}$. This allows us to relate the scalar and vector potentials to the charge and current densities.

This means that we can write down two equations

$$\nabla^2 \phi - \frac{1}{c}\frac{\partial^2 \phi}{\partial t^2} = -\frac{\rho}{\epsilon_0} \tag{2.9}$$

$$\nabla^2 \mathbf{A} - \frac{1}{c^2}\frac{\partial^2 \mathbf{A}}{\partial t^2} = -\mu_0 \mathbf{J} \tag{2.10}$$

which when solved for the scalar and vector potentials will fully describe the electric and magnetic fields. The resulting scalar and vector potentials are termed the Liénard-Wiechert potentials being evaluated in the Lorenz gauge.

2.1.1 Electric and Magnetic Fields at Observer

The Liénard-Wiechert potentials can be used to calculate the electric and magnetic fields at an observer. If the vector from the origin to the observer is $\mathbf{x}$ and the vector from the origin to the position of the charged particle when a photon is emitted is $\mathbf{r}(t')$. The path along which the photon travels, $\mathbf{R}(t')$, can be written as

$$\mathbf{R}(t') = \mathbf{x} - \mathbf{r}(t') \tag{2.11}$$

differentiating gives

$$\frac{d\mathbf{R}(t')}{dt'} = -\frac{d\mathbf{r}(t')}{dt'} = -\mathbf{v}(t') \tag{2.12}$$

where $\mathbf{v}(t')$ is the velocity of the electron. Using the identity

$$\mathbf{a}(t) \cdot \frac{d\mathbf{a}(t)}{dt} = a(t)\frac{da(t)}{dt} \tag{2.13}$$

we can calculate $\mathbf{n}(t')$ which is the unit vector pointing towards the observer along $\mathbf{R}(t')$

$$\begin{aligned} R(t')\frac{dR(t')}{dt} &= \mathbf{R}(t')\frac{d\mathbf{R}(t')}{dt} \\ &= -\mathbf{R}(t')\cdot\mathbf{v}(t') \qquad (2.14) \\ \frac{dR(t')}{dt} &= -\frac{\mathbf{R}(t')}{R(t')}\cdot\mathbf{v}(t') \\ &= -\mathbf{n}(t')\cdot\mathbf{v}(t') \qquad (2.15) \end{aligned}$$

Differentiating the observation time, equation (2.1), with respect to t' gives

$$\frac{dt}{dt'} = 1 + \frac{1}{c}\frac{dR(t')}{dt'} \qquad (2.16)$$

replacing $dR(t')/dt'$ with the result from equation (2.15) gives

$$\frac{dt}{dt'} = 1 - \mathbf{n}(t')\cdot\boldsymbol{\beta}(t') \qquad (2.17)$$

where $\boldsymbol{\beta}(t')$ is the particle velocity as a function of t' divided by the speed of light.

Using the above equations and Green's functions the wave equation for the scalar potential can be solved for the scalar potential at the observer. For a wave equation of the form

$$\nabla^2 u(\mathbf{x},t) - \frac{1}{c^2}\frac{\partial^2}{\partial t^2}u(\mathbf{x},t) = v(\mathbf{r},t') \qquad (2.18)$$

solutions can be written in the form

$$u(\mathbf{x},t) = \int G(\mathbf{R},t-t')v(\mathbf{r},t')d\tau' \qquad (2.19)$$

where $G(\mathbf{R},t-t')$ is the Green's function representing a potential generated by a point source at $\mathbf{r}$ and at time t'. The Green's function must obey a differential equation of the form

$$\nabla^2 G(\mathbf{s},t) - \frac{1}{c^2}\frac{\partial^2}{\partial t^2}G(\mathbf{s},t) = \delta(\mathbf{s})\delta(t') \qquad (2.20)$$

where $\mathbf{s}$ is a position vector and δ is the Dirac delta function. The solution to this differential equation can be written as

$$G(\mathbf{s},t) = \frac{1}{4\pi s}\delta(t \pm \frac{|\mathbf{s}|}{c}) \qquad (2.21)$$

For the geometry of our problem equation (2.21) becomes

$$G(\mathbf{R}, t - t') = \frac{1}{4\pi R}\delta(t - t' \pm \frac{|\mathbf{R}|}{c}) \tag{2.22}$$

due to the delta function equation (2.22) is only non-zero at two times

$$t = t' + \frac{|\mathbf{R}|}{c} \tag{2.23}$$

$$t = t' - \frac{|\mathbf{R}|}{c} \tag{2.24}$$

Equation (2.24) implies that the solution is non-zero when the wave is travelling backwards in time from some *advanced time*. The advanced time solution appears therefore to be non physical and shall be discarded. This leaves only the solution when t is given by equation (2.23). This solution corresponds with the definition of retarded time as given in (2.1).

The Green's function for the retarded time solution describes a spherical wave that is emitted from a point source located at $\mathbf{r}$ at the retarded time t' propagating at the speed of light until it is observed at time t a distance $|\mathbf{R}|$ away from where it was observed. As the wave travels forwards in time the amplitude decreases, with the observed amplitude inversely proportional to the distance of the observer from the source.

The electric and magnetic fields seen by an observer generated by a moving pointlike charge can be calculated using the scalar potential

$$\phi(\mathbf{x}, t) = \frac{q}{4\pi\epsilon_0}\left(\frac{1}{R(t')(1 - \boldsymbol{\beta}(t') \cdot \mathbf{n}')}\right) \tag{2.25}$$

and the vector potential

$$\mathbf{A}(\mathbf{r}, t) = \frac{\mu_0 q}{4\pi}\left(\frac{\dot{\mathbf{r}}(t')}{R(t')(1 - \boldsymbol{\beta}(t') \cdot \mathbf{n}')}\right) \tag{2.26}$$

where $\boldsymbol{\beta}(t')$ is the scaled velocity of the particle, also known as the relativistic beta factor. $\boldsymbol{\beta}(t')$ is given by

$$\boldsymbol{\beta}(t') = \frac{\dot{\mathbf{r}}(t')}{c} \tag{2.27}$$

We are now able to describe the radiation emitted by an electron at all points along its trajectory. The above equations correspond to a point source, by integrating this over all time and space we can determine the electric and magnetic fields from an arbitrary distribution of point sources. A detailed derivation of the electric and magnetic fields from the scalar and vector potentials is available in many textbooks including [42, 43].

From [43] the electric and magnetic fields at an observer are given by:

$$\mathbf{E}(t') = \frac{q}{4\pi\epsilon_0 c}\frac{1}{(1-\boldsymbol{\beta}\cdot\mathbf{m})^3}\left(\frac{c(1-\beta^2)(\mathbf{m}-\boldsymbol{\beta})}{r'^2} + \frac{\mathbf{m}\times((\mathbf{m}-\boldsymbol{\beta})\times\dot{\boldsymbol{\beta}}}{r'}\right) \quad (2.28)$$

$$\mathbf{B}(t') = \frac{1}{c}\left(-\frac{q}{4\pi\epsilon_0 c}\frac{1}{(1-\boldsymbol{\beta}\cdot\mathbf{m})^3}\left(\frac{c((1-\beta^2)\mathbf{m}-(1-\mathbf{m}\cdot\boldsymbol{\beta})\boldsymbol{\beta})}{r'^2} + \frac{(\mathbf{m}\cdot\dot{\boldsymbol{\beta}})\mathbf{m}}{r'}\right)\times\boldsymbol{\beta}\right) \quad (2.29)$$

The electric field equation has a term inversely proportional to r' and a term that is inversely proportional to r'^2. The term inversely proportional to r' is also dependent on $\dot{\beta}$ which is the acceleration term. If there is no acceleration then $\dot{\beta} = 0$ and the term inversely proportional to r' disappears. As a result this term is referred to as the acceleration field.

The component inversely proportional to r'^2 is similar to the classical form of the electric field due to the Coulomb force. The differences are actually the correction factor due to effects that arise from the charge distribution travelling at relativistic velocities. As a result this term is referred to as the velocity field.

We can simplify the equation for the magnetic field by representing all constants and scalars by Θ. Therefore equation (**??**) becomes

$$\mathbf{B}(t) = \frac{1}{c}(\Theta(\mathbf{m}'-\boldsymbol{\beta}))\times\boldsymbol{\beta} \quad (2.30)$$

We can rewrite the cross product using the vector identity

$$(\mathbf{A}-\mathbf{B})\times\mathbf{A} \equiv (\mathbf{A}-\mathbf{B})\times\mathbf{B} \quad (2.31)$$

which allows us to change from β to $\mathbf{m}'$ in the cross product giving

$$\mathbf{B}(t) = \frac{1}{c}(\Theta(\mathbf{m}'-\boldsymbol{\beta}))\times\mathbf{m}' \quad (2.32)$$

By comparing this with the equation for the electric field we can see that the magnetic field can be expressed in terms of the electric field:

$$\mathbf{B}(t) = \frac{1}{c}\mathbf{m}'\times\mathbf{E}(t) \quad (2.33)$$

Equation (2.33) implies that the magnetic and electric fields are always perpendicular and the magnitudes of the two fields are different by a factor of $1/c$.

2.1.2 The Poynting Vector

We now have equations representing the electric and magnetic fields due to moving charges as a function of time. In order to calculate the power radiated by the moving charge we need to derive the Poynting vector. The Poynting vector $\mathbf{S}$ describes the energy flow through space due to the electromagnetic fields. The definition of $\mathbf{S}$ in terms of $\mathbf{E}$ and $\mathbf{B}$ is

$$\mathbf{S} = \epsilon_0 c^2 (\mathbf{E} \times \mathbf{B}) \tag{2.34}$$

Using equation (2.33) we can express the Poynting vector in terms of the electric field only. This means that equation (2.34) becomes

$$\begin{aligned} \mathbf{S} &= \frac{1}{\mu_0 c}(\mathbf{E} \times (\mathbf{m}' \times \mathbf{E})) \\ &= \frac{1}{\mu_0 c}(E^2 \mathbf{m}' - (\mathbf{E} \cdot \mathbf{m}')\mathbf{E}) \end{aligned} \tag{2.35}$$

where the equation $c^2 = 1/(\epsilon_0 \mu_0)$ has been used to rewrite the constant factor. The electric field, given in equation (2.28), has terms that are proportional to $1/r'$ and $1/r'^2$. As r' increases the term proportional to $1/r'$ will dominate. Therefore at large r' we can ignore the term proportional to $1/r'^2$ and so the electric field becomes

$$\mathbf{E}(t) = \frac{q}{4\pi\epsilon_0 c}\left(\frac{\mathbf{m}' \times ((\mathbf{m}' - \boldsymbol{\beta}) \times \dot{\boldsymbol{\beta}})}{r'(1 - \boldsymbol{\beta} \cdot \mathbf{m}')^3}\right) \tag{2.36}$$

This is the electric field in the *far field* approximation. As a result of the far field approximation the electric field, as a consequence of the cross product, is always perpendicular to $\mathbf{m}'$. This implies that $\mathbf{E} \cdot \mathbf{m}' = 0$ therefore equation (2.35) becomes

$$\mathbf{S} = \frac{E^2 \mathbf{m}'}{\mu_0 c} \tag{2.37}$$

This means that in the far field region there are equal amounts of electric and magnetic energy moving at the speed of light in the direction of the unit vector $\mathbf{m}'$.

2.1.3 Fourier Transform of the Electric Field

We have an equation describing the electric field in the time domain observed due to an electron travelling along an arbitrary path. However expressing the electric field as a function of time does not allow for an intuitive interpretation. It would be much better to express the electric field in terms of the frequency. This would allow for a spectral analysis of the electromagnetic

radiation. To convert from the time domain to the frequency domain we use a Fourier Transform,

$$\mathbf{E}(\omega) = \frac{1}{\sqrt{2\pi}} \int_{-\infty}^{\infty} \mathbf{E}(t) e^{i\omega t} \mathrm{d}t \tag{2.38}$$

The integral is evaluated with respect to the observer time t. Assuming that we are in the far field region simplifies the algebra. However the equation for the electric field in the far field region is evaluated using the retarded time t'. As a result we can simplify the integral by changing the integration variable from t to t'. This can be done by replacing t with equation (2.1) and using equation (2.17) to change from $\mathrm{d}t$ to $\mathrm{d}t'$. This means that the Fourier Transform becomes

$$\mathbf{E}(\omega) = \frac{1}{\sqrt{2\pi}} \int_{-\infty}^{\infty} \mathbf{E}(t') e^{i\omega(t' + \frac{r'(t')}{c})} (1 - \mathbf{n}' \cdot \boldsymbol{\beta}(t')) \mathrm{d}t' \tag{2.39}$$

The Fourier Transform can be evaluated to

$$\begin{aligned} \mathbf{E}(\omega) &= \frac{1}{\sqrt{2\pi}} \frac{q}{4\pi\epsilon_0 c} \int_{-\infty}^{\infty} \left(\frac{\mathbf{m}' \times ((\mathbf{m}' - \beta) \times \dot{\boldsymbol{\beta}})}{r'(1 - \boldsymbol{\beta} \cdot \mathbf{m}')^2} \right) e^{i\omega(t' + \frac{r'(t')}{c})} \mathrm{d}t' \\ &= \frac{q}{4\pi\sqrt{2\pi}\epsilon_0 c r'} \left[\left[\frac{\mathbf{m}' \times (\mathbf{m}' \times \boldsymbol{\beta})}{(1 - \boldsymbol{\beta} \cdot \mathbf{m}')} e^{i\omega(t' + \frac{r'(t')}{c})} \right]_{-\infty}^{\infty} + i\omega \int_{-\infty}^{\infty} (\mathbf{m}' \times (\mathbf{m}' \times \boldsymbol{\beta})) e^{i\omega(t' + \frac{r'(t')}{c})} \mathrm{d}t' \right] \end{aligned} \tag{2.40}$$

As the first term in equation (2.40) is evaluated at $t' = \pm\infty$ it can be ignored as it will not be observed. This means that the equation for the electric field, in the far field region, observed due to an electron moving on an arbitrary path is

$$\mathbf{E}(\omega) = \frac{iq\omega}{4\pi\sqrt{2\pi}\epsilon_0 c r'} \int_{-\infty}^{\infty} (\mathbf{m}' \times (\mathbf{m}' \times \boldsymbol{\beta})) e^{i\omega(t' + \frac{r'(t')}{c})} \mathrm{d}t' \tag{2.41}$$

2.2 Synchrotron Radiation in a Bending Magnet

We can now calculate the synchrotron radiation produced by an electron travelling through a magnetic field. The simplest type of magnet used in particle accelerators are dipole or bending magnets. A dipole magnet has a uniform magnetic field and an electron travelling through such a field travels on a circular trajectory. Using dipole magnets to bend an electron into a complete circle is the most basic method of generating synchrotron radiation in particle accelerators. A particle accelerator constructed in such a manner is called a synchrotron.

Figure 2.2 shows the coordinate frame for an electron in a synchrotron. The three coordinates are x and y for the dimensions perpendicular to the electron trajectory and s is the coordinate in the direction of motion. ψ is the angle of the photon trajectory with respect to the $x-s$ plane

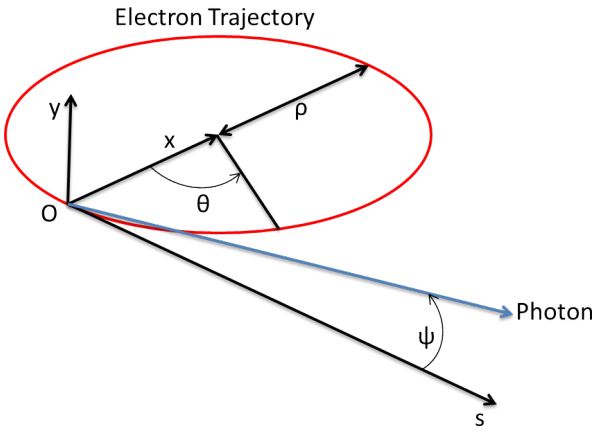

Figure 2.2: Coordinate system of an electron radiating a photon inside a synchrotron.

and θ is the angle in the $y-s$ plane. The angular velocity of the electron in a synchrotron is given by

$$\omega_0 = \frac{\beta c}{\rho} \tag{2.42}$$

where ρ is the bending radius of the electron which in this case is the actual radius of the synchrotron if the electron is on the design orbit. If we choose the retarded time such that $t' = 0$ when the electron is at the origin the position $\mathbf{r}(t')$, scaled velocity $\boldsymbol{\beta}(t')$ and scaled acceleration $\dot{\boldsymbol{\beta}}(t')$ of the electron are given by

$$\mathbf{r}(t') = \begin{pmatrix} x \\ y \\ s \end{pmatrix} = \begin{pmatrix} \rho(1-\cos\omega_0 t') \\ 0 \\ \rho\sin\omega_0 t' \end{pmatrix}, \boldsymbol{\beta}(t') = \begin{pmatrix} \beta\sin\omega_0 t' \\ 0 \\ \beta\cos\omega_0 t' \end{pmatrix}, \dot{\boldsymbol{\beta}}(t') = \begin{pmatrix} \beta\omega_0\cos\omega_0 t' \\ 0 \\ -\beta\omega_0\sin\omega_0 t' \end{pmatrix} \tag{2.43}$$

We can define the unit vector of the photon emission to be

$$\mathbf{n}' = \begin{pmatrix} 0 \\ \sin\psi \\ \cos\psi \end{pmatrix} \tag{2.44}$$

Assuming that we are in the far field region then we can use the equation for the electric field given in equation (2.41). The vector triple product in this equation is

$$\mathbf{n}' \times (\mathbf{n}' \times \boldsymbol{\beta}) = \begin{pmatrix} -\beta \sin \omega_0 t' \\ \beta \cos \psi \sin \psi \cos \omega_0 t' \\ -\beta \sin^2 \psi \cos \omega_0 t' \end{pmatrix} \tag{2.45}$$

As we are in the regime where the relativistic Lorentz factor,γ, is large we can make a series of angular approximations. The vertical opening angle of the radiation, ψ, is inversely proportional to γ. Therefore ψ is very small and only a small part of the electron trajectory contributes to the radiation seen by the observer, $\Delta\theta = \omega_0 t' \ll 1$. This means that we can approximate equation (2.45) using the small angle approximation to

$$\mathbf{n}' \times (\mathbf{n}' \times \beta) \approx \begin{pmatrix} -\beta\omega_0 t' \\ \beta\psi(1 - \frac{\psi^2}{2})(1 - \frac{(\omega_0 t')^2}{2}) \\ -\beta\psi^2(1 - \frac{(\omega_0 t')^2}{2}) \end{pmatrix} \approx \beta \begin{pmatrix} -\omega_0 t' \\ \psi \\ 0 \end{pmatrix} \tag{2.46}$$

We can express the terms of t' in equation (2.41) as

$$\begin{aligned} t' + \frac{r'(t')}{c} &= t' + \frac{\mathbf{n}' \cdot \mathbf{x}}{c} - \frac{\mathbf{n}' \cdot \mathbf{r}}{c} \\ &\approx t' + \frac{x}{c} - \frac{\rho}{c} \sin \omega_0 t' \cos \psi \end{aligned} \tag{2.47}$$

applying the small angle approximation to this gives

$$\begin{aligned} t' + \frac{r'(t')}{c} &\approx t' + \frac{x}{c} - \frac{\rho}{c}\left(\omega_0 t' - \frac{\omega_0^3 t'^3}{6}\right)\left(1 - \frac{\psi^2}{2}\right) \\ &\approx \frac{x}{c} + t'\left(1 - \frac{\rho\omega_0}{c} + \frac{\rho\omega_0\psi^2}{2c}\right) + \frac{\omega_0^3 t'^3 \rho}{6c}\left(1 - \frac{\psi^2}{2}\right) \end{aligned} \tag{2.48}$$

Using equation (2.42) we can replace ω_0 which gives

$$t' + \frac{r'(t')}{c} \approx \frac{x}{c} + t'\left(1 - \beta + \frac{\beta\psi^2}{2}\right) + \frac{\beta^3 t'^3 c^2}{6\rho^2}\left(1 - \frac{\psi^2}{2}\right) \tag{2.49}$$

As β is given by

$$\beta = \sqrt{1 - \frac{1}{\gamma^2}} \approx 1 - \frac{1}{2\gamma^2} \tag{2.50}$$

we can simplify equation (2.49) to

$$t' + \frac{r'(t')}{c} \approx \frac{x}{c} + t'\left(\frac{1}{2\gamma^2} + \frac{\psi^2}{2} - \frac{\psi^2}{4\gamma^2}\right) + \left(\frac{t'^3c^2}{6\rho^2} - \frac{t'^3c^2}{48\rho^2\gamma^6}\right)\left(1 - \frac{\psi^2}{2}\right)$$
$$\approx \frac{x}{c} + \frac{t'}{2\gamma^2}(1 + \gamma^2\psi^2) + \frac{t'^3c^2}{6\rho^2} \tag{2.51}$$

where all terms, except for the first, inversely proportional to orders of γ^2 or greater have been dropped. We can substitute equations (2.46) and (2.51) into our equation for $\mathbf{E}(\omega)$ (2.41) which gives

$$\mathbf{E}(\omega) = \frac{iq\omega}{4\pi\sqrt{2\pi}\epsilon_0 cr'}\int_{-\infty}^{\infty}(\beta\begin{pmatrix}-\omega_0 t'\\ \psi\\ 0\end{pmatrix}e^{i\omega(\frac{x}{c}+\frac{t'}{2\gamma^2}(1+\gamma^2\psi^2)+\frac{t'^3c^2}{6\rho^2})}\mathrm{d}t' \tag{2.52}$$

Using Euler's formula we can rewrite equation (2.52) as

$$\mathbf{E}(\omega) = \frac{iq\omega}{4\pi\sqrt{2\pi}\epsilon_0 cr'}\int_{-\infty}^{\infty}\beta\begin{pmatrix}-\omega_0 t'\\ \psi\\ 0\end{pmatrix}(\cos U + i\sin U)\mathrm{d}t' \tag{2.53}$$

where

$$U = \omega(\frac{x}{c} + \frac{t'}{2\gamma^2}(1 + \gamma^2\psi^2) + \frac{t'^3c^2}{6\rho^2})$$

We can use the approximation that for highly relativistic particles $\beta \approx 1$ to simplify equation (2.53). In addition the term $\omega x/c$ in the equation for U is a constant. This means that it just applies a phase shift to the cosine and sine functions. As this fixed phase shift is not relevant to the physics we can drop it from the equation. Using these approximations we can now solve for the electric field. By solving for the electric field in the x, y and s directions separately we can get more insight into the emitted radiation.

Intuitively from equation (2.53) it can be seen that $E_s(\omega) = 0$. This must be the case as we earlier found that $\mathbf{E}(\omega)$ must be perpendicular to $\mathbf{n}'$. We will now solve for the electric field in the x direction.

$$E_x(\omega) = \frac{-iq\omega\omega_0}{4\pi\sqrt{2\pi}\epsilon_0 cr'}\int_{-\infty}^{\infty}t'(\cos U + i\sin U)\mathrm{d}t' \tag{2.54}$$

The function $t'\cos U$ is an odd function. Therefore we can discount $t'\cos U$ from equation (2.54) which becomes

$$E_x(\omega) = \frac{q\omega\omega_0}{4\pi\sqrt{2\pi}\epsilon_0 c r'} \int_{-\infty}^{\infty} t' \sin\left(\omega\left(\frac{t'}{2\gamma^2}(1+\gamma^2\psi^2) + \frac{t'^3c^2}{6\rho^2}\right)\right)\mathrm{d}t' \tag{2.55}$$

this can be written as

$$E_x(\omega) = \frac{q\omega\omega_0}{4\pi\sqrt{2\pi}\epsilon_0 c r'} \int_{-\infty}^{\infty} t' \sin\left(\frac{\omega t'}{2\gamma^2}(1+\gamma^2\psi^2) + \frac{\omega t'^3c^2}{6\rho^2}\right)\mathrm{d}t' \tag{2.56}$$

We can simplify the algebra slightly by using a substitution of variables. Consider the last term in the cosine function. As we are going to be looking to replace $\mathrm{d}t'$ with $\mathrm{d}u$ we want $u \propto t'$. Therefore we can define u such that

$$\begin{aligned} u^3 &= t'^3\frac{\omega c^2}{2\rho^2} \\ u &= t'\left(\frac{\omega c^2}{2\rho^2}\right)^{\frac{1}{3}} \\ \frac{\mathrm{d}u}{\mathrm{d}t'} &= \left(\frac{\omega c^2}{2\rho^2}\right)^{\frac{1}{3}} \end{aligned}$$

This means that the x component of the electric field becomes

$$\begin{aligned} E_x(\omega) &= \frac{q\omega\omega_0}{4\pi\sqrt{2\pi}\epsilon_0 c r'} \int_{-\infty}^{\infty} \left(\frac{2\rho^2}{\omega c^2}\right)^{\frac{2}{3}} u \sin\left(\frac{\omega}{2\gamma^2}\left(\frac{2\rho^2}{\omega c^2}\right)^{\frac{1}{3}}(1+\gamma^2\psi^2)u + \frac{u^3}{3}\right)\mathrm{d}u \\ &= \frac{q\omega\omega_0}{4\pi\sqrt{2\pi}\epsilon_0 c r'} \left(\frac{2\rho^2}{\omega c^2}\right)^{\frac{2}{3}} \int_{-\infty}^{\infty} u \sin\left(\left(\frac{\omega\rho}{2c\gamma^3}\right)^{\frac{2}{3}}(1+\gamma^2\psi^2)u + \frac{u^3}{3}\right)\mathrm{d}u \end{aligned} \tag{2.57}$$

Similarly for the component of the electric field in the y direction we can write

$$E_y(\omega) = \frac{iq\omega\psi}{4\pi\sqrt{2\pi}\epsilon_0 c r'} \int_{-\infty}^{\infty} (\cos U + i\sin U)\mathrm{d}t' \tag{2.58}$$

The function $\sin x$ is an odd function, this means that when integrated between $-\infty$ and ∞ it will evaluate to zero, therefore it can be ignored. This means that equation (2.58) becomes

$$\begin{aligned} E_y(\omega) &= \frac{iq\omega\psi}{4\pi\sqrt{2\pi}\epsilon_0 c r'} \int_{-\infty}^{\infty} \cos\left(\frac{\omega t'}{2\gamma^2}(1+\gamma^2\psi^2) + \frac{\omega t'^3c^2}{6\rho^2}\right)\mathrm{d}t' \\ &= \frac{iq\omega\psi}{4\pi\sqrt{2\pi}\epsilon_0 c r'} \left(\frac{2\rho^2}{\omega c^2}\right)^{\frac{1}{3}} \int_{-\infty}^{\infty} u \sin\left(\left(\frac{\omega\rho}{2c\gamma^3}\right)^{\frac{2}{3}}(1+\gamma^2\psi^2)u + \frac{u^3}{3}\right)\mathrm{d}u \end{aligned} \tag{2.59}$$

We can write equations (2.57) and (2.59) in a simpler form. However to do this we need to use Airy functions and modified Bessel functions [44, 45].

The Airy function, $Ai(x)$, is

$$Ai(x) = \frac{1}{\pi}\int_0^\infty \cos\left(xt + \frac{t^3}{3}\right)\mathrm{d}t = \frac{1}{\pi}\sqrt{\frac{x}{3}}\mathrm{K}_{1/3}\left(\frac{2x^{\frac{3}{2}}}{3}\right) \tag{2.60}$$

where K is a modified Bessel function and the differential of $Ai(x)$ with respect to x is therefore

$$Ai'(x) = -\frac{1}{\pi}\int_0^\infty t\sin\left(xt + \frac{t^3}{3}\right)\mathrm{d}t = -\frac{1}{\pi}\frac{x}{\sqrt{3}}\mathrm{K}_{2/3}\left(\frac{2x^{\frac{3}{2}}}{3}\right) \tag{2.61}$$

Comparing the Airy function to equation (2.59) we see that $t = u$ and that

$$x = \left(\frac{\omega\rho}{2c\gamma^3}\right)^{\frac{2}{3}}(1+\gamma^2\psi^2)$$

This means that we can express the x and y components of the electric field using Bessel functions.

$$E_x(\omega) = \frac{\sqrt{3}q\gamma}{4\pi\sqrt{2\pi}c\epsilon_0 r'}\left(\frac{2\rho\omega}{3c\gamma^3}\right)(1+\gamma^2\psi^2)\mathrm{K}_{2/3}(G) \tag{2.62}$$

$$E_y(\omega) = \frac{i\sqrt{3}q\psi\gamma^2}{4\pi\sqrt{2\pi}c\epsilon_0 r'}\left(\frac{2\rho\omega}{3c\gamma^3}\right)(1+\gamma^2\psi^2)^{\frac{1}{2}}\mathrm{K}_{1/3}(G) \tag{2.63}$$

where

$$G = \left(\frac{\rho\omega}{3c\gamma^3}\right)(1+\gamma^2\psi^2)^{\frac{3}{2}}$$

2.2.1 Angular Power Distribution

So far we have only considered the observer being point like. However we can examine how the synchrotron radiation power emitted by an electron is related to the angle of emission by defining an observation aperture centred on the observer. If the observation aperture area is defined in terms of a solid angle $\Delta\Omega$ the energy radiated by an electron through the area in the time Δt is

$$W = (\mathbf{n}'\cdot\mathbf{S})\Delta t r'^2\Delta\Omega \tag{2.64}$$

where $\mathbf{S}$ is the Poynting vector. Using the equation (2.37) for the Poynting vector this becomes

$$W = \frac{1}{\mu_0 c}E^2\Delta t r'^2\Delta\Omega \tag{2.65}$$

The total energy that passes through the observation aperture in a single turn of the electron is

$$W = \int_0^{4\pi} \int_{-\infty}^{\infty} \frac{1}{\mu_0 c} E^2(t) r'^2 \mathrm{d}t \mathrm{d}\Omega \tag{2.66}$$

Using equation (2.66) we can calculate the energy received per unit solid angle and the energy received per unit time which is the power. The power that is observed is given by

$$P = \frac{\mathrm{d}W}{\mathrm{d}t} = \int_0^{4\pi} \frac{1}{\mu_0 c} E^2(t) r'^2 \mathrm{d}\Omega \tag{2.67}$$

assuming the observation aperture covers all solid angles. Therefore the energy received per unit solid angle is

$$\frac{\mathrm{d}W}{\mathrm{d}\Omega} = \int_{-\infty}^{\infty} \frac{1}{\mu_0 c} E^2(t) r'^2 \mathrm{d}t \tag{2.68}$$

We can replace $\mathbf{E}(t)$ with its Fourier transform which is

$$\mathbf{E}(t) = \frac{1}{\sqrt{2\pi}} \int_{-\infty}^{\infty} \mathbf{E}(\omega) e^{-i\omega t} \mathrm{d}\omega \tag{2.69}$$

therefore equation (2.68) becomes

$$\frac{\mathrm{d}W}{\mathrm{d}\Omega} = \frac{r'^2}{2\pi\mu_0 c} \int_{-\infty}^{\infty} \int_{-\infty}^{\infty} \int_{-\infty}^{\infty} \mathbf{E}(\omega) e^{-i\omega t} \mathbf{E}(\omega') e^{-i\omega' t} \mathrm{d}\omega \mathrm{d}\omega' \mathrm{d}t \tag{2.70}$$

We can simplify this equation by using a Dirac delta function [44]. The integral form of a Dirac delta function is

$$\delta(x) = \frac{1}{2\pi} \int_{-\infty}^{\infty} e^{ixt} \mathrm{d}t \tag{2.71}$$

Using this equation (2.70) is expressed as

$$\begin{aligned} \frac{\mathrm{d}W}{\mathrm{d}\Omega} &= \frac{r'^2}{2\pi\mu_0 c} \int_{-\infty}^{\infty} \int_{-\infty}^{\infty} \int_{-\infty}^{\infty} \mathbf{E}(\omega) \mathbf{E}(\omega') e^{-i\omega t - i\omega' t} \mathrm{d}\omega \mathrm{d}\omega' \mathrm{d}t \\ \frac{\mathrm{d}W}{\mathrm{d}\Omega} &= \frac{r'^2}{\mu_0 c} \int_{-\infty}^{\infty} \int_{-\infty}^{\infty} \mathbf{E}(\omega) \mathbf{E}(\omega') \delta(-\omega - \omega') \mathrm{d}\omega \mathrm{d}\omega' \end{aligned} \tag{2.72}$$

We can simplify the equation for the energy received per unit solid angle even more by noting that by definition the integral of the delta function is equal to unity. Additionally since $\mathbf{E}(t)$ is a real function, its conjugate $\mathbf{E}^*(t) = \mathbf{E}(t)$. Therefore the conjugate of $\mathbf{E}(\omega)$ is $\mathbf{E}^*(\omega) = \mathbf{E}(-\omega)$. This means that equation (2.72) becomes

$$\frac{\mathrm{d}W}{\mathrm{d}\Omega} = \frac{r'^2}{\mu_0 c}\int_{-\infty}^{\infty} \mathbf{E}(\omega)\mathbf{E}^*(\omega)\mathrm{d}\omega$$
$$= \frac{2r'^2}{\mu_0 c}\int_0^{\infty} |\mathbf{E}(\omega)|^2 \mathrm{d}\omega \tag{2.73}$$

The spectral angular distribution therefore is

$$\frac{\mathrm{d}}{\mathrm{d}\omega}\frac{\mathrm{d}W}{\mathrm{d}\Omega} = \frac{\mathrm{d}^2 W}{\mathrm{d}\Omega \mathrm{d}\omega} = \frac{2r'^2}{\mu_0 c}|\mathbf{E}(\omega)|^2 \tag{2.74}$$

So far we have derived the angular distribution for an electron making one revolution of a synchrotron. However the electron will make $c/2\pi\rho$ revolutions per second where ρ is the bending radius of the electron. This means that we can define the spectral power angular distribution to be

$$\frac{\mathrm{d}^2 P}{\mathrm{d}\Omega \mathrm{d}\omega} = \frac{c}{2\pi\rho}\frac{\mathrm{d}^2 W}{\mathrm{d}\Omega \mathrm{d}\omega} = \frac{r'^2}{\pi\rho\mu_0}|\mathbf{E}(\omega)|^2 \tag{2.75}$$

Using the fact that $E_s(\omega) = 0$ equation (2.75) becomes

$$\frac{\mathrm{d}^2 P}{\mathrm{d}\Omega \mathrm{d}\omega} = \frac{r'^2}{\pi\rho\mu_0}(E_x^2(\omega) + E_y^2(\omega)) \tag{2.76}$$

We can then replace $E_x(\omega)$ and $E_y(\omega)$ using equations (2.62) and (2.63) so that the spectral power angular distribution becomes

$$\frac{\mathrm{d}^2 P}{\mathrm{d}\Omega \mathrm{d}\omega} = \frac{3q^2\gamma^2}{32\pi^4\epsilon_0\rho}\left(\frac{2\rho\omega}{3c\gamma^3}\right)^2 (1+\gamma^2\psi^2)^2 \left(\mathrm{K}_{2/3}^2(G) + \frac{\gamma^2\psi^2}{(1+\gamma^2\psi^2)}\mathrm{K}_{1/3}^2(G)\right) \tag{2.77}$$

We can get the spectral power by integrating over all angles

$$\frac{\mathrm{d}P}{\mathrm{d}\omega} = \int_0^{4\pi} \frac{\mathrm{d}^2 P}{\mathrm{d}\Omega \mathrm{d}\omega}\mathrm{d}\Omega = \int_0^{4\pi} \frac{3q^2\gamma^2}{32\pi^4\epsilon_0\rho}\left(\frac{2\rho\omega}{3c\gamma^3}\right)^2 (1+\gamma^2\psi^2)^2 \left(\mathrm{K}_{2/3}^2(G) + \frac{\gamma^2\psi^2}{(1+\gamma^2\psi^2)}\mathrm{K}_{1/3}^2(G)\right)\mathrm{d}\Omega \tag{2.78}$$

As there is no explicit dependence on the angle θ in the integral, we can convert the integral from the solid angle to the azimuthal angle which gives

$$\frac{\mathrm{d}P}{\mathrm{d}\omega} = 2\pi\int_0^{2\pi} \frac{3q^2\gamma^2}{32\pi^4\epsilon_0\rho}\left(\frac{2\rho\omega}{3c\gamma^3}\right)^2 (1+\gamma^2\psi^2)^2 \left(\mathrm{K}_{2/3}^2(G) + \frac{\gamma^2\psi^2}{(1+\gamma^2\psi^2)}\mathrm{K}_{1/3}^2(G)\right)\mathrm{d}\psi \tag{2.79}$$

We can perform a substitution of variables so that the integral is performed with respect to G. To do this we need to calculate the derivative of G with respect to ψ which is given by

$$\frac{\mathrm{d}G}{\mathrm{d}\psi} = \left(\frac{\rho\omega}{c\gamma}\right)\psi\left(\left(\frac{\rho\omega}{3c\gamma^3}\right) + \left(\frac{\rho\omega}{3c\gamma}\right)\psi^2\right)^{\frac{1}{2}} = \left(\frac{\rho\omega}{c\gamma}\right)\left(\frac{\rho\omega}{3c\gamma^3}\right)\psi(1+\gamma^2\psi^2)^{\frac{1}{2}} \tag{2.80}$$

2.2.2 Photon Flux

A more useful quantity for our application is the number of photons rather than the radiated power. The energy of a photon is given by the equation $\epsilon = \hbar\omega$. If the number of photons emitted with energy ϵ is N then the number of photons emitted per second is $\mathrm{d}N/\mathrm{d}t = \dot{N}$. Therefore the power radiated at a particular photon energy is $\dot{N}\epsilon$. This means that the number of photons emitted per second per solid angle by one electron into a relative photon energy bandwidth $\mathrm{d}\epsilon/\epsilon$ is

$$\frac{\mathrm{d}^2\dot{N}}{\mathrm{d}\Omega\mathrm{d}\epsilon/\epsilon} = \frac{\epsilon\mathrm{d}^2\dot{N}}{\mathrm{d}\Omega\mathrm{d}\epsilon} = \frac{\mathrm{d}^2P}{\mathrm{d}\Omega\mathrm{d}\epsilon} = \frac{\mathrm{d}^2P}{\hbar\mathrm{d}\Omega\mathrm{d}\omega} \tag{2.81}$$

Substituting in equation (2.77) this becomes

$$\frac{\epsilon\mathrm{d}^2\dot{N}}{\mathrm{d}\Omega\mathrm{d}\epsilon} = \frac{3q^2\gamma^2}{32\pi^4\hbar\epsilon_0\rho}\left(\frac{2\rho\omega}{3c\gamma^3}\right)^2(1+\gamma^2\psi^2)^2\left(\mathrm{K}^2_{2/3}(G) + \frac{\gamma^2\psi^2}{(1+\gamma^2\psi^2)}\mathrm{K}^2_{1/3}(G)\right) \tag{2.82}$$

We can simplify the constants in equation (2.82) by using the definition of the fine structure constant, α, which is

$$\alpha = \frac{q^2}{2ch\epsilon_0} = \frac{q^2}{4\pi c\hbar\epsilon_0} \tag{2.83}$$

therefore the number of photons per second per solid angle is

$$\frac{\mathrm{d}\dot{N}}{\mathrm{d}\Omega} = \frac{3\alpha\gamma^2}{4\pi^2}\frac{c}{2\pi\rho}\left(\frac{\Delta\epsilon}{\epsilon}\right)\left(\frac{2\rho\omega}{3c\gamma^3}\right)^2(1+\gamma^2\psi^2)^2\left(\mathrm{K}^2_{2/3}(G) + \frac{\gamma^2\psi^2}{(1+\gamma^2\psi^2)}\mathrm{K}^2_{1/3}(G)\right) \tag{2.84}$$

where the number of revolutions of the electron per second is explicitly factored out of the constants.

So far we have only considered one electron emitting photons. Now we can consider a beam of electrons emitting photons. To do this we need to consider how many electrons pass a given point per second. Typically when considering a beam rather than the number of particles it is the beam current that is quoted. When dealing with an electron beam it is rather easy to convert between the two as the beam current is simply the charge of the electron multiplied by the number of electrons per second. As the electrons are travelling on a closed path they will pass

the same point a number of times per second. This means that the beam current in a circular ring is actually

$$I_b = N_e q \frac{c}{2\pi\rho} \tag{2.85}$$

where I_b is the beam current and N_e is the total number of electrons in the ring. We can therefore write equation (2.84) so that it includes the beam current as shown below

$$\frac{\mathrm{d}\dot{N}}{\mathrm{d}\Omega} = \frac{3\alpha\gamma^2}{4\pi^2}\frac{I_b}{q}\left(\frac{\Delta\epsilon}{\epsilon}\right)\left(\frac{2\rho\omega}{3c\gamma^3}\right)^2 (1+\gamma^2\psi^2)^2 \left(\mathrm{K}^2_{2/3}(G) + \frac{\gamma^2\psi^2}{(1+\gamma^2\psi^2)}\mathrm{K}^2_{1/3}(G)\right) \tag{2.86}$$

The quantity $\mathrm{d}\dot{N}/\mathrm{d}\Omega$ is the spectral angular flux density. We can derive the quantity $\mathrm{d}\dot{N}/\mathrm{d}\epsilon/\epsilon$ using a similar formalism. However to simplify the algebra we will introduce several new terms using [42]. These are the critical frequency ω_c, the critical energy ϵ_c and the total power radiated by one electron P_o.

The critical frequency arises as there are only a finite number of radiation *wave trains* emitted in a given time. The spectrum of radiation will contain significant frequency components up to the critical frequency

$$\omega_c \propto \frac{c\gamma^3}{\rho} = \frac{3c\gamma^3}{2\rho} \tag{2.87}$$

the critical energy is therefore given by

$$\epsilon_c = \hbar\omega_c = \frac{3hc\gamma^3}{4\pi\rho} \tag{2.88}$$

and the total power radiated by one electron is

$$P_0 = \frac{cq^2\gamma^4}{6\pi\epsilon_0\rho^2} \tag{2.89}$$

Therefore the number of photons emitted per electron per second into all angles is

$$\frac{\mathrm{d}\dot{N}}{\mathrm{d}\epsilon/\epsilon} = \frac{\mathrm{d}P}{\hbar\mathrm{d}\omega} \tag{2.90}$$

the solution for the derivative of power with respect to frequency is derived in [46]. Using this means that the number of photons emitted per electron per second into all angles is therefore given by

$$\frac{\mathrm{d}P}{\hbar \mathrm{d}\omega} = \frac{P_0}{\hbar\omega_c} S\left(\frac{\omega}{\omega_c}\right)$$
$$= \frac{cq^2\gamma^4}{6\pi\epsilon_0\rho^2\epsilon_c}\frac{9\sqrt{3}\omega}{8\pi\omega_c}\int_{\omega/\omega_c}^{\infty} \mathrm{K}_{5/3}(u)\mathrm{d}u \tag{2.91}$$

substituting in the definition of ϵ_c into equation (2.91) we get

$$\frac{\mathrm{d}\dot{N}}{\mathrm{d}\epsilon/\epsilon} = \sqrt{3}\gamma\frac{q^2}{2ch\epsilon_0}\frac{c}{2\pi\rho}\left(\frac{\epsilon}{\epsilon_c}\right)\int_{\epsilon/\epsilon_c}^{\infty} \mathrm{K}_{5/3}(u)\mathrm{d}u \tag{2.92}$$

We can rewrite equation (2.92) so that it includes the dependence on the beam current using equation (2.85). We can also introduce the fine structure constant to simplify the equation which results in

$$\frac{\mathrm{d}\dot{N}}{\mathrm{d}\epsilon/\epsilon} = \sqrt{3}\alpha\gamma\frac{I_b}{q}\left(\frac{\epsilon}{\epsilon_c}\right)\int_{\epsilon/\epsilon_c}^{\infty} \mathrm{K}_{5/3}(u)\mathrm{d}u \tag{2.93}$$

We can get the spectral photon flux, $\dot{N}$, by multiplying equation (2.93) by the relative energy bandwidth $\Delta\epsilon/\epsilon$. The spectral photon flux is therefore given by

$$\dot{N} = \sqrt{3}\alpha\gamma\frac{I_b}{q}\left(\frac{\Delta\epsilon}{\epsilon}\right)\left(\frac{\epsilon}{\epsilon_c}\right)\int_{\epsilon/\epsilon_c}^{\infty} \mathrm{K}_{5/3}(u)\mathrm{d}u \tag{2.94}$$

We can rewrite the spectral angular flux density and the spectral photon flux in terms that are more useful in accelerator physics. We define the bandwidth $\Delta\epsilon/\epsilon$ to be 0.1% then the spectral angular flux density in units of photons per second per milliradian per 0.1% bandwidth is

$$\frac{\mathrm{d}\dot{N}}{\mathrm{d}\Omega} = 1.33\times10^{13}E^2I_b\left(\frac{\epsilon}{\epsilon_c}\right)^2(1+\gamma^2\psi^2)^2\left(\mathrm{K}^2_{2/3}(G) + \frac{\gamma^2\psi^2}{(1+\gamma^2\psi^2)}\mathrm{K}^2_{1/3}(G)\right) \tag{2.95}$$

and the spectral photon flux in units of photons per second per milliradian per 0.1% bandwidth is

$$\dot{N} = 2.46\times10^{13}EI_b\left(\frac{\epsilon}{\epsilon_c}\right)\int_{\epsilon/\epsilon_c}^{\infty} \mathrm{K}_{5/3}(u)\mathrm{d}u \tag{2.96}$$

where E is the electron beam energy in GeV and I_b is the beam current in A. We can calculate the spectral angular flux density and the spectral photon flux of a synchrotron given a number of parameters which include the electron beam energy, the beam current, the bending radius and the critical photon energy. Table 2.1 has parameters for the two most recent synchrotron light sources in the UK; Diamond and the SRS. The SRS was sited at Daresbury Laboratory and

was decommissioned in 2008. Diamond is sited at Rutherford Appleton Laboratory and began operation in 2007.

Table 2.1: Beam Parameters for two Synchrotron Light Sources

Parameter	Symbol	Units	SRS	Diamond
Electron Beam Energy	E	GeV	2	3
Electron Beam Current	I_b	mA	200	300
Dipole Field Strength	B	T	1.2	1.4
Bending Radius	ρ	m	5.56	7.15
Critical Photon Energy	ϵ_c	keV	3.19	8.38

Figure 2.3 compares the spectral photon flux for the SRS and Diamond synchrotrons calculated using equation (2.96) with values taken from table 2.1. As can be seen the two synchrotrons have similar levels of peak photon flux. However, the Diamond synchrotron produces a photons with a maximum energy that is twice what the SRS was able to produce. Another key difference is the opening angle of the radiation produced by the two synchrotrons. From equation (2.77) the opening angle of the radiation produced by an electron travelling through a dipole magnet is inversely proportional to γ. This means that as the electron beam energy increases the opening angle of the radiation decreases. For the SRS and Diamond this has some effect as shown in figure **??**. However for the ILC positron source as will be shown later this effect is significant.

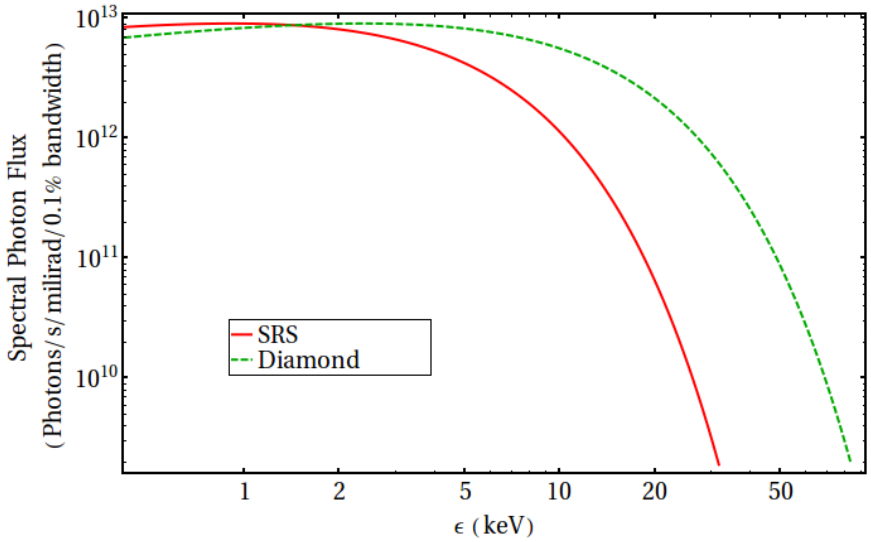

Figure 2.3: Plot comparing the spectral photon flux for the SRS and Diamond synchrotrons calculated using equation (2.96) with values taken from table 2.1. The red curve is the flux from the SRS and the green dashed curve is the flux from Diamond. Plotted using Mathematica 8.

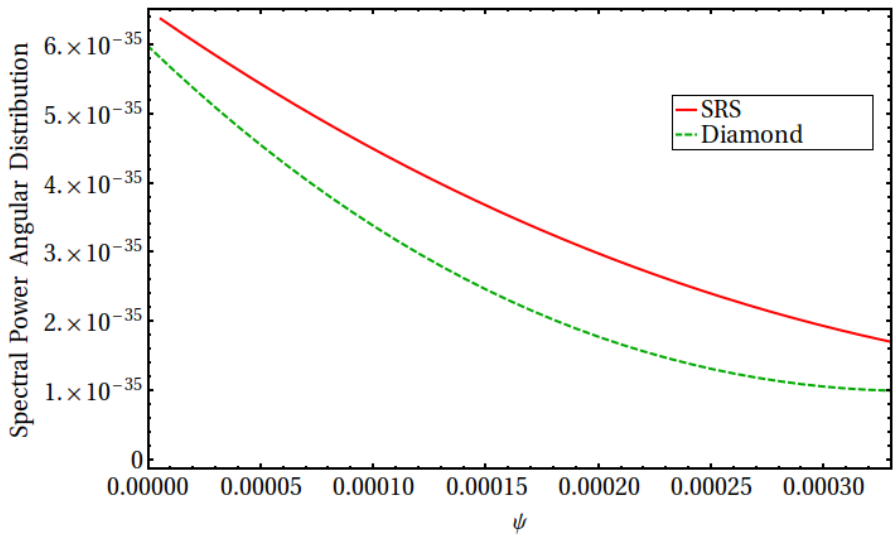

Figure 2.4: Plot comparing the spectral power angular distribution for the SRS and Diamond synchrotrons calculated using equation (2.77) with values taken from table 2.1. The red curve is the flux from the SRS and the green dashed curve is the flux from Diamond. Plotted using Mathematica 8.

2.3 Summary

Synchrotron radiation is a key aspect of undulator-based positron sources. In this chapter we have derived the synchrotron radiation emitted by a point charge moving along an arbitrary path starting from Maxwell's equations. We have then extended this derivation to be able to describe the radiation emitted from an electron moving on a circular orbit due to the effect of dipole magnets. This is a key result for the derivation of radiation from insertion devices as insertion devices can be thought of as an array of dipole magnets. Using the equations derived in this chapter we will now go on and derive the radiation from an undulator.

Chapter 3

Insertion Devices

Having derived the radiation emitted by an electron traversing a bending magnet in chapter 2 we are now able to consider the radiation produced when an electron travels through an insertion device (ID). We will then discuss the difference between undulators and wigglers and how this affects the radiation they produce.

Planar and helical IDs will be considered in this chapter although the derivation of radiation produced by IDs will be done for the planar case as this simplifies the algebra. As the proposed undulator in the undulator-based positron sources are helical devices, for reasons of photon flux and polarisation, the final section in this chapter will show how to calculate the radiation from a helical undulator by following the same method as used to derive the radiation from a planar undulator.

Note, when we derived the radiation emitted by an electron in a synchrotron we referred to the longitudinal position of the electron as s. This is due to a convention in accelerator physics where the distance along the design orbit of a particle accelerator is defined as s. As will be shown later the electron design orbit is not a straight line through an insertion device. This means that the position of the electron along the length of the insertion device is defined to be z instead of s. Whilst s and z are not identical in most applications the difference between s and z is very small and therefore they can be considered to be approximately equal to each other. This approximation is valid as the IDs that we will be considering have a total length on the order of metres whilst the undulation experienced by the electron beam has a typical amplitude on the order of micrometres. This means that the difference between s and z will be of the order of 10^{-4} m or smaller.

3.1 Electron Trajectory in Insertion Devices

To calculate the synchrotron radiation spectrum produced by an ID first the electron trajectory needs to be calculated. There are two main configurations for an ID: planar and helical. In a planar ID the magnetic field has a fixed direction and periodic field strength. In a helical ID the magnetic field has a fixed field strength and a direction that rotates with position along the length of the ID. This means that in the coordinate frame where the electron is travelling in the z direction and the transverse deflections are small, $\mathrm{dx/dz} = \dot{\mathrm{x}} << 1$ and $\mathrm{dy/dz} = \dot{\mathrm{y}} << 1$, then the equations of motion for the electron are

$$\begin{aligned} \ddot{x} &= \frac{d^2x}{dz^2} = \frac{e}{\gamma m_0 c}(B_y - \dot{y}B_z) \\ \ddot{y} &= \frac{d^2y}{dz^2} = \frac{e}{\gamma m_0 c}(\dot{x}B_z - B_x) \end{aligned} \tag{3.1}$$

where m_0 is the rest mass of the electron and B_x, B_y, B_z are the components of the magnetic field of the ID. As IDs do not have a magnetic field in the z direction equation (3.1) simplifies to

$$\begin{aligned} \ddot{x} &= \frac{d^2x}{dz^2} = \frac{e}{\gamma m_0 c}B_y \\ \ddot{y} &= \frac{d^2y}{dz^2} = -\frac{e}{\gamma m_0 c}B_x \end{aligned} \tag{3.2}$$

We will initially calculate the electron trajectory in a planar ID and then calculate the trajectory through a helical ID.

3.1.1 Planar Insertion Device

For a planar ID that only deflects the electron beam in the horizontal plane there is only a vertical magnetic field. If the magnetic field is sinusoidally varying with a peak field strength B_0 and period λ_{ID} equation (3.2) becomes

$$\begin{aligned} \ddot{x} &= -\frac{e}{\gamma m_0 c}B_0 \sin\frac{2\pi z}{\lambda_{\mathrm{ID}}} \\ \ddot{y} &= 0 \end{aligned} \tag{3.3}$$

By integrating equation (3.3) with respect to z we can find $\dot{x}$ which is the horizontal deflection angle.

$$\dot{x} = \frac{B_0 e}{\gamma m_0 c} \frac{\lambda_{\mathrm{ID}}}{2\pi} \cos \frac{2\pi z}{\lambda_{\mathrm{ID}}} \tag{3.4}$$

As equation (3.4) shows that $\dot{x}$ varies sinusoidally the maximum deflection angle experienced by an electron is

$$\frac{\lambda_{\mathrm{ID}} B_0 e}{2\pi\gamma m_0 c}$$

As γ is the only quantity relating to the electron beam, B_0 and λ_{ID} relate to the ID and all other quantities are constants, the maximum deflection angle can be rewritten as $\frac{K}{\gamma}$ where K is the deflection parameter of the ID. K is a dimensionless parameter and is defined as

$$K = \frac{e}{2\pi m_0 c} B_0 \lambda_{\mathrm{ID}} \approx 93.36\, B_0 \lambda_{\mathrm{ID}} \tag{3.5}$$

One of the assumptions that went into equation (3.1) was that $\dot{x} << 1$. For this to hold $\gamma >> K$, as typical values of K range from 1 to 100, we need $\gamma > 1000$ which for an electron means we require an energy greater than 511 MeV. Equation (3.4) can now be expressed as

$$\dot{x} = \frac{K}{\gamma} \cos \frac{2\pi z}{\lambda_{\mathrm{ID}}} \tag{3.6}$$

By integrating equation (3.6) with respect to z we can get the x coordinate of the electron as a function of z in an ID. As the electron is assumed to be injected on-axis and there is no deflection in y the position of an electron in a planar ID, with a vertical magnetic field only, can be fully described by:

$$x = \frac{K}{\gamma} \frac{\lambda_{\mathrm{ID}}}{2\pi} \sin \frac{2\pi z}{\lambda_{\mathrm{ID}}} \tag{3.7}$$

$$y = 0 \tag{3.8}$$

The effect of changing B_0, λ_{ID} and the energy of the electron on the position of an electron travelling through an ID is investigated below. To compare the effect of B_0 and λ_{ID} the position will be calculated for IDs with three different values of the deflection parameter given in table 3.1.

The trajectories for a 10 MeV electron travelling through a planar ID calculated using equation (3.7) are plotted in Figures 3.1 and 3.2. Figure 3.1 shows the effect of changing λ_{ID} with a fixed magnetic field, $B_0 = 2.0$ T on the electron trajectories. Increasing λ_{ID} has two effects; to decrease

Table 3.1: Values of K, B_0 and λ_{ID} used to investigate the position of an electron travelling through a planar ID.

K	$B_0 = 2.0$	$\lambda_{\mathrm{ID}} = 0.05356$
	λ_{ID} (m)	B_0 (T)
1	0.005356	0.20
10	0.05356	2.0
100	0.5356	20

the number of oscillations in a fixed length of ID and to increase the amplitude of the oscillations. The number of oscillations, N, an electron will experience in a given length of ID, L, is

$$N = \frac{L}{\lambda_{\mathrm{ID}}}$$

From equation (3.7) the amplitude of the oscillations is

$$\frac{K\lambda_{\mathrm{ID}}}{2\pi\gamma} \tag{3.9}$$

as $K \propto \lambda_{\mathrm{ID}}$ the oscillation amplitude is therefore proportional to λ_{ID}^2.

Figure 3.2 shows the effect of changing B_0 with a wavelength, $\lambda_{\mathrm{ID}} = 0.05356\,\mathrm{m}$ on the electron trajectories. Increasing B_0 just increases the amplitude of the oscillations. As B_0 does not appear in equation (3.9) and as $K \propto B_0$ the oscillation amplitude increases linearly with B_0.

The energy of the electron beam also affects the amplitude of oscillations in an ID. Figure 3.3 shows how the amplitude of the electron trajectory changes for four different electron energies travelling through an ID with $K = 10$ and $\lambda_{\mathrm{ID}} = 0.05356\,\mathrm{m}$. Increasing the energy of the electron decreases the amplitude of oscillation. The electron energy, E_{e^-}, is proportional to γ. As equation (3.9) has a $1/\gamma$ term the oscillation amplitude is inversely proportional to E_{e^-}.

3.1.2 Helical Insertion Device

A helical ID has magnetic fields in two planes which means that the electron is deflected in a helical trajectory. In general the two magnetic fields can have different field strengths, periods and therefore different K values. For a helical ID with magnetic fields given by

$$\begin{aligned} B_x &= B_{x0}\sin\left(\frac{2\pi z}{\lambda_{x\mathrm{ID}}} + \phi_x\right) \\ B_y &= B_{y0}\cos\left(\frac{2\pi z}{\lambda_{y\mathrm{ID}}} + \phi_y\right) \end{aligned} \tag{3.10}$$

equation (3.2) becomes

$$\begin{aligned} \ddot{x} &= \frac{e}{\gamma m_0 c} B_{y0} \cos\left(\frac{2\pi z}{\lambda_{y\mathrm{ID}}} + \phi_y\right) \\ \ddot{y} &= -\frac{e}{\gamma m_0 c} B_{x0} \sin\left(\frac{2\pi z}{\lambda_{xID}} + \phi_x\right) \end{aligned} \tag{3.11}$$

Integrating (3.11) with respect to z gives

$$\begin{aligned} \dot{x} &= \frac{K_y}{\gamma} \sin\left(\frac{2\pi z}{\lambda_{y\mathrm{ID}}} + \phi_y\right) \\ \dot{y} &= \frac{K_x}{\gamma} \cos\left(\frac{2\pi z}{\lambda_{xID}} + \phi_x\right) \end{aligned} \tag{3.12}$$

The position of the electron in a helical ID is calculated by integrating (3.12) with respect to z which gives

$$\begin{aligned} x &= -\frac{K_y}{\gamma} \frac{\lambda_{y\mathrm{ID}}}{2\pi} \cos\left(\frac{2\pi z}{\lambda_{y\mathrm{ID}}} + \phi_y\right) \\ y &= \frac{K_z}{\gamma} \frac{\lambda_{xID}}{2\pi} \sin\left(\frac{2\pi z}{\lambda_{xID}} + \phi_x\right) \end{aligned} \tag{3.13}$$

Figure 3.4 shows the x and y positions of a 10 MeV electron along an ID one metre long with $K_x = 10$ and $K_y = 11$. The three dimensional trajectory of the electron through the same ID is shown in figure 3.5.

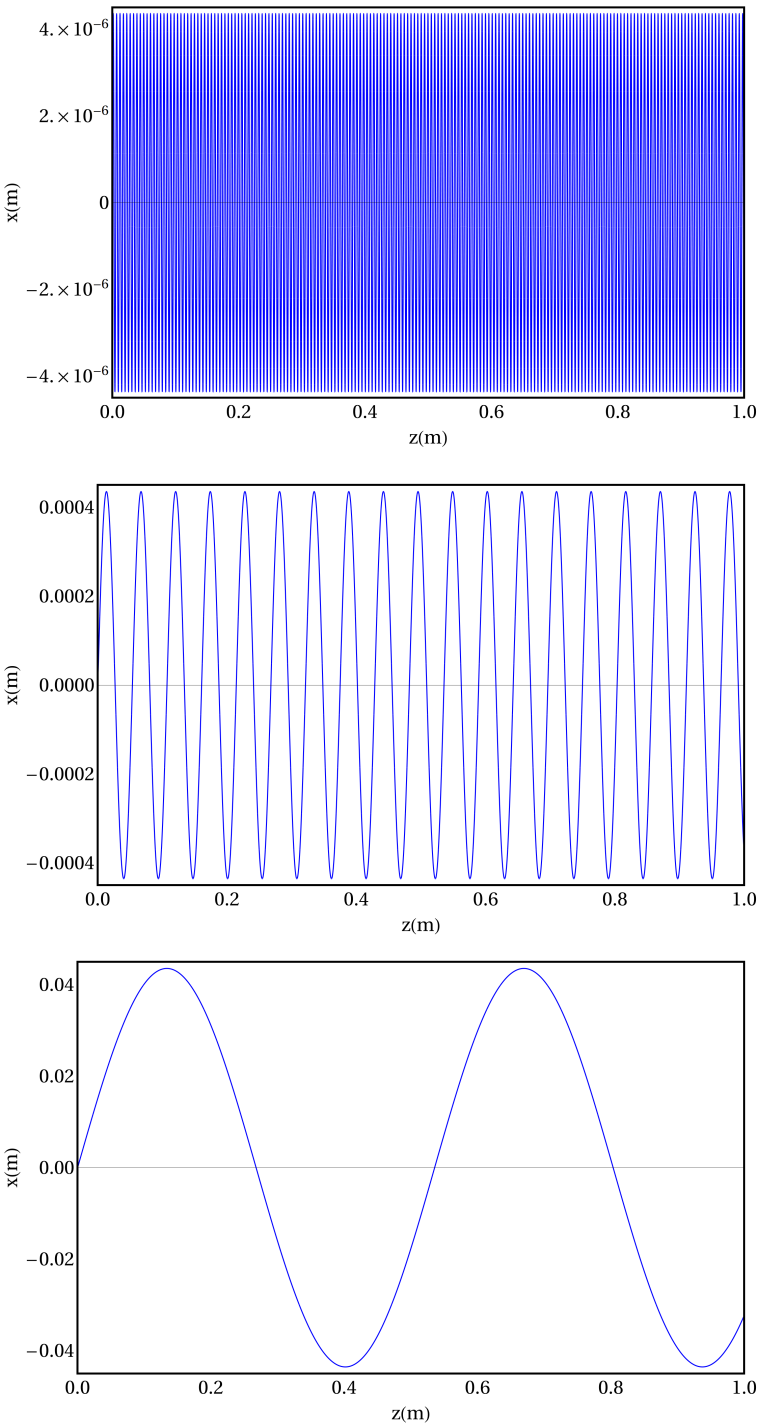

Figure 3.1: Electron Trajectory Plots: Plots showing the trajectory of a 10 MeV electron travelling through three insertion devices calculated using equation (3.7). The insertion devices all have a peak magnet field strength,B_0, of 2.0 T. The top plot is for an Insertion device with $K = 1$, $\lambda_{\mathrm{ID}} = 0.005356\,\mathrm{m}$. The middle plot is for an Insertion device with $K = 10$, $\lambda_{\mathrm{ID}} = 0.05356\,\mathrm{m}$. The bottom plot is for an Insertion device with $K = 100$, $\lambda_{\mathrm{ID}} = 0.5356\,\mathrm{m}$.

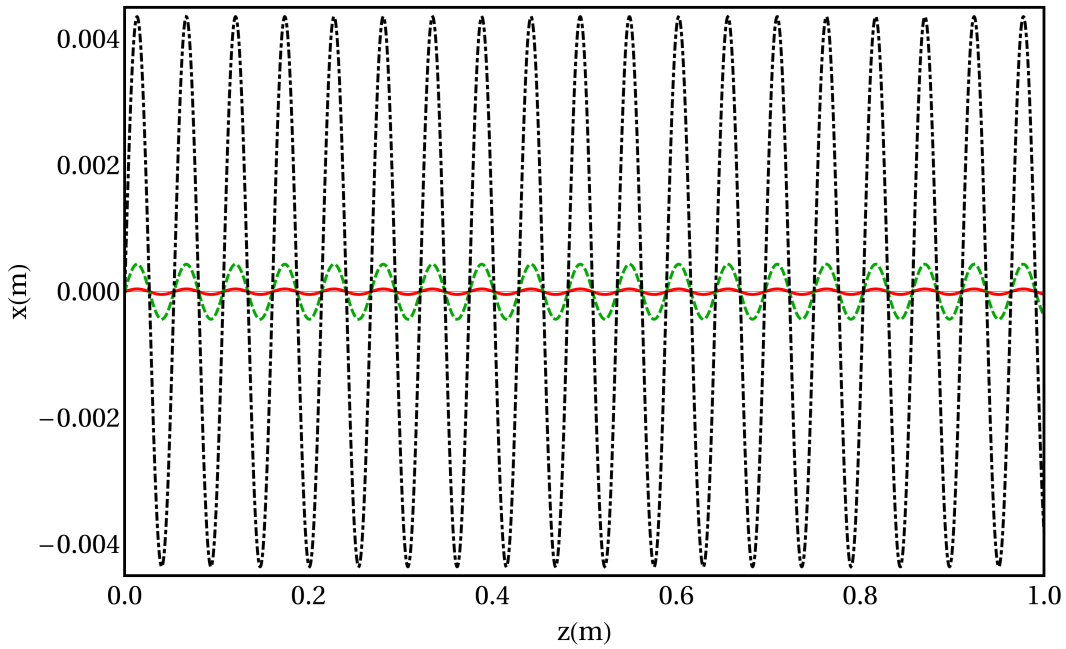

Figure 3.2: Plot showing the trajectory of a 10 MeV electron travelling through three insertion devices calculated using equation (3.7). The insertion devices all have a period, λ_{ID}, of 0.05356 m. The solid red line is for an Insertion device with $K = 1$, $B_0 = 0.2\,\mathrm{T}$. The dashed green line is for an Insertion device with $K = 10$, $B_0 = 2.0\,\mathrm{T}$. The dot dashed black line is for an Insertion device with $K = 100$, $B_0 = 20.0\,\mathrm{T}$.

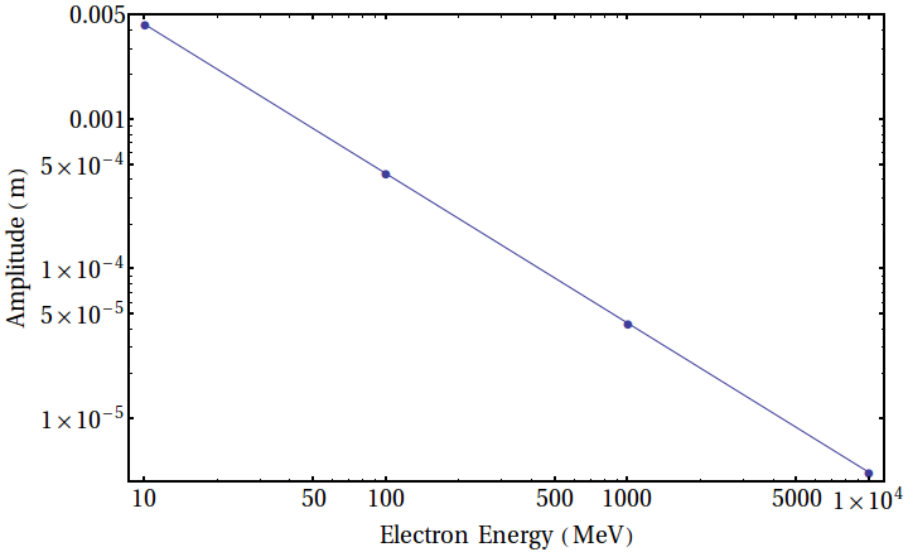

Figure 3.3: Electron Trajectory Plots: Plots showing the variation in amplitude of the electron trajectory travelling through an insertion device with $K = 10$; $B_0 = 2.0\,\mathrm{T}$ and $\lambda_{\mathrm{ID}} = 0.05356\,\mathrm{m}$.

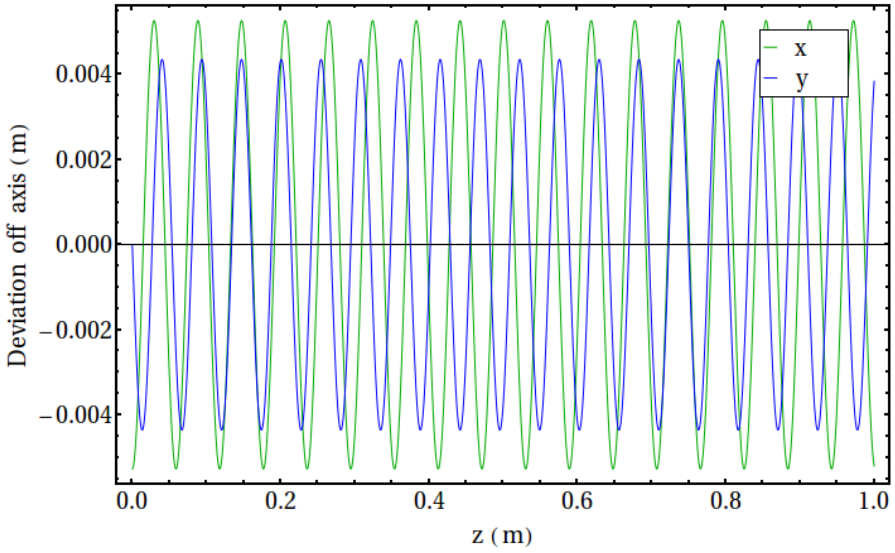

Figure 3.4: Electron Trajectory Plot: Plot showing the x and y projections of the trajectory of a 10 MeV electron travelling through a 1 m long insertion device with $B_0 = 2.0\,\mathrm{T}$ calculated using equation (3.13). The deflection parameters for the x and y trajectories are different, $K_x = 10$ and $K_y = 11$.

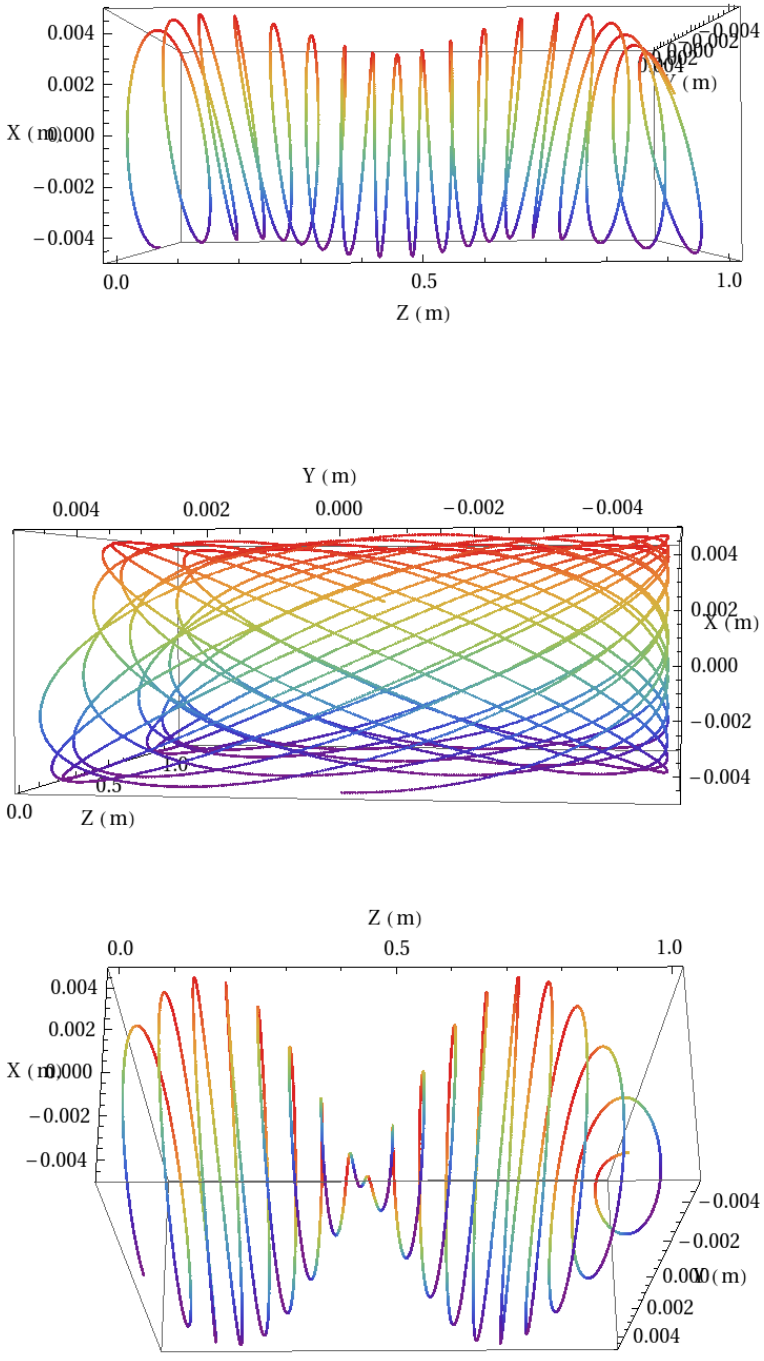

Figure 3.5: Electron Trajectory Plots: Plots showing the trajectory of a 10 MeV electron travelling through a 1 m long helical insertion device with $B_0 = 2.0\,\mathrm{T}$ calculated using equation (3.13). The deflection parameters K_x and K_y are not equal, $K_x = 10$ and $K_y = 11$, this leads to a relatively complex electron trajectory. The top plot shows the electron trajectory in the $x - z$ plane, the middle plot shows the trajectory in the $x - y$ plane and the bottom plot shows the 3D trajectory.

3.2 Undulator or Wiggler

There are two categories of ID; undulator and wigglers. Undulators and wigglers are very similar in design and construction. However there is one main difference between them and that is the radiation spectrum that is emitted. Using the electron trajectories it is possible to calculate the synchrotron radiation that would be emitted from the ID. As shown in equations (3.7) and (3.13) the electron trajectories are of the form $a\sin(2\pi z/\lambda_{\mathrm{ID}})$. We can therefore define the maximum angular deviation, ψ_0, away from the forward direction to be

$$\psi_0 = \frac{2\pi a}{\lambda_{\mathrm{ID}}} = k_{\mathrm{ID}} a \tag{3.14}$$

where k_{ID} is related to the fundamental wave number of the ID. The actual fundamental wave number is given by $k_0 = 2\pi/cT_0$ where T is the time taken for the electron to traverse one period of the ID. As $T \simeq \lambda_{\mathrm{ID}}/\beta$ the fundamental wave number is therefore

$$k_0 = 2\pi\frac{\beta_0}{\lambda_{\mathrm{ID}}} = \beta_0 k_{\mathrm{ID}} \tag{3.15}$$

However when $\gamma >> 1$ the difference between k_0 and k_{ID} is insignificant. As the electrons that we will be considering are ultra-relativistic we will use k_{ID}. Additionally the radiation that is emitted by an ultra-relativistic electron travelling through the ID is confined to a narrow angular window. The angular width of the emission window is $\Delta\theta = O(1/\gamma)$ about the electron trajectory. As the electron moves on a sinusoidal trajectory the beam of radiation that is produced moves back and forth about the forward direction. This means that the relative sizes of ψ_0 and $\Delta\theta$ become important for the radiation that is emitted.

We can also relate the deflection parameter K to the maximum angular deviation by

$$K = \gamma\psi_0 \tag{3.16}$$

The classification of IDs as either undulator or wigglers is a qualitative one. We use the size of K, and therefore the relative sizes of ψ_0 and $\Delta\theta$, to determine whether an ID is an undulator or wiggler. In general we classify undulators as having $K << 1$ or $\psi_0 << \Delta\theta$ and wigglers as having $K >> 1$ or $\psi_0 >> \Delta\theta$. If an ID falls in between these two regimes we use the type of radiation spectra produced to determine whether it is an undulator or wiggler, as the two devices have very different spectra characteristics.

With wigglers ($\psi_0 >> \Delta\theta$) an observer detects a series of pulses of synchrotron radiation. The repetition rate of the the pulses is given by

$$v_0 = \frac{\omega_0}{2\pi} = \frac{ck_{\mathrm{ID}}}{2\pi} = \frac{c}{\lambda_{\mathrm{ID}}} \tag{3.17}$$

The spectrum produced in this case is that of a synchrotron whose bunches are spaced by λ_{ID}. This spectrum is a smooth featureless spectrum which extends from the fundamental frequency, Ω, to the *critical frequency* which is $\gamma^3\Omega$.

For undulators ($\psi_0 << \Delta\theta$) the radiation beam moves negligibly compared to the angular width of the beam. This means that the observer detects a coherent superposition of the contributions from all of the oscillations of the trajectory. In the case of perfect coherence and an infinite number of periods of the ID the radiation observed would be monochromatic. As an infinite number of periods is not physical we must consider what spectrum would be observed from a finite insertion device. For a finite number of periods, N, the spread in frequency is

$$\frac{\Delta\omega}{\omega} = O\left(\frac{1}{N}\right) \tag{3.18}$$

This frequency spread combined with the finite angular acceptance results in a spectrum that is a series of sharp peaks. The most intense peak is the *fundamental*.

We will now look at how the radiation spectrum produced by the two types of ID is calculated. As previously stated we will only consider planar IDs although a similar derivation can be applied to helical IDs.

3.3 Radiation from a Wiggler

The field experienced by an electron travelling through the undulators and wigglers can be described in terms of dipole fields. A planar wiggler is made up of periodic dipoles fields that oscillate between bending the electron trajectory in a positive and negative direction. This is easily seen by considering a permanent magnet planar wiggler, see figure 3.3, which consists of two rows of magnets with the poles alternating between the north pole being above or below the electron beam.

3.3.1 Critical Energy for the Photon Spectrum of a Planar Wiggler

As described in section 3.2 the radiation that is observed from a wiggler is just a series of pulses that add up incoherently to create the photon spectrum from the wiggler. As a result we can consider the wiggler radiation as a sum of a number of overlapping dipole photon spectra. As shown in section 2.1.10 the photon spectrum produced by a dipole can be characterised by the critical photon energy ϵ_c. The critical photon energy for a dipole magnet is given in equation

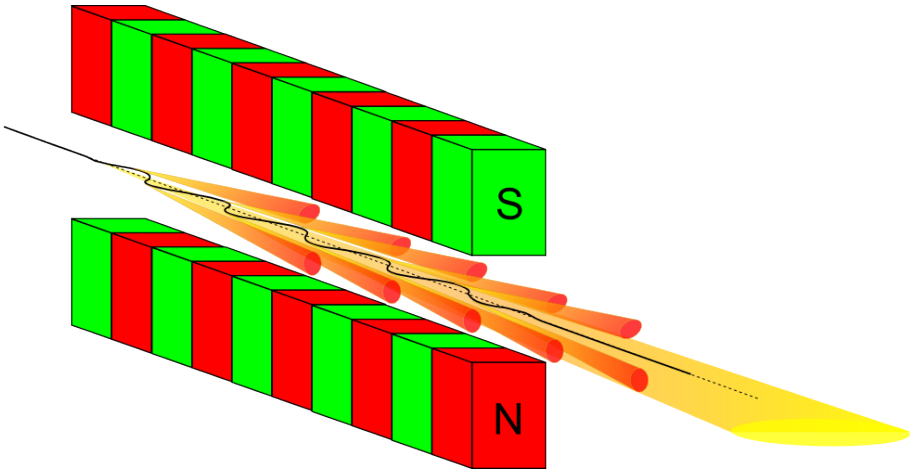

Figure 3.6: Schematic of a permanent magnet planar wiggler. The red magnets are north poles and the green magnets are south poles[47].

(2.88). We can rewrite the critical photon energy in a more useful form

$$\epsilon_c = 665 E^2 B \tag{3.19}$$

where ϵ_c is in units of eV, E is the electron beam energy measured in GeV and B is the strength of the magnetic field measured in T. We can characterise the radiation from a wiggler using the critical photon energy equation. If we consider a wiggler which has an angular deflection of zero, that is $\dot{x} = \theta = 0$ where $\dot{x}$ is calculated using equation (3.6), then the critical energy of the observed photon spectrum is the same as the critical photon energy for a dipole magnet except here we use the amplitude of the magnetic field B_0 (the magnetic field in a planar ID actually varies sinusoidally as a function of z).

In order to calculate the critical photon energy for a wiggler with any value of θ we can replace the magnetic field in equation (3.19) with the equation for the magnetic field in a planar wiggler which is

$$B_y = -B_0 \sin\left(\frac{2\pi z}{\lambda_{\mathrm{ID}}}\right) \tag{3.20}$$

This means that the critical photon energy as a function of z is

$$\epsilon_c(z) = \epsilon_{c0} \left|\sin\left(\frac{2\pi z}{\lambda_{\mathrm{ID}}}\right)\right| \tag{3.21}$$

We can write the critical photon energy as a function of θ as equation (3.6) means that

$$\frac{\dot{x}\gamma}{K} = \cos\left(\frac{2\pi z}{\lambda_{\mathrm{ID}}}\right) \tag{3.22}$$

and we can use the identity

$$\sin^2\theta + \cos^2\theta \equiv 1 \tag{3.23}$$

to rewrite equation (3.21) as

$$\epsilon_c = \epsilon_{c0}\sqrt{1 - \left(\frac{\dot{x}\gamma}{K}\right)^2} \tag{3.24}$$

and because $\dot{x} \equiv \theta$ the critical energy for the photon spectrum generated by a planar wiggler is

$$\epsilon_c = \epsilon_{c0}\sqrt{1 - \left(\frac{\theta\gamma}{K}\right)^2} = \epsilon_{c0}\sqrt{1 - \left(\frac{\theta}{\theta_{max}}\right)^2} \tag{3.25}$$

where $\theta_{max} = K/\gamma$.

3.3.2 Photon Flux from a Planar Wiggler

The photon flux produced by a dipole magnet is given by equation (2.96). As each period of the wiggler can be thought of as two dipoles the spectral photon flux of a wiggler $\dot{N}_W$ is therefore

$$\dot{N}_W = \sum_{i=1}^{2n} \dot{N}_i \tag{3.26}$$

where n is the number of periods in the wiggler and $\dot{N}_i$ is the spectral photon flux from a dipole magnet with a field strength equal to the peak magnetic field of the wiggler and length equal to one period. Figure 3.7 compares the photon flux generated by a 3 GeV electron beam with a beam current of 300 mA travelling through a 2.0 T dipole magnet and a 50 period wiggler with a peak magnetic field strength of 2.0 T.

The benefits of using a wiggler over a dipole magnet for synchrotron light sources are very straightforward. The peak magnetic field of the wiggler can be chosen to meet the required spectral range of an experiment and the spectral photon flux generated is $2n$ times the intensity of a dipole magnet where n is the number of periods of the wiggler. Light sources can install a number of different wigglers at different positions in the beam line to provide different spectral ranges to different experiments.

3.4 Synchrotron Radiation from an Undulator

Unlike in the case of a planar wiggler an undulator can not be simply described as a series of dipole magnets. In terms of visualising a planar undulator magnetic field we can imagine it as a series of alternating dipole fields just as in the case of a wiggler. We can also describe the electron trajectory through an undulator in terms of electron motion through dipole fields. However we can not describe the photon spectrum produced by an undulator in terms of dipole fields. This

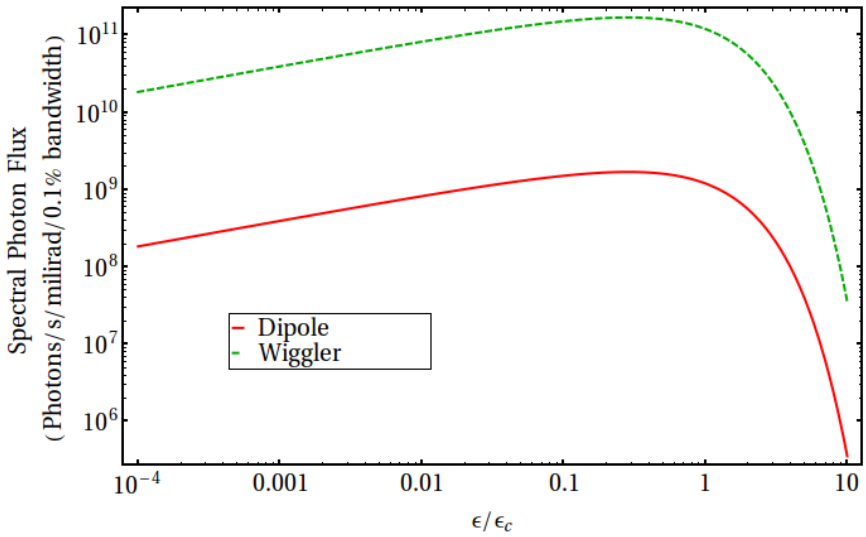

Figure 3.7: Plot comparing the photon flux generated by a 3 GeV electron beam with a beam current of 300 mA travelling through a 2.0 T dipole magnet and a 50 period wiggler with a peak magnetic field strength of 2.0 T. The red curve is the flux from the dipole magnet and the green dashed curve is the flux from the wiggler. Plotted using Mathematica 8.

is due to the interference effects between overlapping cones of synchrotron radiation produced within the undulator as explained in section 3.2.

3.4.1 Interference Effects in an Undulator

We can describe the interference effects as being analogous to those observed in a diffraction grating. As an undulator is made up of multiple periods of the magnetic field there are multiple sources of synchrotron radiation that are evenly spaced. These sources then interfere with each other. The effects that arise from this depend on the undulator period and the angle of observation. The geometry for these interference effects is shown in figure 3.8.

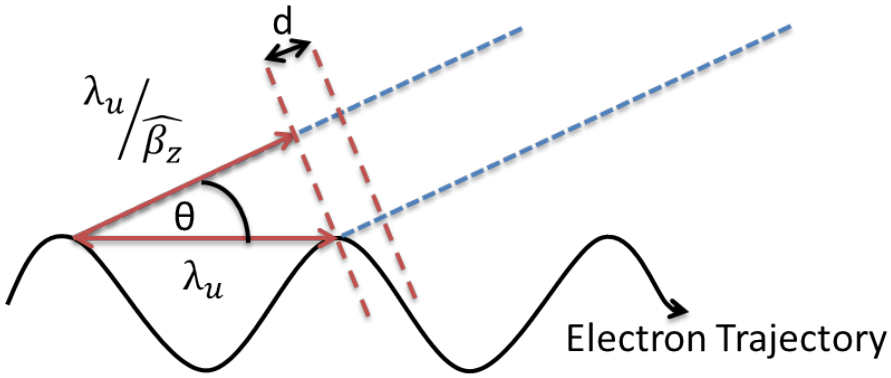

Figure 3.8: Diagram showing the geometry used to describe the interference effects in an undulator

The condition for interference to occur between two different synchrotron radiation wave

fronts produced by the same electron is that the electron must *slip* behind the the first wave-front by an amount equal to an integer number of wavelengths. Assuming that the wave-fronts are emitted at an angle θ then the path difference d between the two consecutive wave-fronts is given by

$$d = \frac{\lambda_u}{\hat{\beta}_z} - \lambda_u \cos\theta \tag{3.27}$$

where $\hat{\beta}_z$ is the average speed of the electron along z.

As the condition for constructive interference is that the path difference must be equal to an integer number of wavelengths of the radiation we can write equation (3.27) as

$$n\lambda = \frac{\lambda_u}{\hat{\beta}_z} - \lambda_u \cos\theta \tag{3.28}$$

where n is an integer and λ is the wavelength of light emitted. In order to solve this equation we need the value $\hat{\beta}_z$. For an electron with a fixed energy β is a constant. This means that any change in β_x will cause a corresponding change in β_y and β_z as

$$\beta^2 = \beta_x^2 + \beta_y^2 + \beta_z^2 \tag{3.29}$$

In the case of a planar undulator $\beta_y = 0$ this means that we can use equation (3.29) to express β_z in terms of β_x and β. Therefore we need to calculate β_x. Equation (3.6) is

$$\frac{\mathrm{d}x}{\mathrm{d}z} = \frac{K}{\gamma} \cos\frac{2\pi z}{\lambda_u} \tag{3.30}$$

As the electron is highly relativistic and the deviation in x is small then to a good approximation $\Delta z = c\Delta t$. Therefore equation (3.30) can be approximated by

$$\frac{\Delta x}{\Delta z} = \frac{\Delta x}{c\Delta t} = \frac{1}{c}\frac{\mathrm{d}x}{\mathrm{d}t} = \frac{K}{\gamma} \cos\frac{2\pi z}{\lambda_u} \tag{3.31}$$

As β is defined as v/c and $v_x = \mathrm{d}x/\mathrm{d}t$ then $\beta_x = (\mathrm{d}x/\mathrm{d}t)/c$. This means that β_x is

$$\beta_x = \frac{K}{\gamma} \cos\frac{2\pi z}{\lambda_u} \tag{3.32}$$

therefore β_z is

$$\begin{aligned} \beta_z^2 &= \beta^2 - \beta_x^2 \\ \beta_z^2 &= \beta^2 - \frac{K^2}{\gamma^2} \cos^2\frac{2\pi z}{\lambda_u} \end{aligned} \tag{3.33}$$

Using the double angle formula $\cos 2\theta = 2\cos^2\theta - 1$ equation (3.33) becomes

$$\beta_z^2 = \beta^2 - \frac{K^2}{2\gamma^2}\left(\cos\left(\frac{4\pi z}{\lambda_u}\right) + 1\right) \tag{3.34}$$

therefore β_z is

$$\beta_z = \beta\left(1 - \frac{K^2}{2\beta^2\gamma^2}\left(\cos\left(\frac{4\pi z}{\lambda_u}\right) + 1\right)\right)^{\frac{1}{2}} \tag{3.35}$$

We can simplify this equation using a series expansion. As the initial assumption for the equations describing the electron trajectory was that $\mathrm{d}x/\mathrm{d}z \ll 1$ then $x \ll z$. We can therefore approximate the series expansion by only excluding terms of $\mathcal{O}(x^2)$ or higher. This means that equation (3.35) becomes

$$\beta_z = \beta\left(1 - \frac{K^2}{4\beta^2\gamma^2} - \frac{K^2}{4\beta^2\gamma^2}\cos\frac{4\pi z}{\lambda_u}\right) \tag{3.36}$$

Therefore β_z simply consists of a constant term and a cosine term. As we are after the average value of β_z the cosine term will average to zero which means that $\hat{\beta_z}$ is

$$\hat{\beta_z} = \beta - \frac{K^2}{4\beta\gamma^2} \tag{3.37}$$

and as $\beta = (1 - (1/\gamma^2))^{1/2}$ equation (3.37) becomes

$$\hat{\beta_z} \approx 1 - \frac{1}{2\gamma^2} - \frac{K^2}{4\beta\gamma^2} \tag{3.38}$$

where we have used a series expansion and as $\gamma > \mathcal{O}(10^3)$ the terms inversely proportional to γ^4 or higher have been ignored. We can now insert this value of $\hat{\beta_z}$ into equation (3.28) which gives

$$n\lambda \approx \lambda_u\left(1 - \frac{1}{2\gamma^2} - \frac{K^2}{4\beta\gamma^2}\right)^{-1} - \lambda_u\cos\theta \tag{3.39}$$

Once again we use a series expansion and ignore the terms with an order of γ^4 or higher which means that the equation for the path difference becomes

$$\begin{aligned} n\lambda &\approx \lambda_u\left(1 + \frac{1}{2\gamma^2} + \frac{K^2}{4\beta\gamma^2}\right) - \lambda_u\cos\theta \\ &\approx \frac{\lambda_u}{2\gamma^2} + \frac{\lambda_u K^2}{4\beta\gamma^2} + \lambda_u(1 - \cos\theta) \end{aligned} \tag{3.40}$$

Using the half angle identity

$$\sin^2\left(\frac{\theta}{2}\right) = \frac{1}{2}(1-\cos\theta) \tag{3.41}$$

and the small angle approximation that $\sin x \approx x$ equation (3.40) simplifies to

$$\begin{aligned} n\lambda &\approx \frac{\lambda_u}{2\gamma^2} + \frac{\lambda_u K^2}{4\beta\gamma^2} + \frac{\lambda_u \theta^2}{2} \\ &\approx \frac{\lambda_u}{2\gamma^2}\left(1 + \frac{K^2}{2\beta} + \theta^2\gamma^2\right) \end{aligned} \tag{3.42}$$

As for highly relativistic particles $\beta \approx 1$ equation (3.42) can be rearranged to

$$\lambda = \frac{\lambda_u}{2n\gamma^2}\left(1 + \frac{K^2}{2} + \theta^2\gamma^2\right) \tag{3.43}$$

This is known as the undulator equation. The undulator equation describes some fundamental properties of undulator radiation. The term λ_u/γ^2 means that an undulator with a period of the order of 10^{-3}m produces light with a wavelength of the order of 10^{-9}m as $\gamma \approx \mathcal{O}(10^3)$. Additionally the undulator equation also means that the wavelength of the synchrotron radiation depends on the undulator period, the electron beam energy, the undulator deflection parameter and the angle of observation.

The dependence on the peak magnetic field gives undulators a very useful feature. By constructing them such that the peak magnetic field is actually a smoothly varying function that can be controlled by the machine operator, the wavelength of light produced can actually be controlled. This allows for a so called *tuning range* over which the wavelength of the radiation can be varied continuously. The wavelength dependence on the peak magnetic field as seen by an on-axis observer $\theta = 0$ is plotted in figure 3.9 for a 1 GeV electron travelling through an undulator with a period of 10 mm.

As the observation angle θ appears in the undulator equation this means that the wavelength of the observed light changes depending on the position of the observer. Figure 3.10 shows the wavelength dependence on the angle of observation for a 1 GeV electron travelling through an undulator with a period of 10 mm and a deflection parameter of $K = 1$.

When we considered the interference condition in an undulator we did not include the effects of the undulator having a finite length. If an undulator consists of N periods the length of the undulator is therefore $L = N\lambda_u$. Therefore the condition for constructive interference over the length of undulator is simply a modification of equation (3.28) which is

$$Nn\lambda = \frac{N\lambda_u}{\hat{\beta}_z} - N\lambda_u\cos\theta \tag{3.44}$$

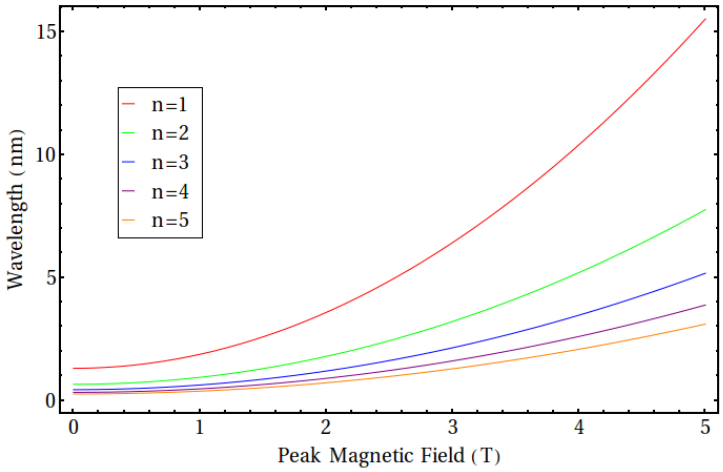

Figure 3.9: The variation in the on-axis wavelength of synchrotron radiation produced by a 1 GeV electron travelling through an undulator with $\lambda_u = 10\,\text{mm}$ as a function of the peak magnetic field of the undulator B_0. The red line corresponds to first harmonic, the green line corresponds to second harmonic, the blue line corresponds to third harmonic, the purple line corresponds to fourth harmonic and the orange line corresponds to fifth harmonic.

Additionally we never considered the case of destructive interference. This occurs when there is one complete extra wavelength advance over the entire undulator. If the wavelength for destructive interference is λ^* the condition for destructive interference is just

$$Nn\lambda^* + \lambda^* = \frac{N\lambda_u}{\hat{\beta}_z} - N\lambda_u \cos\theta \tag{3.45}$$

This means that no 2 consecutive periods of the undulator give constructive interference. If we consider the on-axis case ($\theta = 0$) we can calculate the wavelength range over which there is emission of synchrotron radiation to be $\Delta\lambda = \lambda - \lambda^*$. By considering equations (3.44) and (3.45) we can write λ^* in terms of λ as

$$\lambda^* = \frac{Nn\lambda}{1+Nn} \tag{3.46}$$

This means that the wavelength range for emission is

$$\begin{aligned}\Delta\lambda &= \lambda - \frac{Nn\lambda}{1+Nn} \\ &= \frac{\lambda}{1+Nn}\end{aligned} \tag{3.47}$$

The bandwidth of the emitted radiation, $\Delta\lambda/\lambda$, is

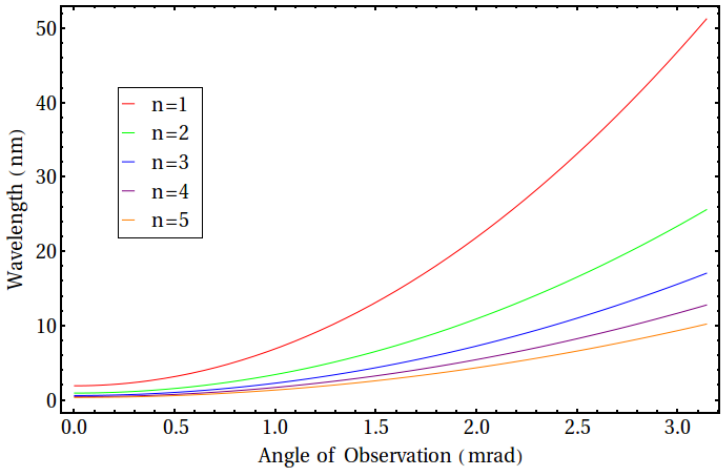

Figure 3.10: The variation in the observed wavelength of synchrotron radiation produced by a 1 GeV electron travelling through an undulator with $\lambda_u = 10\,\text{mm}$ and $K = 1$ as a function of the observation angle θ. The red line corresponds to first harmonic, the green line corresponds to second harmonic, the blue line corresponds to third harmonic, the purple line corresponds to fourth harmonic and the orange line corresponds to fifth harmonic.

$$\begin{aligned}\frac{\Delta\lambda}{\lambda} &= \frac{1}{1+Nn} \\ &\approx \frac{1}{Nn}\end{aligned} \tag{3.48}$$

As the bandwidth is inversely proportional to the harmonic number this means that the bandwidth for each successive harmonic keeps reducing. Typical undulators have $N > 100$ therefore the bandwidth for the first harmonic is $< 1\%$.

3.4.2 Spectral Angular Flux Density for an Undulator

In order to calculate the spectral angular flux density for an undulator we need to use some equations that we derived when considering the synchrotron radiation produced by an electron travelling through a dipole magnet. The spectral angular distribution of the radiation produced by an electron is given in equation (2.74). Assuming we are in the far field regime we can substitute the equation for the electric field (2.41) into (2.74) which gives

$$\begin{aligned}\frac{\mathrm{d}^2W}{\mathrm{d}\Omega\mathrm{d}\omega} &= \frac{2r'^2}{\mu_0 c}\left|\frac{iq\omega}{4\pi\sqrt{2\pi}\epsilon_0 cr'}\int_{-\infty}^{\infty}(\mathbf{n}'\times(\mathbf{n}'\times\boldsymbol{\beta}))e^{i\omega(t'+\frac{r'(t')}{c})}\mathrm{d}t'\right|^2 \\ &= \frac{q^2\omega^2}{16\pi^3 c\epsilon_0}\left|\int_{-\infty}^{\infty}(\mathbf{n}'\times(\mathbf{n}'\times\boldsymbol{\beta}))e^{i\omega(t'+\frac{r'(t')}{c})}\mathrm{d}t'\right|^2\end{aligned} \tag{3.49}$$

using the definitions of $r'(t')$ and the unit vector in the direction of $\mathbf{r}'(t')$ we can rewrite the term in the exponent as

$$t' + \frac{r'(t')}{c} = t' + \frac{\mathbf{n}\cdot\mathbf{x}}{c} - \frac{\mathbf{n}\cdot\mathbf{r}}{c} \tag{3.50}$$

As we have assumed that we are in the far field regime the term $\mathbf{n}\cdot\mathbf{x}/c$ represents the time taken to travel between the origin and the observer. Therefore this can be considered a fixed phase shift and so can be disregarded. Which results in

$$\frac{\mathrm{d}^2W}{\mathrm{d}\Omega\mathrm{d}\omega} = \frac{q^2\omega^2}{16\pi^3 c\epsilon_0}\left|\int_{-\infty}^{\infty}(\mathbf{n}'\times(\mathbf{n}'\times\boldsymbol{\beta}))e^{i\omega(t'-\frac{\mathbf{n}\cdot\mathbf{r}}{c})}\mathrm{d}t'\right|^2 \tag{3.51}$$

As we are considering a finite length undulator constructed from N periods we can express the integral in the above equation as a summation of the integrals for each period of the undulator.

$$\frac{\mathrm{d}^2W}{\mathrm{d}\Omega\mathrm{d}\omega} = \frac{q^2\omega^2}{16\pi^3 c\epsilon_0}\left|\sum_{j=0}^{N-1}\int_{\frac{-\lambda_u}{2c\bar{\beta}_z}}^{\frac{\lambda_u}{2c\bar{\beta}_z}}(\mathbf{n}'\times(\mathbf{n}'\times\boldsymbol{\beta}))e^{i\omega(t'-\frac{\mathbf{n}\cdot\mathbf{r}}{c}+j\frac{d}{c})}\mathrm{d}t'\right|^2 \tag{3.52}$$

where d is the separation in time between successive wave fronts and therefore d/c is the phase difference in time between successive periods in the undulator. The limits for the integral are given by the time taken for the electron to travel between $-\lambda_u/2$ and $\lambda_u/2$. We can separate out the phase terms which gives

$$\begin{aligned}\frac{\mathrm{d}^2W}{\mathrm{d}\Omega\mathrm{d}\omega} &= \frac{q^2\omega^2}{16\pi^3 c\epsilon_0}\left|\sum_{j=0}^{N-1}e^{\frac{i\omega jd}{c}}\times\int_{\frac{-\lambda_u}{2c\bar{\beta}_z}}^{\frac{\lambda_u}{2c\bar{\beta}_z}}(\mathbf{n}'\times(\mathbf{n}'\times\boldsymbol{\beta}))e^{i\omega(t'-\frac{\mathbf{n}\cdot\mathbf{r}}{c})}\mathrm{d}t'\right|^2 \\ &= \frac{q^2\omega^2}{16\pi^3 c\epsilon_0}\left|\sum_{j=0}^{N-1}e^{\frac{i\omega jd}{c}}\right|^2\times\left|\int_{\frac{-\lambda_u}{2c\bar{\beta}_z}}^{\frac{\lambda_u}{2c\bar{\beta}_z}}(\mathbf{n}'\times(\mathbf{n}'\times\boldsymbol{\beta}))e^{i\omega(t'-\frac{\mathbf{n}\cdot\mathbf{r}}{c})}\mathrm{d}t'\right|^2\end{aligned} \tag{3.53}$$

The summation term in equation (3.53) is identical to terms in diffraction grating studies. This is not surprising as the effects of a diffraction grating with N slits is very similar to the radiation emission from a periodic magnetic field made up of N periods. This summation term actually represents the interference term for N periods. Using Euler's formula we can express this interference term, which is also known as the *grating function*, as

$$\left|\sum_{j=0}^{N-1}e^{\frac{i\omega jd}{c}}\right|^2 = \frac{\sin^2\left(\frac{N\omega d}{2c}\right)}{\sin^2\left(\frac{\omega d}{2c}\right)} = \frac{\sin^2\left(\frac{N\pi\omega}{\omega_1}\right)}{\sin^2\left(\frac{\pi\omega}{\omega_1}\right)} \tag{3.54}$$

where ω_1 is the angular frequency corresponding to the first harmonic. Figure 3.11 shows how the grating function varies with respect to ω/ω_1 for two different numbers of periods. As can be seen from figure 3.11 the function peaks when ω/ω_1 is an integer. These peaks are referred to

as the *principal maxima* as there are smaller *secondary maxima* between the principal maxima. The intensity of the principle maxima is given in (3.54) by N^2.

The grating function is a periodic function with a periodicity equal to the angular frequency of the first harmonic. Within each period the grating function peaks N times with the spacing between the peaks given by $\omega_1/(N-1)$.

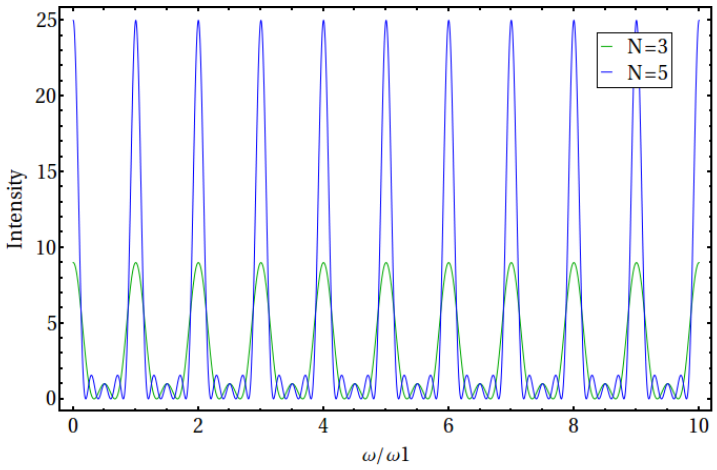

Figure 3.11: Plot showing how the grating function (3.54) varies with respect to ω/ω_1 for two different values of N. The green line represents $N = 3$ and the blue line represents $N = 5$.

In order to analyse the shape of the grating function in more detail we can normalise the function by dividing by N^2. Additionally as we are interested in the principal maxima we will only consider angular frequencies given by $\omega = n\omega_1 + \Delta\omega$ where n is an integer. By modifying equation (3.54) in this manner we end up with what is known as the *line-shape function* which is defined as

$$L\left(\frac{N\Delta\omega}{\omega_1}\right) = \frac{\sin^2\left(\frac{N\pi\Delta\omega}{\omega_1}\right)}{N^2\sin^2\left(\frac{\pi\Delta\omega}{\omega_1}\right)} \tag{3.55}$$

Figure 3.12 shows the line-shape function for four undulators with differing numbers of periods. As can be seen when a realistic number of periods is considered, i.e. N is large, the line-shape function becomes independent of the number of periods.

The principal maxima that is located at $N\Delta\omega/\omega_1 = 0$ drops off from the peak value very rapidly. The normalised intensity is halved when $N\Delta\omega/\omega_1 \approx 0.5$. We can consider the bandwidth of radiation at a particular harmonic n to be the full width half maxima of the principal maxima. Therefore the radiation bandwidth of the n^{th} harmonic is given by

$$\frac{\Delta\omega}{\omega_n} = \frac{1}{nN} \tag{3.56}$$

which is consistent with the bandwidth that was calculated using simple interference argu-

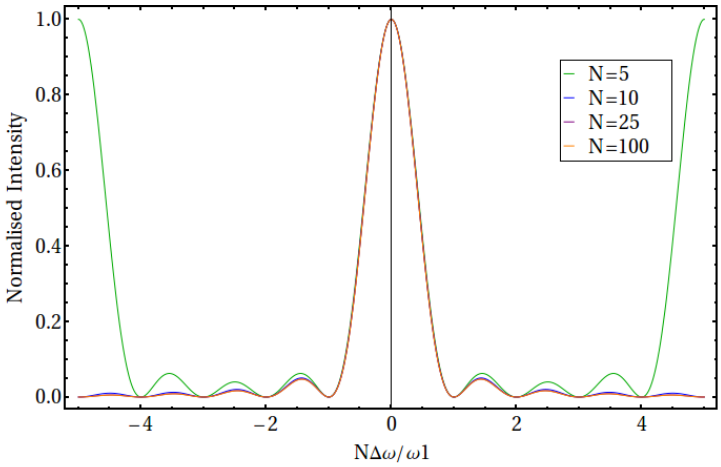

Figure 3.12: Plot comparing the line-shape function for four undulators with different numbers of periods. The green curve corresponds to an undulator with $N = 5$. The blue curve corresponds to an undulator with $N = 10$. The purple curve corresponds to an undulator with $N = 25$. The orange curve corresponds to an undulator with $N = 100$. As N increases the line shape functions tend to converge and become independent of N.

ments, equation (3.48).

We can use the line-shape function in our calculations of the spectral angular flux density from a undulator by replacing the summation in equation (3.53) with N^2L which means that the equation for $\mathrm{d}^2W/\mathrm{d}\Omega\mathrm{d}\omega$ becomes

$$\frac{\mathrm{d}^2W}{\mathrm{d}\Omega\mathrm{d}\omega} = \frac{q^2\omega^2N^2}{16\pi^3c\epsilon_0}L\left(\frac{N\Delta\omega}{\omega_1}\right)\left|\int_{\frac{-\lambda_u}{2c\beta_z}}^{\frac{\lambda_u}{2c\beta_z}}(\mathbf{n}'\times(\mathbf{n}'\times\beta))e^{i\omega(t'-\frac{\mathbf{n}\cdot\mathbf{r}}{c})}\mathrm{d}t'\right|^2 \tag{3.57}$$

To evaluate equation (3.57) we need to be able to calculate the integral. To do this we will consider the triple vector product and the exponential in the integral separately. Appendix A give the calculation of the triple vector product $(\boldsymbol{n'}\times(\boldsymbol{n'}\times\boldsymbol{\beta}))$ and appendix B give the calculation of $e^{i\omega\left(t-\frac{\mathbf{n}\cdot\mathbf{r}}{c}\right)}$.

We can substitute equation (A.7) for the triple vector product and equation (B.12) for the exponential in equation (3.57) which becomes

$$\frac{\mathrm{d}^2W}{\mathrm{d}\Omega\mathrm{d}\omega} = \frac{q^2\omega^2N^2}{16\pi^3c\epsilon_0}L\left(\frac{N\Delta\omega}{\omega_1}\right)\left|\sum_{p=-\infty}^{\infty}J_p(X)\sum_{q=-\infty}^{\infty}J_q(Y)\times\int_{\frac{-\lambda_u}{2c\beta_z}}^{\frac{\lambda_u}{2c\beta_z}}\begin{pmatrix}\theta\cos\phi-\beta_x\\ \theta\sin\phi\\ 0\end{pmatrix}e^{iHt(n-p+2q)}\mathrm{d}t'\right|^2 \tag{3.58}$$

The two non zero components in the integral relate to the horizontal and vertical polarisations. As the integral is performed over a full undulator period it will nominally be equal to zero. However it is not zero when the exponential is equal to one. This occurs when

$$n - p + 2q = 0 \tag{3.59}$$

for terms that are time independent. However as β_x appears in the integral there is an additional time dependent term to consider. From equation (A.4) $\beta_x \propto \cos(Ht)$ this means that the argument in the integral is of the form

$$\begin{aligned}\cos(HT)e^{iHt(n-p+2q)} &= \frac{1}{2}(e^{iHt} + e^{-iHt})e^{iHt(n-p+2q)} \\ &= \frac{1}{2}e^{-iHt}(e^{2iHt} + 1)e^{iHt(n-p+2q)} \\ &= \frac{1}{2}(1 + e^{2iHt})e^{iHt(n-p+2q-1)}\end{aligned} \tag{3.60}$$

This will equal zero over a complete undulator period except when

$$n - p + 2q = \pm 1 \tag{3.61}$$

If we consider the two planes independently this integral is now straightforward to perform. Taking the vertical case first we need $n+2q = p$ so that the exponential is equal to one, therefore equation (3.58) in the vertical plane is

$$\frac{\mathrm{d}^2W}{\mathrm{d}\Omega\mathrm{d}\omega} = \frac{q^2\omega^2N^2}{16\pi^3c\epsilon_0}L\left(\frac{N\Delta\omega}{\omega_1}\right)\left|\frac{\lambda_u}{c\hat{\beta}_z}\theta\sin\phi\sum_{p=-\infty}^{\infty}J_{n+2p}(X)J_p(Y)\right|^2 \tag{3.62}$$

substituting equation (B.7) for ω gives

$$\frac{\mathrm{d}^2W}{\mathrm{d}\Omega\mathrm{d}\omega} = \frac{q^2n^2H^2\gamma^4N^2}{4\pi^3c\epsilon_0A^2}\left(\frac{\lambda_u}{c\hat{\beta}_z}\right)^2L\left(\frac{N\Delta\omega}{\omega_1}\right)\left|\theta\sin\phi\sum_{p=-\infty}^{\infty}J_{n+2p}(X)J_p(Y)\right|^2 \tag{3.63}$$

as $\lambda_u/c\hat{\beta}_z = 2\pi/H$ this becomes

$$\frac{\mathrm{d}^2W}{\mathrm{d}\Omega\mathrm{d}\omega} = \frac{q^2n^2\gamma^4N^2}{\pi c\epsilon_0A^2}L\left(\frac{N\Delta\omega}{\omega_1}\right)\left|\theta\sin\phi\sum_{p=-\infty}^{\infty}J_{n+2p}(X)J_p(Y)\right|^2 \tag{3.64}$$

When considering the horizontal plane a similar route can be followed however additional terms must be included for the cases $n - p + 2q = 1$ and $n - p + 2q = -1$ which are due to β_x. Therefore equation (3.58) in the horizontal plane is

$$\frac{\mathrm{d}^2W}{\mathrm{d}\Omega\mathrm{d}\omega} = \frac{q^2n^2\gamma^4N^2}{\pi c\epsilon_0 A^2}L\left(\frac{N\Delta\omega}{\omega_1}\right)\left|\theta\cos\phi\sum_{p=-\infty}^{\infty}J_{n+2p}(X)J_p(Y)\right.$$
$$\left.-\frac{K}{2\gamma}\left(\sum_{p=-\infty}^{\infty}J_{n+2p-1}(X)J_p(Y)+\sum_{p=-\infty}^{\infty}J_{n+2p+1}(X)J_p(Y)\right)\right|^2 \tag{3.65}$$

On-Axis Radiation

We can now consider the special case when the observer is on-axis, $\theta = 0$. This means that there is no vertical component to the radiation. Additionally as X depends on θ when $\theta = 0$ $X = 0$ which means that

$$Y = \frac{nK^2}{4\left(4\frac{K^2}{2}\right)}$$

The Bessel function sum also simplifies as $J_n(0)$ is only non-zero when $n = 0$. Therefore due to the indices of the Bessel function $J_{n+2p\pm1}(0)$

$$p = \frac{\pm1 - n}{2}$$

as p and n are integers we can see that n must be odd which means that no even harmonics are observed on-axis. The on-axis spectral angular flux density for an undulator therefore is

$$\frac{\mathrm{d}^2W}{\mathrm{d}\Omega\mathrm{d}\omega} = \frac{q^2n^2\gamma^4N^2}{\pi c\epsilon_0 A^2}L\left(\frac{N\Delta\omega}{\omega_1}\right)\left|-\frac{K}{2\gamma}\left(J_{(1-n)/2}(Y)+J_{(-1-n)/2}(Y)\right)\right|^2 \tag{3.66}$$

As we are using Bessel functions of the first kind we can rewrite equation (3.66) using the Bessel function relationship

$$J_{-n}(x) = (-1)^n J_n(x) \tag{3.67}$$

as

$$\frac{\mathrm{d}^2W}{\mathrm{d}\Omega\mathrm{d}\omega} = \frac{q^2n^2\gamma^4N^2}{\pi c\epsilon_0 A^2}L\left(\frac{N\Delta\omega}{\omega_1}\right)\left|\frac{K}{2\gamma}\left(J_{(n+1)/2}(Y)-J_{(n-1)/2}(Y)\right)\right|^2 \tag{3.68}$$

We can easily convert this into the on-axis angular power density by multiplying by the number of electrons per second I_b/q, where I_b is the beam current in amperes. This means that

$$\frac{\mathrm{d}^2W}{\mathrm{d}\Omega\mathrm{d}\omega} = \frac{q^2n^2\gamma^4N^2}{\pi c\epsilon_0 A^2}\frac{I_b}{q}L\left(\frac{N\Delta\omega}{\omega_1}\right)\left|\frac{K}{2\gamma}\left(J_{(n+1)/2}(Y)-J_{(n-1)/2}(Y)\right)\right|^2 \tag{3.69}$$

This can be converted into a number of photons per solid angle per second for an on-axis planar undulator which is expressed in terms of a relative bandwidth $\mathrm{d}\omega/\omega$

$$\frac{\mathrm{d}^2\dot{N}}{\mathrm{d}\Omega \mathrm{d}\omega/\omega} = \frac{q^2 n^2 \gamma^4 N^2}{\pi c \epsilon_0 A^2} \frac{I_b}{q} \frac{2\pi}{h} L\left(\frac{N\Delta\omega}{\omega_1}\right) \left| \frac{K}{2\gamma} \left(J_{(n+1)/2}(Y) - J_{(n-1)/2}(Y) \right) \right|^2 \tag{3.70}$$

which in units of photons per second per mrad^2 per 0.1% bandwidth on-axis is

$$\frac{\mathrm{d}\dot{N}}{\mathrm{d}\Omega}_{\theta=0} = 1.74 \times 10^{14} n^2 N^2 E^2 I_b \frac{K^2}{A^2} \left(J_{(n+1)/2}(Y) - J_{(n-1)/2}(Y) \right)^2 \tag{3.71}$$

where E is the beam energy in GeV and I_b is the beam current in A.

3.4.3 Radiation from a Helical Undulator

Having derived the spectral angular flux density from a planar undulator we can easily extend this to describe the synchrotron radiation produced by a helical undulator. Starting with equation (3.57) which is

$$\frac{\mathrm{d}^2 W}{\mathrm{d}\Omega \mathrm{d}\omega} = \frac{q^2 \omega^2 N^2}{16\pi^3 c \epsilon_0} L\left(\frac{N\Delta\omega}{\omega_1}\right) \left| \int_{\frac{-\lambda_u}{2c\hat{\beta}_z}}^{\frac{\lambda_u}{2c\hat{\beta}_z}} (\mathbf{n}' \times (\mathbf{n}' \times \boldsymbol{\beta})) e^{i\omega(t' - \frac{\mathbf{n}\cdot\mathbf{r}}{c})} \mathrm{d}t' \right|^2$$

we follow the same derivation steps as for a planar undulator.

The main differences appear in the vector triple product calculation and the calculation of the exponent. If we consider the vector triple product first, in a helical undulator B_x is non-zero and therefore β_y is non-zero. Following the same methodology and assumptions we used to derive (A.6) the vector triple product for a helical undulator can be written. The vector triple product for a helical undulator is

$$\mathbf{n} \times (\mathbf{n} \times \boldsymbol{\beta}) = \begin{pmatrix} \theta\cos\phi - \beta_x \\ \theta\sin\phi - \beta_y \\ 0 \end{pmatrix} \tag{3.72}$$

The calculation of the exponent is more complicated for a helical undulator as instead of $\mathbf{r}$ only having 2 dimensions x and z it now depends on x, y and z. Just as when we calculated the exponent for the planar undulator (see (B.5)) we need to express the electron motion in the undulator as a function of time. Therefore the vector $\mathbf{r}$ is

$$\mathbf{r} = \begin{pmatrix} \frac{K_y c}{H\gamma} \sin Ht \\ -\frac{K_x c}{H\gamma} \sin(Ht + \psi) \\ c\hat{\beta}_s t - \frac{c}{8\gamma^2 H} \left(K_y^2 \sin 2Ht + K_x^2 \sin(2Ht + 2\psi) \right) \end{pmatrix} \tag{3.73}$$

and the unit vector is $\mathbf{n} = (\theta\cos\phi, \theta\sin\phi, \cos\theta)$. Therefore the dot product in the the exponent

is

$$\begin{aligned}\mathbf{n}\cdot\mathbf{r} = \frac{K_y c}{H\gamma}\theta\cos\phi\sin Ht - \frac{K_x c}{H\gamma}\theta\sin\phi\sin\left(Ht+\psi\right) + c\hat{\beta}_s t\cos\theta \\ -\frac{c}{8\gamma^2 H}\left(K_y^2\sin 2Ht + K_x^2\sin\left(2Ht+2\psi\right)\right)\cos\theta\end{aligned} \tag{3.74}$$

therefore the exponent is

$$\begin{aligned}\omega\left(t-\frac{\mathbf{n}\cdot\mathbf{r}}{c}\right) = \omega t(1-\hat{\beta}_s\cos\theta) - \frac{\omega K_y}{H\gamma}\theta\cos\phi\sin Ht + \frac{\omega K_x}{H\gamma}\theta\sin\phi\sin\left(Ht+\psi\right) \\ +\frac{\omega}{8\gamma^2 H}\left(K_y^2\sin 2Ht + K_x^2\sin\left(2Ht+2\psi\right)\right)\cos\theta\end{aligned} \tag{3.75}$$

As before if we are considering a realistic undulator with a large number of periods only the harmonics of the spectrum will contain a significant intensity which means that the exponent will only be evaluated at these discrete values of ω that correspond to the frequencies of the harmonics. Equation (B.8) gives the angular frequency as

$$\omega = \frac{nH}{1-\hat{\beta}_z\cos\theta} \tag{3.76}$$

we can rearrange this equation and use it to simplify the first term in equation (3.75) which becomes

$$\begin{aligned}\omega\left(t-\frac{\mathbf{n}\cdot\mathbf{r}}{c}\right) = nHt - \frac{\omega K_y}{H\gamma}\theta\cos\phi\sin Ht + \frac{\omega K_x}{H\gamma}\theta\sin\phi\sin\left(Ht+\psi\right) \\ +\frac{\omega}{8\gamma^2 H}\left(K_y^2\sin 2Ht + K_x^2\sin\left(2Ht+2\psi\right)\right)\cos\theta\end{aligned} \tag{3.77}$$

To simplify the equation further we need to substitute $\hat{\beta}_z$, which for a helical undulator is given by

$$\hat{\beta}_z = \beta\left(1-\frac{K_x^2}{4\gamma^2}-\frac{K_y^2}{4\gamma^2}\right) \tag{3.78}$$

into equation (3.76) and rearrange it by expanding the cosine term using the small angle approximation which results in ω being able to be expressed as

$$\omega = 2nH\gamma^2\left(1+\frac{K_x^2}{2}+\frac{K_y^2}{2}+\gamma^2\theta^2\right)^{-1} = \frac{2nH\gamma^2}{A} \tag{3.79}$$

where $\beta \approx 1$ for relativistic electrons and terms proportional to $K_x^2\theta^2$ and $K_y^2\theta^2$ have been dropped because they are negligible and A is

$$A = 1 + \frac{K_x^2}{2} + \frac{K_y^2}{2} + \gamma^2\theta^2 \tag{3.80}$$

Substituting equation(3.79) into equation (3.77) gives

$$\begin{aligned}\omega\left(t - \frac{\mathbf{n}\cdot\mathbf{r}}{c}\right) = nHt - \frac{2n\gamma K_y}{A}\theta\cos\phi\sin Ht + \frac{2n\gamma K_x}{A}\theta\sin\phi\sin\left(Ht+\psi\right) \\ + \frac{n}{A}\left(K_y^2\sin 2Ht + K_x^2\sin\left(2Ht+2\psi\right)\right)\cos\theta\end{aligned} \tag{3.81}$$

expanding the terms $\sin\left(Ht+\psi\right)$ and $\sin\left(2Ht+2\psi\right)$ using the sine double angle formula means that we can rewrite this equation as

$$\begin{aligned}\omega\left(t - \frac{\mathbf{n}\cdot\mathbf{r}}{c}\right) = nHt - \frac{2n\gamma\theta}{A}\left(K_y\cos\phi\sin\left(Ht\right)\right. \\ \left.-K_x\sin\phi\sin\left(Ht\right)\cos\psi - K_x\sin\phi\sin\psi\cos\left(Ht\right)\right) + \frac{n\cos\theta}{A}\left(K_y^2\sin\left(2Ht\right)\right. \\ \left.+K_x^2\sin\left(2Ht\right)\cos 2\psi + K_x^2\sin 2\psi\cos\left(2Ht\right)\right)\end{aligned} \tag{3.82}$$

we can now gather like terms together. If we consider this part of the equation

$$\frac{2n\gamma\theta}{A}\left(K_y\cos\phi\sin\left(Ht\right) - K_x\sin\phi\sin\left(Ht\right)\cos\psi - K_x\sin\phi\sin\psi\cos\left(Ht\right)\right) \tag{3.83}$$

we can gather the terms in $\sin\left(Ht\right)$ and $\cos\left(Ht\right)$ together as follows

$$M(\sin\left(Ht\right)(K_y\cos\phi - K_x\sin\phi\cos\psi) - \cos\left(Ht\right)K_x\sin\phi\sin\psi) \tag{3.84}$$

where

$$M = \frac{2n\gamma\theta}{A}$$

Equation (3.84) is of the form $X\sin\left(Ht-\Phi\right) = X\sin\left(Ht\right)\cos\Phi - \cos\left(Ht\right)\sin\Phi$ we can therefore define Φ as follows

$$\begin{aligned}X\cos\Phi &= M(K_y\cos\phi - K_x\sin\phi\cos\psi) \\ -X\sin\Phi &= MK_x\sin\phi\sin\psi \\ \tan\Phi = \frac{\sin\Phi}{\cos\Phi} &= -\frac{K_x\sin\phi\sin\psi}{K_y\cos\phi - K_x\sin\phi\cos\psi}\end{aligned} \tag{3.85}$$

Using the identity

$$\sin\theta \equiv \frac{\tan\theta}{\sqrt{1+\tan^2\theta}} \tag{3.86}$$

we can define X as

$$
\begin{aligned}
X &= -MK_x \sin\phi \sin\psi \left(\frac{\sqrt{1+\tan^2\Phi}}{\tan\Phi} \right) \\
X^2 &= \frac{(MK_x \sin\phi\sin\psi)^2}{\tan^2\Phi} + \frac{(MK_x \sin\phi\sin\psi)^2 \tan^2\Phi}{\tan^2\Phi} \\
&= M^2(K_y\cos\phi + K_x \sin\phi\cos\psi)^2 + (MK_x\sin\phi\sin\psi)^2 \\
&= M^2(K_y^2\cos^2\phi + K_x^2\sin^2\phi(cos^2\psi + \sin^2\psi) + 2K_yK_x\sin\phi\cos\phi\cos\psi) \\
X &= M\sqrt{K_y^2\cos^2\phi + K_x^2\sin^2\phi + 2K_yK_x\sin\phi\cos\phi\cos\psi}
\end{aligned} \tag{3.87}
$$

Considering the remaining terms in equation (3.82) we can gather terms in $\sin(2Ht)$ and $\cos(2Ht)$ together as follows

$$
N\sin(2Ht)\left(K_y^2 + K_x^2\cos 2\psi\right) + N\cos(2Ht)K_x^2\sin 2\psi \tag{3.88}
$$

where

$$
N = \frac{n\cos\theta}{A}
$$

This can be rewritten in the form $Y\sin(2Ht+\Psi) = Y\sin(2Ht)\cos\Psi + Y\cos(2Ht)\sin\Psi$. Following a similar methodology as for the terms involving $\sin Ht$ and $\cos Ht$ we can define Y and Ψ to be

$$
Y = N\sqrt{K_x^4 + K_y^4 + 2K_x^2K_y^2\cos(2\psi)} \tag{3.89}
$$

$$
\tan\Psi = \frac{K_x^2\sin 2\psi}{K_y^2 + K_x^2\cos 2\psi} \tag{3.90}
$$

We can therefore write equation (3.82) as

$$
\omega\left(t - \frac{\mathbf{n}\cdot\mathbf{r}}{c}\right) = nHt - X\sin(Ht-\phi) + Y\sin(2Ht+\Psi) \tag{3.91}
$$

We can now substitute equations (3.72) and (3.91) into equation (3.57) to calculate the helical undulator angular flux. This flux is given by

$$
\frac{\mathrm{d}^2W}{\mathrm{d}\Omega\mathrm{d}\omega} = \frac{q^2\omega^2N^2}{16\pi^3c\epsilon_0}L\left(\frac{N\Delta\omega}{\omega_1}\right)\left|\int_{\frac{-\lambda_u}{2c\bar{\beta}_z}}^{\frac{\lambda_u}{2c\bar{\beta}_z}} \begin{pmatrix} \theta\cos\phi - \beta_x \\ \theta\sin\phi - \beta_y \\ 0 \end{pmatrix} e^{i(nHt - X\sin(Ht-\phi) + Y\sin(2Ht+\Psi))}\mathrm{d}t'\right|^2 \tag{3.92}
$$

Using the Jacobi-Anger formula (see equation(B.11)) we can express the exponential as a series of Bessel functions of the first kind. Therefore equation (3.92) becomes

$$\begin{aligned}\frac{\mathrm{d}^2W}{\mathrm{d}\Omega\mathrm{d}\omega} = \frac{q^2\omega^2N^2}{16\pi^3c\epsilon_0}L\left(\frac{N\Delta\omega}{\omega_1}\right)\sum_{p=-\infty}^{\infty}\sum_{q=-\infty}^{\infty}J_p(X)J_q(Y)e^{i(q\Psi-p\phi)} \\ \times\int_{\frac{-\lambda_u}{2c\bar{\beta}_z}}^{\frac{\lambda_u}{2c\bar{\beta}_z}}\begin{pmatrix}\theta\cos\phi-\beta_x\\ \theta\sin\phi-\beta_y\end{pmatrix}e^{iHt(n-p+2q)}\mathrm{d}t'\end{aligned} \tag{3.93}$$

The integral contains two terms that only depend on t. The two terms are due to the polarisation in the two transverse planes, the xz and yz planes. For terms that are constant in the transverse planes then the integral over a complete period must be zero except for when the exponential term evaluates to 1. This occurs when $n-p-2q=0$.

We must now consider the effect of β_x and β_y on the integral. In general β_x and β_y are of the form:

$$\begin{aligned}\beta_x &= \frac{K_y}{\gamma}\cos(Ht)\\ \beta_y &= \frac{K_x}{\gamma}\sin(Ht+\Psi)\end{aligned}$$

The β_x term has the integral of this form

$$\cos(Ht)e^{iHt(n-p+2q)} = \frac{1}{2}e^{iHt(n-p+2q)}\left(1+e^{2iHt}\right) \tag{3.94}$$

When integrated over a complete period this term will be equal to zero except when $n-p-2q=\pm1$. Similarly for the term involving β_y the integral can be simplified in the same manner as for the β_x term. A key step in this is to recognise that the $e^{\pm i\Psi}$ term does not vary in t and so can be factored out of the integral. This means that the integral of the β_y term is non-zero when $n-p+2q=R$ where $R=-1,0,1$.

We can now perform the integral and substituting equation (B.7) for ω gives

$$\frac{\mathrm{d}^2W}{\mathrm{d}\Omega\mathrm{d}\omega} = \frac{q^2\omega^2N^2}{16\pi^3c\epsilon_0A^2}L\left(\frac{N\Delta\omega}{\omega_1}\right)|A_x,A_y|^2 \tag{3.95}$$

where A is given by equation (3.80), and A_x andA_y are given by

$$A_x = 2\gamma\theta\cos\phi Q_0 - K_y(Q_{-1} + Q_1) \tag{3.96}$$

$$A_y = 2\gamma\theta\sin\phi Q_0 - K_x(e^{-i\psi}Q_{-1} + e^{i\psi}Q_1) \tag{3.97}$$

and

$$Q_R = \sum_{p=-\infty}^{\infty} J_p(Y)J_{n+2p+R}(X)e^{i\phi(n+2p+R)}e^{iP\Psi} \tag{3.98}$$

We can simplify these by setting $K_x = K_y = K$, which is the condition required to give a perfectly helical electron trajectory. This means that equations (3.87), (3.89), (3.90) and (3.80) become

$$X = \frac{2n\gamma\theta K}{A}$$

$$Y = 0$$

$$\Psi = 0$$

$$A = 1 + K^2 + \gamma^2\theta^2$$

Therefore equation (3.98) for a helical undulator is

$$Q_R = \sum_{p=-\infty}^{\infty} J_p(0)J_{n+2p+R}(X)e^{i\phi(n+2p+R)} \tag{3.99}$$

As $J_k(0) = 0$ except when $k = 0$ in which case $J_0(0) = 1$ equation (3.99) is only non-zero when $p = 0$. Therefore we can simplify it to

$$Q_R = J_{n+R}(X)e^{i\phi(n+R)} \tag{3.100}$$

substituting this into equations (3.96) and (3.97) we get

$$A_x = 2\gamma\theta\cos\phi J_n(X)e^{i\phi n} - K(J_{n-1}(X)e^{i\phi(n-1)} + J_{n+1}(X)e^{i\phi(n+1)}) \tag{3.101}$$

$$A_y = 2\gamma\theta\sin\phi J_n(X)e^{i\phi n} + iK(J_{n+1}(X)e^{i\phi(n+1)} - J_{n-1}(X)e^{i\phi(n-1)}) \tag{3.102}$$

As the radiation from a helical undulator should be symmetric we can choose ϕ to be any arbitrary value. Setting $\phi = 0$ equations (3.101) and (3.102) become

$$A_x = 2\gamma\theta J_n(X) - K(J_{n-1}(X) + J_{n+1}(X)) \tag{3.103}$$

$$A_y = iK(J_{n+1}(X) - J_{n-1}(X)) \tag{3.104}$$

Using the following relations for Bessel functions of the first kind[45]

$$J_{n-1}(X) + J_{n+1}(X) = \frac{2n}{X} J_n(X)$$
$$J_{n-1}(X) - J_{n+1}(X) = 2\frac{\partial}{\partial X} J_n(X) = 2J'_n(X)$$

we can rewrite equations (3.103) and (3.104) as

$$A_x = \left(2\gamma\theta - \frac{2nK}{X}\right) J_n(X) \tag{3.105}$$

$$A_y = -2iKJ'_n(X) \tag{3.106}$$

We can now evaluate the square in equation (3.95) for a helical undulator. As A_x and A_y are orthogonal there are no cross terms which means that $|A_x, A_y|^2 = |A_x + A_y|^2$. Therefore equation (3.95) is

$$\frac{\mathrm{d}^2W}{\mathrm{d}\Omega\mathrm{d}\omega} = \frac{4K^2q^2\omega^2N^2}{16\pi^3c\epsilon_0(1+K^2)^2} L\left(\frac{N\Delta\omega}{\omega_1}\right)\left(J'_n(X)^2 + J_n(X)^2\left(\frac{\gamma\theta}{K} - \frac{n}{X}\right)^2\right) \tag{3.107}$$

To calculate the energy spectrum per unit solid angle per angular frequency we need to include the contributions from all harmonics. This means that equation (3.107) becomes

$$\frac{\mathrm{d}^2W}{\mathrm{d}\Omega\mathrm{d}\omega} = \frac{4K^2q^2\omega^2N^2}{16\pi^3c\epsilon_0(1+K^2)^2} L\left(\frac{N\Delta\omega}{\omega_1}\right)\sum_{n=1}^{\infty}\left(J'_n(X)^2 + J_n(X)^2\left(\frac{\gamma\theta}{K} - \frac{n}{X}\right)^2\right) \tag{3.108}$$

This equation is the same as that calculated by Kincaid[48] for a perfect undulator. This is the equation that the undulator-based positron source community uses to calculate the radiation expected from an undulator. This is a key result as all simulations of undulator-based positron sources use this equation to describe a perfect undulator.

3.5 Summary

Using the mathematical framework developed in Chapter 2 we have derived analytical expressions for the radiation expected from perfect wigglers and undulators. This has been done by first considering the electron trajectory through insertion devices and then calculating what radiation is expected.

The interference between the electron beam and the radiation it produces determines the radiation spectrum produced and therefore the type of insertion device there is no interference between the electron and the emitted radiation we get wiggler like radiation (3.26). If there are interference effects undulator radiation will be produced, (3.69) for planar radiation and (3.108) for helical radiation. For there to be interference between the radiation and the electron beam then the deviation in the electron beam caused by the insertion device must be smaller than the cone of radiation produced.

The photon spectrum from an undulator has very characteristic harmonic peaks in the spectrum. These peaks mean that as the photon energy increases toward the harmonic energy cut off the number of photons increases. This results in a spectrum that has a high number of photons at specific energies. This high flux of photons was one of the key reasons behind the choice of an undulator rather than a wiggler for use in a positron source for a linear collider. The other key difference is in the size of the oscillations in the electron beam. As an undulator has a much higher deflection parameter,K, than an undulator the electron beam undergoes larger deviations off axis. As the electron beam that is used in the positron source would be the main physics beam then perturbing the beam as little as possible. Therefore the smaller K the better which means that an undulator is preferred from a beam dynamics point of view as well.

Being able to calculate the radiation produced by an undulator is vital for studying undulator-based positron sources as many of the parameters of different components in the undulator-based positron source depend on the radiation produced by the undulator. Equation (3.108) is used in the following chapters to calculate the photon spectrum from ideal undulators with known periods and magnetic fields. In chapter 5 the spectra predicted by this equation is compared with spectra produced by simulation of non-ideal undulators.

Chapter 4

An Undulator-Based Positron Source

This chapter introduces the main components of an undulator-based positron source in which the gamma rays produced by a helical undulator (see chapter 3) are used to produce polarised electron positron pairs. The background theory for each of the subsystems of the undulator source is discussed in the relevant sections. In addition any research and development work that has been conducted during the ILC design phase is discussed.

Section 4.1 details the theory of undulators and the properties of the radiation they produce. Section 4.2 discusses the need for photon collimation in terms of machine protection issues and also using collimation to increase positron polarisation. Discussion of the physics processes that occur in the conversion target and the effect these have on the design of the target are in section 4.3. Section 4.4 describes the capture optics of the positron source including the options for the Optical Matching Device and the details of the radio frequency cavities that form the Capture RF.

4.1 Undulator

The undulator is the key component in an undulator-based positron source. The choice of undulator parameters determines the shape and intensity of the photon spectrum that is used to generate positrons. This means that changing the undulator parameters changes the positron distribution that is generated which then leads to changes in the other components of the source.

The first decision to make is whether the undulator is planar or helical. In general helical undulators are more beneficial as the photon intensity produced by a helical undulator is twice the intensity from a planar undulator. Additionally a helical undulator produces circularly polarised

photons which leads to longitudinally polarised positrons. Polarised positrons are generally desirable however if the polarisation is too low to be well-measured then it can actually be a disadvantage as it introduces more uncertainty into the experiment. In terms of a high-intensity positron source for future linear colliders a helical undulator is used. This decision is mainly based on the increased photon flux however being able to produce polarised positrons is an additional benefit[49].

Having decided on a helical undulator the remaining decisions that must be made include:

- The energy of the electron drive beam E
- The undulator deflection parameter K
- The undulator period λ_u
- The length of the undulator L

The electron drive beam energy is directly related to the energy of the photons produced within the undulator through the undulator equation (3.43). As the energy of the electron drive beam increases, the wavelength of radiation produced decreases. This means that the photon energy increases. Whilst ideally the energy of the electron drive beam would be chosen to maximise the yield from the positron source this is not always possible. In the case of the ILC this is because the electron drive beam will be the main physics beam of the collider. Therefore the maximum energy of the drive beam will be set by the machine parameters and will typically be half the centre of mass energy of the machine.

Other limitations on the choice of the electron drive beam energy are related to the location of the undulator-based positron source. In theory the undulator-based positron source could be located at any position along the main electron linac. The size of the source means this is not always feasible due to the civil engineering requirements. Another limiting factor for the location of the undulator-based positron source is the position of the positron damping ring and the cost of the transfer line needed to take the positrons from the source to the damping ring. For cost reasons the undulator-based positron source at the ILC would be located at the end of the electron main linac. Consequently the nominal energy of the electron drive beam will be 250 GeV. The ILC is designed to perform energy scans which means that the undulator must be able to produce a usable photon spectrum over as wide an energy range as possible. Following the discovery of the Higgs boson at the LHC the ILC intends to run as a Higgs factory. This means that the centre of mass energy range that the ILC will plan to run over is 250 to 500 GeV. Therefore the undulator needs to produce usable photons from a drive beam whose energy can be anywhere in the range of 125 to 250 GeV.

The decision about values of the undulator deflection parameter, K, and the undulator period, λ_u, are linked. This is due to several factors, first and foremost of which is that $K \propto \lambda_u$ (see equation (3.5)).

The wavelength of the undulator radiation is given by the undulator equation (3.43). This equation shows that the wavelength of light produced by an undulator is proportional to λ_u and K^2. The number of photons produced by a helical undulator [26] is given by

$$N_\gamma \approx (3.56 - 0.69K)\frac{K^2}{\lambda_u} \tag{4.1}$$

where N_γ is in units of photons per meter of undulator per electron passing through the undulator and λ_u is given in centimetres.

As K is proportional to the magnetic field on-axis as well as the period of the undulator the values of K and λ_u cannot be chosen just to optimise the photon spectrum, consideration must be given to the construction of the undulator. This is specifically true in the case of the superconducting undulators being consider for use in the undulator-based positron source. Superconductors have a maximum current density in a given magnetic field. As the current density in the conductor is used to generate the magnetic field on-axis in the undulator this means that there is a maximum magnetic field for the undulator.

The period of the undulator also limits the maximum magnetic field on-axis. This is because as the period reduces the distance between the adjacent conductors gets smaller and so the magnetic field generated by one section of conductor affects the adjacent sections more. Therefore the overall magnetic field in the conductor for a given current density increases as the period reduces. When designing a superconducting helical undulator there is a limit on the maximum field on-axis for a given superconductor and given λ_u to avoid the magnet quenching. Two types of superconductor have been considered for use in constructing the helical undulator, niobium titanium and niobium tin, and more detail into the work on designing a helical undulator with these super conductors is given later.

The length of the undulator arises from decisions about the other undulator parameters as well as the required positron flux of the collider. The length of the undulator affects the number of photons generated per electron, equation (4.1) becomes

$$N_\gamma \approx (3.56 - 0.69K)\frac{K^2}{\lambda_u}L \tag{4.2}$$

where N is now in units of photons per electron passing through the undulator, λ_u is again given in centimetres and L, the length of the undulator, is given in metres. The positron requirements of a collider are typically given in terms of number of positrons per electron, N_{e^+/e^-}, which is

given by

$$N_{e^+/e^-} = \rho_{con}\,\rho_{trans}\,\rho_{DR}\,N_\gamma \tag{4.3}$$

where ρ_{con} is the probability of converting a photon to a positron in the target, ρ_{trans} is the probability of capturing a positron and transporting it through the positron source and ρ_{DR} is the probability of the positron being within the damping ring acceptance.

Rearranging equations (4.2) and (4.3) we get an equation for the required length of the undulator

$$L = \frac{N_{e^+/e^-}}{\rho_{con}\rho_{trans}\rho_{DR}} \frac{\lambda_u}{K^2(3.56 - 0.69K)} \tag{4.4}$$

where L is in units of metres and λ_u is in units of centimetres. This means that the final length of the undulator depends on the required yield of positrons, the conversion and capture efficiency of the undulator-based positron source and the design of the damping ring. Therefore the length of the undulator is one of the last parameters of the positron source to be finalised.

4.1.1 Niobium Titanium Undulators

As part of the ILC reference design report scientists at Daresbury Laboratory and Rutherford Appleton Laboratory in the UK designed and constructed a prototype helical undulator for the undulator-based positron source using niobium titanium superconductors. The design used two helical coils of niobium titanium wound around an steel former which encases the beam pipe. The two windings are longitudinally shifted by half a period and the current flows in opposite directions in the two windings. This results in the longitudinal component of the on-axis magnetic field from each winding cancelling out leaving only the transverse components of magnetic field.

The initial investigations into this design for the helical undulator were based on computer simulations using the software packages OPERA 2D and OPERA 3D from Vector Fields Software which are finite element analysis codes[50, 51]. Figure 4.1 shows the undulator model using in OPERA 3D. The atmosphere in the simulation was set to be air at standard temperature and pressure as the undulator winding was implemented as a conductor which is a special type of object in OPERA which is defined with spatial dimensions and a current density. As such the properties of the superconductor other than the current density are not used. Simulating the undulator in air at standard temperature and pressure also means that the dimensions of the former defined in the simulation are those that are used in the manufacture of the prototypes.

The main goal of the simulations was to determine the winding geometry for the undulator. The results of the simulations were that:

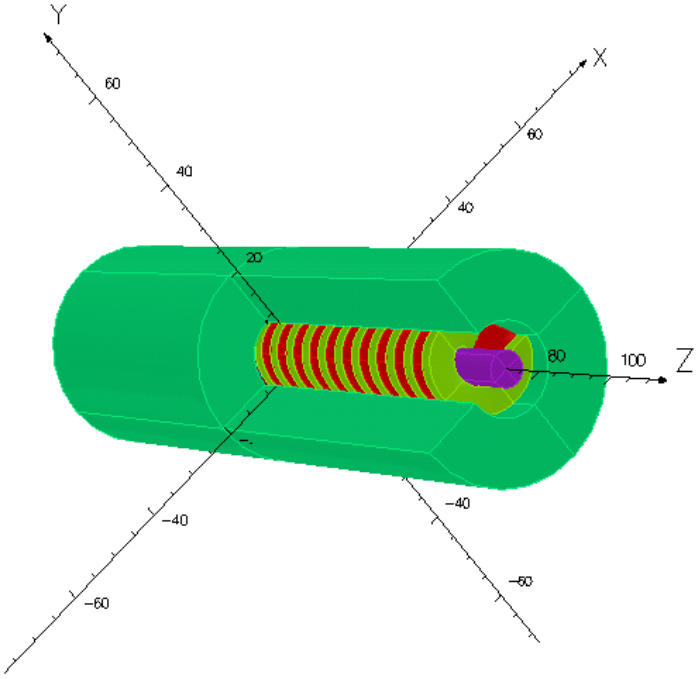

Figure 4.1: Model of the helical undulator used in OPERA 3D simulations.The purple cylinder represents the beam pipe and is assumed to be a vacuum. The bright green is the steel former and the red is the conductor. The darker green represents the atmosphere the undulator is in and for the purposes of the simulation was assumed to be air at standard temperature and pressure.

- A flat shape winding produces the maximum on-axis field for a given current density.
- When using niobium titanium it is essential to construct the former, poles and return yoke from steel (see figure 4.2).
- To ensure the magnet does not quench the cross-section of the conductor used should be square.

Following the simulations of the helical undulator two undulator prototypes were built. These were built as part of the Helical collaboration's[**?**] contribution towards the ILC. Two prototypes were constructed as the final aim of the project was to design an ILC undulator *module* which is a 4 m cryostat containing two helical undulators each 155 periods long. The long undulator therefore would actually be made up of a number of modules each containing two 155 period NbTi undulators. This means that a long undulator has two different lengths, the physical length and the active length. The physical length is how long a space is required to fit all of the components in whilst the active length is the distance that actually has helical magnetic fields. The parameters of the undulator prototypes are given in table 4.1.

Once the two prototypes were constructed they were mounted in the 4 m cryostat and then cooled down to the operating temperature of 4 K. The magnets were then powered and the on-

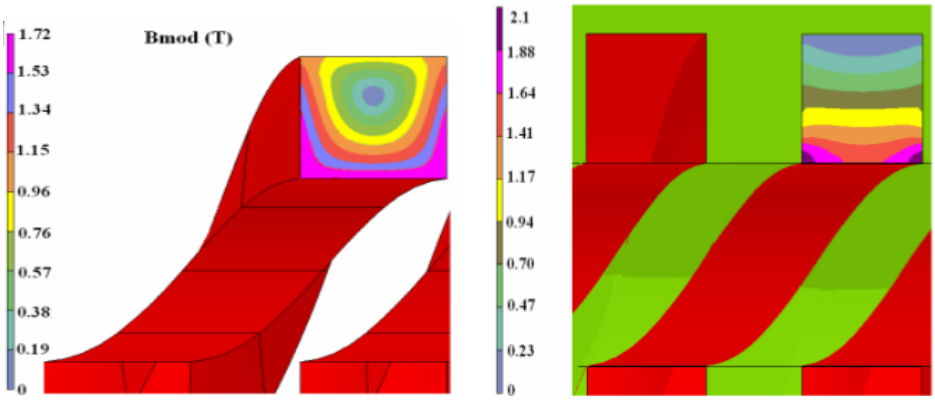

Figure 4.2: Magnetic field through a cross-section of the conductor windings of the helical undulator when the on-axis field is 0.8 T. The image on the left is with no steel former, poles and return yoke. The image on the right is with an steel former, poles and return yoke. Without the steel former a current density of 1000 A mm^{-2} is required and the magnetic field in the conductor peaks at 1.72T. With an steel former a current density of 400 A mm^{-2} is needed and the field in the conductor peaks at 2.1 T [52].

Table 4.1: Parameters for the undulator prototypes developed at Daresbury and Rutherford Appleton Laboratories

Parameter	Symbol	Units	Value
Undulator Period	λ_u	mm	11.5
Number of Periods	N		155
Internal Bore of the Former	I_D	mm	4
Winding Bore	W_D	mm	6
Former Material			Steel
Number of Wires in Conductor			64
Diameter of NbTi Wires		mm	0.44

axis field measured using a hall probe. Following *magnet training* the undulators were observed to quench when the current reached 301 A for prototype 1 and 306 A for prototype 2 [53]. This corresponds to an on-axis field of approximately 1.15 T. This means that the intended operating point of 0.86 T is at 70 % of the *short sample* limit.

4.1.2 Niobium Tin Undulators

An extension of the research and design work on the NbTi undulator prototypes was to consider the effect of changing the superconductor used in the undulator. The superconductor chosen for this was niobium tin (Nb_3Sn). The reason for this choice was that the two superconductors are similar in terms of their mechanical properties however Nb_3Sn wire can support higher magnetic fields than NbTi wire.

The properties of the Nb_3Sn wire chosen for use in the helical undulator are shown in table 4.2. From work done at RAL it was determined that it was not possible to form ribbons of Nb_3Sn wire therefore a different method of packing wires into the conductor region are required.

Table 4.2: Parameters of the Nb_3Sn wire chosen for the helical undulator

Parameter	Units	Value
Diameter	mm	0.63
Insulation Type		Glass Braid
Insulation Thickness	mm	0.065
Number of Filaments in Wire		60

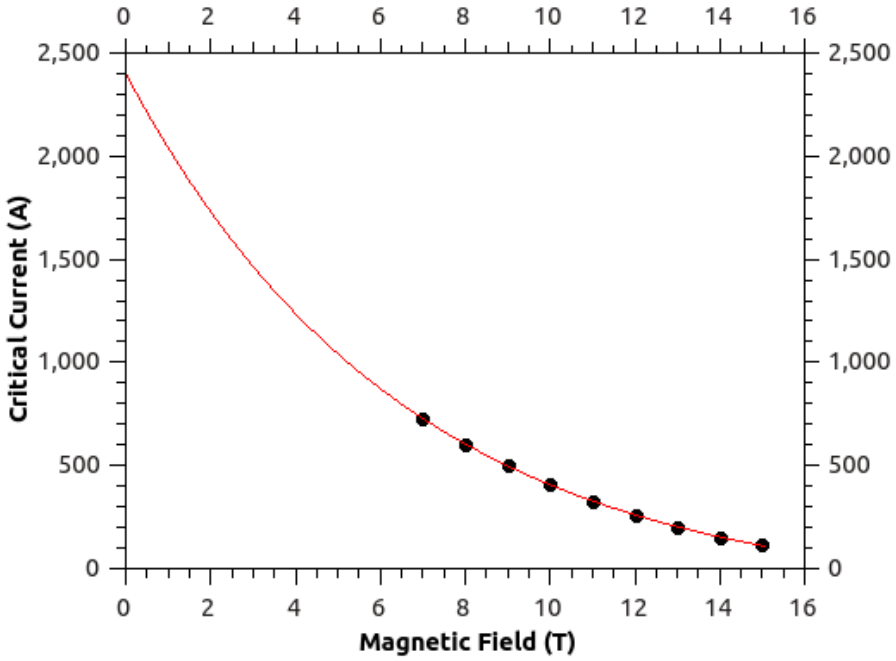

Figure 4.3: Plot of critical current as a function of magnetic field in the conductor for Nb_3Sn wire measured by Karlsruhe Institute of Technology. Critical current is defined as the maximum current that can be supported in the conductor before quenching. Red line is a fit with equation $y = 2548.82e^{-(x/6.559)} - 148.03$.

The optimal wire arrangement for an undulator with a period of 11.5 mm is to use a hexagonal packing arrangement to fit 27 wires into a 3.25 mm wide conductor region. This achieves a packing efficiency of 48%. The Nb_3Sn wire was characterised at the Karlsruhe Institute of Technology and figure 4.3 shows the relationship between the magnetic field in the wire, B, and the critical current, I_c, in the wire. To measure the critical current a length of conductor is immersed in a known magnetic field and current applied to the conductor. The current is increased until the superconductor quenches. The maximum current the conductor can support whilst still being superconducting is the critical current.

A helical undulator constructed with Nb_3Sn conductors was simulated in OPERA 3D using a modified version of the model shown in figure 4.1. In order to calculate the peak on axis magnetic field a Nb_3Sn undulator could generate for a specific undulator period an iterative process was used. By applying simulating the undulator with a given current the simulation results give the

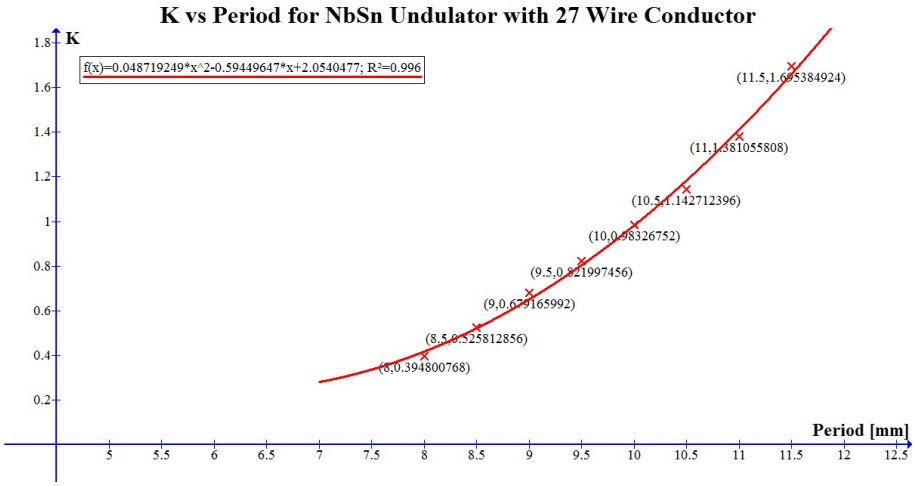

Figure 4.4: Plot of undulator deflection parameter, K, as a function of undulator period for a Nb_3Sn undulator operating at 80% critical current.

magnetic field in the conductor and on the undulator axis. By comparing the magnetic field produced in the conductor from the given current with the data from figure 4.3 it was possible to determine if the given current was higher or lower than 80% of the critical current. If the current that produced the magnetic field in the conductor was higher than the 80% of critical current the current in the conductor was reduced. If the current was below 80% of the critical current the current in the conductor was increased. The undulator was designed to operate at 80% of the critical current instead of the critical current in order to provide a margin of safety to ensure that the device would not quench.

By changing the period of the model and the conductor design an optimal relationship between the undulator deflection parameter, K, and the period, λ_u was determined. Figure 4.4 shows how the undulator deflection parameter changes with undulator period for a conductor constructed from 27 wires operating at 80% of the critical current. This simulation work shows that a Nb_3Sn undulator can achieve a higher on-axis field than a NbTi undulator for a given period. This means that to achieve the same K parameter the Nb_3Sn undulator will have a shorter period. For the undulator-based positron source this means that using Nb_3Sn undulators would provide approximately a 15% reduction in the undulator period which could allow for a similar reduction in the overall undulator length.

4.1.3 Comparison of NbTi and Nb_3Sn Undulators

As already explained an undulator with Nb_3Sn conductors has an advantage over one with NbTi conductors as the superconductor can support higher fields and therefore the same K value can be achieved with a smaller period. This allows the overall length of the undulator to be reduced whilst still maintaining the same number of periods. This reduction in period also affects the

photons that the undulators produce. From the undulator equation (see equation (3.43)) we know that the wavelength of the photons produced is proportional to the undulator period. As energy is inversely proportional to wavelength this means that for a given K the photon energy increases as the undulator period decreases. Table 4.3 compares the energy of photons produced on-axis from an electron with an energy of 250 GeV travelling through NbTi and Nb_3Sn undulators for the first five harmonics.

Table 4.3: Energy of on-axis photons in MeV produced by a 250 GeV electron travelling through a helical undulator with $K = 0.92$.

Harmonic	NbTi	Nb_3Sn
1	36.26	41.70
2	72.52	83.41
3	108.79	125.11
4	145.05	166.81
5	181.32	208.52

This increase in photon energy is important for an undulator-based positron source, as the positron production rate is higher for higher energy incident photons. Using the equation for the photon flux from a helical undulator we can compare the photon spectra produced by NbTi and Nb_3Sn undulators. Figure 4.5 shows the photon spectra generated by a 250 GeV electron travelling through a helical undulator with $K = 0.92$. The comparison of these spectra is very interesting as at energies where an undulator-based positron source is not very efficient, below 30 MeV, the photon flux from a NbTi undulator is higher. At the energies where the undulator-based positron source is efficient the flux from the Nb_3Sn undulator is higher.

Therefore using an undulator constructed using a superconducting wire that can support the highest possible magnetic field in the conductor is the best solution for an undulator-based positron source. This is because it allows the undulator length to be reduced whilst maintaining the required number of periods and the photon spectra produced from such an undulator is more in line with that required to achieve high efficiency. Nb_3Sn undulators have not been chosen as the baseline option as there are problems getting the Nb_3Sn superconductor to work at the low magnetic fields needed for helical undulators. During testing of the conductor at Rutherford Appleton Laboratory there were problems getting the Nb_3Sn to conduct the expected current. It was discovered that the only method of energising the conductor was to have immersed in a magnetic field. As there is no magnetic field produced by the undulator when the conductor is not energised then the undulator design presented here is not usable. Currently there is ongoing work to determine if there is another way to energise the conductor which would allow the undulator to be built as proposed here. An alternative solution is to surround the undulator with a magnet that would provide the needed magnetic field in the conductor to allow it to be energised. This

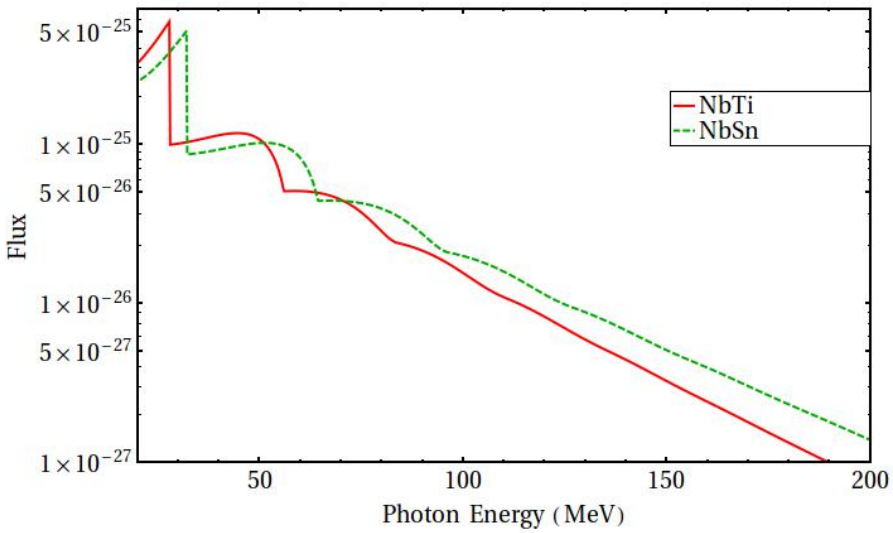

Figure 4.5: Comparison of the photon spectra produced by a 250 GeV electron travelling through a 155 period helical undulator with $K = 0.92$. The flux is defined as number of photons generated by one electron travelling through a one metre long undulator. The red line shows the photon spectrum from an NbTi undulator and the green dashed line the spectrum from an Nb_3Sn undulator. Plotted using Mathematica 8.

additional magnetic field would then be turned off once the undulator was powered. Once the issue of energising the Nb_3Sn conductor is resolved then it is expected that Nb_3Sn undulators will become the baseline design.

4.2 Photon Collimator

An undulator-based positron source produces a high flux of photons in order to achieve the required positron flux. A high photon flux causes problems for the accelerator components as it can damage various components through heating and radiation damage. Therefore to limit the damage caused by the photon beam a collimation system is required.

In addition to collimating for machine protection there is also the possibility of collimating for physics reasons. The main physics reason for collimating the photon beam is to try and increase positron polarisation. The polarisation of the photons produced by an ideal undulator varies with emission angle. The photon polarisation is transferred to the electron-positron pairs that the photon produces. Therefore by collimating out the photons with low polarisation the overall polarisation of the positron beam increases. The collimation systems for machine protection and polarisation are very different and so will be discussed separately.

4.2.1 Photon Collimators and Photon Stops for Machine Protection

Photons produced within the undulator have an angular divergence and the photons travel a long distance, between 10^2 m and 10^3 m, in order to reduce the stress on the conversion target. This means that the radius of the photon beam cross-section will become large (> 10 mm) and could result in photons impacting various accelerator components causing damage. To prevent this a series of photon collimators and photon stops are required.

The two main machine protection issues arising from the photon beam in the undulator are related to the vacuum vessel in the undulator. The vacuum vessel in the undulator region is actually the beam pipe. The electron drive beam travels through this and the undulator modules surrounding it generating photons. If photons impinge on this beam pipe photon-stimulated desorption can occur and the beam pipe is heated which can result in quenching of the superconducting undulators magnets.

Photon-stimulated desorption (PSD) is when an incident photon desorbs a gas molecule from the subsurface layers of the vacuum vessel. This increases the vapour equilibrium gas density which reduces the quality of the vacuum. Normally in superconducting magnet systems a very high vacuum is achieved by cryo-pumping. Cryo-pumping achieves high vacuum by relying on gas molecules in the vacuum being cryo-sorbed into the walls of the vacuum vessel. However due to PSD this technique no longer gives such a high vacuum. As the photons are emitted from the undulator as a cone of radiation PSD will cause most problems towards the end of the undulator. This can be minimised using collimators. For the ILC these collimators consist of cylindrical apertures that are smaller than the vacuum vessel aperture and vacuum pumping ports. The principle behind them is to isolate the PSD effects into small regions where extra vacuum pumping is possible to ensure that the the vacuum pressure of does not exceed 100 nTorr.

The location and number of photon collimators required has been calculated. The challenge for optimising the number of collimators is to ensure that there are enough collimators to prevent a loss of vacuum verses minimising the increase in length of the undulator section. The distance between the collimators, L_c, that is required actually depends on the ratio between the collimator diameter, d_c, and the vacuum vessel diameter, d. For $d_c : d = 1 : 2$, $L_c < 15$ m and for $d_c : d = 3 : 4$, $L_c < 7.5$ m[54].

In addition to causing PSD the incident photons heat the vacuum vessel. The peak synchrotron radiation power load from a helical undulator with parameters suitable for a helical undulator-based positron source is approximately $20\mathrm{Wm}^{-1}$. The undulator will be operating at superconducting temperatures inside a cryogenic system. This system has a maximum allowable heat load of $1\,\mathrm{Wm}^{-1}$. Therefore the photon collimators in the undulator need to absorb some of the photon power and reduce the heat load on the cryogenics. The undulator has been

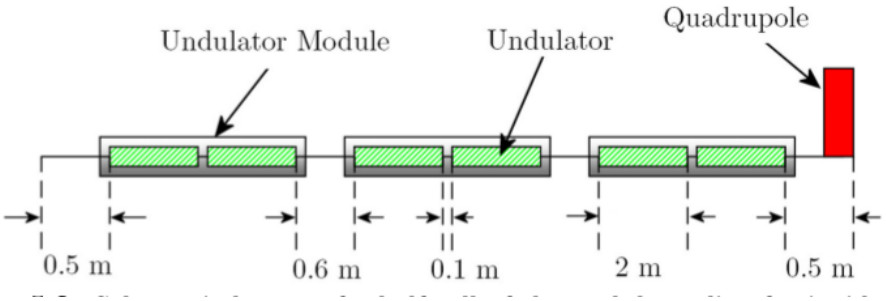

Figure 4.6: Figure showing the layout of half an undulator cell[54]. The cell is symmetric about the centre of the quadrupole magnet.

designed as a series of cells, each of which contains 6 modules. Figure 4.6 shows the schematic layout of half a cell. Locating the collimators in the drift spaces in these cells means that the overall length of the undulator is not increased. The effect of these collimators on the synchrotron radiation power that is incident on the vacuum vessel is shown in figure 4.7. With the collimators in place the peak incident synchrotron radiation power is reduced by four orders of magnitude to approximately $4\,\mathrm{mWm}^{-1}$ which is well within the heat load that can be handled by the cryogenics.

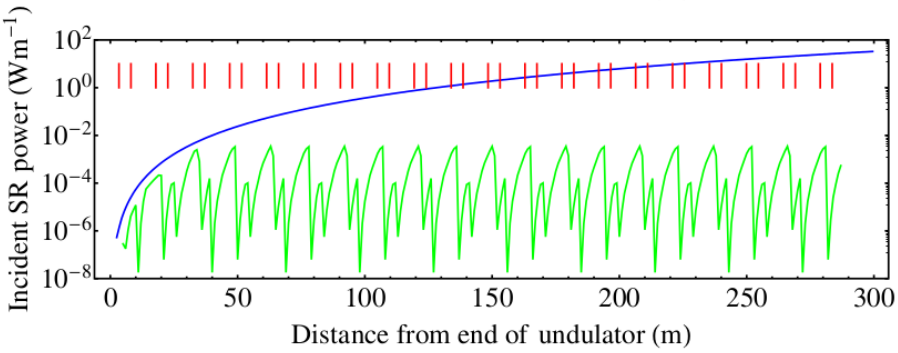

Figure 4.7: Plot showing the incident synchrotron radiation power on the walls of the vacuum vessel in the undulator. The red lines represent the position of the photon collimators. The blue line is the radiation power incident on the walls with no collimators. The green line is the power on the walls with collimators. Plot taken from [54].

4.2.2 Photon Collimator for Polarisation

The helical undulator in the undulator-based positron source produces photons that are circularly polarised. The polarisation is transferred from the photons to the electron-positron pairs that they create[55]. This means that by producing a photon beam with a high polarisation in the undulator the polarisation of the resulting positron beam will be high. From research and design work conducted during the ILC design phase it has been shown that for a perfect undulator with parameters given in table 4.7 the resultant positron beam has a polarisation of $\approx 30\%$. This is partly due to the choice of undulator parameters however the more limiting factor is the way

photon polarisation varies as a function of emission angle.

The dependence of polarisation on the emission angle means that it should be possible to increase the polarisation of the positron beam by allowing only certain regions of the photon beam to impinge on the target and produce positrons. For an ideal undulator the optimal region to produce highly polarised positrons is centred around the axis of the undulator. By highly collimating the photon beam it is possible to produce a positron beam with a polarisation between 50% and 60%. To achieve such a high polarisation the radius of the collimator iris must be between 0.8 mm and 2.0 mm[56]. The actual radius required depends on the energy of the electron drive beam used to produce the photon beam. This is due to the energy-angle relationship of the produced photons. The radius of the collimator iris, R_c, required for high polarisation is approximately given by

$$R_c \approx \frac{K}{\gamma} L \approx K L \frac{E_0}{E} \tag{4.5}$$

where K is the undulator deflection parameter, L is the distance from the centre of the undulator to the collimator, E_0 is the electron rest mass and E is the energy of the electron drive beam.

Equation (4.5) is only an approximation to the required radius. The actual radius of the collimator iris and the corresponding positron polarisation can only be determined by simulation. Table 4.4 shows the polarisation from simulations corresponding to a given collimator iris radius at differing electron drive beam energies.

Table 4.4: Table of different collimator irises required to produce highly polarised positrons at different electron drive beam energies.

Electron Drive Beam Energy (GeV)	Collimator Iris Radius (mm)	Positron Polarisation (%)
150	2.0	55
175	1.4	59
250	1.0	50
250	0.7	59

The changing radius required for collimation means that the design is not straight forward. This combined with the expectation that having a non-ideal undulator will change the relationship between polarisation and emission angle means that producing a collimator that increases the positron polarisation is highly involved. An initial collimator design has been developed at DESY in Germany[57]. This is a multi-stage collimator with each stage having a decreasing iris radius.

Each stage of the collimator is constructed from a series of different materials which are designed to stop the electromagnetic shower developing and to reduce the intensity of the absorbed photon beam. The majority of each collimator stage is constructed from pyrolytic carbon which

is then followed by decreasing lengths of titanium, iron and tungsten. To ensure that the heat load distribution in the carbon and titanium sections varies smoothly, the collimator bore in these sections is conical. To cool the collimator each stage is wrapped in a copper jacket through which a series of water cooling channels are machined. The copper is used to ensure good heat flow from the carbon, titanium, iron and tungsten to the water.

Using a collimator to increase the polarisation of the positron beam reduces the effective photon flux, to regain the lost photon flux the undulator length needs to be increased. However by increasing the undulator length the photon beam spot size increases which can affect the number of photon stops required. Additionally the majority of the photons that are allowed through to the target by this type of collimator are first-harmonic photons. This can cause problems as the photons in the first harmonic are the least effective at producing positrons that are able to be captured and then transported through the positron source and into the damping ring. Therefore a higher photon intensity is required which in turn will increase the heat load on the conversion target and may mean that the target design needs to be re-optimised to ensure survivability when a collimator is used.

The baseline design for the ILC positron source does not include a collimator. This means that there is nothing stopping the halo of the photon beam passing by the conversion target and impacting on other components in the target area. Therefore machine protection requirements dictate that unless a physics collimator is present there will have to be a photon stop just upstream of the target station. This will need an aperture radius of between 5 and 10 mm depending on the final position and will need a total diameter of several metres to protect the vacuum system, motor and electronics in the target station.

4.3 Conversion Target

In order to produce positrons from the high-energy photons generated in the undulator a conversion target is needed. Positrons are generated within the conversion target through the Bethe-Heitler pair production mechanism. This is the same production mechanism that the *conventional* positron source exploits. However there is one main difference; the *conventional* source uses electrons which within a thick conversion target creating photons, which then produce electron-positron pairs. However, as the undulator generates high-energy photons, the thickness of the conversion target is able to be reduced in this case.

The choice of material for the target depends on many factors. Ideally we would optimise the material choice to maximise the pair-production cross-section. This cross-section is given by:

$$\dot{N} = f_\gamma \sigma \tag{4.6}$$

where $\dot{N}$ is the number of positron-electron pairs produced per unit time, f_γ is the number of photons per unit area per unit time and σ is the pair-production cross-section. However, we need to consider the survivability of the conversion target when subjected to the heating load created by the photon beam. The pair-production cross-section gives the probability of interaction between a photon and the atoms in a material. It is calculated using Bethe-Heitler theory applied to theoretical models of materials which take into account corrections from screening and radiative processes[58]. Maximising the pair-production cross-section is important as a higher cross-section means that there is more chance of a photon producing electron-positron pairs within the material. The pair-production cross-sections for four elements; hydrogen, sodium, iron and titanium as well as the pair-production cross-section of tungsten-rhenium, the material of the conversion target at the SLC, are plotted in figures 4.8, 4.9 and 4.10. Figure 4.8 shows the pair-production cross-section due to the nuclear field. Figure 4.9 shows the pair-production cross-section due to the atomic electron field. Figure 4.10 shows the total pair-production cross-section. Data on pair-production cross-sections from [58].

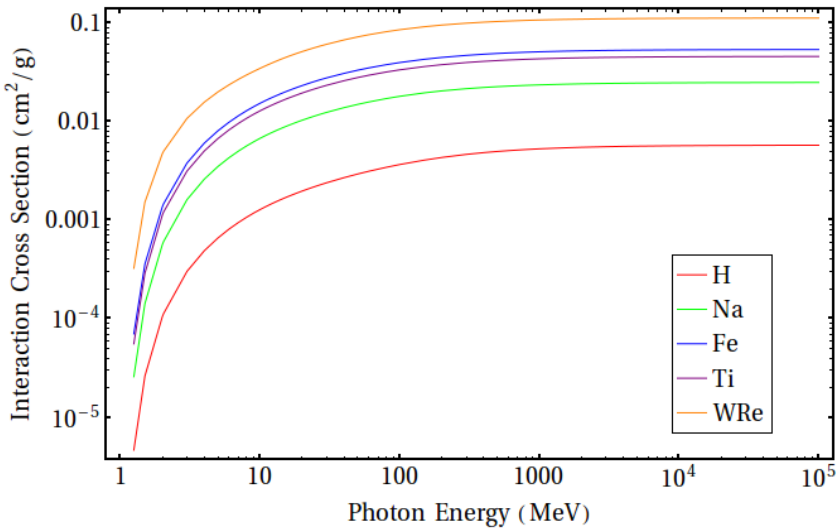

Figure 4.8: Pair-production cross-section due to the nuclear field in units of cm^2/g, normalised by dividing by the atomic mass of the material, as a function of photon energy for four elements and one compound. The red line is for hydrogen, the green line is for sodium, the blue line for iron, the purple line for titanium and the orange line for tungsten-rhenium.

The dominant pair-production cross-section is due to the nuclear field except in the case of hydrogen where the pair-production cross-section due to the electron field dominates at high energies. The pair-production cross-section due to the nuclear field increases with atomic number, however the pair-production cross-section due to the electron field decreases with atomic

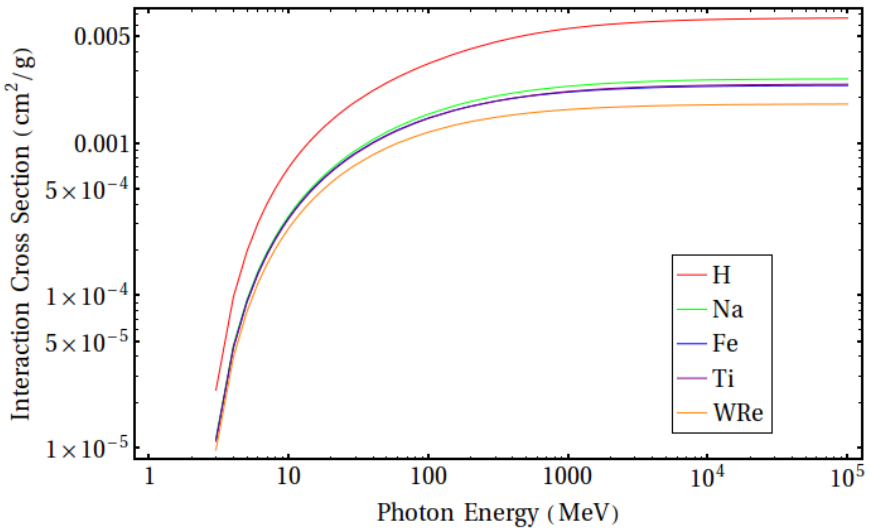

Figure 4.9: Pair-production cross-section due to the electron field in units of cm^2/g, normalised by dividing by the atomic mass of the material, as a function of photon energy for four elements and one compound. The red line is for hydrogen, the green line is for sodium, the blue line for iron, the purple line for titanium and the orange line for tungsten-rhenium.

number. Therefore in order to maximise the pair-production cross-section when constructing the conversion target picking a material with a high Z is desirable.

The thickness of the conversion target is also a key requirement. Conventional positron sources, which use low-energy electron beams to generate positrons, require a thick conversion target. This is due to the need for the electromagnetic shower to develop in the material as the electrons produce photons which then create electron-positron pairs, via the pair-production mechanism, that are captured as they leave the target.

As the undulator produces high-energy photons the target needs to be thick enough to maximise pair-production from the photon beam but thin enough to ensure that the positrons created can exit the target before they can be absorbed by the target material.

Figure 4.11 shows the capturable positron per incident photon yield as a function of radiation length for titanium, iron and tungsten-rhenium targets. The titanium and iron targets both peak at approximately 0.5 radiation lengths although the the region between 0.4 and 0.6 radiation lengths is quite flat. The tungsten target peaks at 0.7 radiation lengths with high yield between 0.6 and 0.9 radiation lengths. This shows that the optimal thickness of the conversion target depends on the target material choice although it is likely to be around 0.6 radiation lengths thick if optimising for positron yield.

The positron production rate is not the only characteristic that is important to the decision about the target thickness. Target survivability needs to be considered as well. Three important considerations about the survivability of the target are the energy deposited by the photon beam,

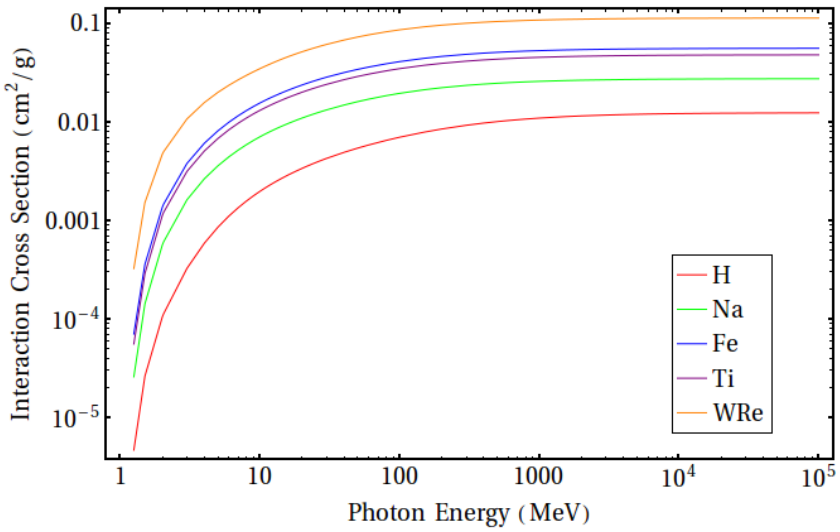

Figure 4.10: The total pair-production cross-section in units of cm^2/g, normalised by dividing by the atomic mass of the material, as a function of photon energy for four elements and one compound. The red line is for hydrogen, the green line is for sodium, the blue line for iron, the purple line for titanium and the orange line for tungsten-rhenium.

the radiation damage to the target and the effect of eddy currents in the target.

Eddy currents are generated inside the target as it is rotating in order to distribute the load on the target. As the target is next to the optical matching device which generates a magnetic field as the target rotates eddy currents are generated within the target that cause heating. In order to evaluate the effects of the eddy currents an experiment was conducted at Daresbury Laboratory[59].

The energy deposited within the target by the photon beam is plotted in figure 4.12 as a function of the thickness of the target for titanium, iron and tungsten-rhenium targets. The energy deposited scales with target thickness as expected. Interestingly the energy deposited scales inversely to the atomic number of the target material. This combined with the data from figure 4.11 suggests that a tungsten-rhenium target 0.6 radiation lengths thick would be the optimal choice.

Although a tungsten-rhenium target appears to be the optimal choice there are concerns about using such a target as part of the undulator-based positron source. The first of these is due to the radiation damage to the target. The SLC used a tungsten target in their positron source and the limiting factor experienced in the lifetime of the target at the SLC was the effect of radiation. The undulator-based positron source is expected to irradiate its conversion target even more than the SLC target and as such the lifetime of a tungsten-rhenium target is expected to be very short. The material the target is constructed from is required to be very radiation hard.

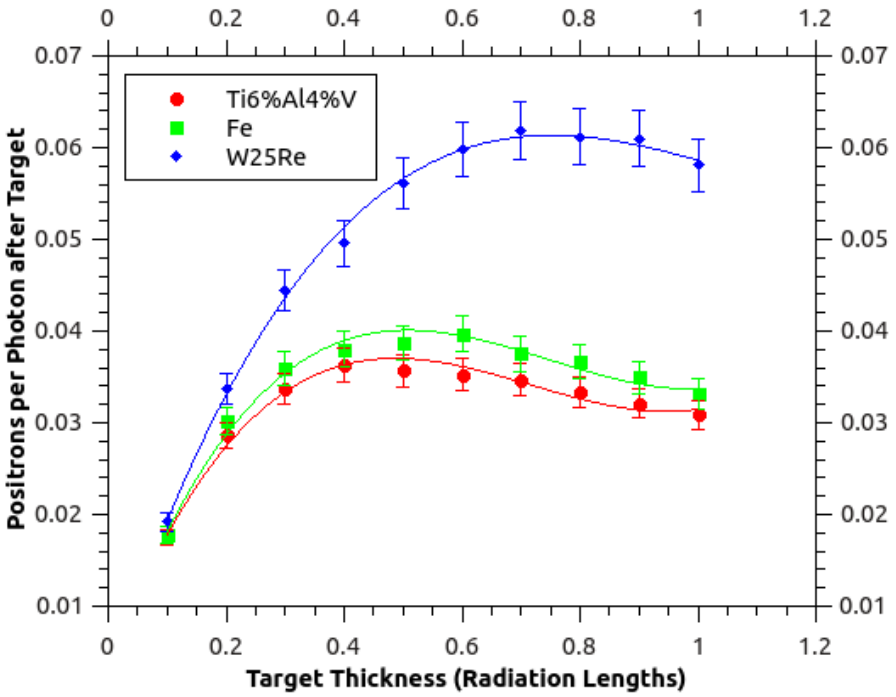

Figure 4.11: Plot showing the capturable positron per incident photon yield as a function of radiation length for titanium (red ellipses), iron (green squares) and tungsten-rhenium (blue diamonds) targets. The titanium and iron targets both peak at approximately 0.5 radiation lengths although the the region between 0.4 and 0.6 radiation lengths is quite flat. The tungsten target peaks at 0.7 radiation lengths with high yield between 0.6 and 0.9 radiation lengths. Interaction simulated using PPS-Sim and plotted using QTiPlot.

Additionally the other issue with using tungsten-rhenium as the conversion target is due to the mechanical stresses on the target. The intention is to rotate the target at high speed to ensure that the heat load from the photon beam is spread out. As the target is rotating there will be stress generated within the target. This is a problem particularly for tungsten-rhenium targets as we would want a target that is 0.6 radiation lengths thick which is only 1.95 mm, such a target would not be suitable. Therefore the preference would be to use a target that has good mechanical strengths in addition to being radiation hard and producing a high positron yield.

A decision was taken that for the ILC undulator-based positron source a titanium alloy, specifically Ti6%Al4%V, that was being used in collimators elsewhere in accelerator, would be used. This alloy is expected to survive the radiation damage from two years of operation of the undulator-based positron source. However as a safety measure the target would be replaced every year. From a mechanical standpoint it is also suitably robust as the alloy is used widely in the aerospace industry. From a positron production viewpoint the ILC conversion target was chosen to be 0.4 radiation lengths, 14.35 mm, thick as this gives the best compromise between positron yield and energy deposited in the target.

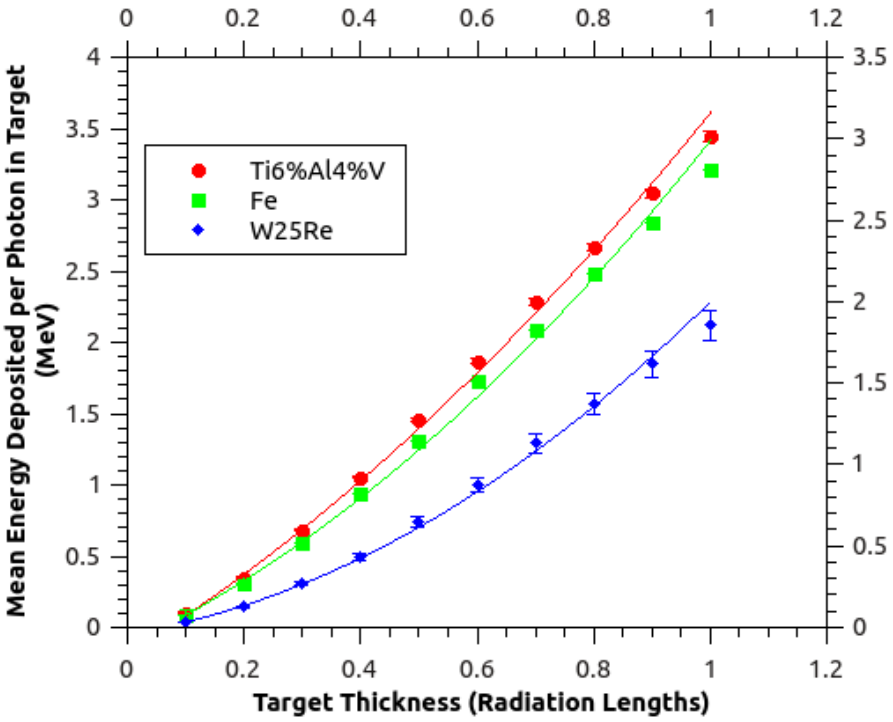

Figure 4.12: Plot showing the energy deposited per incident photon in MeV as a function of radiation length for titanium (red ellipses), iron (green squares) and tungsten-rhenium (blue diamonds) targets. The energy deposited scales with target thickness as expected. Interaction simulated using PPS-Sim and plotted using QTiPlot.

4.4 Capture Optics

The positrons and electrons produced in the conversion target are accelerated up to 125 MeV before being separated by a dipole magnet. This acceleration happens in a normally-conducting linac that is surrounded by a uniform solenoidal field with a field strength of 0.5 T. The solenoidal field is there to provide a transverse focussing field along the length of the linac. To minimise beam loss, the phase space of the beam at the entrance to the linac needs to be matched to the solenoid field. If the beam is correctly matched the phase space distribution will just rotate as the beam travels through the linac.

From simulations of the interaction of the photon beam produced by the undulator and the conversion target the expected positron and electron distribution can be analysed. The distribution has a transverse phase space which would be matched to a solenoid with field strength of the order of 5 T. To correct for this discrepancy an optical matching device (OMD) is required at the start of the capture optics section. Different types of OMD have been considered for use in the undulator-based positron source. In order to ensure high positron capture, the OMD field, needs to be at the required strength at the exit face of the conversion target. Possible OMDs include a quarter wave transformer (QWT), an adiabatic matching device (AMD) and a pulsed flux concentrator (FC).

The *matching* field in all three possible OMDs is produced using a solenoidal field. The QWT is simply a solenoid with a high uniform field strength where the length and strength of the field are determined by the matching condition. The AMD has a solenoid field whose strength decreases smoothly along the length of the magnet. The peak field strength, length of field and taper parameter of the field are all determined from the matching condition. The FC has a magnetic field that rises very quickly to a peak value and then becomes solenoidal and smoothly decreases from the peak field strength in a similar manner to the AMD. The solenoidal component of the FC field is governed by the matching condition, however the initial rise in field strength is designed to reduce eddy currents in the target.

4.4.1 Phase Space Matching

In order to describe the phase space matching with a solenoid we first need to define the transverse canonical variables. For the purposes of this derivation we will only consider the transverse effects. The canonical variables used are x, p_x, y and p_y; where x and y are the position variables and p_x and p_y are the transverse momenta as defined by:

$$p_x = \frac{1}{P_0}(\gamma m v_x + eA_x) \tag{4.7}$$
$$p_y = \frac{1}{P_0}(\gamma m v_y + eA_y)$$

where P_0 is the reference momentum, v_x and v_y are the transverse velocities and A_x and A_y are the transverse components of the electromagnetic vector potential.

The transformation that the phase space of a beam undergoes when travelling through an element of an accelerator lattice, from position 1 to position 2, is given by

$$\begin{pmatrix} x_2 \\ p_{x2} \\ y_2 \\ p_{y2} \end{pmatrix} = M \begin{pmatrix} x_1 \\ p_{x1} \\ y_1 \\ p_{y1} \end{pmatrix} \tag{4.8}$$

where M is the transfer matrix of the lattice element. For a solenoid, of length L and field strength B_s, the transfer matrix is given by

$$M = \begin{pmatrix} \cos^2(\omega L) & \frac{\sin(2\omega L)}{2\omega} & \frac{\sin(2\omega L)}{2} & \frac{\sin^2(2\omega L)}{\omega} \\ -\frac{\omega \sin(2\omega L)}{2} & \cos^2(\omega L) & -\omega \sin^2(\omega L) & \frac{\sin(2\omega L)}{2} \\ -\frac{\sin(2\omega L)}{2} & -\frac{\sin^2(2\omega L)}{\omega} & \cos^2(\omega L) & \frac{\sin(2\omega L)}{2\omega} \\ \omega \sin^2(\omega L) & -\frac{\sin(2\omega L)}{2} & -\frac{\omega \sin(2\omega L)}{2} & \cos^2(\omega L) \end{pmatrix} \tag{4.9}$$

and ω is defined as

$$\omega = \frac{qB_s}{2P_0} \tag{4.10}$$

Equation (4.9) can be expressed as the product of two matrices, a rotation matrix R and another transfer matrix $\tilde{M}$ which are defined as:

$$R = \begin{pmatrix} \cos(\omega L) & 0 & \sin(\omega L) & 0 \\ 0 & \cos(\omega L) & 0 & \sin(\omega L) \\ -\sin(\omega L) & 0 & \cos(\omega L) & 0 \\ 0 & -\sin(\omega L) & 0 & \cos(\omega L) \end{pmatrix} \tag{4.11}$$

$$\tilde{M} = \begin{pmatrix} \cos(\omega L) & \frac{\sin(\omega L)}{\omega} & 0 & 0 \\ -\omega \sin(\omega L) & \cos(\omega L) & 0 & 0 \\ 0 & 0 & \cos(\omega L) & \frac{\sin(\omega L)}{\omega} \\ 0 & 0 & -\omega \sin(\omega L) & \cos(\omega L) \end{pmatrix} \tag{4.12}$$

Interestingly $\tilde{M}$ is a block diagonal matrix where the on-diagonal blocks are identical. This means that $\tilde{M}$ can be written as

$$\tilde{M} = \begin{pmatrix} \tilde{m} & 0 \\ 0 & \tilde{m} \end{pmatrix} \tag{4.13}$$

where $\tilde{m}$ is

$$\tilde{m} = \begin{pmatrix} \cos(\omega L) & \frac{\sin(\omega L)}{\omega} \\ -\omega \sin(\omega L) & \cos(\omega L) \end{pmatrix} \tag{4.14}$$

The matrix $\tilde{m}$ given in (4.14) is the transfer matrix in one degree of freedom for an element, with a focussing strength of ω. This means that the matrix $\tilde{M}$ is a symplectic transfer matrix for an element that focusses both vertically and horizontally.

A phase space distribution in which the horizontal and vertical Courant-Snyder functions[60] are equal and given by

$$\begin{aligned} \alpha &= 0 \\ \beta &= \frac{1}{\omega} \\ \gamma &= \omega \end{aligned} \tag{4.15}$$

has the matrix of second-order moments defined by

$$E = \begin{pmatrix} \frac{\epsilon_x}{\omega} & 0 & 0 & 0 \\ 0 & \omega\epsilon_x & 0 & 0 \\ 0 & 0 & \frac{\epsilon_y}{\omega} & 0 \\ 0 & 0 & 0 & \omega\epsilon_y \end{pmatrix} \tag{4.16}$$

where the horizontal and vertical emittances, ϵ_x and ϵ_y, are defined as

$$\epsilon_x = \gamma x^2 + 2\alpha x p_x + \beta p_x^2 = \omega x^2 + \frac{1}{\omega} p_x^2 \tag{4.17}$$

$$\epsilon_y = \gamma y^2 + 2\alpha y p_y + \beta p_y^2 = \omega y^2 + \frac{1}{\omega} p_y^2 \tag{4.18}$$

The matrix E remains invariant under a transformation described by $\tilde{M}$:

$$E \longrightarrow \tilde{M} \cdot E \cdot \tilde{M}^T = E \tag{4.19}$$

This means that a beam whose distribution is given by (4.16) remains invariant as it traverses a solenoid described by (4.9) if the emittances are equal. Therefore the beam is said to be correctly matched to the solenoid.

The motion of an individual particle through a solenoid correctly matched to the beam can be described as a rotation in phase space of angle ωL, where the coordinate system also rotates by the same angle. If the beam distribution is not correctly matched to the solenoid the beam size will oscillate along the solenoid. This increases the likelihood of beam losses where the oscillation, in the transverse plane, is at a maximum.

The focussing strength ω depends on the reference momentum. Therefore it depends on the particle energy. This means that the energy spread of the beam affects whether a distribution is matched to a solenoid. Only beam distributions with zero energy spread can be perfectly matched. The beam distribution from the conversion target has a large energy spread. This means that the OMD cannot be matched to the distribution analytically. Therefore the optimal parameters of the chosen OMD must be determined from simulations to minimise the positron losses.

4.4.2 Quarter Wave Transformer

A quarter wave transformer (QWT) consists of a short solenoid with a high magnetic field that drops abruptly to 0.5 T which is the field strength of the solenoid in the capture RF. Figure 4.13 shows the proposed B_z field of a QWT for the ILC positron source and figure 4.14 shows the magnetic field distribution in the solenoids making up the QWT and capture RF solenoid. The lengths and focusing strength of the solenoid are chosen so that the product of the two is $\omega L = \pi/2$. This means that for a beam distribution that is matched to the QWT the particles in the beam and the coordinate system will have rotated by $\pi/2$ in phase space by the exit of the QWT.

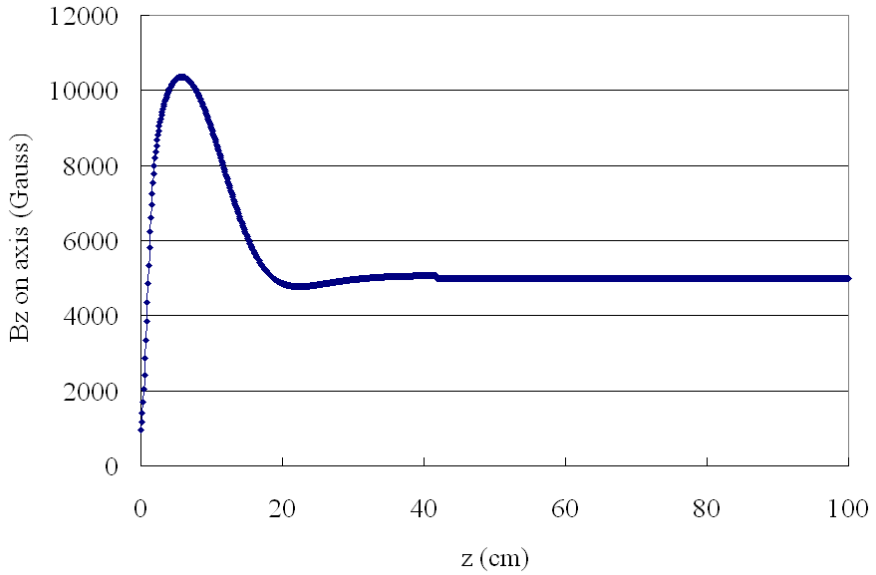

Figure 4.13: Plot showing the longitudinal component of the magnetic field produced by the ILC QWT.

To provide the correct matching field we need to choose the solenoid field strength such that it is a combination of the *Courant-Snyder* β function of the beam at the exit face of the conversion target and the β function of a beam that is matched to the solenoidal field of the capture RF. To choose the optimal field strength we need to use simulations due to the large beam emittance of the positron and electron distribution as it exits the conversion target.

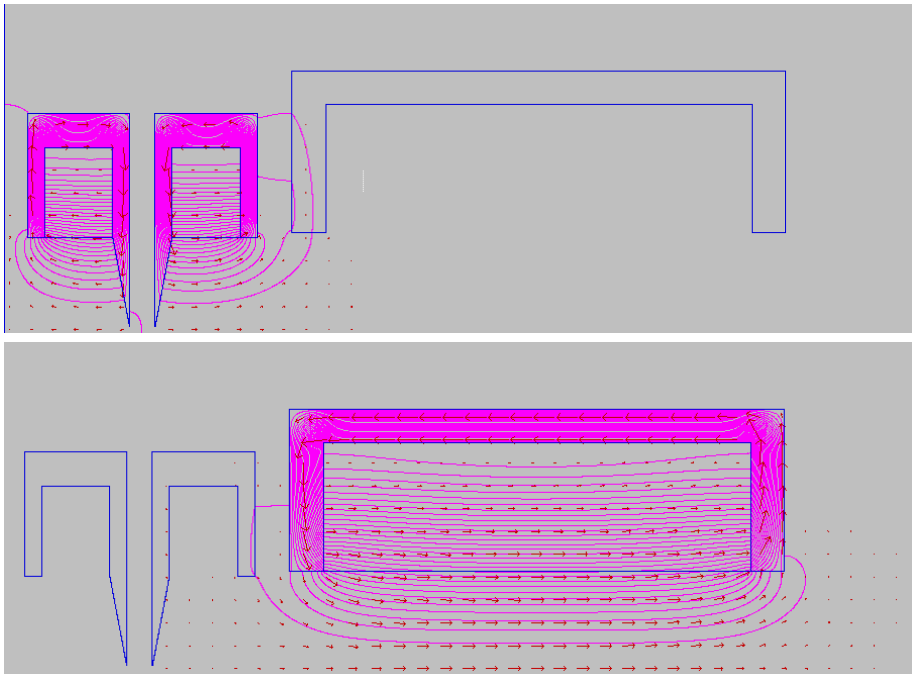

Figure 4.14: Plots showing the magnetic field distribution in the two solenoids forming the QWT (top plot) and the solenoid surrounding the capture RF (bottom plot)[61].

4.4.3 Adiabatic Matching Device

An adiabatic matching device consists of a solenoid field with a a field strength that decreases along the length of the magnet. The field strength is at the maximum at the exit face of the target, $z = 0$, and decreases to a minimum at the start of the capture RF, $z = L$. The minimum field strength is matched to the solenoid field strength in the capture RF, nominally 0.5 T. At a distance z from the exit face of the target the longitudinal field strength in the AMD is given by

$$B_z = \frac{B_0}{1 + gz} \tag{4.20}$$

where g is a constant called the *taper parameter* and is determined by the design of the magnet. The taper parameter describes the rate of variation along the length of the AMD. It is calculated using the equation

$$g = \frac{B_0 - B_{RF}}{B_{RF} L} \tag{4.21}$$

where B_0 is the peak AMD field, B_{RF} is the field in the capture RF and L is the AMD length.

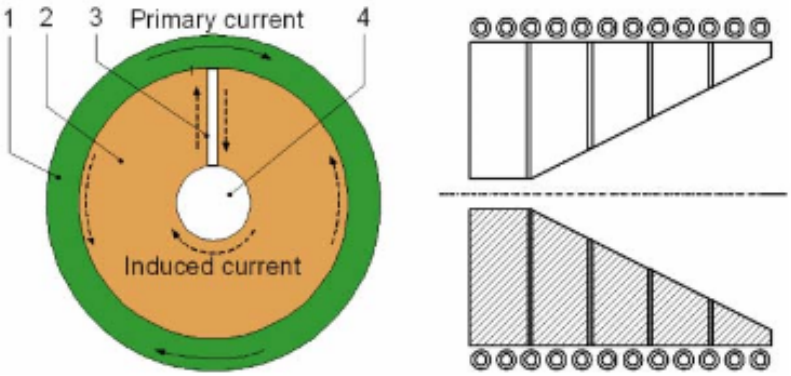

Figure 4.15: Schematic design of the AMD proposed for the ILC[62]. 1 is the primary coil, 2 is the central core, 3 is the radial slot and 4 is the magnet bore through which the beam pipe passes through.

Figure 4.15 shows a schematic of the proposed AMD design for the ILC undulator-based positron source. Based on this design a number of simulations have been conducted and the proposed longitudinal field profile is shown in figure 4.16. The optimal taper parameter to ensure maximum positron transmission through the AMD has been calculated to be $g = 0.6\,\mathrm{cm}^{-1}$[63] from simulations. This corresponds to a capture efficiency of 26.7 %, which is approximately twice the efficiency of the QWT[64].

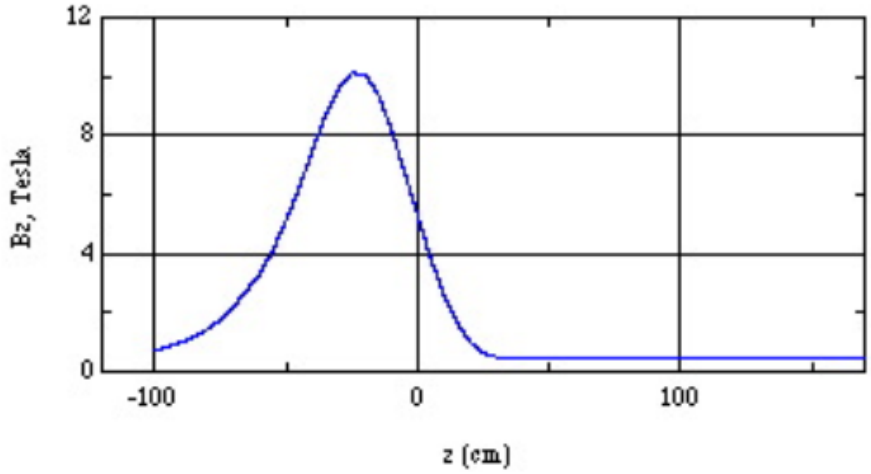

Figure 4.16: Plot showing the longitudinal component of the magnetic field produced by the proposed AMD at the ILC[63]. The exit face of the conversion target is located at z=0.

4.4.4 Pulsed Flux Concentrator

The flux concentrator is identical to the adiabatic matching device except that the flux concentrator has an additional magnetic field component at the start of the magnet. The magnetic field in the additional region is designed so that the longitudinal field component, B_z, starts at a low value and then increases linearly to a peak value which corresponds to the peak value of the adiabatic matching device field. This component was added to the matching device so that the target would be immersed in a smaller magnetic field. This was done as results from target survivability simulations showed that rotating the target in a 6 T magnetic field induced a large heat load on the target due to eddy currents.

A prototype device is under development at Lawrence Livermore National Laboratory in the US. As part of the prototyping process a series of simulations were conducted using Ansoft Maxwell 3D[65]. Figure 4.17 shows the layout used in the simulation and the magnetic field distribution predicted.

The longitudinal field expected from the flux concentrator is shown in figure 4.18. The exit face of the target is located at 130 mm along the x axis which corresponds to the target seeing a field of less than 3 T. Simulations of the positron source with the pulsed flux concentrator give a capture efficiency of 25.8 %. Therefore by using a pulsed flux concentrator compared with the AMD we can achieve nearly the same capture efficiency of positrons whilst increasing the survivability of the conversion target.

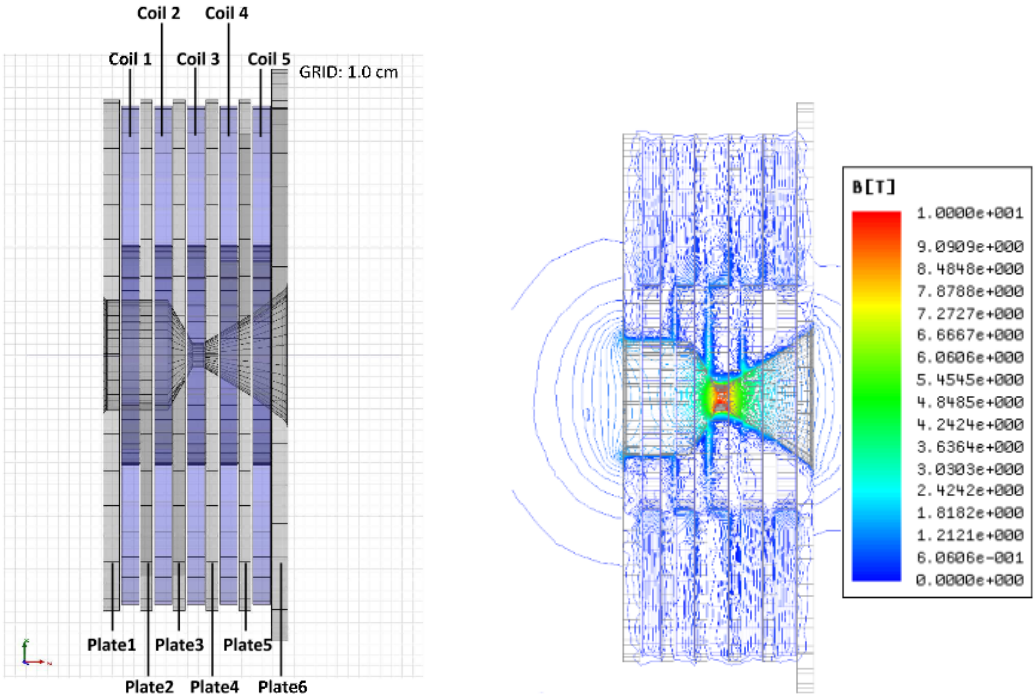

Figure 4.17: Layout of the pulsed flux concentrator simulated in Maxwell 3D and the resulting magnetic field distribution expected[66].

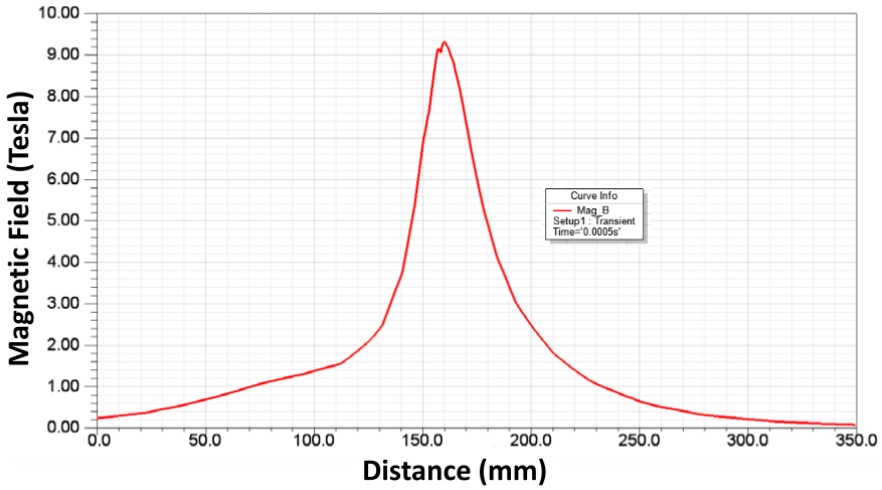

Figure 4.18: Longitudinal magnetic field expected from the pulsed flux concentrator. The exit face of the target is located at 130 mm[66].

4.5 ILC Positron Source Parameters

The ILC Technical Design Report (TDR) was published in 2013 and it contains a detailed baseline design of the entire accelerator[41]. In addition there are also recommended upgrade paths and options for various components of the machine. The baseline positron source parameters are reproduced in table 4.5 and the parameters required for a centre of mass energy upgrade are shown in table 4.6.

Table 4.5: Parameters for the baseline ILC Positron Source

Parameter	Symbol	Units	Value
Positrons per bunch at IP	n_b		2×10^{10}
Bunches per pulse	N_b		1312
Pulse Repetition Rate	f_{rep}	Hz	5
Positron Energy (DR Injection)	E_0	GeV	5
DR Dynamic Aperture	$\gamma(A_x + A_y)$	mrad	< 0.07
DR Energy Acceptance	Δ	%	0.75
DR Longitudinal Acceptance	A_l	cmMeV	3.4×37.5
Electron Drive Beam Energy	E_e	GeV	150/175/250
Undulator Period	λ_u	cm	1.15
Undulator Deflection Parameter	K		0.92/0.75/0.45
Undulator Active Length	L_u	m	147
Photon Energy (1^{st} Harmonic Cut-off)	E_{c1}	MeV	10.1/16.2/42.8
Target Material			Ti6%Al6%V
Target Thickness	L_t	cm	1.40
Incident Photon Spot Size on Target (rms)	σ_i	mm	1.4/1.2/0.8
Positron Polarisation	P	%	31/30/29

Table 4.6: Parameters for the Positron Source after the High Energy ILC Upgrade. Different Parameters are required for 350 GeV and 500 GeV centre of mass energies.

Parameter	Symbol	Units	350 GeV	500 GeV
Electron Drive Beam Energy	E_e	GeV	178	253
Bunches per pulse	N_b		1312	1312
Photon Energy (1^{st} Harmonic Cutoff)	E_{c1}	MeV	16.2	42.8
Photon Opening Angle		μrad	2.9	2
Undulator Period	λ_u	cm	1.15	1.15
Undulator Deflection Parameter	K		0.75	0.45
Undulator Active Length	L_u	m	147	147
Incident Photon Spot Size on Target (rms)	σ_i	mm	1.2	0.8
Average Photon Power on Target		kW	54.7	41.7
Captured Positron Polarisation	P	%	30	30

The key parameters for the main components of the ILC positron source are given in the following tables:

- Table 4.7: Undulator Parameters
- Table 4.8: Target Parameters
- Table 4.9: OMD Parameters

- Table 4.10: Capture RF Parameters

There is no collimator in the baseline positron source at the ILC. One is planned as part of future upgrades to increase positron polarisation however work is still ongoing to finalise the design of the collimator.

Table 4.7: Key parameters for the helical undulator in the ILC positron source at different centre of mass energies.

Parameter	Units	< 300 GeV	300 GeV	350 GeV	500 GeV
Electron Drive Beam Energy	GeV	150	150	178	253
Drive Beam Repetition Rate	Hz	10	5	5	5
Undulator Period	cm	1.15	1.15	1.15	1.15
Undulator Magnetic Field (on-axis)	T	0.86	0.86	0.698	0.42
Undulator Deflection Parameter		0.92	0.92	0.75	0.45

Table 4.8: Key parameters for the target in the ILC positron source.

Parameter	Units	Value
Target Material		Ti6%Al4%V
Target Diameter	m	1.00
Target Thickness	radiation lengths	0.4
Target Thickness	cm	1.40
Target Rim Width	cm	3.0
Target Rim Speed	ms^{-1}	100

Table 4.9: Key parameters for the pulsed flux concentrator in the ILC positron source.

Parameter	Units	Value
OMD Type		FC
Peak Magnetic Field	T	3.2
Ramp Time	ms	1.0
Constant Field Time	ms	1.5
Repetition Rate	Hz	5
Cooling Method		Water

4.6 Summary

In this chapter a summary of each main component in the undulator-based positron source has been presented. Highlights of research and design work conducted under the ILC GDE have been included in the appropriate sections. This includes work carried out by the author on simulating a Nb_3Sn superconducting helical undulator. The parameters of the ILC undulator-based positron source have been reproduced from the ILC TDR[41].

Each component of the undulator-based positron source could form the basis of a thesis. This thesis is now concentrating on optimising the design of the undulator to produce the optimal

Table 4.10: Key parameters for the capture RF cavities in the ILC positron source. The capture RF linac consists of 2 standing wave cavities followed by 3 travelling wave cavities

Parameter	Units	Standing Wave	Travelling Wave
Structure Type		π mode	$3\pi/4$ mode
Number of Cells		11	50
Aperture	mm	60	46
Q-Factor		29700	24842 - 21676
Shunt Impedance	MΩ/m	34.3	48.60 - 39.45
Gradient	MV/m	15.2	8.5

photon spectrum for positron generation using the ILC baseline design for all other components of the source.

Chapter 5

Simulating Undulator Photon Spectra

The undulator is possibly the most important component in the undulator-based positron source as the properties of the undulator are the dominant parameters in determining the positron distribution produced by the undulator-based positron source. Although simulation codes exist to calculate the expected photon spectra from an undulator they have not been applied to the undulator based positron source before. This is due to the design of these codes as they were not intended to be used in the energy regimes in which the undulator-based positron source operates.

One of the most widespread codes used to simulate undulator radiation is SPECTRA[67]. SPECTRA is a C++ based code developed by Takashi Tanaka at the SPring-8 Center. However when SPECTRA was used to simulate the radiation expected from the undulator prototypes developed at Daresbury Laboratory and Rutherford Appleton Laboratory there were computing issues relating to the length of time required to calculate the spectrum and also the accuracy of the spectrum at wide angles. In the typical energy ranges in which light source undulators operate, approximately a several GeV, the number of wide angle photons produced is not significant. At the energies of the undulator based positron source the wide angle photons become very important to the overall spectrum particularly when calculating the heat load on the vacuum vessel. This means that a new simulation code was required for calculating the spectra generated by the undulator-based positron source.

This chapter covers the different methods used to calculate the photon spectrum from the undulator-based positron source. The benchmarking of the chosen simulation method is then discussed before the optimal photon spectra for positron production is calculated. Different undulator configurations are investigated to determine the undulator design that comes closest to achieving the optimal photon spectra.

5.1 Simulation Methods

In order to simulate the photon spectra produced by an undulator there are a number of options available. The main method for determining the spectrum that is used in simulations of the undulator-based positron source is based on equation 25 from the paper by Brian Kincaid on helical undulator radiation [48] (see section 3.4.3). PPS-Sim uses this equation to determine the shape of the undulator spectrum before using monte-carlo routines to generate individual photons from this spectrum. The two other possible simulation tools available are two different codes developed at the Cockcroft Institute.

The first of these was developed by Duncan Scott during his time as part of the helical collaboration. This method called FluxCalc is a Mathematica notebook that implements equations from Chapter 2 to calculate the synchrotron radiation produced by an electron travelling through an arbitrary field map. Although in principle FluxCalc can calculate the radiation from any field map, due to the implementation method in the version available at the time, a helical undulator field map must be used in practice. This is due to FluxCalc using interpolation functions that require the undulator field map to be non-zero in both the xz and yz planes. If either of these planes had no magnetic field then the program would generate errors. A new version is being developed that is written in C++ that would allow both 2D and 3D magnetic field maps.

The other simulation code available is Helical Undulator Synchrotron Radiation (HUSR) developed by David Newton[68]. HUSR works by calculating a Lie Map from a given magnetic field. This is done by interpolating the magnetic field data on the surface of a cylinder. The interpolated data is then Fourier transformed to calculate numerically the generalised gradients for the multipole components of the field. This provides an analytical solution for the transverse magnetic field. The Hamiltonian for an electron travelling through this analytical description of the field is calculated and then integrated. This integrated Hamiltonian is then used to generate a set of Lie Maps that can transport an electron through the field[69]. Once the Lie Maps have been generated the spectrum is calculated at a number of observation points. This is done by calculating the electric field at each observation point using the retarded potential. This field is then Fourier transformed to change from the time domain to the frequency domain. The spectrum is therefore calculated from this electric field.

A comparison was carried out by Duncan Scott between FluxCalc, HUSR and SPECTRA to determine where the different codes agree and where they differ in their results. This comparison was done using the undulator parameters from an early undulator prototype for the ILC positron source. Table 5.1 contains the parameters used in the simulations. These parameters are very close to those of the ILC TDR positron source. The key difference is that the number of periods in the undulator is much lower. Although the aperture that represents the face of the target is

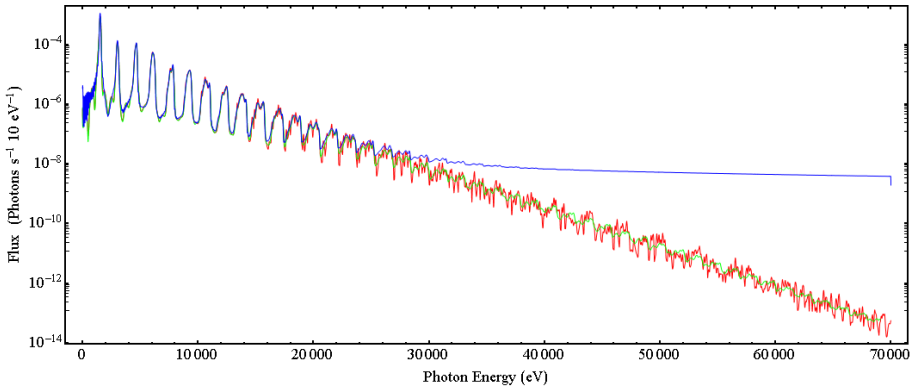

Figure 5.1: Comparison between the photon flux from a single electron through a 1 mm^2 aperture predicted by different simulation codes. Blue line is from SPECTRA, red line is from FluxCalc and green line is from HUSR[1].

much closer to the end of the undulator the angular size of the aperture is comparable to that of the target rim in the ILC TDR positron source. Figure 5.1 shows the results from SPECTRA in blue, FluxCalc, in red and HUSR in green. In the region below 30 keV there is good agreement between the three codes. However above 30 keV SPECTRA no longer agrees with FluxCalc and HUSR. The photon spectrum is only plotted up to 70 keV as it is obvious by this point that the number of photons from SPECTRA just keeps increasing with energy. As the undulator-based positron source produces photons with an average energy of approximately 13 MeV from an electron with an energy of 150 GeV. The results shown in figure 5.1 suggests that HUSR and FluxCalc will be better suited for simulating the photon spectrum from the undulator of the undulator-based positron source.

Table 5.1: Table showing the parameters used in simulations to compare FluxCalc, HUSR and SPECTRA[1].

Parameter	Units	Value
Electron Energy	GeV	150
Undulator Period	mm	10.0
Undulator Deflection Parameter (K)		1
Number of Periods		10
Distance to Aperture	m	10
Aperture Area	mm^2	1.00

FluxCalc and HUSR were then compared with each other in terms of functionality, speed and ease of modification to determine which would be more suitable for the task of simulating the photon spectra from different undulator configurations. In terms of functionality both codes were very similar however it was determined that HUSR had more scope for extending the functionality. Additionally it would be easier to extend the functionality of HUSR with it being a C++ code. However the main advantage of HUSR was the speed of calculation. This was even more pronounced as it was possible to modify HUSR so it would be able to run on the

High End Computing (HEC) cluster at Lancaster which would allow multiple simulations to be run simultaneously. Therefore HUSR was used for simulating the undulator photon spectra presented in this chapter.

5.2 Benchmarking HUSR

The first task to be completed with HUSR was to benchmark the code. A comparison between HUSR, SPECTRA and FluxCalc was already completed (see figure 5.1). To further benchmark the code a comparison was made between the undulator photon spectrum calculated by HUSR and the spectrum from the analytical equation from [48]. Equation 25 from [48] was corrected, there is a typographical error, and then modified to give results in SI units. The corrected equation for an infinitely long perfect undulator is

$$\frac{\mathrm{d}I}{\mathrm{d}\omega} = \frac{Nq^2K^2r}{\epsilon_0 c}\sum_{n=1}^{\infty}\left[J_n^{|2}(x_n) + \left(\frac{\alpha_n}{K} - \frac{n}{x_n}\right)^2 J_n^2(x_n)\right] H(\alpha_n^2) \tag{5.1}$$

where N is the number of periods in the undulator, q is the charge of the electron, K is the undulator deflection parameter, H is the unit step function, J and J' are Bessel functions of the first kind and

$$\begin{aligned} \alpha_n^2 &= \frac{n}{r} - 1 - K^2 \\ r &= \frac{\omega}{2\gamma\omega_0} \\ \omega_0 &= \frac{2\pi c}{\lambda_u}\left(1 - \frac{1}{2\gamma^2} - \frac{K^2}{2\gamma^2}\right) \end{aligned}$$

Using this equation we can determine how accurate the output from HUSR is. A comparison between HUSR and the spectrum predicted by (5.1) was conducted for an ILC TDR undulator; $N = 155$, $K = 0.92$ and $\lambda_u = 11.5\,\mathrm{mm}$. Figure 5.2 shows the photon energy spectrum generated by a 150 GeV electron by equation (5.1) in red and HUSR in green. There is noise in the HUSR spectrum due to having a finite number of observation points. This noise is particularly noticeable at higher photon energies as the flux in that region is smaller. The agreement between HUSR and equation (5.1), is very good for large numbers of observation points, for 10000 observation points there is less than 0.02 % difference. This work in addition to comparisons conducted by Duncan Scott, discussed in section 5.1, shows that HUSR is very accurate, and will give results that can be trusted when simulating ideal undulators.

Whilst investigating non-ideal undulators a limitation in HUSR was discovered. In the ideal case the radiation produced by a helical undulator is circularly symmetric this means that by sampling along one radius of the observation plane, which is perpendicular to the axis of the

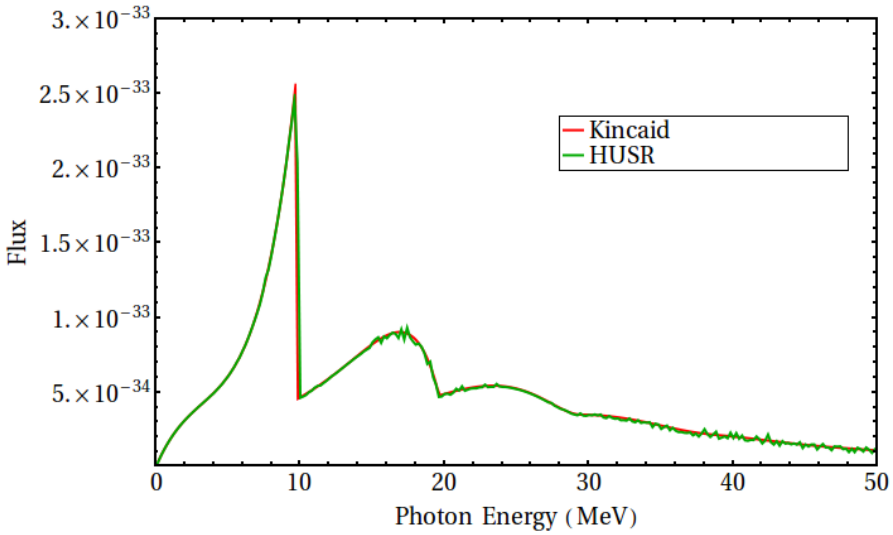

Figure 5.2: Comparison between the photon spectrum predicted by an analytical equation (red curve) and HUSR (green curve) for a 150 GeV electron travelling through an ILC TDR undulator.

undulator, you can accurately characterise the photon spectrum produced. In non-ideal undulators the radiation is no longer circularly symmetric so sampling at one angle on the observation plane is no longer sufficient. To correct for this the author of the thesis has modified HUSR to allow for sampling at multiple angles on the observation plane.

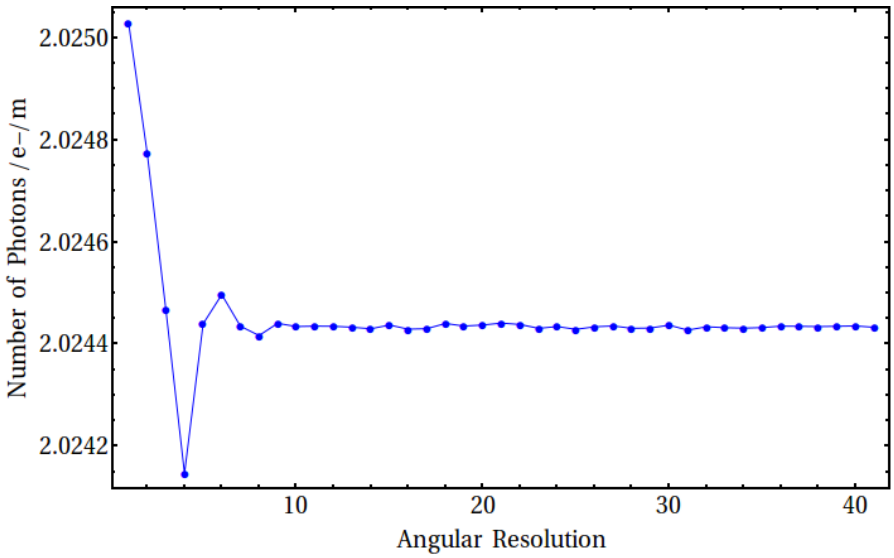

Figure 5.3: Plot showing the effect of increasing the angular resolution of HUSR on the total number of photons in a spectrum.

Figure 5.3 shows the effect that sampling at multiple angles has on the total photon number from a spectrum. As the angular resolution increases the number of photons converges to a stable value. Based on this work simulations in HUSR sampled the observation plane along a minimum of 12 different radii evenly distributed around the plane.

5.3 Optimal Photon Spectra

In order to evaluate photon spectra that are generated using HUSR we need to know what the optimal photon spectrum shape for positron production is. To determine this spectrum shape a series of simulations were conducted in PPS-Sim with a positron source that matched the ILC TDR parameters. However instead of using an undulator spectrum as the input to the simulations a probe spectrum was used (see figure 5.4). The probe spectrum is a top hat shape with a width of 1 MeV. The height of the spectrum used is 1×10^{-6} because PPS-Sim normalises the area under the curve to 1.

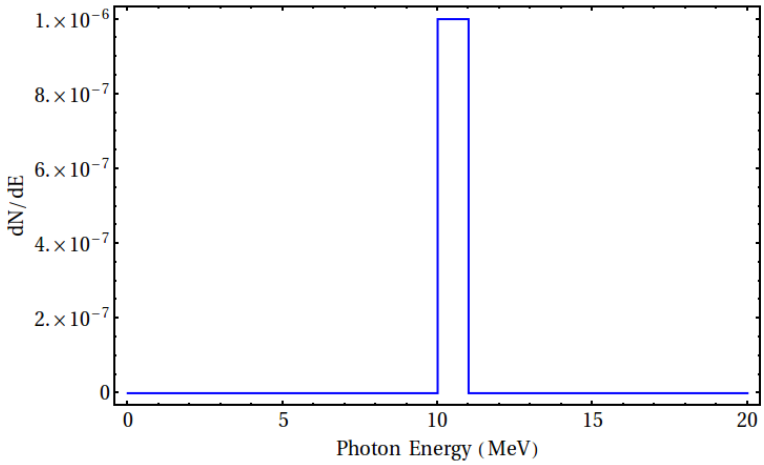

Figure 5.4: Probe spectrum input into PPS-Sim to determine the optimal photon energy spectrum.

Using this probe spectrum shape at different photon energies we are able to calculate the positrons per photon produced as a function of photon energy. Figure 5.5 shows the positrons per photon produced after at the target (red data points) and the positrons per photon that travel through the positron source and would be accepted by the ILC damping ring (green data points). The top plot shows positron production over the entire photon energy range investigated. The dominant trend is in the positrons produced at the target, increases with energy with the highest gradient being in the 5 to 30 MeV region. The important value in terms of *usable* photons is the positrons that are within the ILC damping ring acceptance. The bottom plot is a *zoomed-in* version of the top plot which highlights the energy range which produces the most positrons that would enter the damping ring. The optimal region for positron production inferred from this plot is the 40 to 100 MeV range. The region that produces the least usable positrons is the 0 to 10 MeV.

Based on these results the optimal photon spectrum shape for positron production is shown in figure 5.6. This is a very different photon spectra shape to that produced by the ILC positron source undulators which is shown in figure 4.5. This spectrum peaks at low photon energies, less

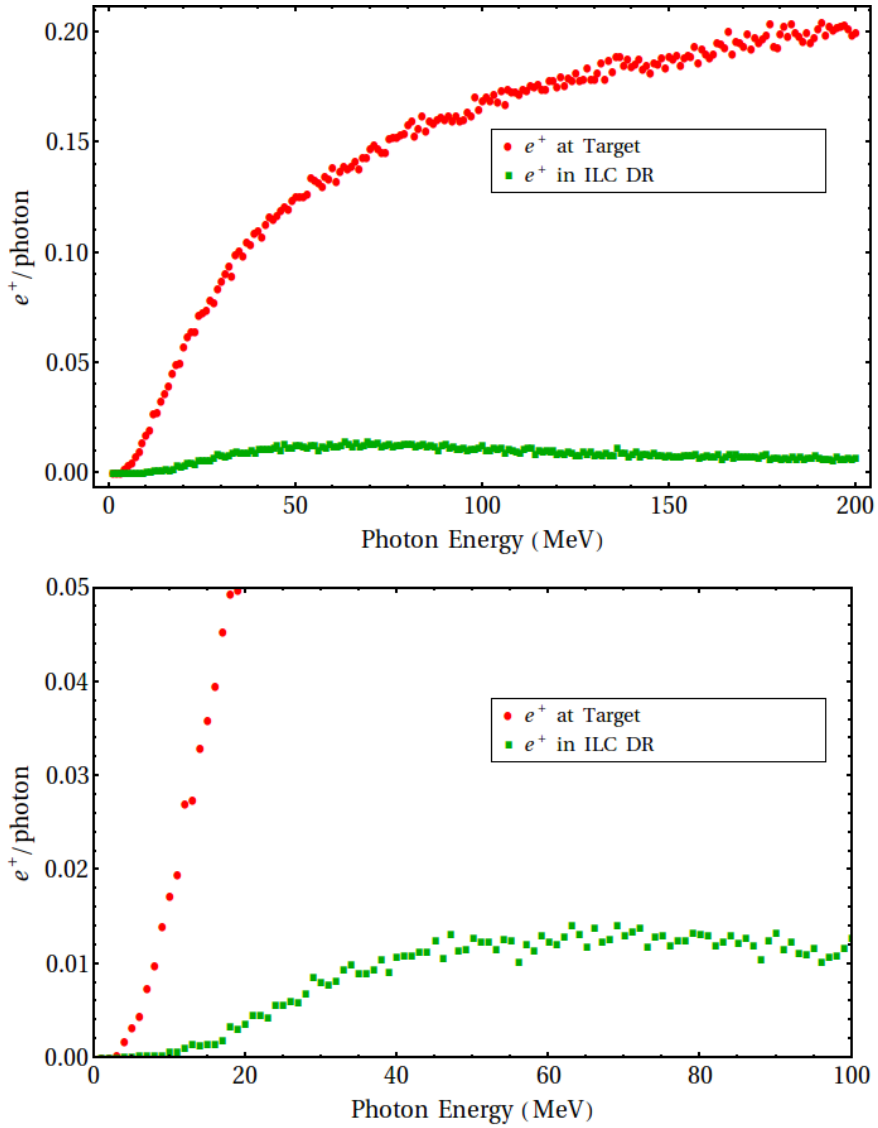

Figure 5.5: Plots of positron per photon produced at the conversion target (red data points) and in positrons per photon within the ILC damping ring acceptance (green data points). The top plot shows the positron production over the entire photon energy range investigated. The lower plot shows the region which produces the most *usable* positrons.

than 1 MeV, and at the first harmonic which varies with drive beam energy but is typically in the region of 10 to 30 MeV. From this peak the photon flux then decreases significantly. Therefore attempting to replicate the optimal photon spectrum will require a very different undulator configuration.

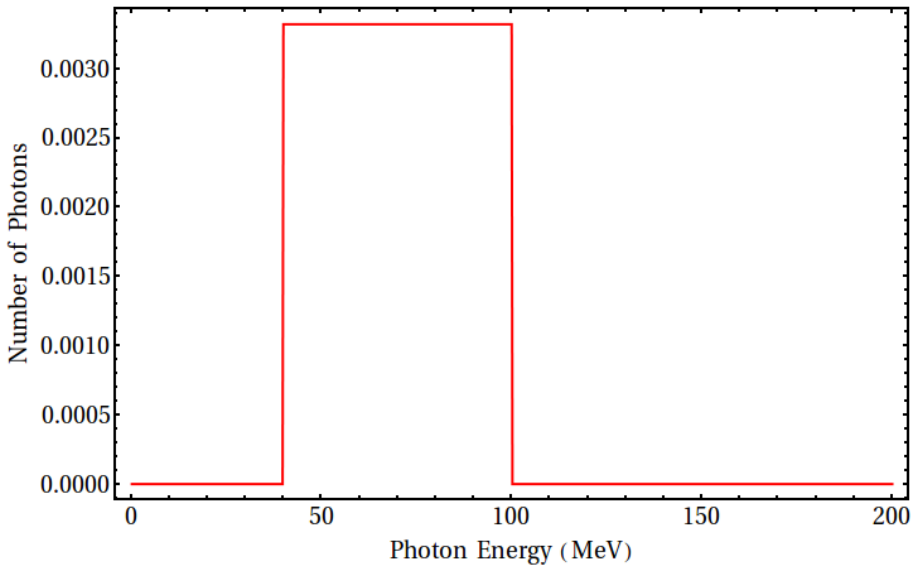

Figure 5.6: Plot showing the optimal photon spectrum for positron production based on results shown in figure 5.5. Number of photons in the spectrum has been normalised to 1.

5.4 Non-Ideal Undulator Spectra

Up until now all simulations of the undulator-based positron source have used a photon spectrum calculated using analytic equations which describe an ideal undulator. However we will not be able to produce a perfect undulator and therefore we will need to be able to conduct simulations using the photon spectra from non-ideal undulators.

Using HUSR this is possible as we are able to introduce errors into the undulator magnetic field map. One method HUSR uses for constructing the overall field map is by adding multiple instances of the map for a single undulator period together. Therefore using this method in HUSR we can introduce random errors into each period of the magnet.

Using the Hall probe measurements of the two undulator prototypes constructed at Rutherford Appleton Laboratory we are able to get a characteristic size of the errors that can be expected in the actual undulator modules that would be used in an undulator-based positron source. The maximum size of the errors in the magnetic field amplitude measured from the undulator prototypes are $\pm 10\%$. Using this value we can then use a Gaussian distribution to introduce random errors into the field and period.

If we consider an undulator with $N = 155$, $K = 0.92$ and $\lambda_u = 11.5\,\text{mm}$ we can compare the track of an electron through a non-ideal undulator with an ideal undulator. An electron travelling though an ideal undulator travels on a helical trajectory around the central axis of the undulator. The radius of this helix is inversely proportional to the energy of the electron. Comparing this with figures 5.7, 5.8 and 5.9 which show the track of an electron through a non-ideal undulator at three different energies gives some interesting insight. The electron trajectory is no longer centred along the axis of the undulator. Although the x coordinate of the trajectory oscillates close to the axis, the centre of the oscillation varies along the length of the undulator. The y coordinate varies even more and although the electron is injected on-axis the final y position of the electron is tens or, for a 60 GeV electron, hundreds of nanometres off the central axis.

The large variation in the y coordinate is due to discontinuities in the undulator windings. Due to the construction method used in the undulator prototypes at Rutherford Appleton Laboratory the conductor could not be made from a single winding. The final prototypes ended up with three joins in the winding which were located at a point where the y component of the field is zero and when the x component was maximum. In practice either the x or y component of the field can be maximum where the joins occur. However, for the simulations carried out the discontinuities in the field were all when the x component was maximum as this is what was seen in the Hall probe measurements of the prototypes. This discontinuity provides a kick in the yz plane. As the electron beam energy increases the effect of this kick is reduced.

To investigate if a small deviation off-axis would get bigger, a simple random walk[70] through

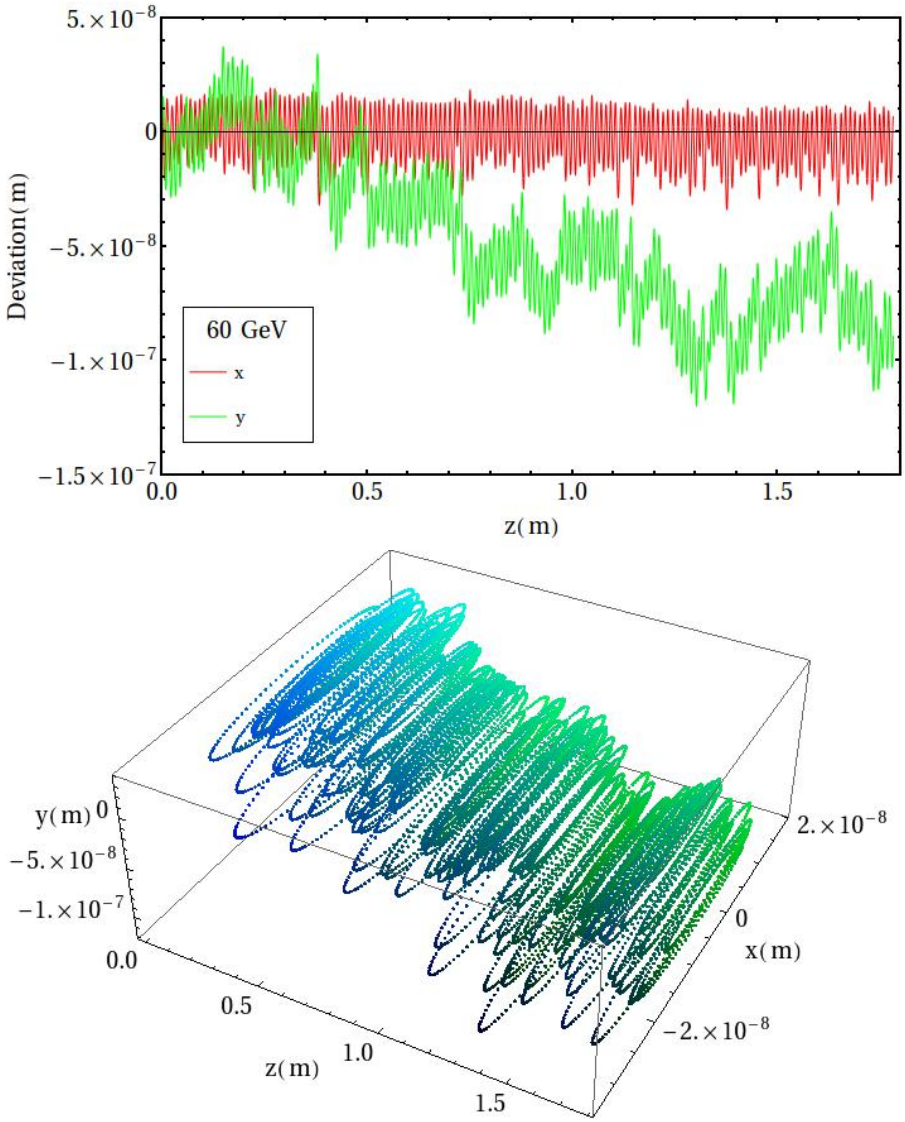

Figure 5.7: Plots showing the trajectory of a 60 GeV electron travelling through a non-ideal undulator with $N = 155$, $K = 0.92$ and $\lambda_u = 11.5$ mm. The top plot shows the x (red line) and y (green) position of the electron along the length of the undulator. The bottom plot shows the 3D trajectory of the electron.

100 undulator modules was implemented. This was done by simulating ten realistic undulators to determine a characteristic amplitude for the off axis deviation. This deviation was then input into a one dimensional random walk routine that had equal probability of deviating in the positive and negative y direction.

Figure 5.10 shows the maximum off-axis deviation for three different electron drive beam energies. This shows that we could expect up to a micron deviation off-axis through an undulator 100 modules long. Just as with the ideal undulator the size of the oscillation is inversely proportional to the electron energy as is the magnitude of the off-axis drift.

Using these tracks we can generate the photon spectrum which would be produced from this non-ideal undulator. Figures 5.11, 5.12 and 5.13 compare the spectrum produced by this non-

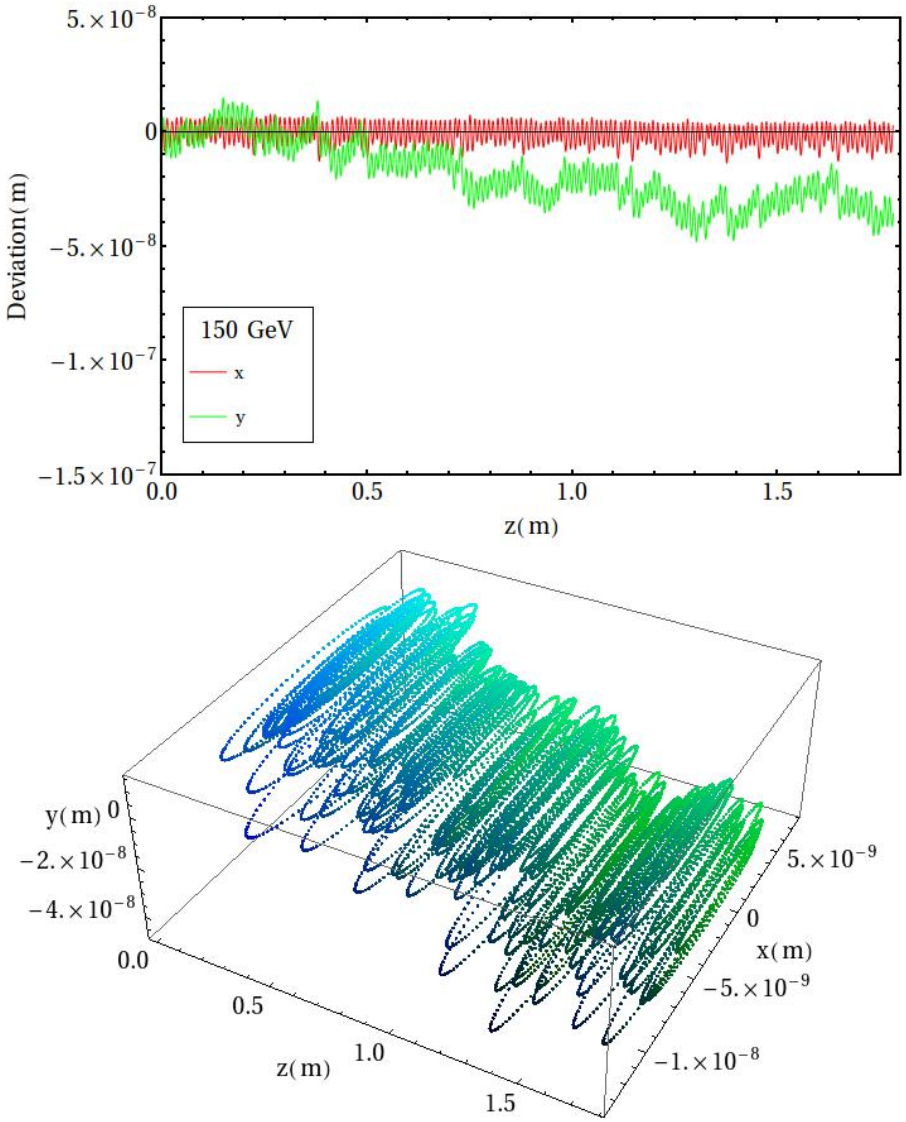

Figure 5.8: Plots showing the trajectory of a 150 GeV electron travelling through a non-ideal undulator with $N = 155$, $K = 0.92$ and $\lambda_u = 11.5$ mm. The top plot shows the x (red line) and y (green) position of the electron along the length of the undulator. The bottom plot shows the 3D trajectory of the electron.

ideal undulator with that from an ideal undulator and the spectrum predicted by equation (5.1) for electron energies of 60, 150 and 250 GeV respectively.

Introducing errors into an undulator field map 155 periods long is very interesting in terms of positron production. The main effect a non-ideal undulator has is in smoothing out the harmonic peaks. This effect is present at all three energies and means that the harmonics in the non-ideal undulator spectrum do not reach the same peak value as the ideal undulator. The drop-off from the harmonic peak is no longer as as rapid, which means the non-ideal spectrum actually has more photons than the ideal undulator in the energy regime between the harmonic cut off energies.

Comparing this to the optimal photon spectrum discussed in section 4.3 means that a non-

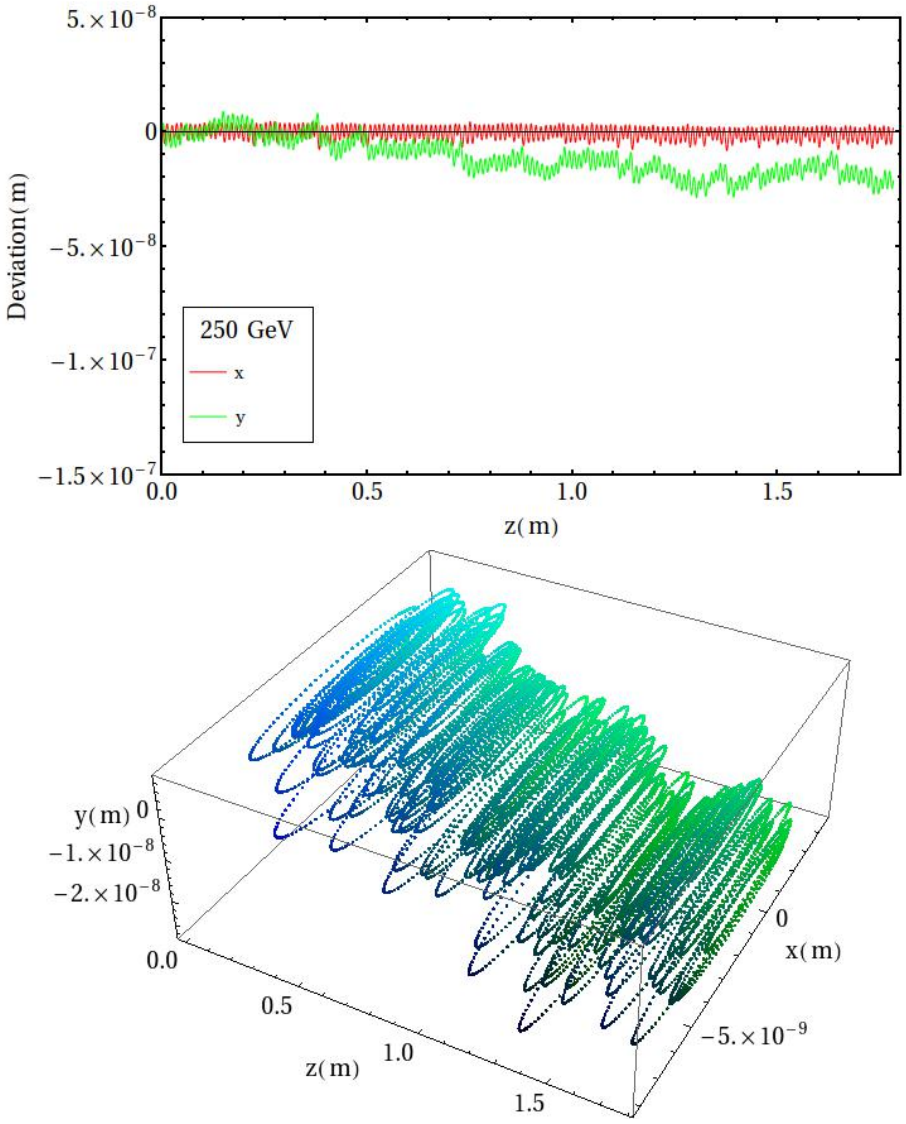

Figure 5.9: Plots showing the trajectory of a 250 GeV electron travelling through a non-ideal undulator with $N = 155$, $K = 0.92$ and $\lambda_u = 11.5\,\text{mm}$. The top plot shows the x (red line) and y (green) position of the electron along the length of the undulator. The bottom plot shows the 3D trajectory of the electron.

ideal spectrum is closer to the optimal spectrum than an ideal spectrum. This is because non-ideal spectra have more photons in the energy range of 40 to 100 MeV. To investigate why this may be the case a number of studies were carried out into how different undulator parameters change the spectrum shape. A parameter that may help explain why non-ideal undulators have this spectra shape is the undulator length.

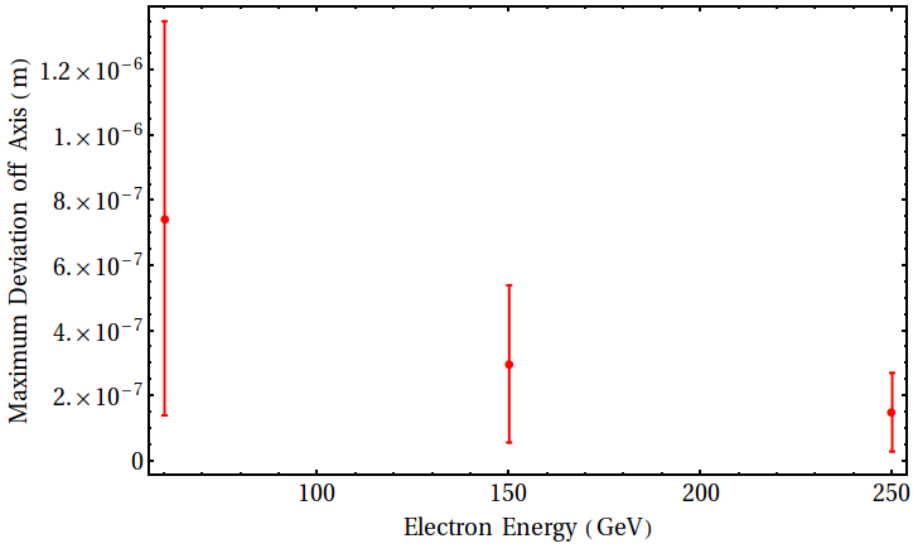

Figure 5.10: Plot showing the maximum off-axis deviation through an undulator 100 modules long as a function of electron drive beam energy. The data points show the mean value from 1000 different undulators and the error bars show the standard deviation.

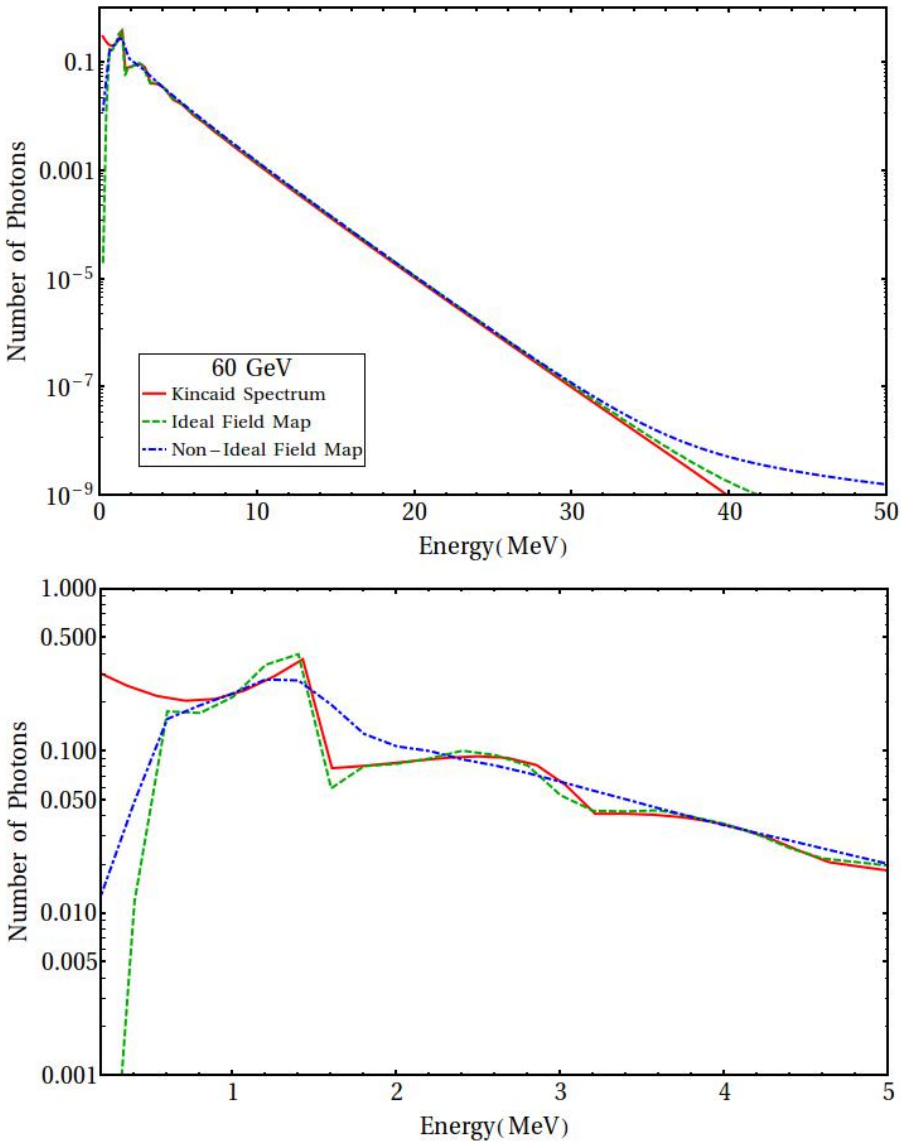

Figure 5.11: Plots showing the photon spectra of a 60 GeV electron travelling along an undulator with $N = 155$, $K = 0.92$ and $\lambda_u = 11.5\,\text{mm}$. The red line shows the spectrum predicted by equation (5.1). The green line shows the simulated spectrum from an ideal undulator. The blue line shows the simulated spectrum from a realistic undulator. The bottom plot is a *zoomed-in* version of the top plot showing the first three harmonics. The energy resolution of the simulations is 200 keV.

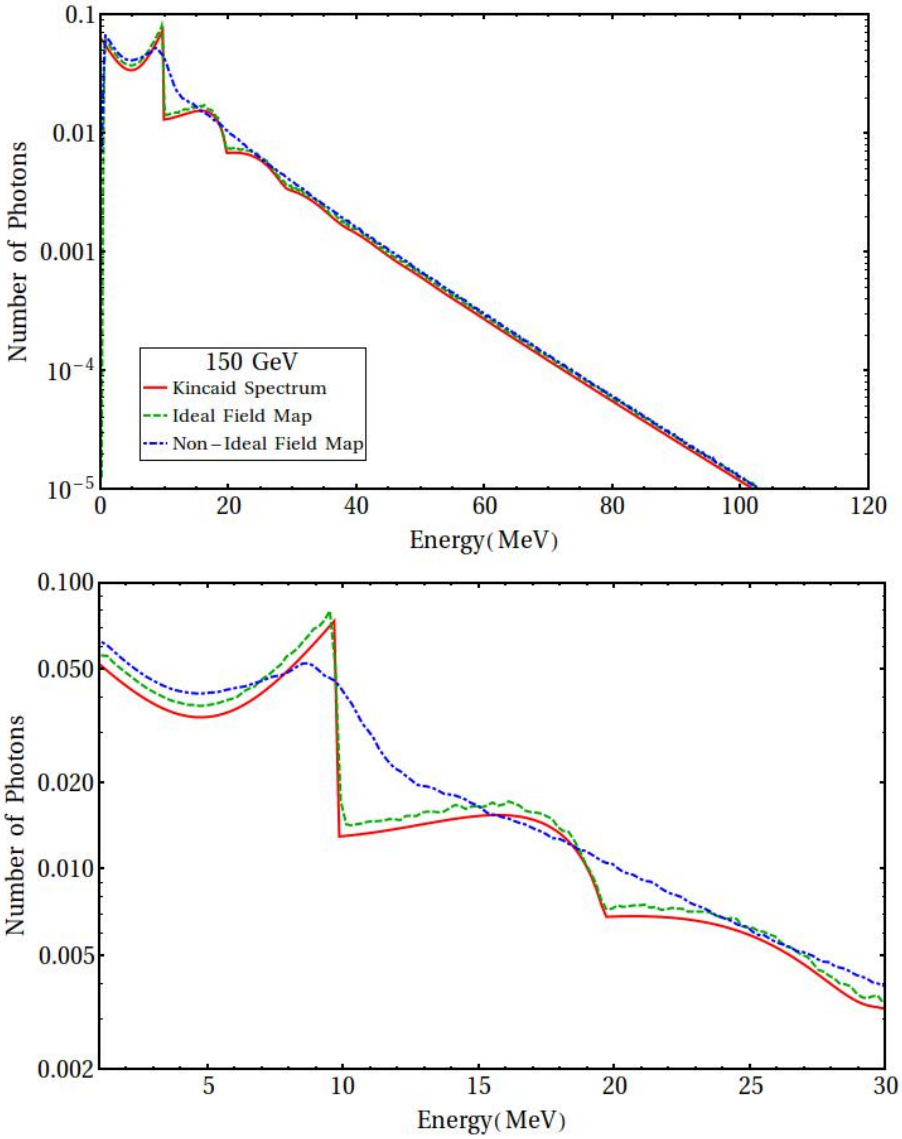

Figure 5.12: Plots showing the photon spectra of a 150 GeV electron travelling along an undulator with $N = 155$, $K = 0.92$ and $\lambda_u = 11.5\,\text{mm}$. The red line shows the spectrum predicted by equation (5.1). The green line shows the simulated spectrum from an ideal undulator. The blue line shows the simulated spectrum from a realistic undulator. The bottom plot is a *zoomed-in* version of the top plot showing the first three harmonics. The energy resolution of the simulations is 200 keV.

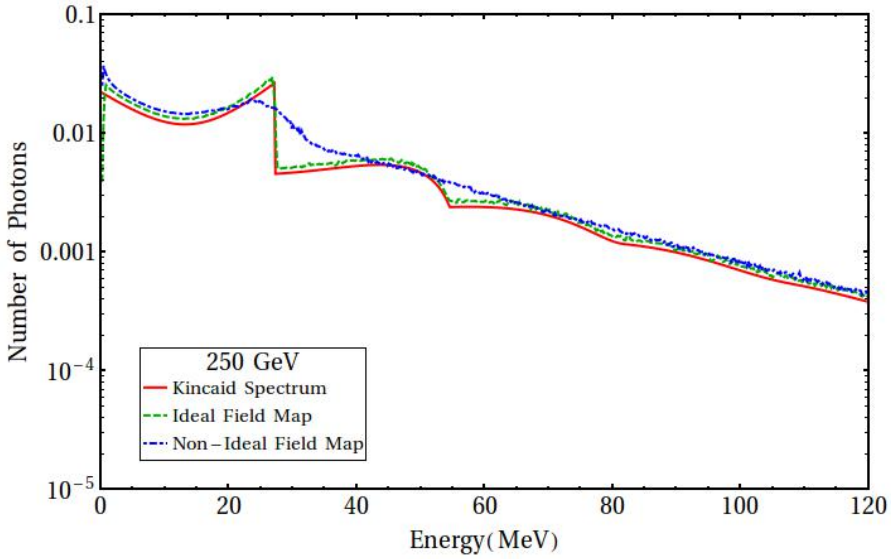

Figure 5.13: Plot showing the photon spectra of a 250 GeV electron travelling along an undulator with $N = 155$, $K = 0.92$ and $\lambda_u = 11.5\,\text{mm}$. The red line shows the spectrum predicted by equation (5.1). The green line shows the simulated spectrum from an ideal undulator. The blue line shows the simulated spectrum from a realistic undulator. The energy resolution of the simulations is 200 keV

5.5 Undulator Length

The effect which undulator length has on the photon spectrum is of interest as the key property of radiation that determines the shape of the undulator spectrum is interference. The constructive and destructive interference that happens within the undulator is what produces the harmonic peaks. The undulator needs to be long enough to allow this interference to occur and create the distinctive spectrum shape. In this thesis the length needed to create this interference will be referred to as the *interference length*.

A number of simulations were conducted to investigate the length an undulator needs in order to create this interference effect. The simulations were conducted using HUSR with a 150 GeV electron travelling through an undulator with $K = 0.92$ and $\lambda_u = 11.5$ mm. Figure 5.14 shows the spectra produced from the undulator with a number of periods from to 1 to 14.

As can be seen, the spectrum produced by an undulator with $N = 1$ is smooth. This is to be expected, as an undulator with only one period can be described as two dipole magnets and the synchrotron radiation produced by a dipole magnet is simply a smooth spectrum (see section 2.2). For $N > 1$ there starts to be features present, however the first harmonic peak only starts to gain a sharp cut off when $N > 10$.

Figure 5.15 shows the spectra from the same undulator with periods in the range of 10 to 100. From these plots we can see that the effect of the undulator having more than 20 periods is to increase the flux, there is no enhancement of the spectra shape, as the radiation adds incoherently. This means that five undulators which are 20 periods long will give the same spectrum as one undulator 100 periods long.

If we compare the shape of the first harmonic from the different spectra in figure 5.14 with the spectra from a non-ideal undulator shown in figure 5.12 we can see similar features. The first harmonic in the spectra from the non-ideal undulator peaks at 9 MeV and then decays slowly until approximately 12 MeV. There is a very similar shape in the first harmonics from an ideal undulator that is less than ten periods long. This suggests that one of the effects of the errors in the undulator magnetic field map is to break the undulator into a series of undulators with a length less than the interference length of the perfect undulator.

The non-ideal undulator spectrum was closer to the optimal photon spectrum for positron production. Designing an undulator that deliberately breaks the interference length condition produces a photon spectrum that is better optimised for the positron source.

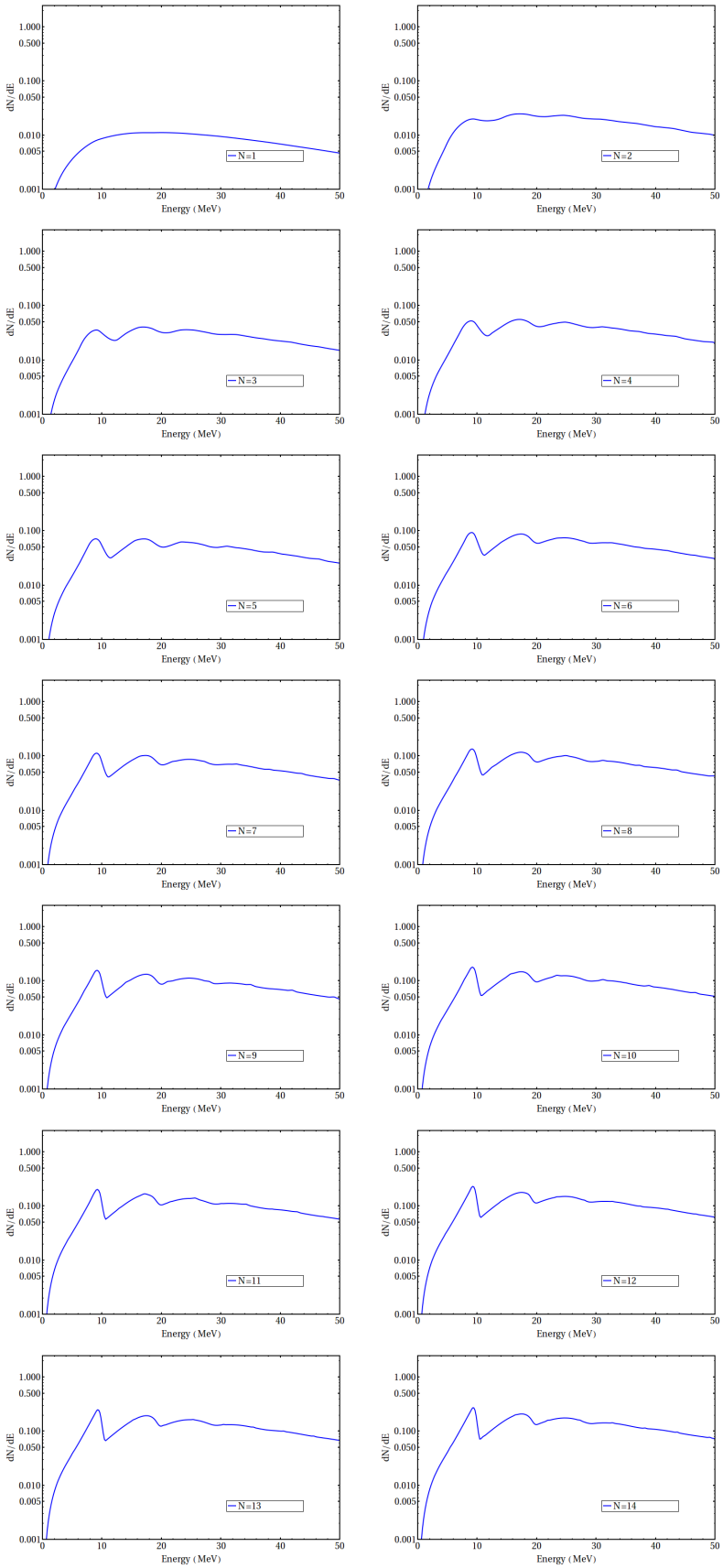

Figure 5.14: Plots showing spectra produced by a 150 GeV electron travelling through an undulator with $K = 0.92$ and $\lambda_u = 11.5\,\text{mm}$. Each plot shows the spectra produced by a different number of periods starting with $N = 1$ up to $N = 14$.

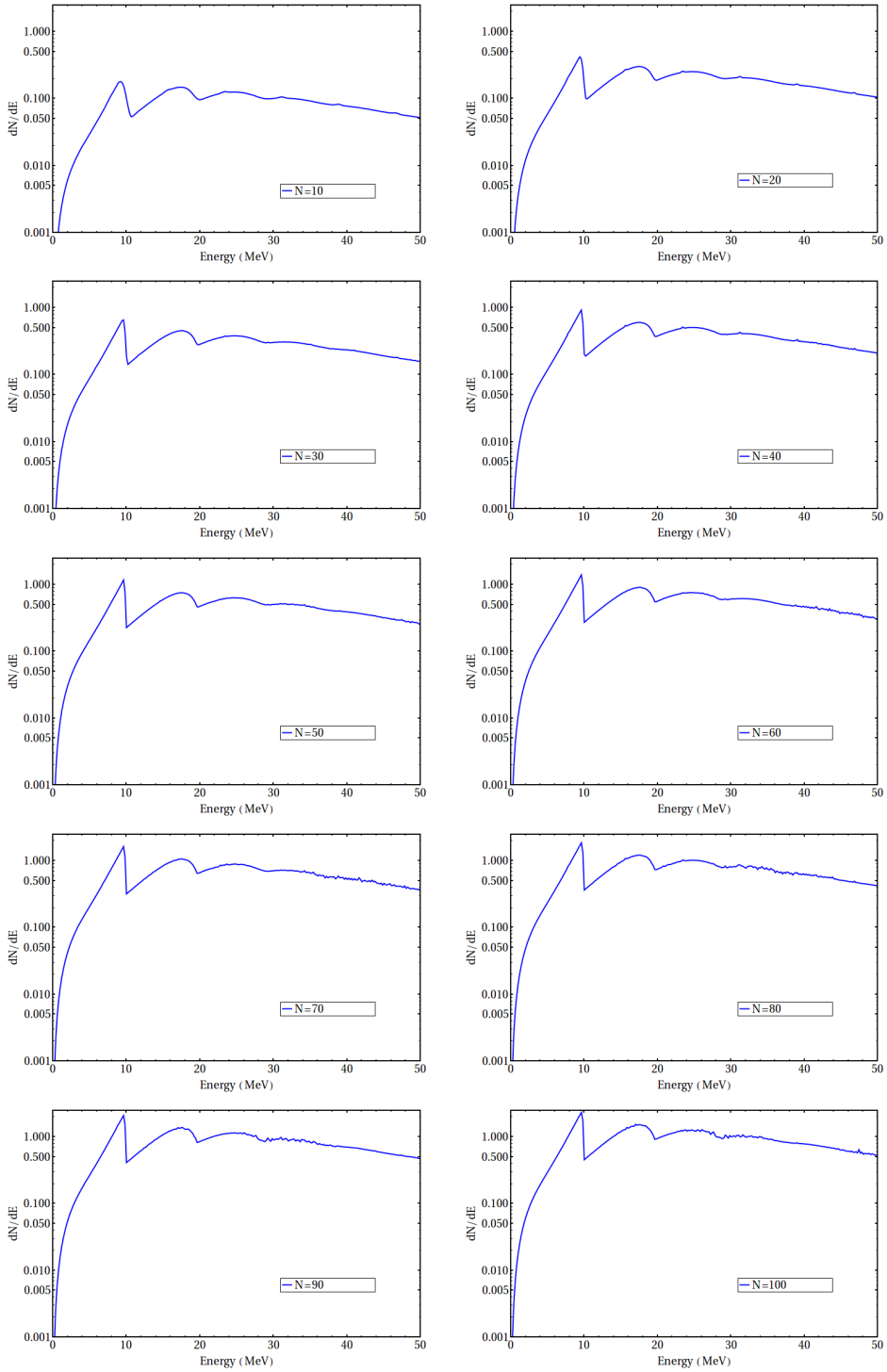

Figure 5.15: Plots showing spectra produced by a 150 GeV electron travelling through an undulator with $K = 0.92$ and $\lambda_u = 11.5\,\text{mm}$. Each plot shows the spectra produced by a different number of periods starting with $N = 10$ up to $N = 100$.

5.6 Tapering Undulators

The trajectory of the electrons through the undulator is affected by errors in the undulator period and field strength. This is a problem considering that there are approximately one hundred undulator modules in the undulator-based positron source. Therefore some form of trajectory correction is required. The initial solution that was proposed was to use corrector magnets to steer the beam back on to the axis of the undulator. These are already in the undulator lattice as, even with an ideal undulator, the ability to steer the beam is required. This is because helical undulators have a small region at the start and end where there is only magnetic field in one plane (due to the phase difference between the x and y magnetic fields). This region kicks the electron off-axis and so the beam has to be injected at an angle if the electron is to travel along the axis of the undulator.

Figure 5.16 shows the calculated trajectory of a 150 GeV electron travelling through the undulator prototype constructed at Rutherford Appleton Laboratory. The injection angle of the beam into the undulator module has been calculated such that the beam exits the undulator with a transverse position as close to the one it entered as possible. The largest issue with this technique is that the electrons are no longer travelling along the centre of the undulator the predicted spectrum is no longer correct due to the change in trajectory dominating the oscillations caused by the helical field.

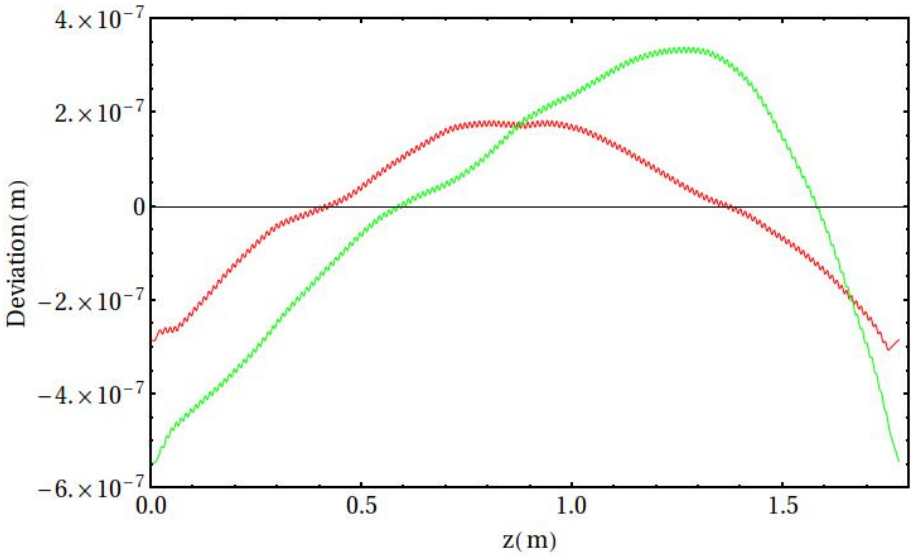

Figure 5.16: Plot showing the x (red line) and y (green line) positions of a 150 GeV electron travelling through the undulator prototype constructed at Rutherford Appleton Laboratory. The electron has been injected off-axis to ensure the electron leaves the undulator at the same position it entered.

Each undulator will have a different field map and so the steering needs to be calculated on a module by module basis. This is potentially a large problem as there is no room within

the lattice for steering magnets between the two undulator modules within a cryomodule. This means that the steering needs to be calculated to ensure the electron beam is able to traverse two modules correctly.

In order to simplify this issue a tapering undulator design is proposed. By having the on-axis magnetic field increase linearly from zero to the required field in a short distance at the start of the undulator and then linearly decrease back to zero at the end of the undulator, the effect of injection and extraction kicks are minimised. Figure 5.17 shows the proposed field map. The length of the taper can be determined through simulation. Using the conclusions from the work on the interference length of the undulator we know that the contribution to the synchrotron radiation produced by the taper will just be dipole-like. This is because the taper gradient is such that no two consecutive periods have the same magnetic field value.

Tapering has an impact on the overall flux of the undulator as the radiation produced in the taper is not as intense as the radiation from the rest of the undulator. The radiation in the main part of the undulator is of a higher intensity due to the effect of constructive interference. This means that in a tapering undulator the *active length* needs to be considered as the length of the undulator minus the length of the tapers. This means that for an undulator that is 155 periods long with tapers 15 periods long the active length is 80.6% of the undulator length.

Figure 5.18 shows the trajectory of a 150 GeV electron travelling through an ideal and non-ideal tapering undulator with $K = 0.92$, $\lambda_u = 11.5\,\text{mm}$ and $N = 155$ where the tapers are 15 periods long at each end. There is a difference in the x and y trajectories as there is still a kick in x that has not been fully cancelled in either the ideal or non-ideal case. The electron trajectory for an ideal undulator is as expected: the electron corkscrews around the central axis of the undulator with the radius of the trajectory proportional to the magnetic field. As the field at the start and end of the undulator is very small this means that the kicks due to injection and extraction are minimised.

The trajectory through a non-ideal undulator is greatly improved; although there are still variations in the centre position of the helical trajectory the electron no longer moves such a large distance off-axis as was the case without tapering. This means that steering magnets are not required between the two undulator modules inside the cryostat.

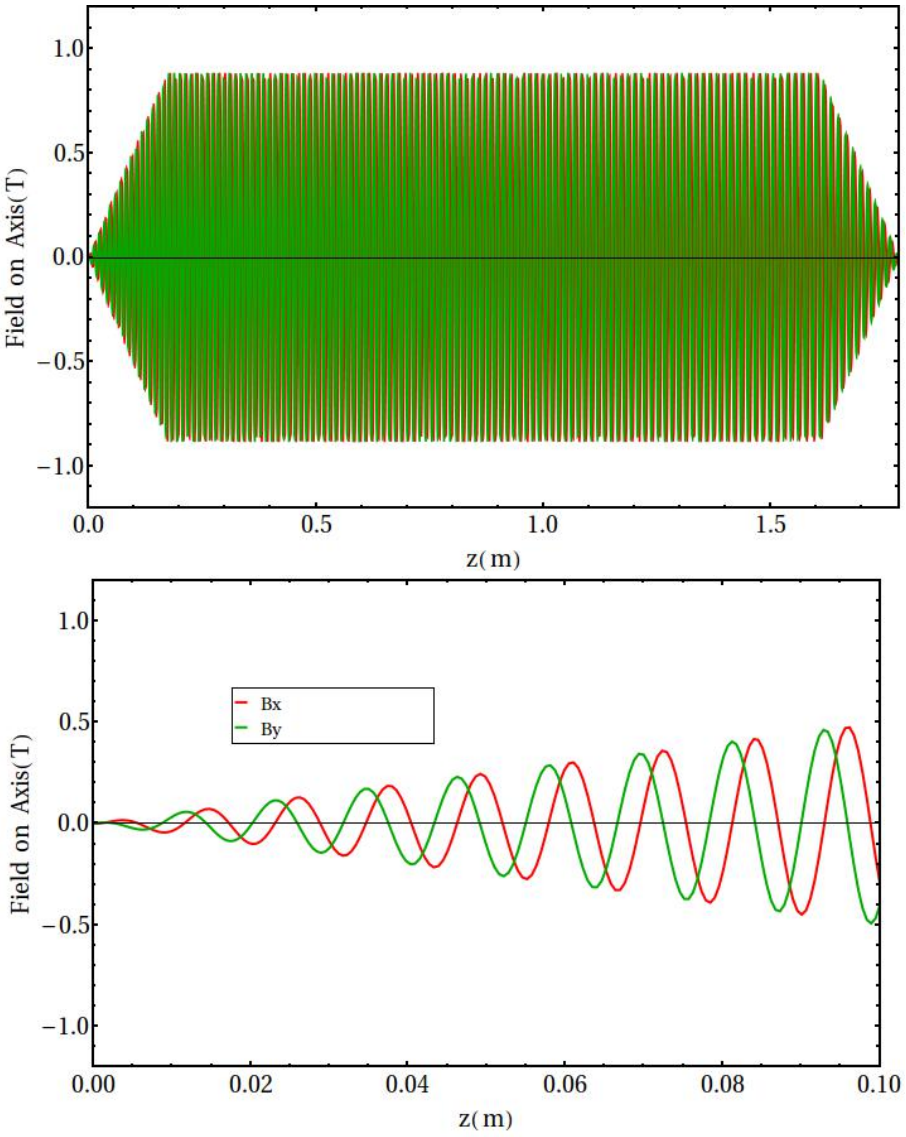

Figure 5.17: Plots showing the tapering undulator magnetic field map. The red line shows the B_x field profile and the green line shows B_y field profile. The lower plot shows a detailed view of the taper at the start of the undulator.

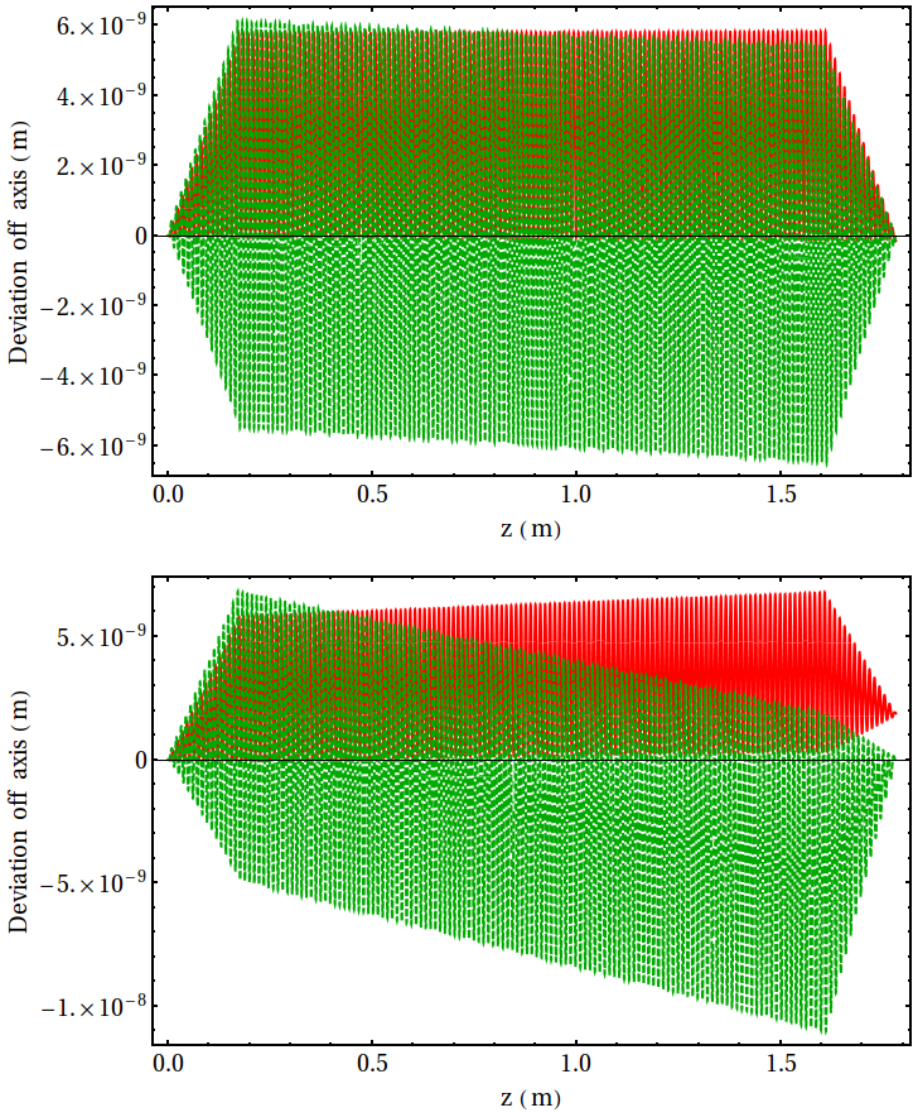

Figure 5.18: Plots showing the trajectory of a 150 GeV electron through ideal and non-ideal tapering undulator magnetic field maps with $K = 0.92$, $\lambda_u = 11.5\,\text{mm}$ and $N = 155$. The red line shows the x position and the dashed green line the y position of the electron. The upper plot is for an ideal tapering undulator and the lower plot is for a non-ideal tapering undulator

5.7 Variable Period Undulator

An idea based on the research conducted into the *interference length* of an undulator is a *variable* or *growing period* undulator. The idea behind this is that having a small number of periods is favourable as it smooths out the harmonic peaks present in the undulator spectrum. However having short undulators is problematic as it increases the overall length of the undulator portion of the undulator-based positron source.

By designing the undulator such that the period of the undulator varies along its length we can create effectively a number of short undulators superimposed on each other. The rate of change in the period affects the effective interference length of the multiple superimposed undulators. Having a fast-changing period is equivalent to having many very short undulators whilst a slower-changing period means there are fewer longer undulators. If the rate of change in period is slow the radiation produced approaches that produced by a non-ideal undulator.

The variation in period investigated is given by

$$\lambda_u = \lambda_0 \left(1 + \frac{z}{nL}\right) \tag{5.2}$$

where λ_0 is the size of the first period in the undulator, L is the length of the undulator, z is the position along the length of the undulator and n is a parameter describing how rapidly the period changes along the length of the undulator.

The simulated undulator is 155 periods long including two 15 period tapers. The maximum magnetic field is 0.86 T and the initial period, λ_0 is 11.5 mm. Figure 5.19 shows the magnetic field map of such an undulator.

The trajectory of a 150 GeV electron through a *growing period* undulator with the field map shown in figure is plotted in figure 5.20. The period of the oscillation varies with the period of the undulator as expected. The radius of the oscillations, outside of the taper regions, increases along the length of the undulator. This is due to amplitude of the electron trajectory being proportional to K. As K is proportional to the period of the undulator the amplitude of the oscillations increases with the period.

Figure 5.21 shows the spectra produced by a 150 GeV electron travelling through *growing period* undulators with different values of n. As the value of n increases the rate of change in period decreases and the spectrum becomes closer to the ideal spectra. Having a very rapidly-changing period, $n = 1$, results in a spectra that is very smooth with no discernible harmonics. For $n = 2$ the first harmonic becomes visible however the harmonic is at a much lower photon energy than the ideal spectrum. It is only when $n > 4$ that multiple harmonics start to appear. In terms of spectrum shape the one that shows most promise of achieving a high positron production

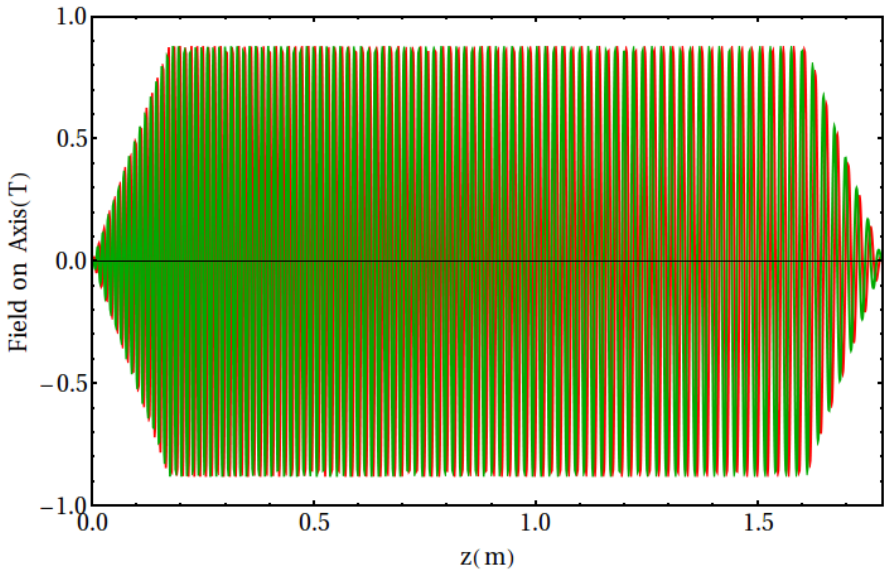

Figure 5.19: Plot of the field map for a growing period undulator. The maximum magnetic field is 0.86 T and the initial period, λ_0 is 11.5 mm. The B_x component is shown in red and the B_y component is in green.

efficiency is $n = 4$. However at 150 GeV it is further from the optimal spectrum than that produced by an ideal undulator. This undulator would not work in a positron source with a drive beam energy of 150 GeV. Increasing the drive beam energy shifts the photon energy range closer to the optimal photon spectrum. Therefore this type of undulator may be a good choice for the ILC high-energy upgrade or for an undulator-based positron source at CLIC.

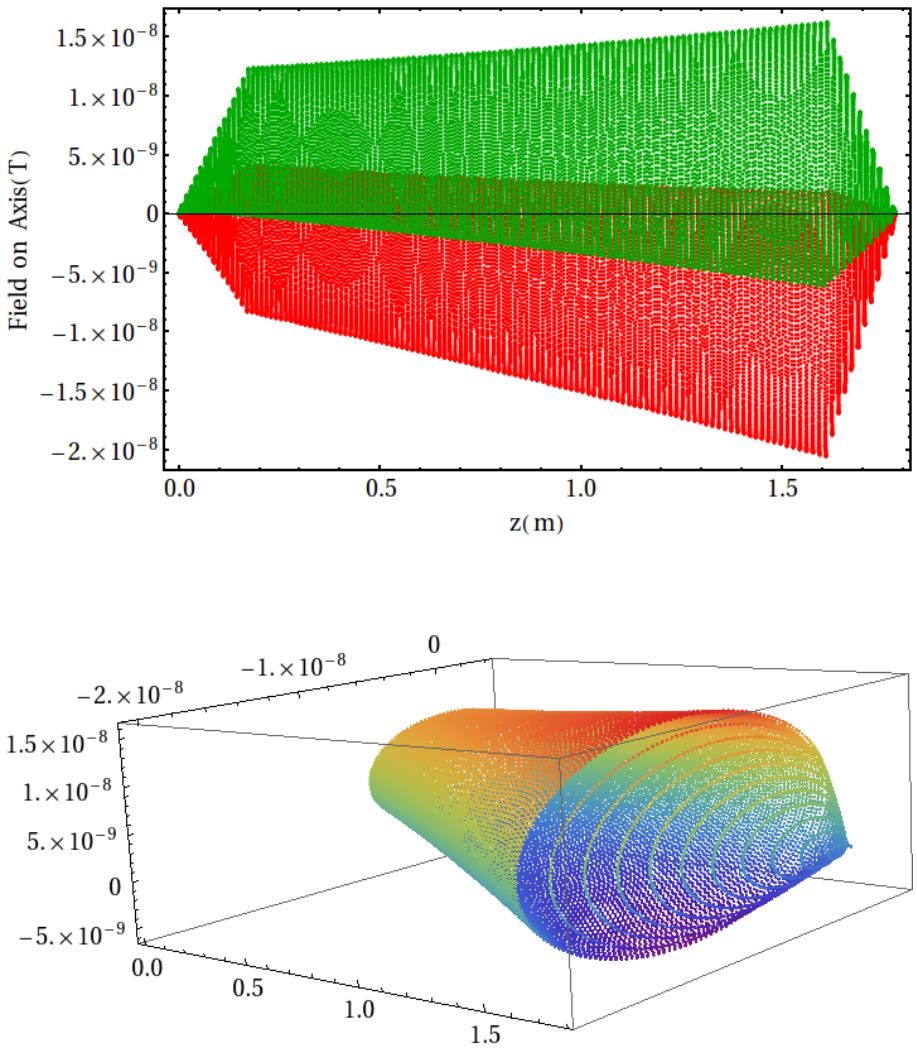

Figure 5.20: Plots showing the trajectory of a 150 GeV electron through a growing period undulator with the field map shown in figure 5.19. The upper plot shows the x component of the trajectory in red and the y component in green. The lower plot shows a 3D representation of the trajectory.

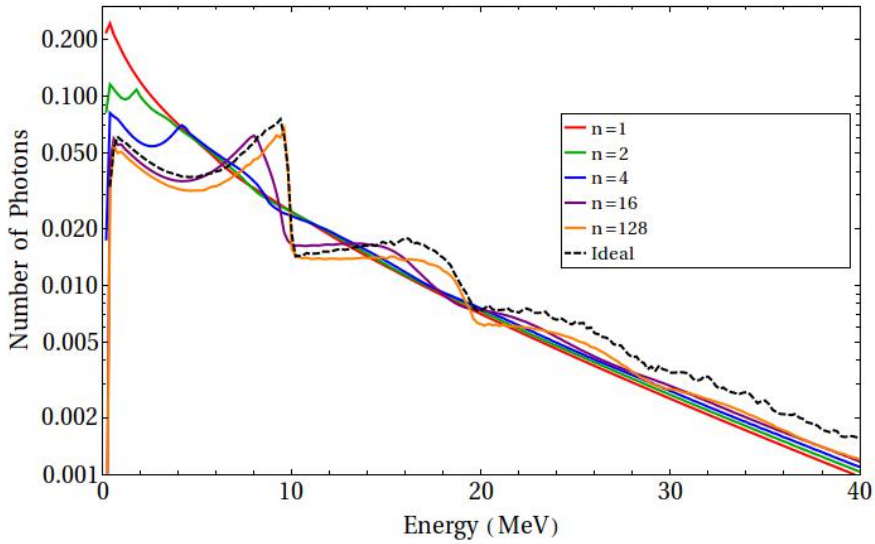

Figure 5.21: Plot showing the spectra produced by a 150 GeV electron travelling through *growing period* undulators with different values of n. As a comparison the spectrum from an ideal undulator with $\lambda_u = 11.5\,\text{mm}$, $K = 0.92$ and $N = 155$ is plotted as a black dashed line.

5.8 A Multi K Undulator

The *growing period* undulator study did not result in a photon spectrum that would be useful in terms of optimising the efficiency of an undulator-based positron source over a large range of drive beam energies. Considering the work done on comparing NbTi and Nb_3Sn undulators and the effect that changing the K value has on the undulator photon spectrum, a multi K undulator design was developed.

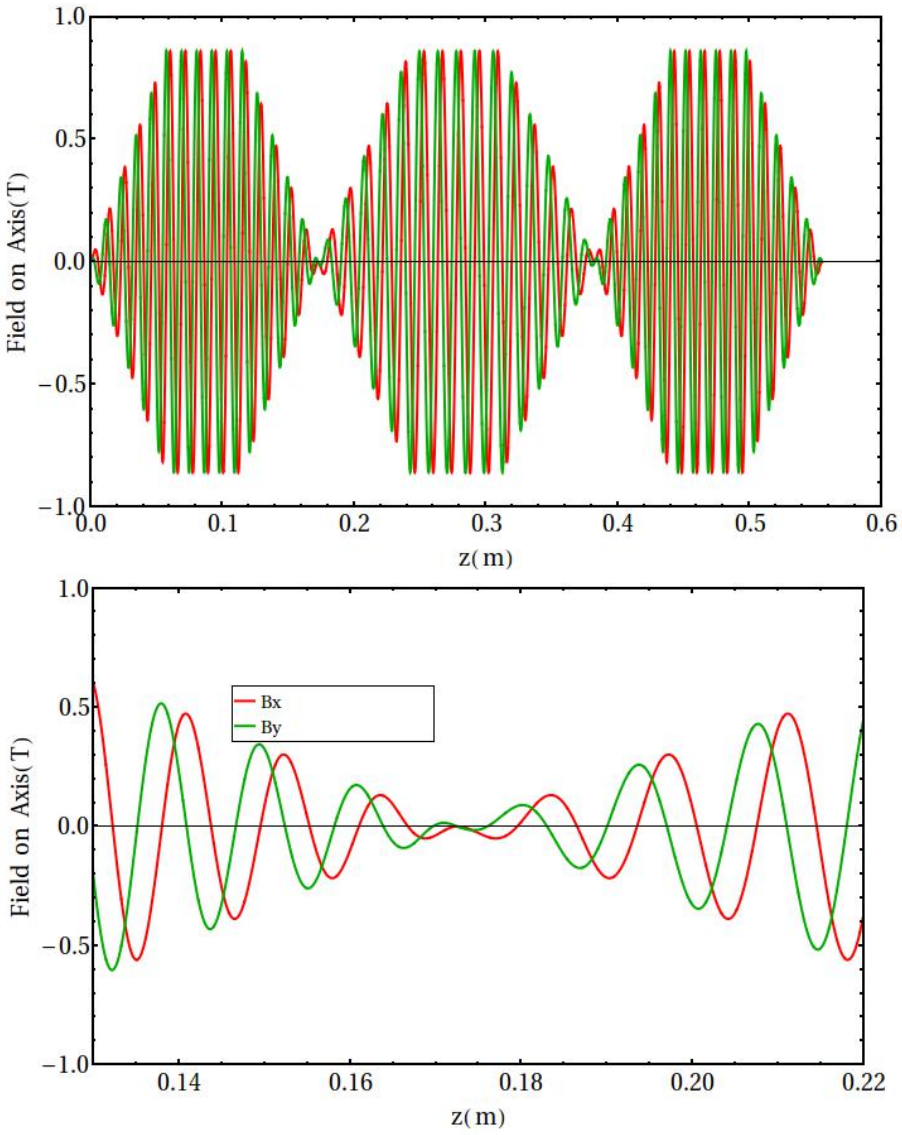

Figure 5.22: Plots showing the B_x component (red line) and the B_y component (green line) of the magnetic field in a multi K undulator. The upper plot shows the overall field map and the lower plot shows how the field between two tapers is designed to ensure there are no discontinuities.

This design uses tapering to allow short lengths of undulator to be joined together even though the adjacent undulators have different K values. An example of such an undulator field map is shown in figure 5.22. The short undulators in this field map are 15 periods long. The first 5 periods are a taper section with increasing field along the taper. Then there are 5 periods with

the maximum on-axis field and finally the last 5 periods are a taper with decreasing magnetic field along the taper. The lower plot in figure shows how the two taper regions between undulators with different K values are design so that there is no discontinuity in the field.

There are numerous variations possible for a multi K undulator. Some of the variables available in terms of designing a multi K undulator are:

- The length of the short undulators.
- The number of different K values used.
- The K value of the undulators.
- How K is changed; changes in B, λ_u or both.

A number of different configurations were studied and the most promising in terms of producing a photon spectrum that is better for positron production than the ideal undulator spectrum was to use very short undulators. This is because the photon spectrum does not develop the sharp harmonic peaks and so the the region with increased flux is broader (see section 5.5).

From the modelling of NbTi and Nb_3Sn undulators there is a maximum limit on the on-axis magnetic field that can be achieved with a given period. To ensure that the multi K undulators would be below this limit a decision was taken to limit the peak on-axis field to 0.86 T which is the maximum operating magnetic field strength of a NbTi undulator with a period of 11.5 mm.

Figure 5.23 shows photon spectra produced by a multi K undulator consisting of a section with $\lambda_u = 11.5\,\text{mm}$ and $K = 0.92$ followed by a section with $\lambda_u = 14.0\,\text{mm}$ and $K = 1.12$, finally a third section which is the same as the first. The upper plot shows the spectra produced by a 150 GeV electron and the lower plot the spectra produced by a 250 GeV electron. In order to be compared with the spectrum produced by an ideal undulator with the ILC baseline parameters the spectra have been normalised.

The spectrum produced by this multi K undulator is very similar to the spectra from a non-ideal undulator. However, the principle advantage of the multi K undulator is that it produces a photon flux comparable to that from a non-ideal undulator whilst being much shorter. The standard ILC undulators are 155 periods long which means the active length of the undulator is 1.47 m. The multi K undulator simulated here is only 45 periods long which has an active length of 0.555 m. This means that the undulator could be made much shorter. Although the active length of the multi K undulator is 37.8 % that of the non-ideal undulator the physical length would be roughly half that of the ILC undulator due to the other hardware that is required to power the undulator and provide mechanical support.

In addition to the reduction in length the most promising features of the shape of the photon spectra are that the first and second harmonics have been broadened out and the first harmonic

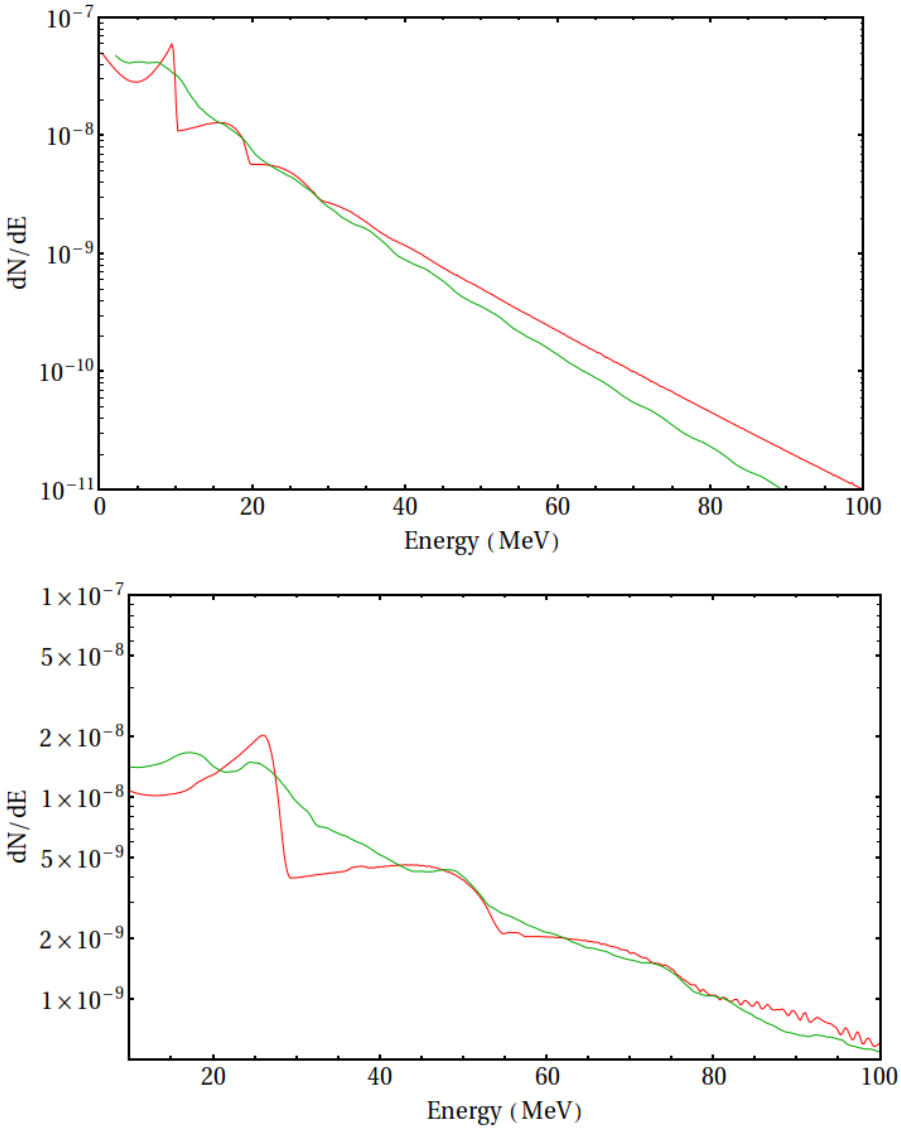

Figure 5.23: Plots comparing the photon spectrum produced from a multi K undulator with that produced from an undulator with parameters matching the ILC TDR. The ILC undulator spectrum is the red line and the multi K undulator spectrum is the green line. The upper plot shows spectra produced by a 150 GeV electron and the lower plot the spectra from a 250 GeV electron.

peak value reduced. This means that for the spectra from a 150 GeV electron the photon flux from a multi K undulator is higher than that produced by the ILC undulator in the 10 to 23 MeV energy range. Although this is not the optimal energy range for positron production, it is an improvement. However the spectra produced by a 250 GeV electron is much closer to the optimal. The multi K undulator spectrum produces a photon flux that is greater than or equal to the flux from the ILC undulator in the 27 to 60 MeV energy range. This is the energy regime in which the positron source is most efficient at converting photons into capturable positrons.

The photons produced by a helical undulator are circularly polarised. This is important as the polarisation of the photons is transferred to the positrons they produce. Positron polarisation is important as it increases the effective luminosity and can reduce the background on certain interactions. The photon polarisation, P_{e^+}, is calculated by the following equation:

$$P_{e^+} = \frac{N_L - N_R}{N_L + N_R} \tag{5.3}$$

where N_L is the number of left handed photons and N_R is the number of right handed photons. Using this equation we can calculate the photon polarisation as a function of photon energy.

Figure 5.24 shows the the photon polarisation from the multi K undulator compared to the polarisation produced from the ILC undulator. The red line shows the photon polarisation from the ILC undulator and the green line the polarisation from the multi K undulator. The upper plot shows the polarisation of the photon spectrum produced by a 150 GeV electron and the lower plot the polarisation of the photon spectrum produced by a 250 GeV electron.

The positron polarisation is discussed in terms of the average polarisation in a positron bunch. Therefore the important considerations are not just the peak polarisation value but spread in the photon polarisation. The photon polarisation from a multi K undulator has a lower peak value than the ILC undulator. The ILC undulator polarisation increases as the photon energy gets closer to the harmonic cut off before decreasing rapidly at the cut off. In comparison the polarisation from the multi K undulator increase up to a maximum value at the first harmonic then decreases very slightly. This means that at photon energies higher than the first harmonic cut off energy the polarisation from a multi K undulator is greater than or equal to the polarisation from the ILC undulator. A multi K undulator will produce a higher average positron polarisation which will increase the effective luminosity.

A multi K undulator is a very promising design in terms of producing positrons with high polarisation. This combined with the increased photon flux in the optimal positron production energy regime means that a multi K undulator should be a significant step in optimising an undulator-based positron source.

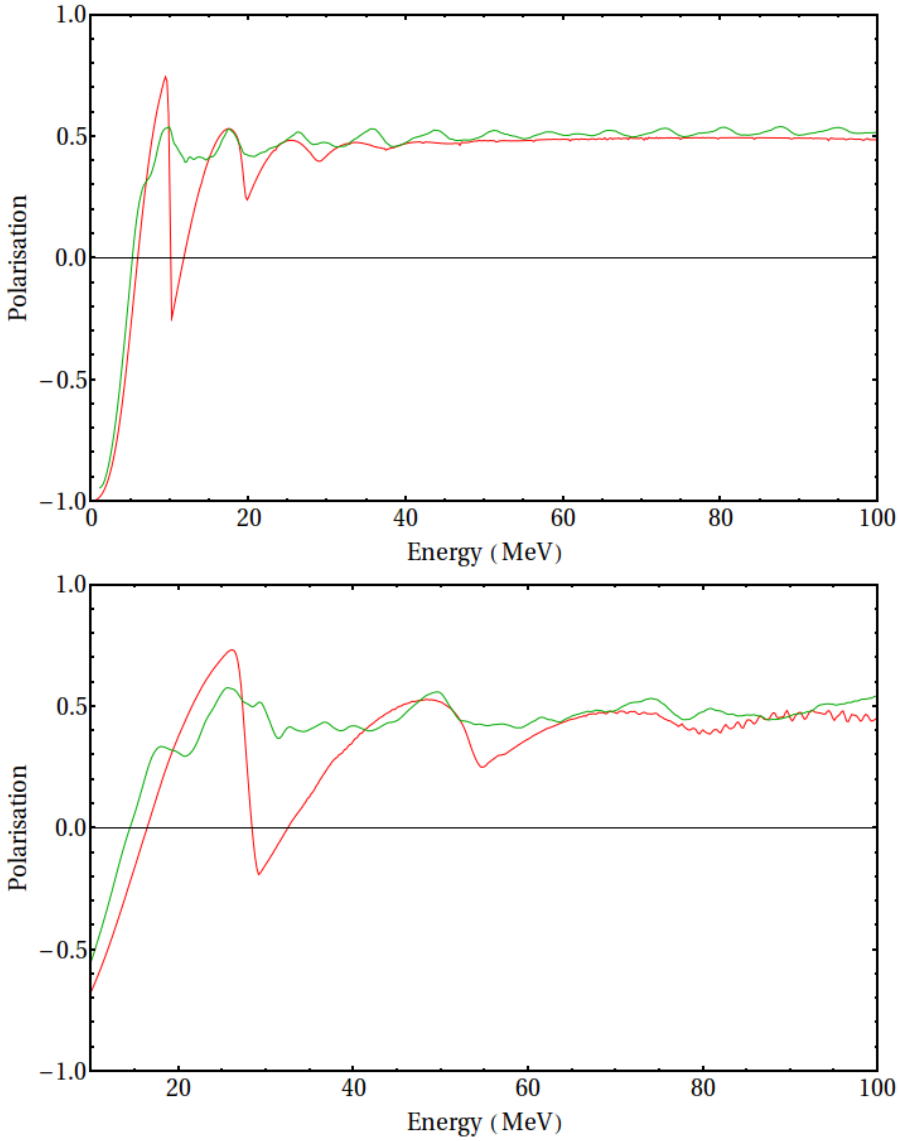

Figure 5.24: Plots comparing the photon polarisation, calculated using equation (5.3), as a function of photon energy produced from a multi K undulator with that produced from an undulator with parameters matching the ILC TDR. The ILC undulator photon polarisation is the red line and the multi K undulator photon polarisation is the green line. The upper plot shows spectra produced by a 150 GeV electron and the lower plot the spectra from a 250 GeV electron.

5.8.1 Non-Ideal Multi K Undulator

The photon spectrum from a multi K undulator has some interesting features which suggest it may provide benefits over a standard undulator when it comes to positron production. To investigate the effect errors had on the undulator spectrum a series of simulations were carried out. The errors applied to the multi K undulator were of the same order of magnitude as those measured in the ILC prototypes constructed at Rutherford Appleton Laboratory. The photon spectrum resulting from these simulations is shown in figure 5.25.

Introducing errors into the multi K undulator field map does not have a significant effect on the shape or the flux produced from the undulator. The errors seem to smear out the photon spectrum leveling some of the peaks due to the harmonics. This result is not unexpected based on the work on the interference length of the undulator presented earlier. Introducing errors into an ideal field map has the effect of reducing the interference length of the undulator. As the multi K undulator was designed to have shorter interference lengths than the ILC TDR undulator the impact of shortening these even further is lessened. To fully understand whether the magnitude of the errors assumed for the multi K undulator are valid a multi K undulator prototype would need to be constructed and then the field measured using a Hall probe as was done for the ILC undulator prototypes.

5.9 Summary

Using software developed at Daresbury Laboratory a number of studies into the radiation produced by the undulator in an undulator-based positron source have been conducted. During the course of these investigations a number of new features were added to HUSR by the author in order to improve the accuracy of the simulations. This resulted in HUSR having a better than 99.98 % agreement to the analytical equation for radiation produced by a perfect helical undulator derived in section 3.4.3.

Having benchmarked HUSR to ensure accuracy a number of studies were conducted to determine the effect of non-ideal undulators on the photon spectrum. The non-ideal helical undulator produced a photon spectrum that is closer to an optimal photon spectrum for positron production than the ideal spectrum. To understand why this is the case research which led to an interesting conclusion regarding the length of an undulator. Increasing the length of an undulator past twenty periods does not affect the shape of the photon spectrum only the flux produced.

Using this it was attempted to optimise the photon spectrum shape by controlling the *interference length* of the undulator which resulted in two new designs, a *growing period* undulator and a multi K undulator. Of these the multi K undulator shows more promise in terms of

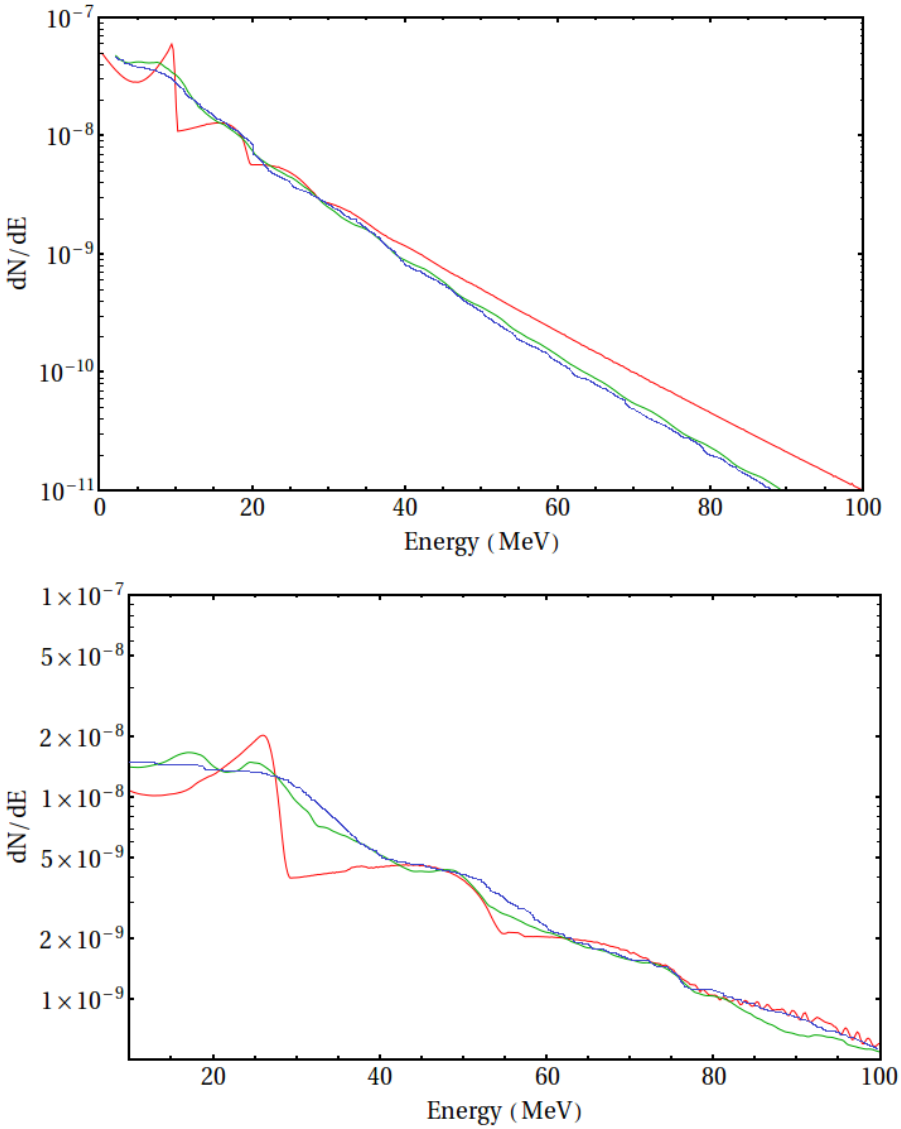

Figure 5.25: Plots comparing the photon spectrum produced from a non-ideal multi K undulator with those from an ideal multi K undulator and an undulator with parameters matching the ILC TDR. The ILC undulator spectrum is the red line, the ideal multi K undulator spectrum is the green line and the non-deal multi K undulator is the blue line. The upper plot shows spectra produced by a 150 GeV electron and the lower plot the spectra from a 250 GeV electron. Plotted using Mathematica 10.

positron production. The photon spectra from the multi K undulator design will be used in a simulation of the positron source to determine how effective it is at positron production.

Chapter 6

Optimising an Undulator-Based Positron Source for the ILC

The undulator-based positron source is the baseline positron source for the ILC. Therefore the research into optimising the positron source for the ILC focused on the undulator-based source. This chapter presents simulations of the undulator-based positron source at the ILC conducted using PPS-Sim. The design of PPS-Sim is explained in section 6.1. Results from simulations for different configurations of the undulator are then presented.

First simulations of a source matching the ILC TDR parameters were conducted to ensure that the results were consistent with those in the TDR. The natural extension to this work was to then investigate the effect of using the photon spectrum from a non-ideal undulator. After investigating the ILC TDR parameters, work was conducted into how to achieve high positron polarisation. Finally the spectra from the multi-K undulator design (discussed in chapter 5) is used to determine how effective such an undulator would be for positron production at the ILC.

When analysing the results from these simulations we are mainly concerned with the number of positrons that exit the source and are within the longitudinal and transverse acceptance of the ILC damping ring. This number will be referred to as the positron yield and is given in e^+/e^-. To calculate this we calculate e^+/γ which is done using PPS-Sim and γ/e^- which is done using the photon spectrum. The other key result is the longitudinal projection of the positron polarisation. Only the longitudinal projection is of interest as the ILC has been designed to try and preserve longitudinal polarisation only. Therefore when discussing positron polarisation we mean the longitudinal projection of polarisation only.

6.1 Simulating an Undulator-Based Positron Source

In order to calculate the positron distribution that is produced from an undulator-based positron source we need to be able to simulate the different effects that all the components have on positron production, preferably in a single software package. The program that has been used to simulate the positron source in this thesis is PPS-Sim [71, 72]. PPS-Sim is an open source program originally developed at DESY in Germany. PPS-Sim was written as an interface to GEANT4[73] which is a Monte Carlo program designed to simulate particles passing through matter. PPS-Sim sets up all of the relevant geometries of the components of an undulator-based positron source and then uses GEANT4 libraries to perform the calculations that describe the tracking and interactions of particles within the positron source.

In order to provide a statistically-valid result all simulations in this chapter conducted using PPS-Sim are comprised of 25 *runs*. Each run consists of PPS-Sim generating 100000 photons on target using a different pseudo-random number seed. Due to losses in the collimator and production of wide angle photons that would miss the target 100000 photons on target requires the generation of approximately 125000 photons from the undulator. The actual number of photons required to produce 100000 photons on target depends on the undulator spectrum, pseudo-random number seed and the collimator radius. Of these the collimator radius has the biggest effect particularly for very small radii.

6.1.1 Undulator

PPS-Sim has three different methods of simulating the photons produced by an undulator. The default method for generating the undulator photons is using an analytic approximation. This methodology uses the equations for the photon spectrum from a helical undulator derived by Brian Kincaid [48]. Once the photon spectrum shape has been calculated, PPS-Sim uses a pseudo-random number generator to determine the angle and energy of a photon from the distribution described by the photon spectrum.

The second way PPS-Sim generates the photon distribution produced by the undulator is similar to the first method with the undulator spectrum shape being used to determine the energy of the produced photons and the angle of emission. However instead of using analytic equations to determine the photon spectrum PPS-Sim reads the photon spectrum from an external file and uses that to generate photons.

The final method was added to PPS-Sim by the author of this thesis for a specific simulation and this method is completely different to the first two. Instead of generating photons from a photon spectrum PPS-Sim can read in values for individual photon properties and this allows for

a photon distribution that has been created in another software package to be input into PPS-Sim. This method unlike the first two is not random and therefore allows the user to control exactly what properties the photons have.

6.1.2 Collimator

The collimator in PPS-Sim is represented by a geometric cut and a number recording the energy deposited in the collimator. When performing the particle tracking PPS-Sim determines whether a particular photon would pass through the collimator aperture that is given. If it does then the tracking continues however if the photon would not pass through the collimator aperture then the track ends and the energy of the photon is added to the energy deposited in the collimator. As the collimator does not have any extent within PPS-Sim it means that calculating the energy deposited within the collimator to a high accuracy is difficult as the photon tracks terminate and there is no electromagnetic showering simulated. This means that there is no chance of secondary particles being emitted from the collimator which could lead to an over estimation of the energy deposited in the collimator.

6.1.3 Target

PPS-Sim allows for a variety of target shapes and materials to be simulated. There is a wide range of material choice available with all the materials from the GEANT4 libraries as well as materials specifically implemented within PPS-Sim for the positron source simulations such as Ti6Al4V alloy.

The two main types of target geometry used within PPS-Sim are *rim* and *liquid* targets. The rim type target is based upon the prototype target wheel that was used in the eddy current experiment carried out at Daresbury Lab. The rim geometry has a fixed curvature corresponding to a 1 m diameter wheel and the width of the rim is fixed to be 40 mm. The rim thickness is a parameter chosen by the user.

The liquid target implemented within PPS-Sim is more complicated. This geometry uses two different materials one for the liquid target itself and one for the two thin windows at the start and end of the target which are used to hold the liquid in place. The liquid target is a cylindrical geometry with the radius and length of the target specified by user inputs. Although some simulations were done with the liquid target the work presented in this thesis uses the rim target geometry.

6.1.4 OMD

There are three optical matching devices implemented within PPS-Sim: a Quarter Wave Transformer (QWT), an Adiabatic Matching Device (AMD) and a Lithium Lens. The QWT and AMD (see section 4.4) have been implemented in PPS-Sim as a *surface* after the target, representing the area that the OMD would take up, and the magnetic fields that are used to capture and focus the positrons. The surface is used by PPS-Sim to determine which particle tracks would strike the OMD, these tracks are then terminated and the energy that would be deposited within the OMD by these particles is recorded.

The lithium lens is a optical matching device that is simply a rod of lithium with an electric current inside it which co-propagates with the particle beam and focusses the positrons[74]. Interestingly the lithium lens only focuses either positive or negatively charged particles not both which means that whilst it is focusing the positrons produced in the target it also defocusses the electrons that are produced. As the particle beam is travelling through the lithium it will heat and this means that the lithium will actually be molten. Therefore two boron nitride windows are required, one at each end of the lithium rod, to contain the liquid metal. Boron nitride was chosen as boron has a long radiation length, and hence a thin boron window will lead to very little energy deposition of the beam inside the window.

PPS-Sim simulates the lithium lens using a similar geometry set up as for the liquid metal target however the radius of the cylinder and the material of the rod and windows is *hard coded* within PPS-Sim. The user can specify the length of the lithium rod and the peak current in the lithium. As the lithium lens was not a baseline or alternative option for the optical matching device in the undulator-based positron source at either the ILC or CLIC very few simulations were completed using the lithium lens. The majority of simulations presented in this thesis use the AMD.

6.1.5 Capture RF

The capture RF implemented within PPS-Sim is very simple. The capture RF is represented by the electric and magnetic fields that would be present in the first capture RF cavity. This cavity is a standing wave cavity surrounded by a 0.5 T solenoidal magnetic field. Only the first RF cavity is included in the simulation as by the end of the first capture RF cavity the particle distribution should be stable and losses in the subsequent cavities are expected to be small. Additionally GEANT4 is not well suited to performing beam tracking in RF cavities and so the implementation of more capture RF cavities would reduce the performance of the code.

6.2 ILC TDR Positron Source Simulations

In order to simulate the ILC TDR positron source PPS-Sim was used. The parameters chosen for the various components of the positron source within PPS-Sim were those given in the ILC TDR. The undulator, target and damping ring parameters used were those for a drive beam energy of 150 GeV from table 4.5.

A collimator was used even though there is no collimator specified in the ILC TDR baseline source. As the collimator is implemented within PPS-Sim as a simple geometric cut the only parameter that was required was the collimator radius which was set to 20 mm. This was chosen as the target rim width is 40 mm. The reason for using a collimator is that there will need to be some form of machine protection system to ensure components downstream of the target are not affected by photons that would miss the target.

The optical matching device that was used for the simulations was the flux concentrator with parameters matching those from table 4.9. The fields representing the capture RF within PPS-Sim match those produced by cavities with parameters given in table 4.10.

6.2.1 Ideal Undulator Spectra

The ideal undulator photon spectra used in these simulations are shown in figure 6.1. The spectra have been calculated for two different drive beam energies, 150 GeV and 250 GeV, keeping the undulator parameters constant. Also shown is the photon polarisation as a function of photon energy. Using these spectra as input into PPS-Sim a number of simulations were conducted to calculate the positron yield and polarisation. In order to achieve accurate values the simulations were run multiple times changing the random number seed.

Table 6.1 shows the positron yield in terms of positrons per electron and the average positron polarisation at the two drive beam energies. The ILC positron source needs to achieve a flux of 1.5 positrons per electron to cope with positron losses throughout the machine and still maintain an equal flux of positrons and electrons at the interaction point[41]. The TDR expects a positron polarisation of 31% for a drive beam energy of 150 GeV.

Table 6.1: Table showing the positron yield and polarisation produced by the ILC TDR positron source for drive beam energies of 150 and 250 GeV.

	150 GeV	250 GeV
Positron Yield (e^+/e^-)	2.49 ± 0.01	4.56 ± 0.02
Positron Polarisation (%)	21.93 ± 1.39	16.88 ± 0.76
Positron Polarisation Spread(%)	16.65 ± 1.06	2.04 ± 0.09

The simulations show that the positron yield produced by this source matches the yield required by the ILC TDR. However the predicted polarisation does not match with the ILC

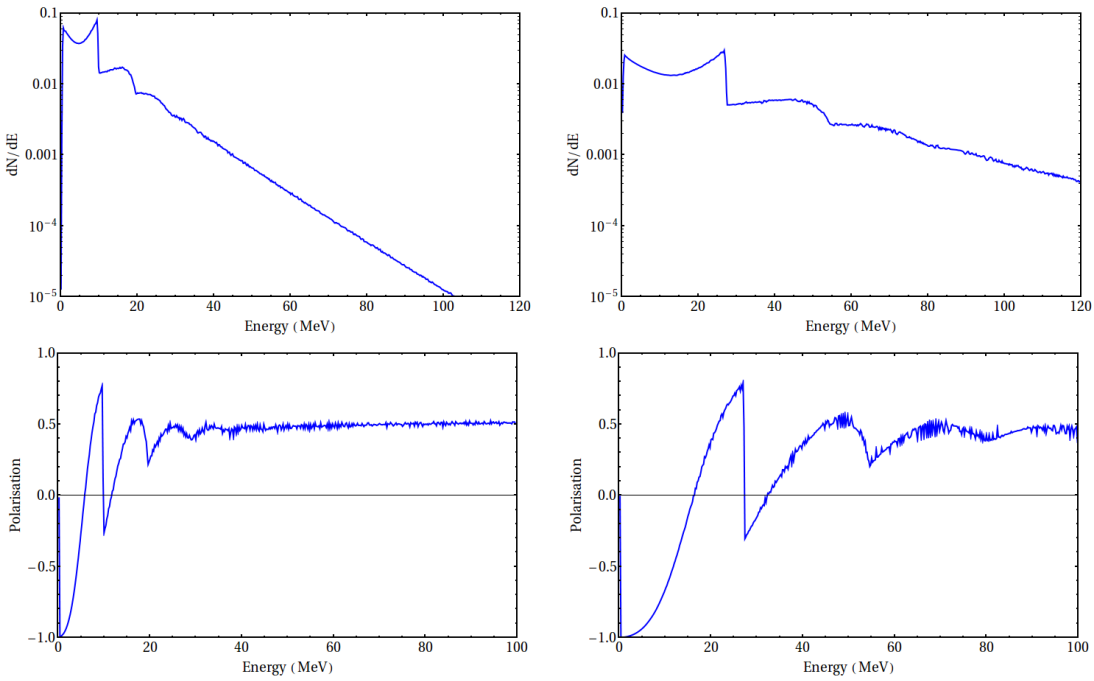

Figure 6.1: The photon spectra produced by an electron travelling through an ideal undulator with $N = 155$, $K = 0.92$ and $\lambda_u = 11.5\,\text{mm}$. The upper left plot shows the spectrum from a 150 GeV electron and the upper right plot shows the spectrum from a 250 GeV electron. The lower plots show the photon polarisation as a function of photon energy produced by a 150 GeV electron on the left and a 250 GeV electron on the right. Photon spectra were simulated using HUSR and plotted using Mathematica 8.

TDR value. The reason for this disagreement is not understood as PPS-Sim has been cross-checked repeatedly by the developers at DESY with other simulation codes used by the positron source community. This suggests that the difference in the predicted polarisation and the TDR value is to do with one of the assumptions made in the simulation. The most likely assumption that is behind this discrepancy is the collimator radius used in the simulation. The polarisation of the produced positrons is highly-dependent on the radius of the photon collimator and an earlier design of the undulator based positron source had a collimator radius of between 2 and 3 mm.

6.2.2 Realistic Undulator Spectra

The realistic or non-ideal undulator photon spectra used in these simulations are shown in figure 6.2. The spectra have been calculated for two different drive beam energies, 150 GeV and 250 GeV, keeping the undulator parameters constant. Also shown is the photon polarisation as a function of photon energy. These spectra are input into PPS-Sim to calculate the positron yield and polarisation.

Table 6.2 shows the positron yield in terms of positrons per electron and the average positron polarisation at the different drive beam energies. The realistic undulator photon spectrum pro-

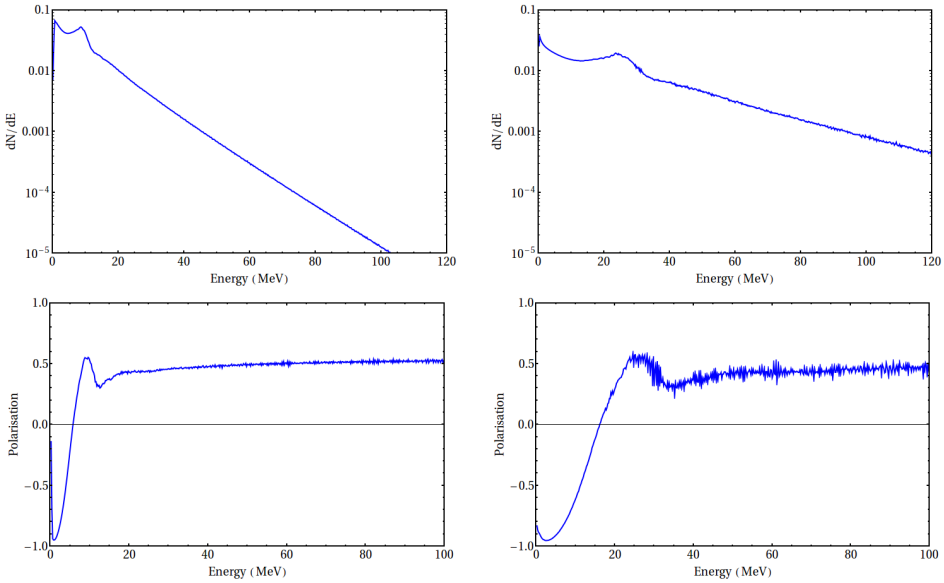

Figure 6.2: The photon spectra produced by an electron travelling through a non-ideal undulator with $N = 155$, $K = 0.92$ and $\lambda_u = 11.5\,\text{mm}$. The upper left plot shows the spectrum from a 150 GeV electron and the upper right plot shows the spectrum from a 250 GeV electron. The lower plots show the photon polarisation as a function of photon energy produced by a 150 GeV electron on the left and a 250 GeV electron on the right. Photon spectra were simulated using HUSR and plotted using Mathematica 8.

duces a higher yield of positrons than the ideal undulator photon spectra. This was predicted by the analysis of the spectra conducted in chapter 5.

Table 6.2: Table showing the positron yield and polarisation produced by the ILC TDR positron source using a non-ideal undulator spectrum for drive beam energies of 150 and 250 GeV.

	150 GeV	250 GeV
Positron Yield (e^+/e^-)	2.72 ± 0.04	4.73 ± 0.04
Positron Polarisation (%)	37.80 ± 2.29	19.66 ± 0.90
Positron Polarisation Spread(%)	17.44 ± 1.06	5.56 ± 0.26

The interesting effect is that the non-ideal spectra shows an increase in positron polarisation. However after more detailed study of the way the photon polarisation varies as a function of photon energy this makes sense. Figure 6.3 compares the photon polarisation from a 150 GeV electron traversing ideal and non-ideal undulators and figure 6.4 compares the photon polarisation from a 550 GeV electron traversing ideal and non-ideal undulators. The photon polarisation does not vary as dramatically with energy in a non-ideal undulator compared to the ideal undulator in the energy range corresponding to the first three harmonics of the undulator spectrum.

The effect this has on the distribution of photon polarisation is summarised in table 6.3. For non-ideal undulators the mean photon polarisation is higher than in the ideal case. Additionally the spread in polarisation is lower for non-ideal undulators. This explains why the positron polarisation increases when simulating the undulator-based positron source with a non-ideal undulator.

Table 6.3: Table comparing the photon polarisation produced by ideal and non-ideal undulators for drive beam energies of 150 and 250 GeV.

	Mean Polarisation (%)	Polarisation Spread (%)
Ideal Undulator (150 GeV)	17.26	21.80
Non-Ideal Undulator (150 GeV)	23.45	16.94
Ideal Undulator (250 GeV)	32.70	33.71
Non-Ideal Undulator (250 GeV)	35.09	31.38

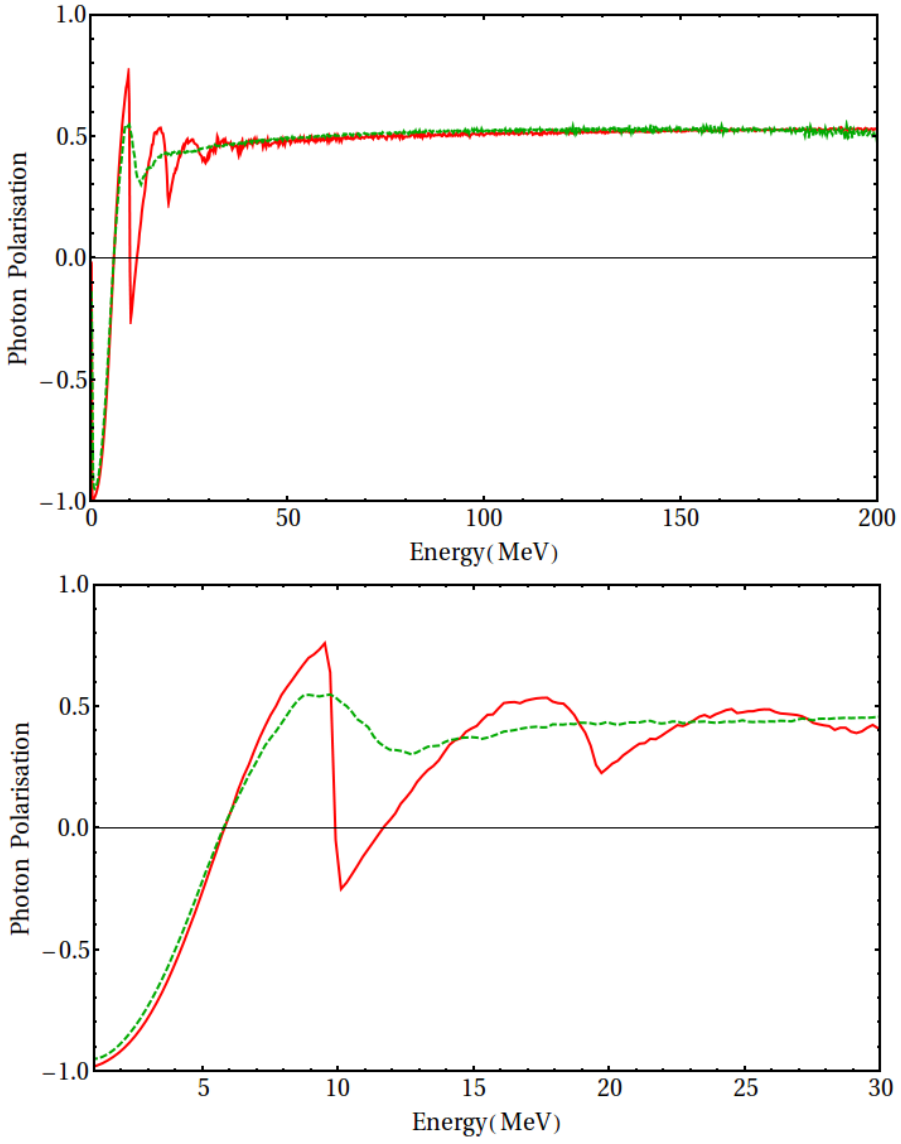

Figure 6.3: Plots comparing the photon polarisation due to a 150 GeV electron travelling through ideal and non-ideal undulators. The red line corresponds to the polarisation from an ideal undulator and the green dashed line the polarisation from a non ideal undulator. The upper plot shows the polarisation for photons with energies up to 200 MeV. The lower plot shows the photon polarisation in the first three harmonics. Photon spectra were simulated using HUSR and plotted using Mathematica 8.

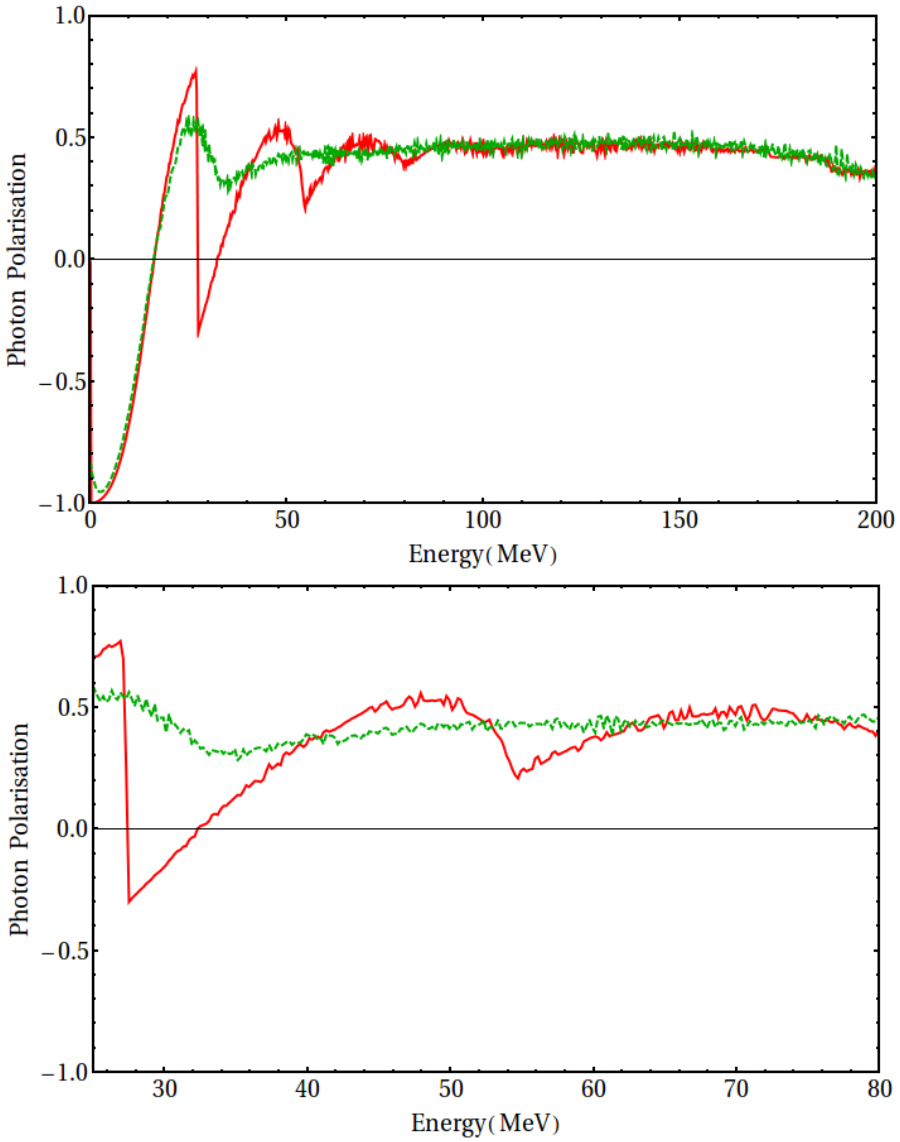

Figure 6.4: Plots comparing the photon polarisation due to a 250 GeV electron travelling through ideal and non-ideal undulators. The red line corresponds to the polarisation from an ideal undulator and the green dashed line the polarisation from a non ideal undulator. The upper plot shows the polarisation for photons with energies up to 200 MeV. The lower plot shows the photon polarisation in the second and third harmonics. Photon spectra were simulated using HUSR and plotted using Mathematica 8.

6.3 Collimation Effects on Positron Production

In order to explain the difference in polarisation a study into the effect of collimator radius on polarisation was conducted. Another key aim of this study was to investigate how the positron polarisation from a realistic undulator is affected by changing the collimator radius. This is important as the current method for achieving high positron polarisation is to tightly collimate the photon beam.

The spectra used for this simulation are those shown in figures 6.1 and 6.2. These were input into a positron source which matches the TDR parameters with the exception of the collimator radius which was varied between 1 and 20 mm in steps of 1 mm. Figure 6.5 shows how the positron yield changes with collimator radius for an ideal undulator. The positron yield after target is plotted for a 150 GeV drive beam (red circles) and with a 250 GeV drive beam (red diamonds). Also plotted is the yield in the ILC Damping ring with a 150 GeV drive beam (green square) and with a 250 GeV drive beam (green triangles).

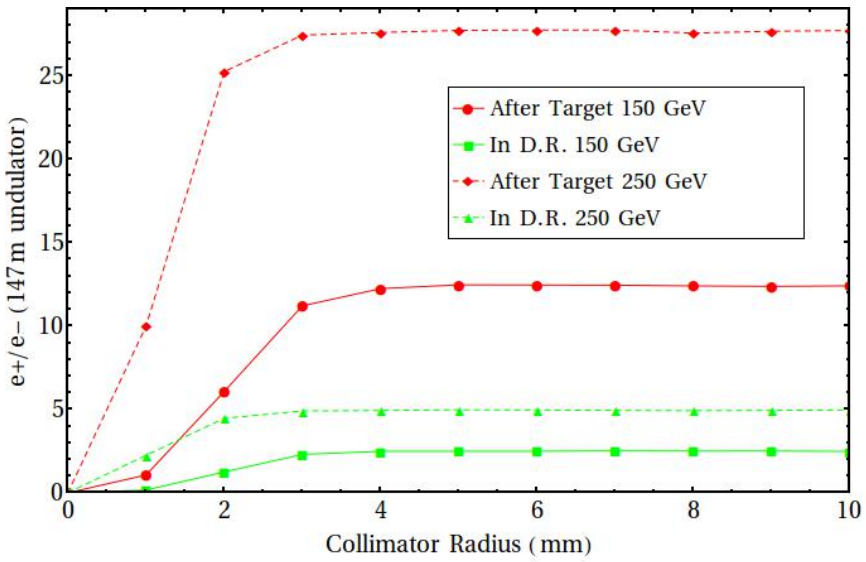

Figure 6.5: Plot showing how the positron yield changes with collimator radius for an ideal undulator. The positron yield is plotted for yield after target with a 150 GeV drive beam (red circles) and with a 250 GeV drive beam (red diamonds). Also plotted is the yield in the ILC Damping ring with a 150 GeV drive beam (green square) and with a 250 GeV drive beam (green triangles).

The positron yield only depends on the collimator radius when the radius is less than 3 mm. However when considering the usable positrons, the ones that are within the damping ring acceptance, the collimator radius does not have an effect on yield unless the radius is less than 4 mm. The positron polarisation corresponding to these yield results is shown in figure 6.6. The positron polarisation is plotted for yield after target with a 150 GeV drive beam (red circles) and with a 250 GeV drive beam (red diamonds). Also plotted is the polarisation in the ILC Damping

ring with a 150 GeV drive beam (green square) and with a 250 GeV drive beam (green triangles).

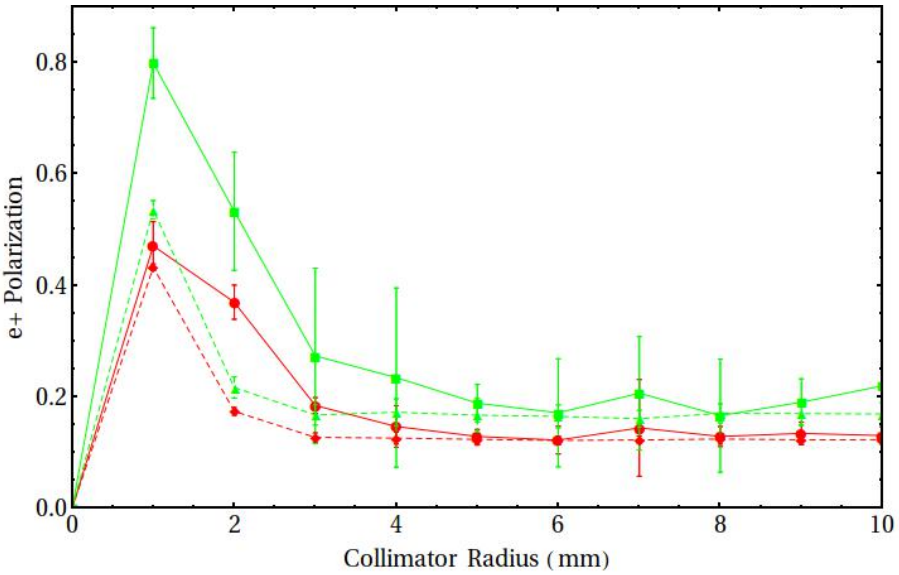

Figure 6.6: Plot showing how the positron polarisation changes with collimator radius for an ideal undulator. The positron polarisation is plotted for yield after target with a 150 GeV drive beam (red circles) and with a 250 GeV drive beam (red diamonds). Also plotted is the polarisation in the ILC Damping ring with a 150 GeV drive beam (green square) and with a 250 GeV drive beam (green triangles). The error bars represent the spread in positron polarisation.

For a collimator with a radius greater than 5 mm the polarisation can be considered to be constant. As the collimator radius decreases below 5 mm the polarisation increases. To achieve the polarisation required by the TDR these results suggest that the collimator radius needs to be between 2 and 3 mm. This suggests that the TDR source design work has been conducted with the collimator that was present in the ILC SB2009 design which had a radius of 2.3 mm.

The results from simulations using a non-ideal undulator which is closer to what will be present in a realistic source are shown in figures 6.7 and 6.8. The results after the target with a 150 GeV drive beam are plotted as red circles and with a 150 GeV drive beam are plotted as red diamonds. The results for positrons in the damping ring acceptance with a 150 GeV drive beam are plotted as green square and with a 150 GeV drive beam are plotted as green triangles. As a result of the simulations using an ideal undulator the maximum collimator radius was reduced to 10 mm.

Figure 6.7 shows how the positron yield changes with radius and although the general trend, increasing yield with radius, is the same as for the results from the ideal undulator the major differences are that the yield after target is nearly double the ideal and that the yield does not vary smoothly with collimator radius.

Figure 6.8 shows the positron polarisation results. These results are very different to the results from the ideal undulator. There appears to be no clear relationship between positron polarisation and collimator radius. Additionally the uncertainty on the polarisation is much

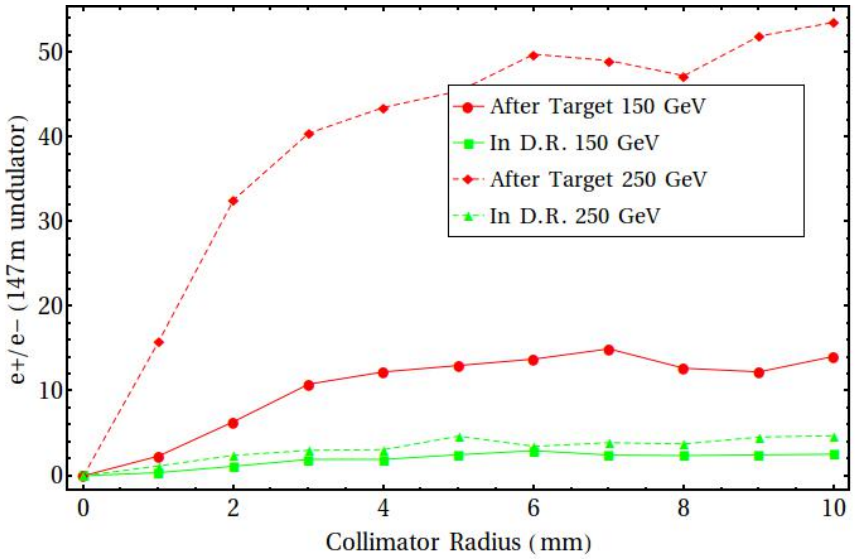

Figure 6.7: Plot showing how the positron yield changes with collimator radius for a non-ideal undulator.The positron yield is plotted for yield after target with a 150 GeV drive beam (red circles) and with a 250 GeV drive beam (red diamonds). Also plotted is the yield in the ILC Damping ring with a 150 GeV drive beam (green square) and with a 250 GeV drive beam (green triangles).

higher than in the ideal case. This means that the collimator is not a robust way to increase the polarisation.

This is due to the actual distribution of photons at the conversion target. Figure 6.9 compares the photon distribution at the target face for ideal and non-ideal undulator photon spectra with a drive beam energy of 150 GeV. The ideal undulator produces a distribution that peaks on-axis and decreases rapidly. The majority of the photon flux is within a circular region centred on-axis with a radius of 4 mm. This explains why the yield from an ideal undulator becomes constant when the collimator radius exceeds 5 mm.

In comparison the photon distribution from the non-ideal undulator peaks in an annulus and is at a minimum on-axis. The inner radius of the annulus where the distribution peaks is 1.5 mm which corresponds to an emission angle of K/γ. The region of high flux is also more extended than in the ideal case. These two factors explain why the yield curve is the shape it is: collimating tightly, < 2 mm, means that the majority of the flux is excluded and therefore the yield is very low. As the region of high flux extends to a radius of between 6 and 7 mm this explains why the yield increases until the collimator radius exceeds 7 mm.

Figure 6.10 shows the distribution of the photon polarisation at the conversion target from an undulator with a 150 GeV drive beam. The left plot shows the distribution from an ideal undulator and the right plot shows the distribution from a non-ideal undulator. As with the photon distribution, the polarisation distribution from an ideal undulator peaks on-axis and decreases rapidly until the polarisation goes negative at a radius of greater than 4 mm. This

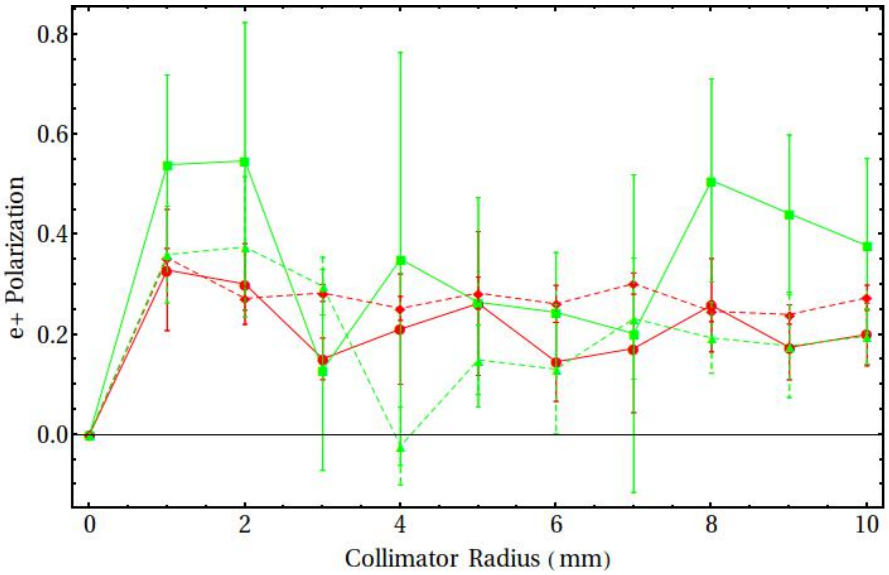

Figure 6.8: Plot showing how the positron polarisation changes with collimator radius for a non-ideal undulator. The positron polarisation is plotted for yield after target with a 150 GeV drive beam (red circles) and with a 250 GeV drive beam (red diamonds). Also plotted is the polarisation in the ILC Damping ring with a 150 GeV drive beam (green square) and with a 250 GeV drive beam (green triangles). The error bars represent the spread in positron polarisation.

shape explains the trends seen in the positron polarisation as when the collimator radius is less than 4 mm the polarisation increases as the radius decreases. With a radius above 4 mm the polarisation becomes constant as the negative and positive polarisations partly cancel out leaving a small net polarisation.

In the case of the realistic undulator the photon polarisation does not follow a simple trend. Instead the polarisation is negative on-axis and then increases to a maximum positive polarisation in an annulus with a radius of 1.5 mm before decreasing again. The polarisation then achieves a maximum negative polarisation in an annulus with a radius of 6 mm. The polarisation then levels out. This explains why the positron polarisation from this spectrum is relatively constant for a collimator radius of between 1 and 2 mm. After this the polarisation varies rapidly and does not become stable.

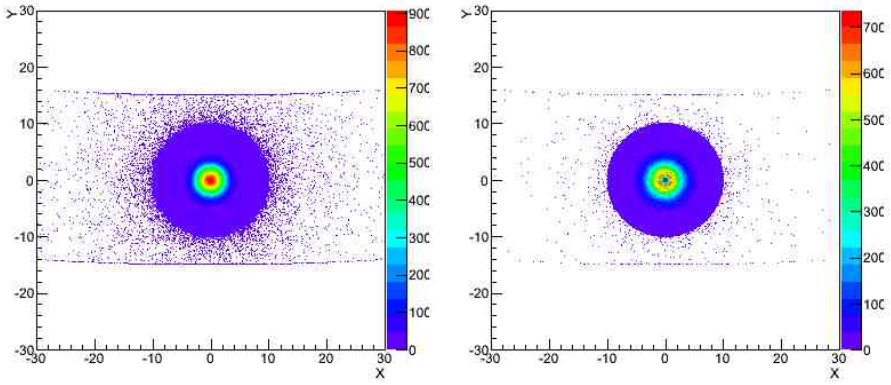

Figure 6.9: Plots showing the photon distribution at the conversion target from an undulator with a 150 GeV drive beam. The distribution from an ideal undulator is shown on the left and a non-ideal undulator on the right. The colour scale corresponds to the photon intensity with purple being low intensity and red high intensity. Plotted using Root[75].

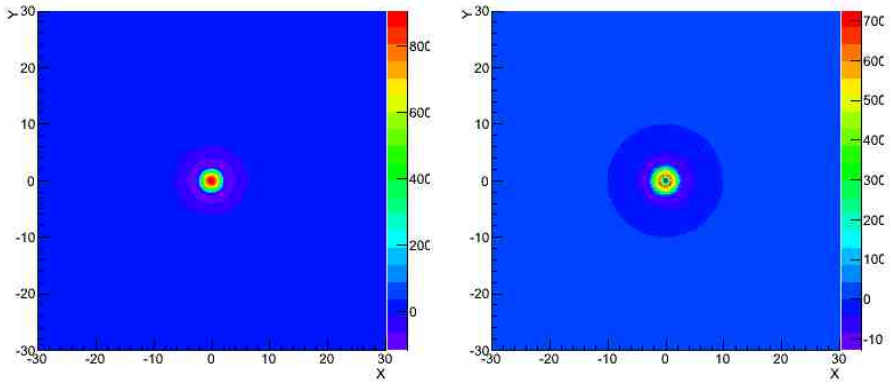

Figure 6.10: Plots showing the distribution of photon polarisation at the conversion target from an undulator with a 150 GeV drive beam. The distribution from an ideal undulator is shown on the left and a non-ideal undulator on the right.The colour scale corresponds to the total photon polarisation with purple being negative polarisation, blue zero polarisation and red high positive polarisation. Plotted using Root[75].

6.4 A Multi K Undulator at the ILC

Following the detailed study into producing an optimal photon spectrum for positron production discussed in chapter 5 simulations were done to determine how effective the multi K undulator spectra shown in figure 5.23 are at producing positrons at the ILC. A series of simulations were conducted in PPS-Sim using the TDR parameters for the target, flux concentrator and capture RF. A 20 mm radius collimator was used in the simulations. Simulations were conducted using the spectrum produced by a 150 GeV electron and a 250 GeV electron.

Table 6.4: Table showing the positron yield and polarisation produced from photons generated in a multi K undulator entering the ILC TDR positron source for drive beam energies of 150 and 250 GeV.

	150 GeV	250 GeV
Positron Yield (e^+/e^-)	2.46 ± 0.05	5.06 ± 0.02
Positron Polarisation (%)	41.93 ± 3.39	23.88 ± 1.06
Positron Polarisation Spread(%)	22.15 ± 3.06	7.04 ± 0.49

Table 6.4 shows the results of these simulations. Comparing them to the results from an ideal undulator (table 6.1) and a non-ideal undulator (table 6.2) we can see that the multi K undulator is more efficient at positron production for a 250 GeV electron beam. With the 150 GeV electron beam the multi K undulator produces a lower flux than the non-ideal undulator but a comparable flux to the ideal undulator. However the positron polarisation is comparable to that expected from a non-ideal undulator for both drive beam energies. This means that a multi K undulator such as that proposed in section 5.8 is a promising design for optimising polarised positron production at the ILC.

To determine the effect of a non-ideal multi K undulator on the positron yield and polarisation a series of simulations were carried out using the spectrum for an non-ideal multi K undulator shown in figure 5.25. The were conducted in PPS-Sim using the TDR parameters for the target, flux concentrator and capture RF. A 20 mm radius collimator was used in the simulations. Simulations were conducted using the spectrum produced by a 150 GeV electron and a 250 GeV electron. The results of these simulations are shown in table 6.5. The results are comparable to those of an ideal multi K undulator. However, it should be noted that the uncertainties on yield, polarisation and polarisation spread have increased. The positron yield at 150 GeV from a non-ideal multi K undulator is lower than the ideal case although it is still above the 1.5 positrons per electron level required.

Table 6.5: Table showing the positron yield and polarisation produced from photons generated in a non-ideal multi K undulator entering the ILC TDR positron source for drive beam energies of 150 and 250 GeV.

	150 GeV	250 GeV
Positron Yield (e^+/e^-)	2.41 ± 0.12	5.36 ± 0.17
Positron Polarisation (%)	43.82 ± 4.01	24.12 ± 1.86
Positron Polarisation Spread(%)	26.28 ± 3.71	7.36 ± 0.75

6.5 Summary

Using PPS-Sim a number of studies into an undulator-based positron source at the ILC have been conducted. The results from simulations of an ideal undulator-based positron source at the ILC have been compared with those conducted by other groups to ensure that the simulations are reliable. Using software that has not been available to the positron source community before we have simulated realistic undulator-based positron sources to estimate what we would expect if such a source was constructed.

Using the ideal and realistic simulations a study into polarised positron production at the ILC was conducted. Based on investigations into the effect of collimator radius on polarisation it appears that for a non-ideal photon spectrum collimating tightly to increase polarisation will not be successful. This means that a new method for increasing polarisation is required. One option is to use a multi K undulator to produce a spectrum that has higher average photon polarisation. The positron polarisation is up to 20 % higher than compared to the positron polarisation produced by an ideal undulator-based positron source.

Chapter 7

Novel Extensions to an Undulator-based Positron Source

Throughout the course of this PhD a number of interesting ways to evolve an undulator-based positron source have been briefly studied. Presented in this chapter are three of the more possible designs. These are a multi-target undulator-based positron source (this was presented at IPAC 2012 in New Orleans by the author of this thesis[76]), a positron amplifier and a Free Electron Laser (FEL) positron source. All three designs are in the very early stages of research and design.

7.1 Multi-Target Undulator-Based Positron Source

A multi-target positron source has been simulated using PPS-Sim. The layout of the multi-target source is shown in Figure 7.1. The 150 GeV electron drive beam passes through a helical undulator to produce a photon beam. This photon beam is incident on each target in turn producing electrons and positrons which are captured by an Optical Matching Device(OMD) and then accelerated up to 125 MeV by the capture RF. The positrons and electrons then enter a dipole magnet to separate them into their respective transfer lines whilst the photons interact with the next target. After travelling through all the targets the photon beam is dumped as are the electrons produced in the targets. The positrons are then accelerated up to 5 GeV for injection to the damping ring.

The simulation of the multi-target source used ILC RDR undulator parameters with a drive beam energy of 150 GeV, an undulator length of 147 m, a Flux Concentrator as the OMD and the photon collimator radius set to 10 cm. In order to provide a more accurate result 25 different simulations were conducted each with a different random number seed. Each *run* consisted of $100,000$ photons striking the first target. Results from simulations with six targets are shown in

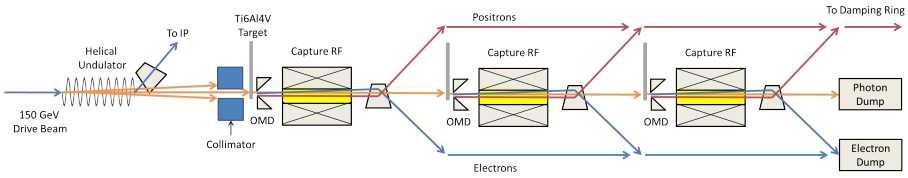

Figure 7.1: Schematic of a multiple target positron source with 3 conversion targets. Red arrows represent e^+, blue arrows represent e^- and orange arrows represent γ. The Optical Matching Device(OMD) can be a Quarter Wave Transformer(QWT), Adiabatic Matching Device(AMD) or a Flux Concentrator(FC).

Figure 7.2. Positron yield is plotted in terms of positrons within the damping ring acceptance per electron in the undulator(e^+/e^-). The requirement of the ILC design is to achieve a yield of $e^+/e^- = 1.5$. The yield from each of the first 5 targets is greater than the ILC design yield. If the positrons produced in each target can be combined into a single bunch in the damping ring then the length or deflection parameter of the undulator for the ILC positron source can be reduced whilst maintaining the design yield.

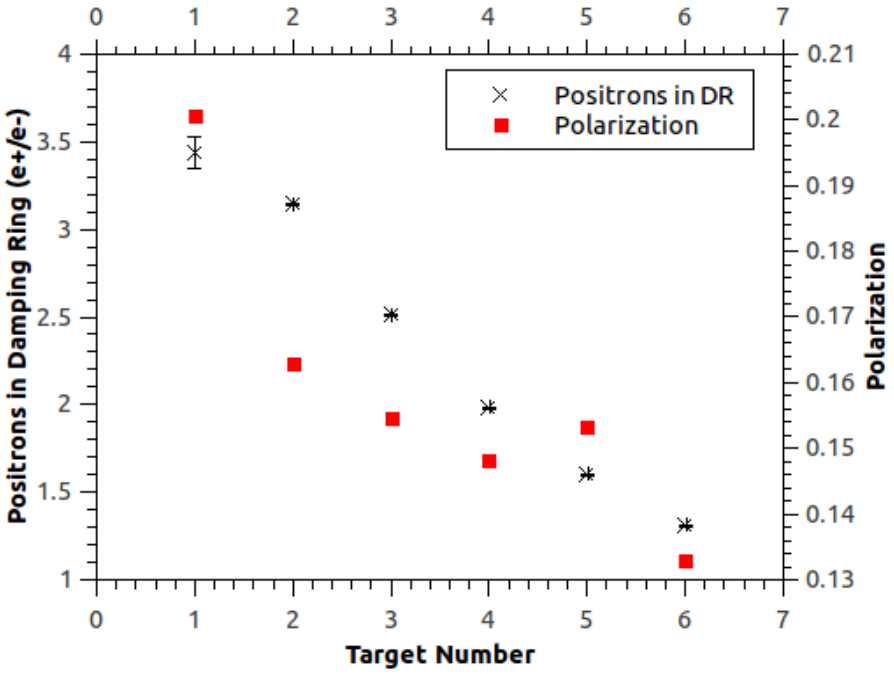

Figure 7.2: Plot of yield and polarisation for 6 targets with $K = 0.92$ and $\lambda = 1.15\,\text{cm}$. Each point is the mean value calculated from the 25 different simulation runs. The error bars are the standard deviation of the 25 runs. Data plotted using QTiPlot[77]

The effect of reducing the undulator deflection parameter on positron yield in the damping ring whilst keeping $\lambda = 1.15\,\text{cm}$ is shown in Figure 7.3. As expected later targets tend to have lower yield than earlier targets. However, of interest is the yield of the first and second targets when K is between 0.50 and 0.78 as the yield is in fact higher in the second target compared

to the first. This is due to the smaller opening angle of the radiation for undulators when K is between 0.50 and 0.78. As the angle of radiation is smaller the secondary photons produced in the first target impinge on the second target which means the effective photon flux on the second target is higher than the first target.

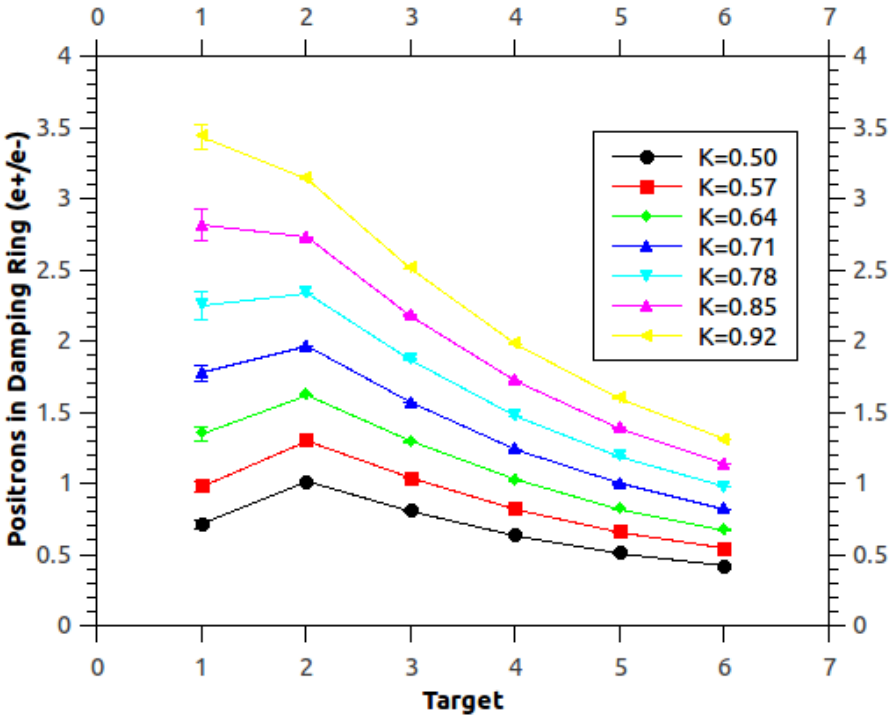

Figure 7.3: Plot of yield for 6 targets with undulator period $\lambda = 1.15\,\text{cm}$ and varying values of K. Each point is the mean value calculated from the 25 different simulation runs. The error bars are the standard deviation of the 25 runs. Data plotted using QTiPlot[77]

Assuming that the positrons produced in multiple targets can be captured and injected into one bucket in the damping ring the yield and polarisation for a 6 target positron source as a function of K is shown in Figure 7.4. This assumption is a relatively safe one as only positrons that are within the damping ring acceptance are included and the spread in time of arrival of positron bunches from different targets into the damping ring is of the order of picoseconds. This is a problem for the current damping ring design as the spacing of the bunches is too short for them to be injected independently into the damping ring. Although the spacing is of the order of picoseconds this may actually mean that the bunches are too far apart to be injected cleanly into the damping ring.

One possible solution to this problem would be to use a stacking ring similar to that proposed for a LASER-Compton based source. This would be a separate ring to the damping ring which would have larger RF buckets that the bunches could be injected into. This would then damp the multiple bunches enough that they would fit into one RF bucket in the damping ring. Another possibility would be to have multiple transfer lines from the positron source to the damping ring.

Each target could have its own transfer line which would inject separately into the damping ring. This would require multiple injection positions in the damping ring which would possibly require a a new damping ring design.

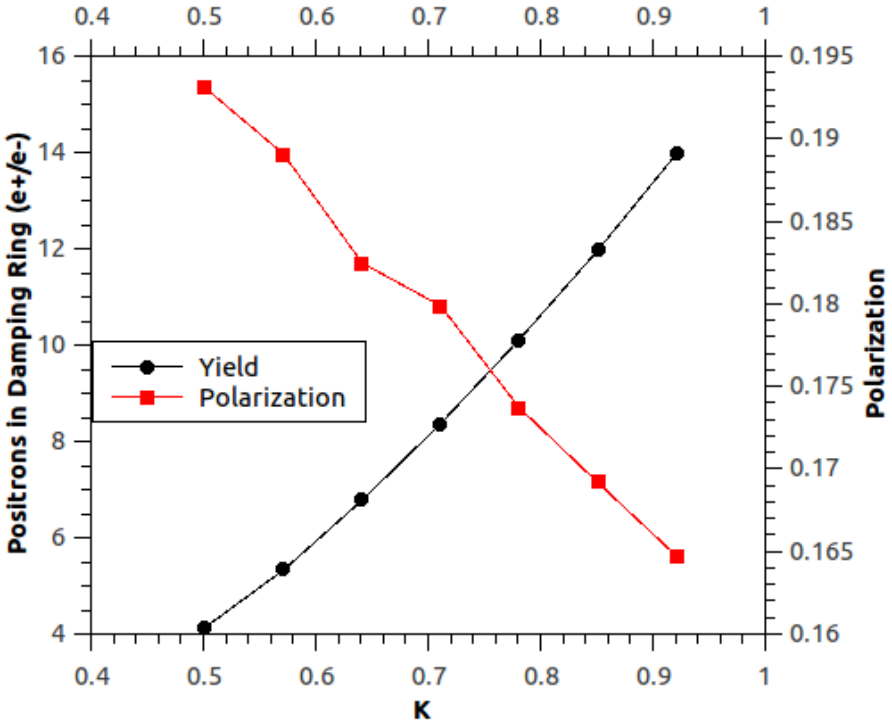

Figure 7.4: Plot of yield and polarisation in damping ring from a 6 target undulator-based positron source with undulator period $\lambda = 1.15\,\text{cm}$ as a function of K. Each point is the mean value calculated from the 25 different simulation runs. Data plotted using QTiPlot[77]

This source with 6 targets produces a yield of between 4 and 14 e^+/e^- depending on the choice of K. This means that other parameters of the positron source can be relaxed such as undulator length.

7.2 A Positron Amplifier

The idea behind a positron amplifier is that you start with a small flux of positrons and send them through the undulator of an undulator-based positron source. The photons produced by the positrons will produce more positrons as the nominal design for the positron source produces two positrons for every lepton that travels through the undulator. The main use for a positron amplifier is in a self-seeding positron source.

The need for a high-energy lepton drive beam to produce the photon beam that is used to pair-produce the positrons means that for e^+e^-colliders, such as the ILC, this means that the electron and positron arms of the machine are interdependent. This is because the positron source is located at the end of the electron main linac. For CLIC where the undulator based positron

source is a possible upgrade to produce polarised positrons there is no interdependency as there will be a full intensity positron source able to be used as the drive beam for the undulator. The idea of using positrons to create more positrons in a self-seeding positron source suitable for the ILC was initially proposed by A. A. Mikhailichenko[78].

The self-seeding positron source at the ILC would comprise a low intensity conventional positron source and an undulator-based positron source acting as the positron amplifier. The low intensity conventional source is already in the ILC design as a commissioning source which will be used to test the positron arm of the machine separately from the electron arm during the commissioning phase. As part of the self-seeding source the commissioning source would be used to provide the initial positron pulse train at 1% of the nominal positron design flux. This pulse train will then be accelerated in the positron main linac to half the centre of mass energy, in the case of a centre of mass energy that is less than 300 GeV the positron pulse will be accelerated to 150 GeV. This pulse then travels through the undulator-based positron source to produce more positrons and the initial pulse is then dumped. The newly generated pulse is then accelerated up to the appropriate energy before it travels through the undulator-based positron source to produce a pulse with higher intensity. This process is repeated until the design intensity is reached. The number of passes required to achieve the design intensity can be calculated from the following equation

$$I_F = A^p I_I \tag{7.1}$$

where I_F is the final positron intensity, I_I is the initial positron intensity from the conventional source, A is the amplification factor provided by the positron source and p is the number of passes.

For a self-seeding source at the ILC using the undulator-positron source design and the commissioning source design from the TDR equation (7.1) can be rearranged to calculate the number of passes required to achieve the design intensity as follows $100 = 2^p \Rightarrow p = \log_2(100)$. The number of passes has to be an integer number. Therefore using this equation 7 passes must be taken. This means that the positron beam intensity would be 1.28 times the design intensity. Subsequent passes through the source, which are required to produce the next positron pulse, would only increase the intensity past the design intensity even further. Figure 7.5 shows a plot of the positron yield from such a source as a function of the number of passes through the source.

Therefore a key component of a self-seeding source is the ability to control the amplification factor on a pulse by pulse basis. The limitation with this is that the NbTi undulators used in the ILC undulator-based positron source have a nominal operating current of 215 A and the current can only be changed at a rate of $10\,\mathrm{A}\,s^{-1}$. As the pulse repetition rate is 5 Hz and each pulse

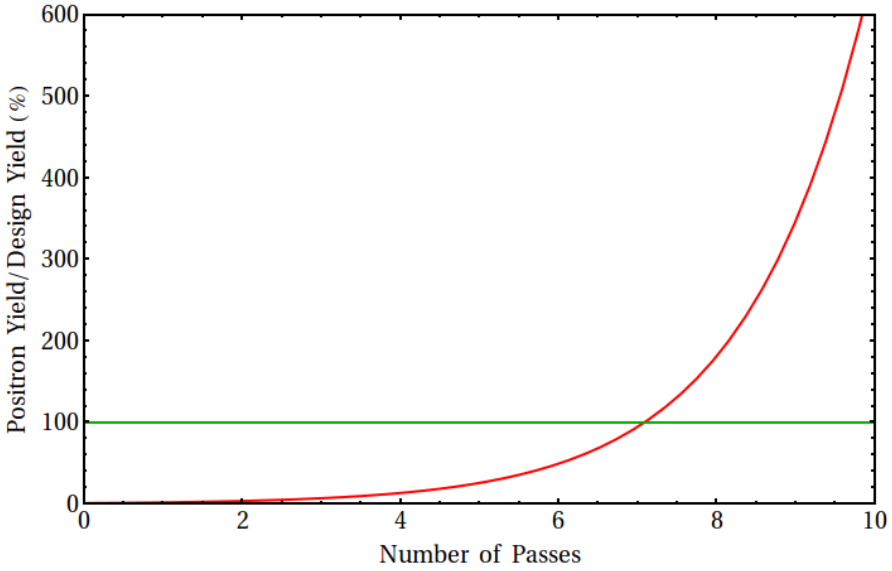

Figure 7.5: Plot of showing the positron yield from a self -seeding positron source as a function of the number of passes through the source. The red line is calculated using equation (7.1). The green line corresponds to the design yield. Plotted using Mathematica 8[79]

is a millisecond long this means that the current in the undulators can change by less than 2 A between pulses. This would not be enough of a change to suppress the exponential growth rate; therefore a different undulator configuration is required for a self-seeding positron source.

For a viable self-seeding source to work therefore the amplification factor needs to be around 1.05. This would mean that after 95 passes, which at 5 Hz would take 19 s, the positron intensity would be 1.030 times the design intensity. From earlier simulation work it was shown that an ideal ILC undulator-based positron source produces $0.0150\,e^+/e^-/m$. This means that an undulator with an active length of 70.16 m would provide the correct amplification factor. After 95 passes the intensity will be 3% higher than required. As it takes 19 seconds to reach this level there is enough time to effectively turn off undulator modules which will reduce the amplification factor to a level that will achieve the correct yield.

The largest issue facing a self-seeding positron source is the positron losses that occur throughout the machine. At the ILC the baseline positron source is designed to produce 1.5 times the required yield to allow for any losses. This is a problem for the self-seeding source as unless the losses are constant any excess in positron yield will be amplified. Therefore the design and commissioning of a self-seeding source is very important as the source needs to produce enough positrons to cope with losses but also to have a very controllable amplification factor on a short time-scale.

A detailed self-seeding source design requires a highly detailed simulation of the entire accelerator to determine what the expected positron losses will be and how variable the losses are. By determining these two parameters the self-seeding source design can be completed. Currently

there are two possible options for ensuring a highly controllable positron amplification factor. These are a multi-target design and also a segmented undulator design. The principle behind these two designs is that the positron source operates normally increasing the positron yield on a pulse by pulse basis until a nominal yield is reached. When this nominal yield is achieved the amplification factor is reduced down to a level just below that required to match the losses. This ensures that any deviation in the loss level does not result in an exponential growth in positron yield. Once the yield has decreased to a certain level the amplification factor is turned back up until the nominal yield is once again achieved and the whole operating procedure is repeated.

The multi-target design is similar to that presented in section 7.1. The design layout is the same as in figure 7.1. However the design is complicated as each target station needs to be able to be moved out of the photon beam on a pulse by pulse basis to rapidly change the amplification factor. This can be done by using a mechanism similar to that used in the push-pull system for the ILC detectors. The idea would be that the target station, which consists of the target, motor and cooling system, is mounted on a moveable platform. This platform would then be moved by approximately twice the width of the target to remove the target from the photon beam. This means that the platform needs to be moved by a system that can accelerate the platform at 3ms^{-2}.

An alternative is to use a multi-target design where the circumference of each target is crenelated. This means that by controlling the rotation speeds of individual targets the total target length seen by the beam can be changed. Such a source would need to be designed such that two targets are required to maintain the positron flux at a constant value. This means that we can use three or more targets to provide an amplification effect and use one target to reduce the positron flux.

The segmented undulator design (see figure 7.6) is conceptually simpler to understand. The idea of the segmented undulator is that as the different undulator modules do not coherently add their radiation together each undulator module can be considered as just producing a given photon spectrum. These photon spectra can then be added together to give the final spectrum. This means that by changing the number of undulator modules that the drive beam travels through the intensity of the photon spectrum changes but the shape does not. Therefore by stopping undulator modules contributing to to the spectrum the amplification factor is reduced. To achieve this the undulator is split up into segments.

The first segment is long enough to maintain a constant yield after taking into account the positron losses in the accelerator. The remaining segments are there to increase the amplification in stages to allow for fine control over the positron amplifier. Rather than moving the separate sections away from the drive beam, the drive beam is actually kicked out of the undulator after

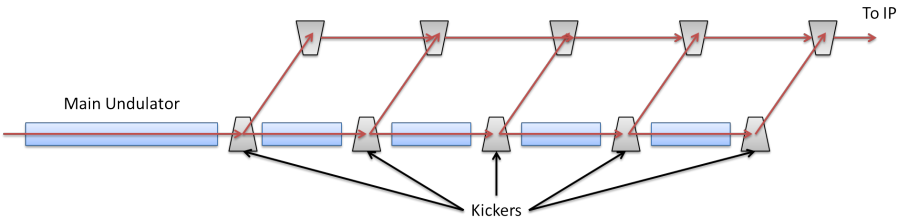

Figure 7.6: Schematic showing the design of segmented undulator for a self-seeding positron source. The undulators are shown in blue, the kicker magnets in grey and the positron path shown by the red arrows. The main undulator is the segment of the undulator that is long enough to maintain a constant positron yield.

the appropriate number of segments have been traversed. To transport the drive beam after it has been kicked out of the undulator a transport line is constructed running the length of the undulator. The drive beam is diverted into this transport line which transports the beam to the end of the undulator where it is injected back into the main linac beam line.

The technical challenge for this design is the actual kickers themselves which need to be able to be turned on and kick a beam of several hundred GeV. This will be challenging as the kicker needs to be very quick to turn on and then kick the entire pulse train with as small a disruption to the beam as possible. The position of the kickers can only be determined after a fully detailed simulation of the entire accelerator which will determine the losses experienced and therefore the length of undulator required to compensate.

7.3 A FEL Positron Source

The undulator-based positron sources discussed so far in this thesis all require a high-energy lepton drive beam travelling through a long undulator to produce a high flux of gamma rays that in turn produce positrons. The idea behind a free electron laser (FEL) based positron source is that the energy of the drive beam is much lower. This means that a FEL-based positron source is much more flexible and would be able to be used at a larger range of particle accelerators.

The inspiration for the FEL-based positron source came from a proposal by Z. Huang as part of the design of SAPPHiRE, Small Accelerator for Photon-Photon Higgs production using Recirculating Electrons, which is an evolution of the LHeC-ERL design[80]. The idea proposed for SAPPHiRE was to use two oscillator FELs to produce light in the visible spectrum. The intensity of light then builds up in the mirror cavity of the oscillator FEL. The electron beam from one FEL then interacts with the photons in the other FEL to produce high-energy photons through Compton back-scattering.

The FEL-based positron source consists of an FEL powered by an electron beam with an energy of around 300 MeV. The FEL produces light with a wavelength of 350 nm which enters

an optical cavity. The optical cavity is used to build up the intensity of photons and to focus them. The electrons that travel through the undulator in the FEL are transported from the end of the FEL to the optical cavity. The electrons are injected into the optical cavity at the focal point of the photon beam. These electrons interact with the photons in the cavity and produce high-energy photons, $E_\gamma > 1\,\text{MeV}$, through Compton back-scattering. These photons are then transported to a conversion target and used to produce positrons through the same mechanisms as in an undulator-based positron source. Figure 7.7 shows a possible layout of a FEL-based positron source.

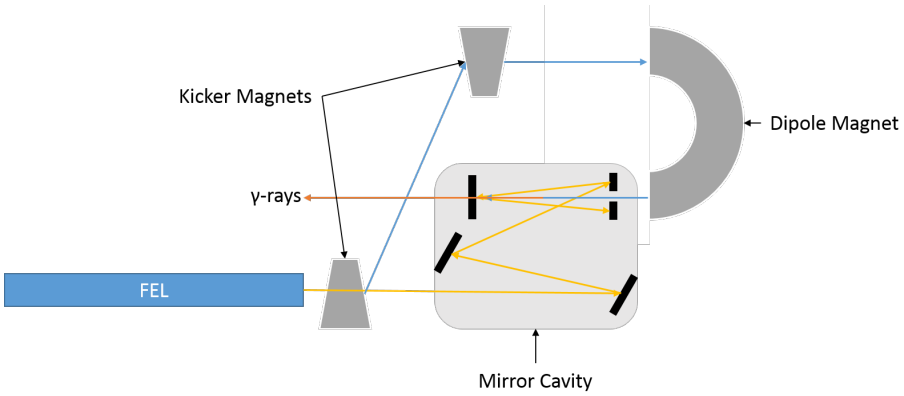

Figure 7.7: Schematic showing the design of a FEL-based positron source. The FEL undulators are shown in blue, the kicker and dipole magnets in grey. The blue arrow shows the electron trajectory, the yellow arrows show the trajectory of photons and the positron path is shown by the red arrows.

The interaction between relativistic electrons and a focused beam of monochromatic photons results in a pencil like beam of high-energy photons produced by Compton backscattering[81]. The energy of the produced photons can be calculated using the following formula

$$E_\gamma = \frac{E_L(1-\beta\cos\theta_L)}{1-\beta\cos\theta_L + E_{L/e^-}(1-\cos(\theta_L-\theta))} \tag{7.2}$$

where E_L is the energy of the photon beam, θ_L is the collision angle between the photon beam and the electron beam, E_{L/e^-} is the energy of the photon beam divided by the energy of the electron beam, β is the relativistic beta of the electron beam and θ is the backscattering angle.

Using equation (7.2) we are able to calculate the energy of the back-scattered photons as a function of the collision angle and the back-scattering angle. Using an FEL that produces light at 350 nm from a 250 MeV electron beam, the gamma ray photons produced will have an energy-angle spectrum shown in figure 7.8. The photon spectrum peaks when $\theta_L = \pi$ and $\theta = 0$. The strongest angular dependence is on the backscattering angle.

By accelerating the electron beam up to 350 MeV after it leaves the FEL the photon energy spectrum changes to that shown in figure 7.9. The shape of the spectrum has not changed

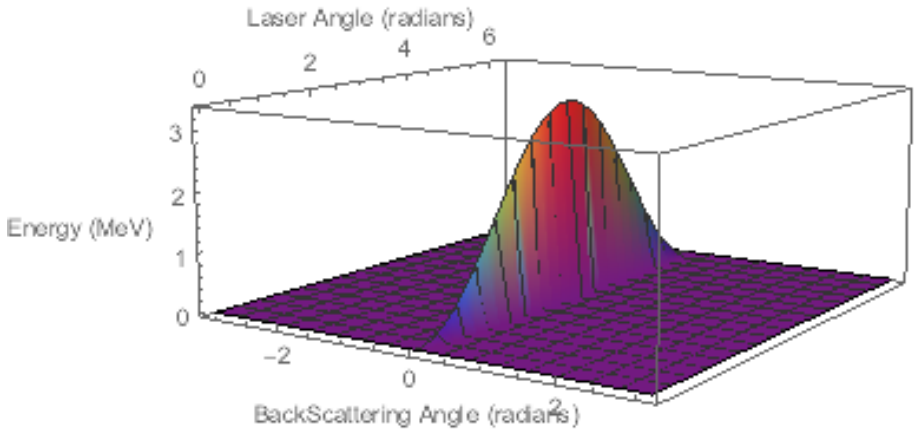

Figure 7.8: Plot showing how the energy of the back scattered photons depends on the angle of the collision, LASER angle, and the back scattering angle. This interaction is between light from a 350 nm LASER and a 250 MeV electron. Plotted using Mathematica 8[79]

significantly. The major change is that the maximum energy that a backscattered photon can have has increased from 3.35 MeV to 6.52 MeV. This is a significant increase in photon energy in terms of positron production which makes the acceleration of the electron beam worthwhile.

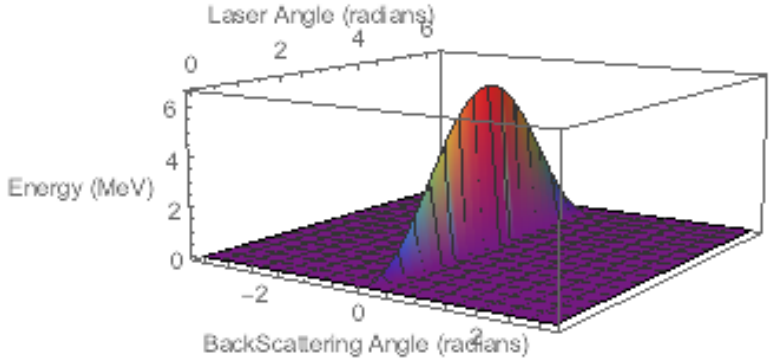

Figure 7.9: Plot showing how the energy of the back scattered photons depends on the angle of the collision, LASER angle, and the back scattering angle. This interaction is between light from a 350 nm LASER and a 350 MeV electron. Plotted using Mathematica 8[79]

Although the photon spectrum depends on the backscattering angle and the collision angle we can remove one of these angular dependencies. This is because we can control the collision angle by arranging where the electrons are injected into the optical cavity. If we ensure that the collisions are head on, $\theta_L = \pi$, the backscattered photon energy as a function of the scattering angle is shown in figure 7.10. The backscattered photon energies are plotted for three different electron energies. The upper plot shows how photon energy depends on the angle θ. There appears to be only one line shown as the overall shape does not change dramatically with electron energy. The lower plot shows a *zoomed-in* view of the peak. This clearly shows the three different energies and highlights how only the region around $\theta = 0$ changes with electron energy.

The research conducted so far into a FEL-based positron source is in the theoretical stage.

The scheme as described seems plausible but more work is required to determine whether this source would supply a sufficient flux. The FEL section is very feasible as a number of FELs have been designed that are able to produce the required light. The FEL design used as the basis for the work so far is CLARA[82]. Currently CLARA is in the final design stage at Daresbury Laboratory and construction work is expected to begin soon.

The next stage in development of a FEL-based positron source is to simulate the interaction between the electron and photon beams to get a spectrum for the back scattered photons that would be used for positron production. A possible software tool that could be used to produce such a spectrum is CAIN[83]. Once this spectrum has been calculated the feasibility of a FEL-based positron source can be truly judged. This spectrum can be input into PPS-Sim to determine the positron yield and also to determine what choice of conversion target, OMD and capture RF would be required.

7.4 Summary

Three novel extensions to the undulator-based positron source design have been presented. The multi-target undulator-based positron source is the most mature of these designs and offers a way to use the photon beam produced by the undulator more efficiently. This design would allow the undulator in the ILC undulator-based positron source to be reduced in length whilst maintaining positron yield. It may also allow for much lower energy running without increasing the undulator length as the multiple targets compensate for a lower yield at lower electron drive beam energies.

The self-seeding positron source has been proposed however the simulations conducted in this study show the complexity of the design required which may out weigh the benefits of decoupling the electron and positron arms of a linear collider. To further investigate the benefits of a self-seeding source a complete simulation of the linear collider needs to be conducted to determine exactly what positron losses are expected and whether the self-seeding source can replace the lost positrons without increasing the positron flux past the design yield.

The FEL-based positron source is of interest for two reasons. First it would completely decouple the positron source from the main electron linac in the linear collider and therefore provide similar benefits to the self-seeding positron source. In addition as part of the mechanism for producing positrons we need to be able to construct a FEL that can generate gamma rays through Compton backscattering the electron beam with the light it produces. If this process is shown to work it will allow for high-intensity gamma ray sources to be constructed which will be of interest to other branches of physics.

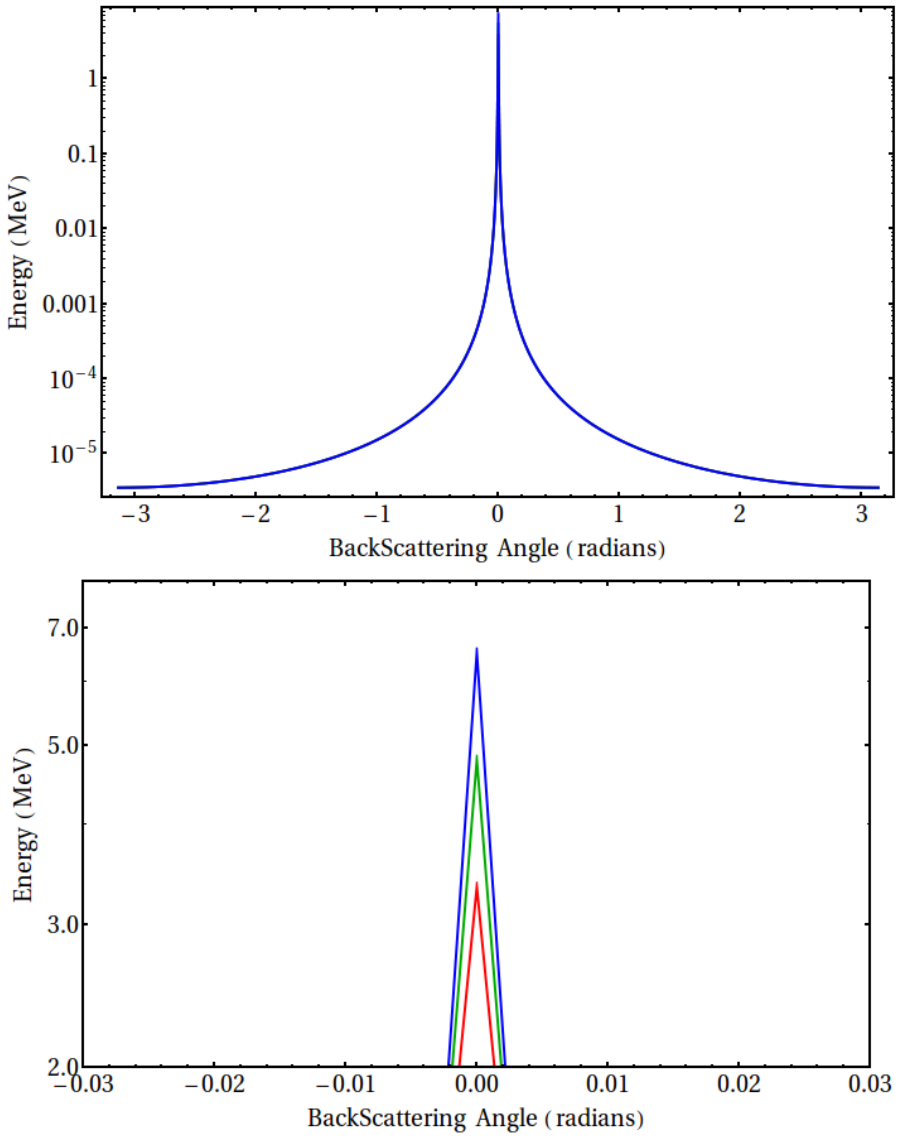

Figure 7.10: Plots showing the relationship between energy and backscattering angle, θ, for photons produced by Compton backscattering when the collision angle, $\theta_L = \pi$, for three different electron energies. The red line corresponds to 250 MeV electrons, the green line corresponds to 300 MeV electrons and the blue line corresponds to 350 MeV electrons. The upper plot shows how photon energy evolves as a function of θ. There appears to be only one line shown as the overall shape does not change dramatically with electron energy. The lower plot shows a *zoomed-in* view of the peak, this clearly shows the three different energies and highlights how only the region around $\theta = 0$ changes with electron energy. Plotted using Mathematica 8[79]

Chapter 8

Conclusion

An undulator-based positron source is the baseline design for positron production at the ILC. In an attempt to optimise the source a number of studies into different undulator configurations have been carried out. In order to fully understand the radiation produced by an undulator we have derived the synchrotron radiation emitted by a point charge moving along an arbitrary path starting from Maxwell's equations. This derivation describes the radiation emitted from an electron moving on a circular orbit due to the effect of dipole magnets. This is a key result for the derivation of radiation from insertion devices as insertion devices can be thought of as an array of dipole magnets. Using the equations describing the radiation from dipole magnets we have derived analytical equations for the radiation expected from perfect wigglers and undulators. To do this we have considered the electron trajectory through insertion devices and then calculated the expected radiation. Being able to calculate the radiation produced by an undulator is vital for studying undulator-based positron sources as many of the parameters of different components in the undulator-based positron source depend on the radiation produced by the undulator.

Having derived an equation to calculate the radiation produced by an undulator we used it to evaluate software developed at Daresbury Laboratory that calculate photon spectra from undulators. Based on this evaluation work it was decided to use HUSR to calculate the photon spectra from undulators. HUSR was used in a number of studies to generate the photon spectrum expected from the undulator in an undulator-based positron source. During the course of these investigations a number of new features were added to HUSR by the author in order to improve the accuracy of the simulations. This resulted in HUSR having a better than 99.98 % agreement with the analytical equation for radiation produced by a perfect helical undulator derived in section 3.4.3.

Having benchmarked HUSR to ensure accuracy a number of studies were conducted to determine the effect of non-ideal undulators on the photon spectrum. The non-ideal helical undulator

produced a photon spectrum that is closer to an optimal photon spectrum for positron production than the ideal spectrum. To understand why this is the case research was carried out which led to an interesting conclusion regarding the length of an undulator. Increasing the length of an undulator past twenty periods does not affect the shape of the photon spectrum only the flux produced. Using this fact it was attempted to optimise the photon spectrum shape by controlling the *interference length* of the undulator which resulted in two new design; a *growing period* undulator and a multi-K undulator.

To simulate the effect that differing undulators have on positron production in an undulator-based positron source at the ILC, PPS-Sim, which is a Geant4 based code developed at DESY, has been used. The results from simulations of an ideal undulator-based positron source at the ILC have been compared with those conducted by other groups to ensure that the simulations are reliable. Using software that has not been available to the positron source community before we have simulated realistic undulator-based positron sources to estimate what we would expect if such a source was constructed.

Additionally a study into polarised positron production at the ILC was conducted. Based on investigations into the effect of collimator radius on polarisation it appears that for a non-ideal photon spectrum collimating tightly to increase polarisation will not be successful. This means that a new method for increasing polarisation is required. One option is to use a multi K undulator to produce a spectrum that has higher average photon polarisation. This then increases the positron polarisation by as much as 20 % compared to the positron polarisation produced by an ideal undulator-based positron source.

The design of an undulator-based positron source can be explored further. As part of this thesis three novel extensions to the undulator-based positron source design have been presented. The multi-target undulator-based positron source is the most mature of these designs and offers a way to use the photon beam produced by the undulator more efficiently. This design would allow the undulator in the ILC undulator-based positron source to be reduced in length whilst maintaining positron yield. It may also allow for much lower energy running without increasing the undulator length as the multiple targets compensate for a lower yield at lower electron drive beam energies.

The self-seeding positron source has been proposed however the simulations conducted in this study show the complexity of the design required which may out-weigh the benefits of decoupling the electron and positron arms of a linear collider. To further investigate the benefits of a self-seeding source a complete simulation of the linear collider needs to be conducted to determine exactly what positron losses are expected and whether the self-seeding source can replace the lost positrons without increasing the positron flux past the design yield.

The FEL-based positron source is of interest for two reasons. First it would completely decouple the positron source from the linear collider and therefore provide similar benefits to the self-seeding positron source. In addition as part of the mechanism for producing positrons we need to be able to construct a FEL that can generate gamma rays through Compton backscattering the electron beam with the light produced. If this process is shown to work it will allow for high-intensity gamma ray sources to be constructed which will be of interest to other branches of physics.

There is still scope for further development of these and other modifications to the undulator-based positron source design. For the ILC and other high energy electron-positron linear colliders the most promising area for optimising the design of an undulator-based positron source is to optimise the undulator. This thesis has shown that changing the undulator can change the positron distribution significantly. Therefore to evaluate any modifications to other parts of the positron source design simulations using realistic undulators must be conducted. This is particularly true when attempting to modify the design to increase positron polarisation as was shown when evaluating how changes in the collimator radius affect positron yield and polarisation.

Appendix A

Calculating $\mathbf{n} \times (\mathbf{n} \times \boldsymbol{\beta})$

By considering the geometry of an electron travelling through a planar undulator, only the B_y component of the magnetic field is non-zero, we can express the vector triple product obtained in section 3.4.2 in more manageable terms. From figure we see that the unit vector is

$$\mathbf{n} = \begin{pmatrix} \sin\theta\cos\phi \\ \sin\theta\sin\phi \\ \cos\theta \end{pmatrix} \tag{A.1}$$

As the B_x component of the magnetic field is zero then for an electron travelling along the axis of the undulator then the v_y component of the electron velocity is zero. As $\boldsymbol{\beta} = \mathbf{v}/c$ this means that $\boldsymbol{\beta}$ is

$$\boldsymbol{\beta} = \begin{pmatrix} \beta_x \\ 0 \\ \beta_z \end{pmatrix} \tag{A.2}$$

From equation (3.32) we know that in a planar undulator β_x is

$$\beta_x = \frac{K}{\gamma}\cos\frac{2\pi z}{\lambda_u}$$

and from equation (3.36) we know that β_z is

$$\beta_z = \beta\left(1 - \frac{K^2}{4\beta^2\gamma^2} - \frac{K^2}{4\beta^2\gamma^2}\cos\frac{4\pi z}{\lambda_u}\right)$$

Using equation (3.37) and assuming that the electron is relativistic, i.e. $\beta \approx 1$, β_z becomes

$$\beta_z = \hat{\beta_z} - \frac{K^2}{4\gamma^2}\cos\frac{4\pi z}{\lambda_u} \tag{A.3}$$

However as the integral in equation (3.57) is evaluated with respect to time we need to convert our values of β_x and β_z to be functions of t rather than z. As $z = \hat{\beta}_z ct$ this means that $\boldsymbol{\beta}$ becomes

$$\boldsymbol{\beta} = \begin{pmatrix} \frac{K}{\gamma} \cos \frac{2\pi \hat{\beta}_z ct}{\lambda_u} \\ 0 \\ \hat{\beta}_z - \frac{K^2}{4\gamma^2} \cos \frac{4\pi \hat{\beta}_z ct}{\lambda_u} \end{pmatrix} = \begin{pmatrix} \frac{K}{\gamma} \cos Ht \\ 0 \\ \hat{\beta}_z - \frac{K^2}{4\gamma^2} \cos 2Ht \end{pmatrix} \tag{A.4}$$

where

$$H = \frac{2\pi \hat{\beta}_z c}{\lambda_u}$$

We can now evaluate the vector triple product. We start by using the vector triple product identity to express it as

$$(\mathbf{n} \cdot \boldsymbol{\beta})\mathbf{n} - \boldsymbol{\beta}$$

using the values for $\mathbf{n}$ and $\boldsymbol{\beta}$ we have just derived we can solve this expression in stages

$$\begin{aligned} (\mathbf{n} \cdot \boldsymbol{\beta}) &= \beta_x \sin\theta \cos\phi + \beta_z \cos\theta \\ (\mathbf{n} \cdot \boldsymbol{\beta})\mathbf{n} &= \begin{pmatrix} \beta_x \sin^2\theta \cos^2\phi + \beta_z \cos\theta \sin\theta \cos\phi \\ \beta_x \sin^2\theta \cos\phi \sin\phi + \beta_z \cos\theta \sin\theta \sin\phi \\ \beta_x \sin\theta \cos\theta \cos\phi + \beta_z \cos^2\theta \end{pmatrix} \\ (\mathbf{n} \cdot \boldsymbol{\beta})\mathbf{n} - \boldsymbol{\beta} &= \begin{pmatrix} \beta_x \sin^2\theta \cos^2\phi + \beta_z \cos\theta \sin\theta \cos\phi - \beta_x \\ \beta_x \sin^2\theta \cos\phi \sin\phi + \beta_z \cos\theta \sin\theta \sin\phi \\ \beta_x \sin\theta \cos\theta \cos\phi + \beta_z \cos^2\theta - \beta z \end{pmatrix} \end{aligned} \tag{A.5}$$

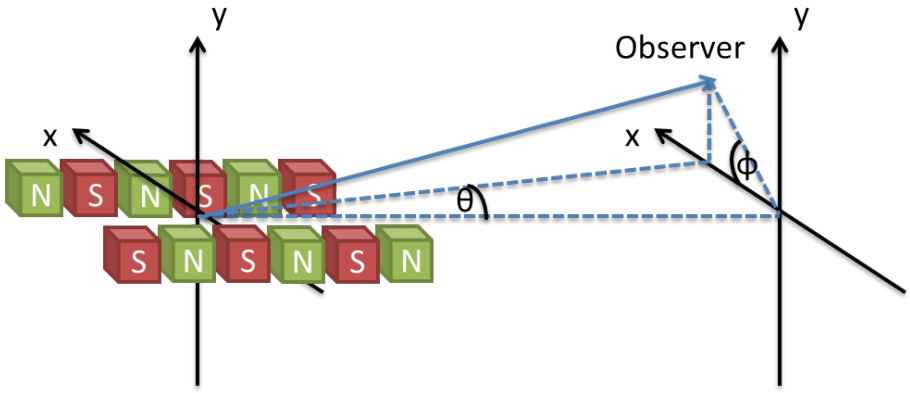

Figure A.1: Diagram showing the observer position relative to the center of the undulator.

From figure A.1 we see that θ is the angle from the centre of the undulator to the x position

of the observer. Therefore $\tan\theta = x/z_{\text{obs}}$ where z_{obs} is the distance to the observation plane from the centre of the undulator. As for realistic undulators the condition $z_{\text{obs}} \gg x$ holds we can use the small angle approximation for all functions of θ in equation (A.5). Therefore equation (A.5) becomes

$$(\mathbf{n}\cdot\boldsymbol{\beta})\mathbf{n} - \boldsymbol{\beta} = \begin{pmatrix} \beta_x\theta^2\cos^2\phi + \beta_z\theta\cos\phi\left(1-\frac{\theta^2}{2}\right) - \beta_x \\ \beta_x\theta^2\cos\phi\sin\phi + \beta_z\theta\sin\phi\left(1-\frac{\theta^2}{2}\right) \\ \beta_x\theta\cos\phi\left(1-\frac{\theta^2}{2}\right) + \beta_z\left(1-\frac{\theta^2}{2}\right)^2 - \beta z \end{pmatrix} = \begin{pmatrix} \beta_z\theta\cos\phi - \beta_x \\ \beta_z\theta\sin\phi \\ \beta_x\theta\cos\phi \end{pmatrix} \tag{A.6}$$

where we have dropped all terms of order θ^2 or higher. Additionally if we assume that $\beta_x \ll \beta_z$ and as $\beta \approx 1$ this means that $\beta_z \approx 1$. Therefore equation (A.6) becomes

$$(\mathbf{n}\cdot\boldsymbol{\beta})\mathbf{n} - \boldsymbol{\beta} = \begin{pmatrix} \theta\cos\phi - \beta_x \\ \theta\sin\phi \\ 0 \end{pmatrix} \tag{A.7}$$

This result is used in section 3.4.2.

Appendix B

Calculating $e^{i\omega\left(t-\frac{\mathbf{n}\cdot\mathbf{r}}{c}\right)}$

The next term in the integral in equation (3.57) in section 3.4.2 is an exponential. To calculate the exponent we will need $\mathbf{r}$ which is the path of the electron. As we are assuming that the electron is travelling through the centre of the undulator, there is no vertical component to $\mathbf{r}$. Therefore we just need to describe the electron motion in x and z. Equation (3.7) gives the x position of the electron and so we just need to calculate the z position of the electron. This can be done by integrating the longitudinal component of the electron velocity:

$$z = \int v_z \mathrm{d}t = \int c\beta_z \mathrm{d}t \tag{B.1}$$

Substituting for our value of β_z from equation (A.4) the z position of the electron as a function of time is

$$\begin{aligned} z &= c\int \hat{\beta}_z - \frac{K^2}{4\gamma^2}\cos\left(2Ht\right)\mathrm{d}t \\ &= c\hat{\beta}_z t - \frac{cK^2}{8H\gamma^2}\sin\left(2Ht\right) \end{aligned} \tag{B.2}$$

therefore the position vector of the electron as a function of time is

$$\mathbf{r} = \begin{pmatrix} \frac{cK}{H\gamma}\sin\left(Ht\right) \\ 0 \\ c\hat{\beta}_z t - \frac{cK^2}{8H\gamma^2}\sin\left(2Ht\right) \end{pmatrix} \tag{B.3}$$

The dot product term in the exponent is therefore

$$\frac{\mathbf{n}\cdot\mathbf{r}}{c} = \frac{K}{H\gamma}\sin\left(Ht\right)\sin\theta\cos\phi + \left(\hat{\beta}_z t - \frac{K^2}{8H\gamma^2}\sin\left(2Ht\right)\right)\cos\theta \tag{B.4}$$

This means that the exponent in equation (3.57) evaluates to

$$\begin{aligned}\omega\left(t-\frac{\mathbf{n}\cdot\mathbf{r}}{c}\right) &= \omega t-\frac{\omega K}{H\gamma}\sin\left(Ht\right)\sin\theta\cos\phi-\omega\hat{\beta}_z t\cos\theta+\frac{\omega K^2}{8H\gamma^2}\sin\left(2Ht\right)\cos\theta \\ &= \omega t(1-\hat{\beta}_z\cos\theta)-\frac{\omega\theta\cos\phi}{H}\frac{K}{\gamma}\sin\left(Ht\right)+\frac{\omega\cos\theta}{8H}\left(\frac{K}{\gamma}\right)^2\sin\left(2Ht\right) \end{aligned} \tag{B.5}$$

where we have replaced $\sin\theta$ using the small angle approximation.

From the investigation into the behaviour of the line-shape function in section 3.4.2 we know that for an undulator consisting of a realistic number of periods there will only be a significant flux intensity observed in a narrow bandwidth around the harmonics. This means that we only need to evaluate the integral in equation (3.57) at these discrete harmonics. Therefore we only need to consider angular frequencies given by

$$\omega = m\omega_1 = \frac{2\pi mc}{\lambda_1} \tag{B.6}$$

λ_1 is the wavelength of light observed at the first harmonic. Therefore λ_1 is the wavelength calculated from the undulator equation when $n=1$. Therefore we can replace λ_1 with equation (3.43) which means that ω becomes

$$\begin{aligned}\omega &= 2\pi mc\left(\frac{1}{\frac{\lambda_u}{2\gamma^2}\left(1+\frac{K^2}{2}+\theta^2\gamma^2\right)}\right) \\ &= \frac{4\pi\gamma^2 mc}{\lambda_u\left(1+\frac{K^2}{2}+\theta^2\gamma^2\right)} \\ &= \frac{2mH\gamma^2}{\hat{\beta}_z A}\end{aligned} \tag{B.7}$$

where

$$A = 1+\frac{K^2}{2}+\theta^2\gamma^2$$

analogously we can also replace λ_1 with the equation for the interference condition (3.27) and again setting $n=1$ which means that the angular frequency becomes

$$\begin{aligned}\omega &= \frac{2\pi mc}{\left(\frac{\lambda_u}{\hat{\beta}_z}\right)-\lambda_u\cos\theta} \\ &= \frac{nH}{1-\hat{\beta}_z\cos\theta}\end{aligned} \tag{B.8}$$

We can substitute the two equations (B.7) and (B.8) into the equation for the exponent (B.5) which becomes

$$\begin{aligned}\omega\left(t-\frac{\mathbf{n}\cdot\mathbf{r}}{c}\right) &= nHt-\frac{2nH\gamma^2}{\hat{\beta}_z A}\frac{\theta\cos\phi}{H}\frac{K}{\gamma}\sin(Ht)+\frac{2nH\gamma^2}{\hat{\beta}_z A}\frac{\cos\theta}{8H}\left(\frac{K}{\gamma}\right)^2\sin(2Ht)\\ &= nHt-\frac{2nK\gamma}{\hat{\beta}_z A}\theta\cos\phi\sin(Ht)+\frac{nK^2}{4\hat{\beta}_z A}\cos\theta\sin(2Ht)\\ &= nHt-X\sin(Ht)+Y\sin(2Ht) \qquad \text{(B.9)}\end{aligned}$$

where

$$X=\frac{2nK\gamma\theta\cos\phi}{\hat{\beta}_z A}$$
$$Y=\frac{nK^2\cos\theta}{4\hat{\beta}_z A}$$

The exponential in equation (3.57) therefore becomes

$$e^{i\omega\left(t-\frac{\mathbf{n}\cdot\mathbf{r}}{c}\right)}=e^{i(nHt-X\sin(Ht)+Y\sin(2Ht))}=e^{inHt}e^{-iX\sin(Ht)}e^{iY\sin(2Ht)} \qquad \text{(B.10)}$$

We can rewrite the exponential functions which contain a sine term in the exponent as Bessel functions of the first kind using the Jacobi-Anger expansion which is shown below

$$e^{iz\sin\theta}=\sum_{n=-\infty}^{\infty}J_n(z)e^{in\theta} \qquad \text{(B.11)}$$

This means that equation (B.10) becomes

$$\begin{aligned}e^{i\omega\left(t-\frac{\mathbf{n}\cdot\mathbf{r}}{c}\right)} &= e^{inHt}\sum_{p=-\infty}^{\infty}J_p(X)e^{-ipHt}\sum_{q=-\infty}^{\infty}J_q(Y)e^{2iqHT}\\ &= \sum_{p=-\infty}^{\infty}J_p(X)\sum_{q=-\infty}^{\infty}J_q(Y)e^{iHt(n-p+2q)} \qquad \text{(B.12)}\end{aligned}$$

This result is used from section 3.4.2 onwards.

Bibliography

[1] D.J. Scott. *Private communication.* 2010-10-19.

[2] S. Berryman. *Ancient atomism.* Stanford Encyclopedia of Philosophy. 2005.

[3] M. H. Carré. *Pierre Gassendi and the new philosophy*, volume 33 of *Philosophy.* Cambridge Univ Press, 1958.

[4] I. Newton. *Opticks: Or, a Treatise of the Reflections, Refractions, Inflections, and Colors of Light.* Digireads.com Publishing, 2011.

[5] J. Dalton. *A new system of chemical philosophy*, volume 1. Cambridge University Press, 2010.

[6] J. F. Donoghue, E. Golowich, and B. R. Holstein. *Dynamics of the standard model*, volume 35. Cambridge university press, 2014.

[7] J. Beringer, J. F. Arguin, R. M. Barnett, K. Copic, O. Dahl, D. E. Groom, C. J. Lin, J. Lys, H. Murayama, C. G. Wohl, W. M. Yao, P. A. Zyla, and others. *Review of Particle Physics*, volume 86. American Physical Society, Jul 2012.

[8] LHC Study Group and European Organization for Nuclear Research. *Design study of the large hadron collider (LHC): a multiparticle collider in the LEP tunnel.* Number 3. 1991.

[9] A. Blondel, A. Chao, W. Chou, J. Gao, D. Schulte, and K. Yokoya. *Report of the ICFA Beam Dynamics Workshop'Accelerators for a Higgs Factory: Linear vs. Circular'(HF2012).* arXiv preprint arXiv:1302.3318. 2013.

[10] J. Brau, Y. Okada, N.J. Walker, A. Djouadi, J. Lykken, K. Monig, M. Oreglia, S. Yamashita, N. Phinney, N. Toge, et al. *International Linear Collider reference design report.* 2007.

[11] H. Braun, R. Corsini, JP Delahaye, A. De Roeck, S. Döbert, A. Ferrari, G. Geschonke, A. Grudiev, C. Hauviller, B. Jeanneret, et al. *CLIC 2008 parameters.* CLIC-Note-764.

[12] G. Moortgat-Pick, T. Abe, G. Alexander, B. Ananthanarayan, A.A. Babich, V. Bharadwaj, D. Barber, et al. *Polarized positrons and electrons at the linear collider*, volume 460. 2008.

[13] LHeC Study Group. *A Large Hadron Electron Collider at CERN*. 2012.

[14] H.E. Haber. *Non-Minimal Higgs Sectors: The Decoupling Limit and its Phenomenological Implications*. Arxiv preprint hep-ph/9501320. 1995.

[15] M.E. Peskin. *Comparison of LHC and ILC capabilities for Higgs boson coupling measurements*. arXiv preprint arXiv:1207.2516. 2012.

[16] M. Drees, R.M. Godbole, and P. Roy. *Theory and phenomenology of sparticles*, volume 1. 2004.

[17] P. F. Pérez and S. Spinner. *Fate of R parity*, volume 83 of *Physical Review D*. APS, 2011.

[18] S.P. Martin. *Perspectives on Supersymmetry*. Editor GL Kane, World Scientific. 1998.

[19] R.M. Godbole, M. Guchait, and D.P. Roy. *Using tau polarization to discriminate between SUSY models and determine SUSY parameters at ILC*, volume 618 of *Physics Letters B*. Elsevier, 2005.

[20] L. Calibbi, Y. Mambrini, and S.K. Vempati. *SUSY-GUTs, SUSY-seesaw and the neutralino dark matter*, volume 2007 of *Journal of High Energy Physics*. IOP Publishing, 2007.

[21] R. Benbrik and C.K. Chua. *Lepton flavor violating l l^{} γ and Z ll [over¯]^{} decays induced by scalar leptoquarks*, volume 78 of *Physical Review D*. APS, 2008.

[22] D.J. Miller. *Linear collider physics*, volume 20 of *International Journal of Modern Physics A*. World Scientific, 2005.

[23] H. Wiedemann. *Synchrotron Radiation*. Springer, 2003.

[24] H.F. Schopper. *LEP: The Lord of the collider rings at CERN 1980-2000: The Making, operation and legacy of the world's largest scientific instrument*. Springer, 2009.

[25] C. Blood. *A primer on quantum mechanics and its interpretations*. arXiv preprint arXiv:1001.3080. 2010.

[26] K. Flöttmann. *Investigations toward the development of polarized and unpolarized high intensity positron sources for linear colliders*, volume 93 of *Preprint DESY*. 1993.

[27] W. Kilian, PM Zerwas, et al. *Higgs-strahlung and WW fusion in e+ e-collisions*, volume 373 of *Physics Letters B*. Elsevier, 1996.

[28] J. Erler, K. Flottmann, S. Heinemeyer, K. Monig, G. Moortgat-Pick, PC Rowson, E. Torrence, G. Weiglein, and GW Wilson. *Positron polarisation and low energy running at a Linear Collider*. arXiv preprint hep-ph/0112070. 2001.

[29] J.T. Seeman. *The Stanford linear collider*, volume 249. 1992.

[30] T. Abe, S. Schuwalow, M. Yamauchi, J. Schaffran, H. Ikeda, W. Qian, W. Waltenberger, Z. Liang, A. Brogna, M. Merk, et al. *The international large detector: Letter of intent.* 2010.

[31] P. Burrows H. Aihara and M. Oreglia. *SiD letter of intent.* arXiv preprint arXiv:0911.0006. 2009.

[32] T. Behnke, J. E. Brau, B. Foster, J. Fuster, M. Harrison, J. M. Paterson, M. Peskin, M. Stanitzki, N. Walker, and H. Yamamoto. *The International Linear Collider Technical Design Report-Volume 1: Executive Summary.* arXiv preprint arXiv:1306.6327. 2013.

[33] P Lebrun, L Linssen, A Lucaci-Timoce, D Schulte, F Simon, S Stapnes, N Toge, H Weerts, and J Wells. *The CLIC Programme: Towards a Staged e+ e-Linear Collider Exploring the Terascale: CLIC Conceptual Design Report.* arXiv preprint arXiv:1209.2543. 2012.

[34] W. Heitler. *The quantum theory of radiation.* 1984.

[35] T. Omori, T. Takahashi, S. Riemann, W. Gai, J. Gao, S. Kawada, W. Liu, N. Okuda, G. Pei, J. Urakawa, et al. *A conventional positron source for international linear collider*, volume 672 of *Nuclear Instruments and Methods in Physics Research Section A: Accelerators, Spectrometers, Detectors and Associated Equipment.* Elsevier, 2012.

[36] S. Araki, Y. Higashi, Y. Honda, Y. Kurihara, M. Kuriki, T. Okugi, T. Omori, T. Taniguchi, N. Terunuma, J. Urakawa, et al. *Design of a polarised positron source based on laser compton scattering.* arXiv preprint physics/0509016. 2005.

[37] T. Omori, T. Aoki, K. Dobashi, T. Hirose, Y. Kurihara, T. Okugi, I. Sakai, A. Tsunemi, J. Urakawa, M. Washio, et al. *Design of a polarized positron source for linear colliders*, volume 500 of *Nuclear Instruments and Methods in Physics Research Section A: Accelerators, Spectrometers, Detectors and Associated Equipment.* Elsevier, 2003.

[38] I Chaikovska, O Dadoun, P Lepercq, A Variola, et al. *Polarized Positron Source with a Compton Multiple IPs Line.* 2012.

[39] T. Akagi, S. Araki, J. Bonis, I. Chaikovska, R. Chiche, R. Cizeron, M. Cohen, E. Cormier, P. Cornebise, N. Delerue, et al. *Production of gamma rays by pulsed laser beam Compton scattering off GeV-electrons using a non-planar four-mirror optical cavity*, volume 7 of *Journal of Instrumentation.* IOP Publishing, 2012.

[40] R. Brinkmann, Tesla Collaboration, et al. *Linear Collider Projects at DESY.* EPAC98, Stockholm, Sweden. 1998.

[41] T. Behnke et al. *ILC TDR and DBD*. ILC-Report-2013-040. http://www. linearcollider. org/ILC/Publications/Technical-Design-Report. 2013.

[42] J.D Jackson. *Classical Electrodynamics*. John Wiley & Sons: New York, 1999.

[43] J.A. Clarke. *The science and technology of undulators and wigglers*. Oxford University Press, 2004.

[44] D. Zwillinger. *CRC standard mathematical tables and formulae*. Taylor & Francis US, 2011.

[45] M. Abramowitz and I. A. Stegun. *Handbook of mathematical functions: with formulas, graphs, and mathematical tables*. Number 55. Courier Dover Publications, 1972.

[46] A. Hofmann. *Characteristics of synchrotron radiation*, volume 98-04. 1998.

[47] DESY. Storage rings as synchrotron radiation sources. `http://photon-science.desy.de/research/studentsteaching/primers/storage_rings__beamlines/index_eng.html`, September 2013.

[48] B.M. Kincaid. *A short-period helical wiggler as an improved source of synchrotron radiation*, volume 48 of *Journal of Applied Physics*. 1977.

[49] G. Moortgat-Pick, T. Abe, G. Alexander, B. Ananthanarayan, A. A. Babich, V. Bharadwaj, D. Barber, A. Bartl, A. Brachmann, S. Chen, et al. *Revealing fundamental interactions: the role of polarized positrons and electrons at the Linear Collider*. 2005.

[50] Vector Fields. *OPERA-2d User Guide*. Vector Fields Limited, England. 1999.

[51] Vector Fields. *OPERA-3d Reference Manual*. Vector Fields Limited, England. 2004.

[52] J. Rochford. *The development of a Superconducting Undulator for the ILC Positron Source*.

[53] D.J. Scott, J.A. Clarke, D.E. Baynham, V. Bayliss, T. Bradshaw, G. Burton, A. Brummitt, S. Carr, A. Lintern, J. Rochford, et al. *Demonstration of a High-Field Short-Period Superconducting Helical Undulator Suitable for Future TeV-Scale Linear Collider Positron Sources*, volume 107 of *Physical Review Letters*. APS, 2011.

[54] D. J. Scott. *An Investigation into the Design of the Helical Undulator for the International Linear Collider Positron Source*. PhD thesis, University of Liverpool, 2008.

[55] J. W. Motz, H. A. Olsen, and H. W. Koch. *Pair production by photons*, volume 41 of *Reviews of Modern Physics*. APS, 1969.

[56] F. Staufenbiel, O. S. Adeyemi, V. Kovalenko, G. Moortgat-Pick, L. Malysheva, S. Riemann, A. Ushakov, et al. *Heat Load Studies in Target and Collimator Materials for the ILC Positron Source*. IPAC, 2012.

[57] F. Staufenbiel, O. S. Adeyemi, V. Kovalenko, G. Moortgat-Pick, L. Malysheva, S. Riemann, and A. Ushakov. *Heat Load and Stress Studies for an Design of the Photon Collimator for the ILC Positron Source*. arXiv preprint arXiv:1202.5987. 2012.

[58] M. J. Berger, J. H. Hubbell, S. M. Seltzer, J. Chang, J. S. Coursey, R. Sukumar, D. S. Zucker, and K. Olsen. *XCOM: photon cross sections database*.

[59] I. R. Bailey, J. A. Clarke, D. J. Scott, C. G. Brown, J. Gronberg, L. B. Hagler, W. T. Piggott, L. J. Jenner, and L. Zang. *Eddy current studies from the undulator-based positron source target wheel prototype*. 2010.

[60] S. Lee. *Accelerator physics*. World Scientific, 2004.

[61] V. Kovalenko, O. S. Adeyemi, A. Hartin, G. Moortgat-Pick, L. Malysheva, S. Riemann, F. Staufenbiel, and A. Ushakov. *Spin Tracking at the ILC Positron Source*. arXiv preprint arXiv:1202.0751. 2012.

[62] H. Wang, W. Liu, W. Gai, T. Wong, and A. Kanareykin. *Design and Prototyping of the AMD for the ILC*. 2007.

[63] Y. K. Batygin. *Positron Collection in the ILC*, volume 97. 2005.

[64] A. Ushakov, S. Riemann, and A. Schalicke. *Polarized positron production and tracking at the ILC positron source*. 2007.

[65] SI Maxwell. *3D Version 4.0, Ansoft Corporation, Pittsburgh, PA*.

[66] J. Gronberg, R. Abbott, C. Brown, J. Javedani, W. T. Piggott, and J. A. Clarke. *Design of a Pulsed Flux Concentrator for the ILC Positron Source,*. IPAC10, Kyoto, May. 2010.

[67] T. Tanaka and H. Kitamura. *SPECTRA: a synchrotron radiation calculation code*, volume 8 of *Journal of synchrotron radiation*. International Union of Crystallography, 2001.

[68] D. Newton. *The rapid calculation of synchrotron radiation output from long undulator systems*. 2010.

[69] D. Newton and A. Wolski. *Fast, accurate calculation of dynamical maps from magnetic field data using generalised gradients*. Proc. PAC09.

[70] F. Spitzer. *Principles of random walk*. Springer, 1964.

[71] A. Schälicke, K. Laihem, and P. Starovoitov. *Polarised Geant4–Applications at the ILC.* Arxiv preprint arXiv:0712.2336. 2007.

[72] A. Ushakov, S. Riemann, and A. Schälicke. *Positron source simulations using GEANT4.* 2010.

[73] S. Agostinelli, J. Allison, K. Amako, J. Apostolakis, H. Araujo, P. Arce, M. Asai, D. Axen, S. Banerjee, G. Barrand, et al. *Geant4-a simulation toolkit*, volume 506 of *Nuclear Instruments and Methods in Physics Research-Section A Only.* Amsterdam: North-Holland, 1984-, 2003.

[74] A.A. Mikhailichenko. *Lithium Lens for Positron Production System*, volume 25 of *EPAC08-WEPP157, June.* 2008.

[75] I. Antcheva, M. Ballintijn, B. Bellenot, M. Biskup, R. Brun, N. Buncic, P. Canal, D. Casadei, O. Couet, V. Fine, et al. *ROOT: A C++ framework for petabyte data storage, statistical analysis and visualization*, volume 182 of *Computer Physics Communications.* Elsevier, 2011.

[76] M. Jenkins and I. R. Bailey. *Novel designs for undulator based positron sources.* IEEE, 2012.

[77] I. Vasilief. *QtiPlotdata analysis and scientific visualisation.* 2011.

[78] A.A. Mikhailichenko. *Independent Operation of Electron/Positron Wings of ILC.* 2006.

[79] S. Wolfram. *The Mathematica Book.* Wolfram Media, Incorporated, 1996.

[80] S. A. Bogacz, J. Ellis, L. Lusito, D. Schulte, T. Takahashi, M. Velasco, M. Zanetti, and F. Zimmermann. *SAPPHiRE: a Small Gamma-Gamma Higgs Factory.* arXiv preprint arXiv:1208.2827. 2012.

[81] K. Aoki, K. Hosono, T. Hadame, H. Munenaga, K. Kinoshita, M. Toda, S. Amano, S. Miyamoto, T. Mochizuki, M. Aoki, et al. *High-energy photon beam production with laser-Compton backscattering*, volume 516 of *Nuclear Instruments and Methods in Physics Research Section A: Accelerators, Spectrometers, Detectors and Associated Equipment.* Elsevier, 2004.

[82] J. A. Clarke, D. Angal-Kalinin, R. Bartolini, D. J. Dunning, S. Jamison, J. K. Jones, I. P. S. Martin, J. W. McKenzie, B. L. Militsyn, N. R. Thompson, et al. *CLARA: a proposed new FEL test facility for the UK*, volume 12 of *IPAC.* 2012.

[83] K. Yokoya. *CAIN,: A computer simulation code for the interaction of electron, positron, gamma beams and strong lasers.* available at http://www-acc-theory. kek. jp/members/cain/i.